anshul

Thesis_final_draft.pdf

Indian Institute of Technology Jodhpur

Document Details

Submission ID
trn:oid:::29334:140635931

Submission Date
May 27, 2026, 2:02 PM GMT+5:30

Download Date
May 27, 2026, 2:33 PM GMT+5:30

File Name
Thesis_final_draft.pdf

File Size
13.8 MB

234 Pages

56,076 Words

310,334 Characters

7% Overall Similarity

The combined total of all matches, including overlapping sources, for each database.

Filtered from the Report

- Bibliography
- Quoted Text
- Cited Text
- Small Matches (less than 10 words)

Exclusions

- 3 Excluded Sources
- 119 Excluded Matches

Match Groups

252 Not Cited or Quoted 7%
Matches with neither in-text citation nor quotation marks

0 Missing Quotations 0%
Matches that are still very similar to source material

0 Missing Citation 0%
Matches that have quotation marks, but no in-text citation

0 Cited and Quoted 0%
Matches with in-text citation present, but no quotation marks

Top Sources

4% Internet sources
3% Publications
3% Submitted works (Student Papers)

Integrity Flags

0 Integrity Flags for Review

No suspicious text manipulations found.

Our system's algorithms look deeply at a document for any inconsistencies that would set it apart from a normal submission. If we notice something strange, we flag it for you to review.

A Flag is not necessarily an indicator of a problem. However, we'd recommend you focus your attention there for further review.

Match Groups

252 Not Cited or Quoted 7%
Matches with neither in-text citation nor quotation marks

0 Missing Quotations 0%
Matches that are still very similar to source material

0 Missing Citation 0%
Matches that have quotation marks, but no in-text citation

0 Cited and Quoted 0%
Matches with in-text citation present, but no quotation marks

Top Sources

4% Internet sources
3% Publications
3% Submitted works (Student Papers)

Top Sources

The sources with the highest number of matches within the submission. Overlapping sources will not be displayed.

1	Internet	
jnep.sumdu.edu.ua		<1%
2	Submitted works	
Karunya University on 2018-05-19		<1%
3	Internet	
link.springer.com		<1%
4	Submitted works	
City University of Hong Kong on 2025-06-20		<1%
5	Internet	
ir.library.nitw.ac.in:8080		<1%
6	Publication	
Anshul, Rishu Chaujar. "Numerical Evaluation of the Gate Stacked GNR FET for im...		<1%
7	Internet	
dspace.chitkara.edu.in		<1%
8	Publication	
Khurshed Ahmad Shah, Farooq Ahmad Khanday. "Nanoscale Electronic Devices a...		<1%
9	Submitted works	
Gujarat Technological University on 2026-03-05		<1%
10	Submitted works	
Indian School of Mines on 2017-09-23		<1%

11 Publication
Sweepe, Richard Thomas, III. "Fabrication and Integration Strategies for Atomical... <1%

12 Internet
documents.mx <1%

13 Internet
mobt3ath.com <1%

14 Internet
www.ideals.illinois.edu <1%

15 Submitted works
IIT Delhi on 2026-05-20 <1%

16 Internet
cmt.dur.ac.uk <1%

17 Internet
tudr.thapar.edu <1%

18 Publication
Jwaifel, Arwa Mahmoud Yousef. "Analysis of Some Cooperative Methods for Wirel... <1%

19 Publication
Tahereh Radsar, Hassan Khalesi, Vahid Ghods. "Graphene NanoRibbon Field Effec... <1%

20 Publication
Blackwell, Raymond E.. "Exploration of Magnetic Edge and Dopant States in Nano... <1%

21 Internet
d-scholarship.pitt.edu <1%

22 Internet
hdl.handle.net <1%

23 Internet
www.vliz.be <1%

24 Publication
Huda Yahya Maky, Gholamreza Karimi, Fouad N. Ajeel. "Engineering thermoelect... <1%

25 Submitted works
University of Mosul on 2026-03-15 <1%

26 Internet
ojs.uok.edu.in <1%

27 Internet
publications.lib.chalmers.se <1%

28 Publication
Afreen Khursheed, Kavita Khare. "Nano Interconnects - Device Physics, Modeling ... <1%

29 Internet
lib.buet.ac.bd:8080 <1%

30 Internet
tel.archives-ouvertes.fr <1%

31 Submitted works
Graphic Era University on 2016-06-22 <1%

32 Submitted works
National Institute of Technology, Silchar on 2022-05-10 <1%

33 Publication
Navjeet Bagga, Saheli Sarkhel. "Emerging FET architectures—part II", Elsevier BV,... <1%

34 Submitted works
University of North Texas on 2017-04-25 <1%

35 Internet
archive.org <1%

36 Internet
dokumen.pub <1%

37 Internet
dspace.iiti.ac.in <1%

38 Internet
pdfcoffee.com <1%

39 Internet
theses.gla.ac.uk <1%

40 Publication
Naderi, Ali, and Parviz Keshavarzi. "Electrically-activated source extension graphe... <1%

41 Internet
shizuoka.repo.nii.ac.jp <1%

42 Publication
Bikramjit Basumatary, Agile Mathew. "Electronic and transport properties of U-c... <1%

43 Submitted works
IIT Delhi on 2016-04-04 <1%

44 Submitted works
Manipal University on 2021-04-14 <1%

45 Submitted works
VIT University on 2011-04-14 <1%

46 Submitted works
Rutgers University, New Brunswick on 2021-11-30 <1%

47 Submitted works
Anna University on 2026-05-11 <1%

48 Publication
Elnaeem, Mohammed Altahir Eliebid. "Measurements of Two- and Three-Phase R... <1%

49 Submitted works
Nanyang Technological University on 2026-04-16 <1%

50 Submitted works
Polytechnic of Turin on 2024-10-07 <1%

51 Internet
boristheses.unibe.ch <1%

52 Publication
Amir Mohammad Karimi Forood, Maryam Nayeri, Melikasadat Jalalat Atashgah, E... <1%

53 Publication
Bhavya Kumar, Ajay Kumar, Rishu Chaujar. "The Effect of Gate Stack and High-κ S... <1%

54 Publication
Bhavya Kumar, Rishu Chaujar. "Numerical Study of JAM-GS-GAA FinFET: A Fin Asp... <1%

55 Publication
Christina Dinh, Muhammed Yusufoglu, Kentaro Yumigeta, Amogh Kinikar et al. "... <1%

56 Submitted works
Delhi Technological University on 2019-10-30 <1%

57 Submitted works
Higher Education Commission Pakistan on 2024-08-21 <1%

58 Publication
Khalil Tamersit, Mohammad Khaleqi Qaleh Jooq, Mohammad Hossein Moaiyeri. "... <1%

59 Publication
Li, Wenwen. "Design and Fabrication of Vertical GaN Transistors for High-Power a... <1%

60 Publication
Linton, Nathan. "Integrating DFT and Machine Learning to Predict Structural Pro... <1%

61 Publication
Md Akram Ahmad, Bhubon C. Mech. "Impact of JL Structure on Analog/RF Parame... <1%

62 Submitted works
Tikrit University on 2026-02-07 <1%

63 Internet
backend.orbit.dtu.dk <1%

64 Internet
ethesis.nitrkl.ac.in <1%

65 Publication
Argiles Castillo, Diana. "Biochemical and Structural Studies of HACE1: A Human H... <1%

66 Submitted works
Dublin City University on 2017-04-18 <1%

67 Submitted works
IIT Delhi on 2022-07-12 <1%

68 Submitted works
Indian School of Mines on 2026-05-03 <1%

69 Publication
M. Pourfath, A. Yazdanpanah, M. Fathipour, H. Kosina. "On the role of line-edge r... <1%

70 Publication
M. Pourfath. "Separated carrier injection control in carbon nanotube field-effect t... <1%

71 Internet
arxiv.org <1%

72 Internet
digitalassets.lib.berkeley.edu <1%

73 Internet
www.hindawi.com <1%

74 Internet
www.slideshare.net <1%

75 Publication
Amir Ghadiyani, Hossein Karimiyan Alidash. "New Approach for Designing and O... <1%

76 Publication
Dimitrijev, Sima. "Principles of Semiconductor Devices; International Second Editi... <1%

77 Submitted works
Indian School of Mines on 2023-05-10 <1%

78 Publication
Kallolini Banerjee, Abhijit Biswas. "Improvement of digital, analog/RF and linearit... <1%

79 Publication
Naveen Kumar, Prateek Kumar, Ankit Dixit, Prabhat Singh. "Classical to Quantum... <1%

80 Submitted works
Rochester Institute of Technology on 2017-04-20 <1%

81 Submitted works
Sim University on 2016-05-04 <1%

82 Submitted works
UBDCanvasLTI1.3 on 2025-09-21 <1%

83 Submitted works
Universiti Teknologi Malaysia on 2017-11-27 <1%

84 Submitted works
University of Florida on 2007-07-31 <1%

85 Publication
Vanitha Indhur, Umamaheshwari Dupati, Manasa Lakkarasu, sravya sanga et al. ... <1%

86 Internet
hi.tamu.edu <1%

87 Internet
intech-files.s3.amazonaws.com <1%

88 Internet
koreascience.kr <1%

89 Internet
repos.ust.edu.sd:8080 <1%

90 Publication
"Advanced Ultra Low-Power Semiconductor Devices", Wiley, 2023 <1%

91 Publication
"First-Principles Simulations of Electron Transport in Atomic-Scale Systems", Han... <1%

92 Publication
"Nanoscale CMOS", Wiley, 2013 <1%

93 Submitted works
ABV-Indian Institute of Information Technology and Management Gwalior on 202... <1%

94 Publication
Arnab Som, Meenu Yadav, Sanjay Kumar Jana. "Design and analysis of gate under... <1%

95 Publication
Cleghorn, William. "Mechanics of Machines", Oxford University Press <1%

96 Publication
Hot Carrier Design Considerations for MOS Devices and Circuits, 1992. <1%

97 Publication
I. Lindgren. "Construction of accurate Kohn-Sham potentials for the lowest states... <1%

98 Submitted works
Jyväskyla University on 2022-06-14 <1%

99 Submitted works
King Abdullah University of Science and Technology (KAUST) on 2025-11-29 <1%

100 Publication
Klaus D. Sattler. "Fundamentals of PICOSCIENCE", CRC Press, 2013 <1%

101 Publication
Md Akram Ahmad. "Analog and RF Performance Analysis of Double-Gate CNT-FET... <1%

102 Submitted works
National Institute of Technology, Silchar on 2015-05-27 <1%

103 Publication
Nazanin Baghban Bousari, Mohammad K. Anvarifard, Saeed Haji-Nasiri. "Improvi... <1%

104 Publication
Nhlabatsi, Zanele Precious. "Formation of Glycine in the Interstellar Medium: Co... <1%

105 Publication
Patidar, Sunil Kumar. "Dispersion Corrected Density Functional Theory Study of Si... <1%

106 Publication
Rajamohanan, Bijesh. "Fabrication, Characterization and Physics of III-V Tunnelin... <1%

107 Publication
Ramesh Kumar Vobulapuram, Javid Basha Shaik, Venkatramana P., Durga Prasad ... <1%

108 Submitted works
Rochester Institute of Technology on 2023-05-04 <1%

109 Publication
Shital Joshi, Saraju P. Mohanty, Elias Kougianos, Venkata P. Yanambaka. "Graphe... <1%

110 Publication
Taki Eddine Taouririt, Afak Meftah, Nouredine Sengouga. "Effect of the interfacial... <1%

111 Submitted works
Universiti Teknologi Malaysia on 2011-11-24 <1%

112 Submitted works
University of Technology, Sydney on 2009-11-09 <1%

113 Submitted works
VIT University on 2025-03-21 <1%

114 Publication
Youngki Yoon. "Performance Comparison of Graphene Nanoribbon FETs With Sch... <1%

115 Internet
burjcdigital.urjc.es <1%

116 Internet
d-nb.info <1%

117 Internet
tdr.lib.ntu.edu.tw <1%

118 Internet
ufdc.ufl.edu <1%

119 Internet
www.repository.cam.ac.uk <1%

120 Internet
www.science.gov <1%

121 Publication
"Handbook of Graphene", Wiley, 2019 <1%

122 Submitted works
Anna University on 2025-10-29 <1%

123 Publication
Anurag Bhandari, Nitin K. Puri, Piyush Dua, Rishu Chaujar. "A deep insight into th... <1%

124 Publication
Arash Yazdanpanah Goharrizi, Mahdi Pourfath, Morteza Fathipour, Hans Kosina. ... <1%

125 Publication
Atiye Khosravi, Xichun Luo, Wenkun Xie, Xiaolei Zhang. "First-principles mechanis... <1%

126 Submitted works
Birla Institute of Technology and Science Pilani on 2024-05-19 <1%

127 Publication
Brenner, Kevin A.. "Benchmarking and Chemical Doping Techniques for Nanoscal... <1%

128 Publication
Chun, Ji Ye. "Efficient Computing for Three-Dimensional Quantitative Phase Imagi... <1%

129 Publication
D. S. L. Abergel. "Properties of graphene: a theoretical perspective", Advances In ... <1%

130 Publication
Declan Nell, Miloš M. Radonjić, Ivan Rungger, Liviu Chioncel, Stefano Sanvito, And... <1%

131 Submitted works
East Tennessee State University on 2024-04-01 <1%

132 Publication
Erfan Abbasian, Maedeh Orouji, Shilpi Birla, Sana Taghipour Anvar. "An Efficient ... <1%

133 Submitted works
IIT Delhi on 2015-06-22 <1%

134 Submitted works
Indian Institute of Technology, Kanpur on 2024-06-21 <1%

135 Publication
Islam, Md. Shariful. "Fabrication and Characterization of an In-Situ Nano-Mechani... <1%

136 Publication
Jeshanth Madda, Sresta Valasa, Venkata Ramakrishna Kotha, Sunitha Bhukya, Na... <1%

137 Publication
Jun Liang Looi, Yuki Wong, Nurul Ezaila Alias, Suhana Mohamed Sultan, Tian Swe... <1%

138 Publication
Köroğlu, Çağil. "Thermal Management and Transistor Modeling for Three-Dimens... <1%

139 Publication
Marzieh Ramezani Farani, Mohammadreza Esmaeilidehkordi, Iraj Alipourfard, Ma... <1%

140 Publication
Md Kaab Bin Hossen, Istiak Ahmed Ovi, Md Anas Bin Hossen, Md Adil Hossain. "C... <1%

141 Publication
Mohammad Bagher Nasrollahnejad, Parviz Keshavarzi. "逆 Stone-Thrower-Wales ... <1%

142 Publication
Mohammad K. Anvarifard. "Non-Linearity and RF Intermodulation Distortion Che... <1%

143 Publication
Muhammad Riaz, M. Sana Ullah Sahar, Syed Mansoor Ali, Muhammad Faizan Sha... <1%

144 Submitted works
National University of Singapore on 2013-03-18 <1%

145 Submitted works
Ohio University on 2014-10-09 <1%

146 Publication
Pankaj Srivastava, Subhra Dhar, Neeraj K. Jaiswal. "Ab initio study of gold-doped z... <1%

147 Publication
Poonam Parkar, Ajay Chaudhari, Mahadev Rangnath Sonawane, Balasaheb Jijaba ... <1%

148 Publication
R. Bhuvaneswari, V. Nagarajan, R. Chandiramouli. "Molecular interaction studies ... <1%

149 Publication
Ruolan Wen, Zhenhong Jiang, Rui Miao, Lei Wang, Yujian Liang, Jingui Deng, Qing... <1%

150 Publication
Shasanka Sekhar Rout, Akash Saxena, Suman Lata Tripathi. "Smart Electronics De... <1%

151 Submitted works
University of California, Los Angeles on 2016-03-17 <1%

152 Submitted works
University of Florida on 2012-04-26 <1%

153 Submitted works
University of Witwatersrand on 2024-03-19 <1%

154 Submitted works
Unizin, LLC on 2025-06-09 <1%

155 Submitted works
VIT University on 2013-05-29 <1%

156 Internet
assets-eu.researchsquare.com <1%

157 Internet
docs.quantumwise.com <1%

158 Internet
docshare.tips <1%

159 Internet
dr.ntu.edu.sg <1%

160 Internet
era.ed.ac.uk <1%

161 Internet
etds.lib.ncku.edu.tw <1%

162 Internet
fa.ee.sut.ac.ir <1%

163 Submitted works
iGroup on 2018-07-05 <1%

164 Internet
ikee.lib.auth.gr <1%

165	Internet	
monarch.qucosa.de		<1%
166	Internet	
mspace.lib.umanitoba.ca		<1%
167	Internet	
pdffox.com		<1%
168	Internet	
repositories.lib.utexas.edu		<1%
169	Internet	
repository.iiitd.edu.in		<1%
170	Internet	
tud.qucosa.de		<1%
171	Internet	
vtechworks.lib.vt.edu		<1%
172	Internet	
www.dtic.mil		<1%
173	Internet	
www.duo.uio.no		<1%
174	Internet	
www.researchgate.net		<1%
175	Internet	
www.sid.ir		<1%

SEMI - EMPIRICAL DFT - BASED ATOMIC SCALE MODELING OF GATE-STACK ARMCHAIR GRAPHENE NANORIBBON FET FOR PERFORMANCE ENHANCEMENT AND SENSOR APPLICATION

A Thesis Submitted
In Partial Fulfillment of the Requirements
for the degree of

DOCTOR OF PHILOSOPHY

by

Anshul
(Roll No. 2K20/PHDAP/502)

Under the Supervision of

Prof. RISHU CHAUJAR
Professor, Department of Applied Physics
Delhi Technological University

Department of Applied Physics
DELHI TECHNOLOGICAL UNIVERSITY
(Formerly Delhi College of Engineering)
Shahbad Daulatpur, Main Bawana Road, Delhi-110042. India

May 2026

Dedicated to

my

Papa & Mimo

nows t₃ ol s µ– w– r tl hw µt oκ₂ t₃

3Y⁵⁶—ε³⁵¹ ' '"(— b η⁻⁶9η−W'ε¹ ³ ⁻³"' T"⁶ Gη−CAAK4

.Pö≠ s≠z"%Nszvw%Mözzsus%öt%OÅuwÅss≠wÅu/

%%%%%%%%%%%%%%%%vovpor No. zo≈ü. ≠2Lo—oÅo] öor 2%Nszvw37766: 8

l hµntnh₃ o≡₂ (nol whκh₃ t– µ

S%sqzo≠s%vo≈%vs%s±so≠qv%ö≠y%ö≠s±sÅ≈sr %Å%vw±%vs±w±%Å≈wzsr %±% ***Semi - empirical DFT - based Atomic Scale Modeling of Gate-Stack Armchair Graphene Nanoribbon FET for Performance Enhancement and Sensor Application*** %ö≠%vs%ö≈owÅ~ sÅ≈%öt%vs%su≠ss%öt%Nöq≈ö≠%öt%Zvwzö±öüv"% wÅ%Zv"±wq±%vo±%pssÅ%qöÅr .q≈sr %p"% s2%.År s≠%vs%u..wzoÅqs%öt%Z≠öt4%] w±v..%Mvo. xo≠%t≠ö~ %vs% Nsüo≠≈ sÅ≈%öt%Küüzwsr %Zv"±wq±2%Nszvw%bsqvÅözöuwqoz%o Åw≈s≠±w≈"2%Nszvw%bvw±%ö≠y%vo±%Åö≈%pssÅ% ü≠s–wö. ±z"%.p~ w≈sr 2%w≈s≠%üo≠≈wzz"%ö≠%Å%w±%Å≈ws≈"2%ö%Å"%ö≈vs≠%oqor s~ wq%Å±≈w. ≈wöÅ%tö≠%Å"% r su≠ss%ö≠%wüzö~ o4%S%sqzo≠s%vo≈%vw±%vs±w±%stzsq≈±%~ "%wso±%s"ü≠s±±sr %Å%~ "%ö—Å%ö≠r ±4% e vs≠s–s≠%vs%wso±%ö≠%ö≠r ±%öt%ö≈vs≠±%o–s%pssÅ%Åqö≠üö≠o≈sr 2%üü≠öü≠wo≈s%qwo≈wöÅ%År %st s≠sÅqwÅu% vo–s%pssÅ%ü≠ö–wsr %ö%qyÅö—zsr us%vs%ö. ≠qs±4%S%oz±ö%qöÅtw≠~ %vo≈%S%o–s%.üvszr %vs%ü≠wÅqwüzs±% öt%oqor s~ wq%öÅs±≈"%År %Å≈su≠w≈"%År %vo≈%S%o–s%Åö≈%o w≠sü≠s±sÅ≈sr 2%op≠wqo≈sr 2%ö≠%oz±wtwsr %Å"% wÅtö≠~ o≈wöÅ2%o≈o2%oq≈2%ö≠%ö. ≠qs±%Å%~ "%.p~ w±±wöÅ4%

x Q.h

] özz%X ö4%U865ZRNKZ5=68%

Nsüo≠≈ sÅ≈%öt%Küüzwsr %Zv"±wq±%

Nszvw%bsqvÅözöuwqoz%o Åw≈s≠±w≈"%

nows t₃ ol s µ– w– r tl h w µt oκ₂ t₃

3Y⁵⁶—ε³⁵¹ ’ ”(— b η⁻⁶9η–W’ε¹ ³ ⁻³’’’ T“⁶ Gη–CAAK4

.Pö≠~ s≠z’’%szvw%bzzsus%t%ÅuwÅss≠wÅu/

%%%%%%%%%%%%%%%%%vovpor No. zo~ü. ≠2Lo—oÅo] öor 2%szvw37766: 8

<u>CERTIFICATE</u>

b vw≠%w≠%ö%φs≠w’’%vo≈%vs%vs±w≠%wzsr % ***Semi - empirical DFT - based Atomic Scale Modeling of Gate-Stack Armchair Graphene Nanoribbon FET for Performance Enhancement and Sensor Application*** %w≠%psWÅu%.p~ w≈sr %p’’ ***Ms. Anshul*** with registration number ***2K20/PHDAP/502*** to the Delhi Technological University for the award of the degree of Doctor of Philosophy in Physics. The work embodied in this thesis is a record of Bonafide research work carried out by me in the Microelectronics Research Lab, Department of Applied Physics, Delhi Technological University (Formerly Delhi College of Engineering), New Delhi, under the guidance of ***PROF. RISHU CHAUJAR***. It is further certified that this work is original and has not been submitted in part or fully to any other University or Institute for the award of any degree or diploma.

Anshul

Roll No.2K20/PHDAP/502

This is to certify that the above statement made by the candidate is correct to the best of our knowledge.

a **.**	***a*** **.**
n⁸ µ’⁴⁻³⁵η⁴(3k⁴η–’⁵⁵η⁴4(	*c ’–’’(η–(W’µ–⁴⁶β ’γ⁶*
W’µ–⁴⁶β ’γ⁶(η–(Tµµε³’ ’’(k¹ ⁵³“⁵	*W’µ–⁴⁶β ’γ⁶(η–(Tµµε³’ ’’(k¹ ⁵³“⁵*
W’ε¹ ³(o’ “¹ γηεη×³“–ε(p γ³⁻ ’⁴⁵³⁶	*W’ε¹ ³(o’ “¹ γηεη×³“–ε(p γ³⁻ ’⁴⁵³⁶*
W’ε¹ ³7(dy ’’³–	*W’ε¹ ³7(dy ’’³–*

ACKNOWLEDGMENTS

My Ph.D. journey has been much more than an academic experience; it has been a journey of personal growth and transformation. When I started, I lacked patience, confidence and even the basic research skills that this work demanded. Over time, through continuous learning and the challenges that came with it, I grew both as a researcher and as an individual. There were many ups and downs, especially in the initial phase when my papers were not getting accepted, but the constant support of my family and close friends gave me the strength to keep moving forward. This journey has taught me resilience, patience and the importance of believing in myself. Looking back, I realise that my Ph.D. has not only contributed to my academic development but has also shaped me into a stronger and more mature person.

27 *I would like to sincerely thank my supervisor,* ***Prof. Rishu Chaujar****, for your constant support, encouragement, and belief in me throughout this journey. This Ph.D. would not have been possible without your guidance. You have always supported me with kindness and care, while also making sure I stayed focused whenever I lost track of my work or deadlines. I am especially grateful for the way you carefully and timely reviewed every document, thesis chapter, and research work throughout my Ph.D. Your prompt feedback and constant attention made this journey much smoother and more manageable for me. What I admire most about you is not just your academic guidance, but also the kind and understanding person you are. I truly feel fortunate to have had such an inspiring* [illegible] *learned many valuable life lessons from you, that will stay with me forever. Thank you,* [illegible]

I am thankful to ***Prof. Vinod Singh*** *(DRC Chairman and HoD, Applied Physics, DTU) and* ***Prof. Prateek Sharma*** *(Vice Chancellor, DTU) for providing the necessary resources to facilitate the research activity. I further thank the experts and members of the SRC and DRC*
117 *for generously dedicating their valuable time to serve on my committee and providing their invaluable support of my thesis.*

68 *Also, I thank all the faculty members of the Department for their helpful recommendations*

and advice during my Ph.D. journey. I appreciate all the care and support shown to me by the Staff Members of the Department (especially ***Babita Ji****,* ***Deepak Ji****,* ***Suresh Ji****,* ***Krishna Ji****, and* ***Naresh Ji****).*

The Ph.D. journey feels overwhelming in the beginning because everything including the research culture, environment, and way of working was completely new. During that phase, having a supportive senior makes all the difference, and I feel truly fortunate to have ***Dr. Bhavya Kumar*** *as my senior. I still remember when I first joined the lab; you was among the first people who made me feel comfortable and welcomed. Sir, you have taught me so many things like plotting graphs properly and maintaining their quality to understanding how research papers should actually be presented. Your guidance in both research and life* ¹ ’ɛμ’ ’’(β ’(×⁴η₂ (–(ɛη⁶9(d(⁵⁶³ɛ(⁵β ³ε’(⁴ ’β ’β —’⁴³γ ×(⁶¹ ’(₂ – (η⁸ (⁸ ⁵ ’ ’’(⁶η(–⁵α7(T⁸ ⁴(—⁶–ηR (³γ(⁶¹ ’(⁴ ’⁵ ’–⁴ ‘¹ (‘ηγ⁶’₃ ⁶7(₂ ¹ ³ε’(d(₂ η⁸ε’’(‘–⁵⁸ –ɛ (⁴ ’με 7(n³⁴7(⁵—(—’’¹ ³ –7(—μ(—⁶– ³ ’7 (–γ ’’(*then you would just silently look at me for a few seconds. More than a senior, you have been like an elder brother to me. Whenever I needed guidance or support, you were always there. Thank you so much, sir, for all your support and encouragement throughout this journey. Also, I want to thank* ***Dr. Samriti Sharma****,* ***Dr. Megha Sharma****,* ***Dr. Mekonenn Getnet****,* ***Dr. Yash Pathak*** *for all the healthy discussions we had in lab that have helped me through this journey. Next, I want to thank* ***Dr. Ankita banwal*** *who offered valuable advice for navigating the challenges in the professional and personal life.*

Among all the blessings this Ph.D. journey gave me, I consider myself the most fortunate to found a labmate who became a friend, a sister, and family to me, ***Dr. Rashi Mann****. You have helped me in ways I can never fully express. I still remember the phase when I spent days and nights running simulations continuously for months, yet nothing was working and no results were coming. At that time, you patiently guided me every single day by suggesting* γ ’₂ (–μμ⁴η–‘¹ ’⁵7(–γ ’’(‘ηγ⁵⁶–γ⁶ε (β η⁶³⁻–⁶³γ ×(β ’(—(⁵– ³γ ×7(u ’(⁶⁴y kar sakte hain, ye paper μ–’’¹ (ɛη9 (a⁴ηβ (⁵ηε⁻³γ ×(⁴ ’⁵ ’–⁴ ‘¹ (μ⁴η–ɛ’β ⁵(⁶η(¹ –γ ’’ε³γ ×(ε³–’(’’³⁵ ‘⁸ ⁵⁵³ηγ ⁵7(η⁸ (₂ ’⁴ ’(–ɛ₂ – ⁵(*there for me. Thank you for always helping me, supporting me, choosing what was right for me, and even scolding me whenever I was wrong. Badi Didi, you truly hold a very special place in my life.*

When it comes to my juniors (***Ayushi Lamba****,* ***Dr. Kajal Verma****,* ***Shubhda,Vishal Deswal,***

Shikha Singh, Ashish Chopra, Kajal Sharma, Anu, Vipin, Dedraj, Vishwas kumar, Aman, and Kislay Kumar *), the love, respect, care, and comfort I received from you guys made this journey so much more special and memorable. Even though we shared a senior-junior relationship, it never felt formal; instead, it always felt warm, genuine, and full of support. Whether it was helping each other with work, sharing random conversations, laughing together, or simply spending time in the lab, every moment became a beautiful memory for me.* ***Ayushi Lamba****, you have always been like a younger sister to me, and I deeply cherish our bond.* ***Shubhda, Vishal, Ashish, and Shikha*** *gave me some of the funniest and happiest lab memories. I also appreciate* ***Vipin, Anu, and Kajal Sharma*** *for their respect and admiration.* ***Aman and Kislay Kumar*** *you both are absolute lifesaver! Whenever I request your help, you both effortlessly takes care of all the tasks, leaving me worry-free. Also, I would like to thank* ***Sushil Kumar, Dr. Yakshansh Kumar, Abhishek Saini, Ashwani Sharma, Abhishek Verma, Naresh Nautiyal, Naveen Kumar, Preeti Pateriya, Tanuj Kumar, Sandeep Bahgel, Navodit, Anurag Bhandari, Dr. Megha Narwan and Dr. Shaveta*** *for being the incredible friends9d m grateful for your presence in my life. Among them,* ***Sushil Kumar****, you are not just my best friend but also the best brother I found at DTU and my personal secret diary. Thank you, bhaiya, for always standing by me whenever I needed support. From bringing home-cooked food when I was sick to always being there during difficult times, your care and support truly mean a lot to me.*

22 *I would like to express my heartfelt gratitude to my husband,* ***Adv Akash Dalal****, for your unconditional love, understanding, and constant support throughout this journey. From supporting me during my thesis writing to reminding me about deadlines and motivating me to complete chapters on time, you always stood by me at every step. Whenever I felt stressed η⁴(η⁻’⁴₂ ¹’εβ’”7(η⁸(–ε₂ – ⁵(“ηβ –η⁴⁶’”(β’(—(⁵– ³γ ×7(o’γ⁵³ηγ(β –⁶(εη7β –³γ(¹ ηηγ(γ–7(—⁵(–μγ’(α—β(μ–⁴(–η“⁸⁵(α–⁴η7(–γ”(⁶¹η⁵’(₂ η⁴”⁵(×–⁻’(β’(³β β’γ⁵’(⁵⁶⁴’γ ×⁶¹(–γ d peace. Your “ηγ⁵⁶–γ⁶(’γ“η⁸⁴–×’β’γ⁶7(’⁵μ’“³–æ(Wη(₂ ¹–⁶’⁻’⁴(³⁵(—’⁵⁶(–η⁴(η⁸7U——7(–ε₂ – ⁵(β –”’(β’(feel supported and understood. Thank you love for always being there for me through every phase of this journey.*

135 *I owe my deepest gratitude to my father,* ***Mr. Rampal Singh****, and my mother,* ***Mrs. Kamla,*** *whose love and support have been my greatest strength throughout this journey. Papa, without you, none of this would have been possible. Whatever I am today and whatever I*

*have achieved is because of your constant motivation, belief in me, and encouragement to always move forward in life. I can never repay everything you have done for me. My sweet Mimo, you have always taken care of me with so much love and affection. From asking whether I had eaten properly to constantly reminding me to take care of my health, while managing my work. Your care gave me emotional strength during the toughest times. You both are truly my biggest support system, and I will always remain grateful for your unconditional love and sacrifices. I would also like to dedicate this achievement to my late younger brother, **Anirudh**, whose love, memories, and presence still remain close to my heart and continue to give me strength every day. I also dedicate this thesis to my late grandmother, **Mrs. Dhanno Devi**9(W–"³7(η⁸⁴(εη⁻'7(–ε'⁵⁵³γ×⁵7(–γ"(₂ η⁴"⁵(f⁸⁵³(—'⁶–7(³γ"–×³(β'³γ(μ–"¹(α–⁴(α⁸"¹(—γγ–(–⁸⁴(—¹⁸⁶(–"¹'(α—β(α–⁴γ–7(α³⁵³(αη("⁸α¹(β–⁶("'γ– (⁵⁶³εε(motivate and inspire me every day. Thank you dadi for always being my source of strength and love.*

*I would also like to express my sincere gratitude to my father-in-law, **Mr. Ashok Dalal**, for his constant support, wisdom, and encouragement throughout my Ph.D. journey. Papa ji, you always motivated me to stay positive, focus on my work, and keep moving forward in life without taking unnecessary stress. Your guidance and kind words gave me confidence during difficult phases. I am equally thankful to my mother-in-law, **Mrs. Suman Dalal**, whose love, care, and affection have been a constant source of comfort for me. During my thesis-writing phase, she took such good care of me and pampered me with so much warmth that she truly made me feel like her own daughter. Before marriage, I had many fears about relationships, but you made me realize that a mother-in-law can truly be like a mother. I feel incredibly grateful and fortunate to have both of them in my life. I would also like to thank my brother-in-law, **Sagar**, for being such an inspiring person. Although our interactions have been limited, the dedication and sincerity with which you work always motivate me to stay focused and disciplined in my own life. You are truly a wonderful person, and I have learned a lot just by observing your commitment and work ethic.*

*When I shifted to a rented place during my Ph.D. journey, I never imagined that I would form such a close bond with my landlords and their family. I would like to sincerely thank **Mrs. Santosh Devi** and **Mr. Naresh Kumar** for treating me like their own daughter and always taking care of me whenever I was unwell. I am equally grateful to **Tarun Bhaiya***

and ***Rakhi Bhabhi*** *for their love and warmth.* ***Bhaiya*** *and* ***Bhabhi****, I have countless fun memories with you both. You are truly like my buddies and besties, and every moment spent together has always been filled with laughter, comfort, and happiness. A special thanks to* ***Puneet Bhai*** *for always making me laugh and helping me whenever needed.* ***Monit****, my little nephew, your innocent love and cheerful presence always made my stressful days feel lighter and happier. I would also like to thank my younger sister,* ***Amrita****, for always supporting me and being there for me. Talking to you always brought me comfort and happiness, and whenever you stayed with me, everything felt much better. I truly wish you achieve great success and happiness in life. Thank you for always standing by my side. I would also like to sincerely thank my entire family members, whose love, encouragement, and support in different ways continuously motivated me throughout my Ph.D. journey.*

d(d(1 –⁻ ’(8 γ 3γ 6’γ 63ηγ–εε (β 355 ’ ”(β ’γ 63ηγ 3γ ×(–γ ηγ ’ 5(γ–β ’7(d(2 η 8 ε”(563εε(ε3α’(6η(53γ “’4 ’ε (thank every person who, in any way, became a part of my Ph.D. journey and supported me throughout this phase of my life.

Last but not least, I would like to dedicate all that I am and all that I have achieved to ***Lord Krishna****, whose divine blessings, guidance, and grace gave me the strength, courage, and purpose to complete this journey. I feel deeply grateful for His presence in my life and for blessing me with this beautiful human birth and the opportunity to grow, learn, and serve.*

(Anshul)

New Delhi, 2026

ABSTRACT

Semi - empirical DFT - based Atomic Scale Modeling of Gate-Stack Armchair Graphene Nanoribbon FET for Performance Enhancement and Sensor Application

The continuous downscaling of conventional MOSFETs has reached a point where short-channel effects, leakage, and static power dissipation increasingly limit further miniaturization, and motivate researchers to find new material for channel and device architectures that can overcome these limitations. Among the emerging materials, armchair graphene nanoribbons (AGNRs) offer tunable bandgaps, atomically smooth edges, and quasi-ballistic transport, making them well suited for replacing the silicon channel in next-generation field-effect transistors. The present thesis develops an atomistic-scale investigation of a gate-stack armchair graphene nanoribbon field-effect transistor (GS-AGNRFET) using Quantum ATK simulation tool and systematically examines dielectric engineering, channel-width engineering, computational-model reliability, and edge-passivation chemistry for the dual for ultra-low-power logic and gas sensing applications.

The present study begins with a density functional theory-based analysis of the GS-AGNRFET, in which the gate-stack architecture reduces the off-state current by nearly 73% and improve the switching ratio (SR) by a factor of approximately 213 over the conventional GNRFET. A temperature-dependent analysis from 250 K to 350 K reveals reduction by 48% in on-state current, degradation of SR by 98%, increase in subthreshold swing by 56%, which confirms that the proposed device is suitable for low-temperature regimes such as cryogenic electronics and biomedical instrumentation. Further, edge passivation of AGNR with boron (13^{th} group element) reduces the bandgap and raise the density of states near the Fermi level and reduces the off-state current by ~7.8×10^5 times, enhances the on-state

current by ~139 times, and improving the SR from ~7.1 × 10^3 to ~1.45 × 10^8 relative to the pristine AGNRFET. After this, channel-width engineering is subsequently examined for AGNRs belonging to the 3p + 1 family (N = 4, 7, 10, 13) using a Slater Koster DFT framework. The study shows that the GS AGNR (N = 4) FET exhibits the largest bandgap of approximately 1.98 eV, suppressed density of states near the Fermi level, and superior gate control. Also, GS AGNRFET shows improved transfer qvo≈s≠o≈w± over all other configurations, which is further confirmed through transmission spectra analysis, projected density of states analysis and electrostatic potential profiles. Further, to analyze the reliability of the findings across simulation methodologies, the Extended Hückel (EH) model with self-consistent iteration within the NEGF formalism is then employed. The comparison between the AGNR (N = 4) and AGNR (N = 7) as a channel material in device configurations using EH model shows that widening the channel from N = 4 to N = 7 increases the on-state current by 481 times, lowers the off-state current by 99.92%, reduces the threshold voltage by 27.59%, and improves DIBL by 16%. After that, the study of edge passivation using the remaining Icosagens elements (group 13th elements namely Al, Ga, and In) indicates that passivation of heavier Icosagens atoms on AGNR (N = 7) shows metallic bandgap and therefore unsuitable for semiconducting use, whereas the same elements substantially enhance the performance of the AGNR (N = 4) channel. The aluminium passivated GS AGNRFET (Al-AGNRFET) shows improved results in terms of on-state current (rise from 1.06 µA to 18.4 µA), reduction of the off-state current, and improvement in SR. Also, transconductance, device efficiency, transmission probability, and transfer characteristics analysis highlights Al AGNRFET and Ga passivated GS AGNRFET are suitable candidates for high speed logic, low power memory devices, quantum computing in space exploration, and neuromorphic computing applications. Lasty, the proposed Al AGNRFET is analysed as a nanoscale gas sensor for the detection of toxic gases like NO_2 and NH_3 using a two-step methodology that combines Linear Cobination of Atomic Orbitals calculator for bulk configurations analysis and EH model for simulation at the device level. The pristine AGNR exhibits chemisorption with physically unrealistic recovery times, while the Al-passivated ribbon shows stable physisorption with recovery times of 5.4 × 10 ⁝ s for NO_2 and 1.1 × 10 $^{76\%}$s for NH_3. The sensitivity values of 736% for XY %År %7>+ %ö≠%XR %n Al AGNR, which are 3.36 and 6.60 times higher than the P-AGNR, respectively. At device level, ≈vs%üüö±ws%v≠s±vözr %öz≈ous%≥vwt≈%t%6476%1 %År %

+0.15 V under NH_3 and NO_2 exposure, along with an on-current-based selectivity coefficient of 12.12, confirm that the proposed Al - AGNRFET device is suitbale to detect and distinct between the two gases.

Overall, the proposed GS-AGNRFET device is optimised through gate-stack architecture, channel - width tuning, computational model reliability and Icosagens edge passivation, and shows high switching ratio, reduced off-state current, reliable performance at low temperature and selectively detect NO_2 and NH_3 gases. Owing to these improvements, the proposed device is a suitable candidate for use in low-power logic, toxic gas sensing, bio-medical applications and energy- efficient nanoelectronics areas.

TABLE OF CONTENTS

List Of Figures

LIST OF TABLES

List Of Abbreviations

AG-GNRFET	Asymmetric Gate Graphene Nanoribbon Field Effect Transistor
AGNR	Armchair Graphene Nanoribbon
AGNRFET	Armchair Graphene Nanoribbon Field Effect Transistor
Al-AGNR	Aluminium-passivated Armchair Graphene Nanoribbon
Al-AGNRFET	Aluminium-passivated Armchair Graphene Nanoribbon Field Effect Transistor
ATK	Atomistic Toolkit
B-AGNR	Boron-passivated Armchair Graphene Nanoribbon
B-AGNRFET	Boron-passivated Armchair Graphene Nanoribbon Field Effect Transistor
BTBT	Band-to-Band Tunneling
CMOS	Complementary Metal-Oxide-Semiconductor
CNT	Carbon Nanotube
CNTFET	Carbon Nanotube Field Effect Transistor
DFT	Density Functional Theory
DG-GNRFET	Double Gate Graphene Nanoribbon Field Effect Transistor
DIBL	Drain-Induced Barrier Lowering
DMG	Dual Material Gate
DMG-GNRFET	Dual Material Gate Graphene Nanoribbon Field Effect Transistor
DOS	Density of States
EBL	Electron Beam Lithography
EDP	Energy-Delay Product
EH	Extended Hückel
EPF	Extra Peak Electric Field
EPF-GNRFET	Extra Peak Electric Field Graphene Nanoribbon Field Effect Transistor
ESE	Electrically Activated Source Extension
FD-SOI	Fully Depleted Silicon-on-Insulator
FET	Field Effect Transistor
Ga-AGNR	Gallium-passivated Armchair Graphene Nanoribbon
GGA	Generalized Gradient Approximation

GNR	Graphene Nanoribbon
GNRFET	Graphene Nanoribbon Field Effect Transistor
GS	Gate Stack
GS-AGNRFET	Gate-Stack Armchair Graphene Nanoribbon Field Effect Transistor
HSQ	Hydrogen Silsesquioxane
IC	Integrated Circuit
In-AGNR	Indium-passivated Armchair Graphene Nanoribbon
IRDS	International Roadmap for Devices and Systems
ITRS	International Technology Roadmap for Semiconductors
JLFET	Junctionless Field-Effect Transistor
LCAO	Linear Combination of Atomic Orbitals
LDA	Local Density Approximation
LDD	Lightly Doped Drain
LDDS	Lightly Doped Drain and Source
LDDS-GNRFET	Lightly Doped Drain and Source Graphene Nanoribbon Field Effect Transistor
LER	Line Edge Roughness
MOSFET	Metal-Oxide-Semiconductor Field-Effect Transistor
N-AGNR	Nitrogen-passivated Armchair Graphene Nanoribbon
NEGF	Non-Equilibrium Green's Function
P-AGNR	Pristine Armchair Graphene Nanoribbon
P-AGNRFET	Pristine Armchair Graphene Nanoribbon Field Effect Transistor
PBE	Perdew–Burke–Ernzerhof
PDOS	Projected Density of States
PDP	Power-Delay Product
PLDOS	Projected Local Density of States
SB	Schottky Barrier
SB-GNRFET	Schottky Barrier Graphene Nanoribbon Field Effect Transistor
SCE	Short-Channel Effect
SCF	Self-Consistent Field
SE	Semi-empirical
SEM	Scanning Electron Microscope
SG-GNRFET	Single Gate Graphene Nanoribbon Field Effect Transistor
SK	Slater - Koster

SOI	Silicon-on-Insulator
SR	Switching Ratio
SS	Subthreshold Swing
STM	Scanning Tunneling Microscope
TDI-GNRFET	Two Different Gate Insulators Graphene Nanoribbon Field Effect Transistor
TFET	Tunneling Field Effect Transistor
VLSI	Very Large-Scale Integration

LIST OF PUBLICATIONS

PUBLICATIONS RESULTING FROM THIS THESIS WORK

ARTICLES IN INTERNATIONAL REFEREED JOURNALS (4):

1. **Anshul** oÅr %þ 4⁄Mvo. xo≠2⁄ a s~ wempirical DFT based investigation of electronic and quantum transport properties of novel GS-KQX] %.X/%POb 2 %***IEEE Transactions on Nanotechnology***, vol. 23, pp. 400 407, 2024. (SCIE index, IF 2.5)

2. **Anshul** oÅr %] 4⁄Mvo. xo≠2⁄ b ö—o≠r ±⁄s"≈sÅr sr %R qysz⁄~ ör sz-based reliability performance enhancement of gate stack graphene nanoribbon field effect ≈≠oÅ±w≠ö≠2 %*Microelectronics Reliability*, vol. 173, pp. 115869, 2025. (SCIE index, IF 1.9)

3. **Anshul** oÅr %] 4⁄Mvo. xo≠2⁄ O"≈sÅr sr %R qysz⁄NPb-based study of Icosagens passivation at the edge of armchair graphene nanoribbon for next generation ÅoÅöszsq≈öÅwq±%öüüzwqo≈wÅ±2 %*Micro and Nanostructures*, vol. 207, pp. 208263 2025. (SCIE index, IF 3.0)

4. **Anshul** oÅr %þ 4⁄Mvo. xo≠2⁄Kz .~ wÅw.~ -passivated AGNRFET as a nanoscale sensor for toxic gases: A density functional theory-po±sr %öüü≠öoqv2 communicated in **APS Review B** journal. (SCIE index, IF 3.7)

ARTICLES IN INTERNATIONAL CONFERENCES (5):

1. **Anshul** oÅr %þ 4⁄Mvo. xo≠2⁄X. .~ s≠wqoz⁄s–oz .o≈wÅ⁄öt%vs %oo≈s%≈oqysr %QX] %POb %ö≠⁄% w~ ü≠ö–sr %s–wqs %≈—wqvwÅu2 %Å*Proc. Int. Conf. Recent Trends Microelectronics, Automat., Comput. Commun. Syst.*, pp. 88 91, 2022.

2. **Anshul** oÅr %þ 4⁄Mvo. xo≠2⁄S~ üoq≈%öt %s~ üs≠o≈.≠s %ö%ö~ wq⁄oqozs %Å%NM%År %Åozöu% üs≠ö≠~ oÅqs %öt %Qo≈s%≈oqy %QX] POb 2⁄ö≠s±sÅsr %Å*10th International Conference on Microelectronics Circuits and Systems (MICRO-2023)* held at Hotel Vivanta, Guwahati, Assam, India, 1st to 3rd July, 2023.

3. **Anshul** oÅr %] 4⁄Mvo. xo≠2⁄ O"≈sÅr sr %R .qysz⁄Wör sz-based DFT Performance Analysis of GS-QX] %POb %ö≠⁄Vö—%Zö—s≠⁄Küüzwqo≈wÅ± 2⁄ü≠s±sÅsr %Å⁄*11th International Conference on Microelectronics Circuits and Systems (Micro 2024)* held at DTU, 16 17th May 2024.

4. **Anshul** and R. Chaujar, "DFT based analysis of Boron and Nitrogen passivation at the edge of Armchair Graphene Nanoribbon for low power applications." in proceedings of *19th International Conference on Nano/Micro Engineered and Molecular Systems (NEMS)*, pp. 1-4, 2024.

5. **Anshul** oÅr ‰ 4‰vo. xo≠‰ SÅ–s±≈wo≈öÅ‰t ‰s~ üs≠o≈ .≠s ‰ o≠w≈öÅ‰Å‰NM‰År ‰ Åozöu‰ Performance of Gate Stack GNRFET Using DFT-Lo±sr ‰≈ö~ wq‰qozs ‰ör szzwÅu2 ‰ in proceedings of the *2025 IEEE Devices for Integrated Circuit (DevIC - 2025)*, pp. 337 341, 2025.

Publications Other Than This Thesis Work (1)

1. R. Maan, **Anshul**2‰År ‰ 4‰vo. xo≠2‰NPb ‰po±sr ‰Åoz'±w‰öt ‰R t Y 8‰o"s≠‰o±w≈sr ‰ XMPOb ‰tö≠‰VwÅso≠w"‰Zs≠tö≠~ oÅqs ‰wÅ‰vs ‰ü≠öqssr wÅu±‰öt ‰*IEEE Asia-Pacific Microwave Conference (APMC 2024)*, 17 - 20 Nov, 2024.

1

CHAPTER

Introduction

- *This chapter presents a thorough background of the research work, emphasizing the importance of GNRFET in the contemporary integrated circuit industry.*
- *The problems related to MOSFET down scaling and the different short-channel effects have been comprehensively reviewed in this chapter.*
- *In addition to these, this chapter encompasses an examination of several engineering methods, such as junctionless engineering, gate engineering, and dual-k spacer engineering, as well as advanced FET architectures, including SOI MOSFET, TFET, and CNTFET, as documented in different research publications, for reducing the short-channel effects.*
- *Furthermore, this chapter discusses GNRFET as a potential approach to address the limitations. Then the different architecture of GNRFETs, categorization, basic working principles, possible benefits, and challenges confronted by GNRFET technology are discussed.*
- *Finally, the chapter provides an overview of the thesis research objectives, followed by a summary of all the chapters.*

1.1 BACKGROUND

The reduction in size of the electronic components has been one of the biggest drivers of the modern semiconductor industry. The development of the integrated circuit (IC) by Jack Kilby at Texas Instruments in 1958 enabled the fabrication of many electronic components on a single semiconductor substrate [1]. This fabrication of many electronic components on single IC ≠s–öz.≈öÅws r ⁰⁄vs⁰⁄zs q≈öÅwq±⁰⁄År . ±≈≠'4⁰⁄vw±⁰⁄o±⁰⁄ . ≠vs≠⁰⁄"üsr ws r ⁰⁄p"⁰⁄vs ⁰⁄Å≈ör . q≈öÅ⁰⁄t ⁰⁄Wöö≠s ±⁰⁄ Law in 1965 by Gordon Moore. This law states that the number of transistors on a chip doubles typically after every eighteen months [2]. As illustrated in Figure 1.1 this trend has persisted for more than five decades and has served as the main driving force for the progress in IC performance, reduction in cost and the mass adoption of electronic products such as smart phones, personal computers to improved biomedical instruments [3].

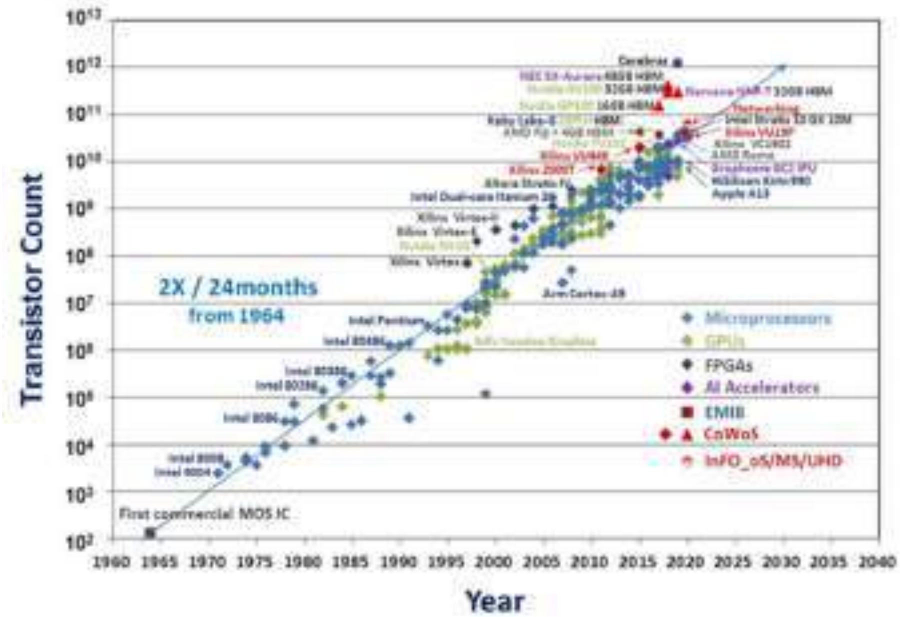

Figure 1.1: Log plot of transistor counts per microprocessor against calendar years [3]

Figure 1.2 depicts the evolution of semiconductor technology from conventional silicon-based Metal-Oxide-Semiconductor Field-Effect Transistor (MOSFET)s to graphene nanoribbon (GNR)-

based nanoelectronics. The text below describes the detailed analysis of Figure 1.2. The MOSFET was the basic building block of the ICs in the 1960s era. The silicon (Si) based MOSFET has been invented by Mohamed Atalla and Dawon Kahng at Bell Labs in 1959, which was foundational breakthrough for modern electronics [4]. Then, the Si based MOSFET was scaled down via technology generations. Early Si based devices had gate lengths in tens of micrometers. After decades of down scaling in the dimensions of transistors, the industry finds itself presently at the sub-5 nm realm [5]. The downscaling of transistors dimensions has given real benefits; less power dissipation, fast switching due to the reduction of parasitic capacitances. The criteria for downscaling were defined by Dennard et al. [6] in 1974, which states that reducing all device dimensions and voltages by a factor of % 1 will keep the internal electric field constant while enhancing performance.

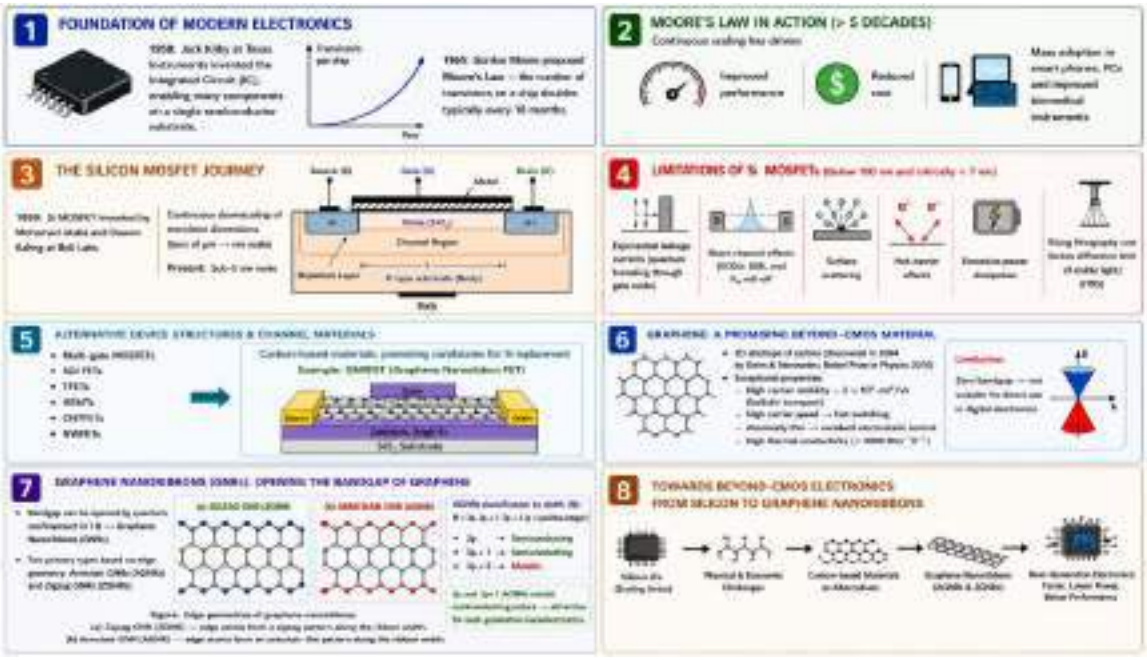

Figure 1.2: Evolution of semiconductor technology from conventional silicon-based MOSFETs to graphene nanoribbon (GNR)-based nanoelectronics [4 20]

However, as channel lengths have been pushed below the 100 nm node, and more critically below the 7 nm node, Si - based MOSFETs have started facing serious physical limitations [7]. These include exponentially increasing leakage currents due to quantum mechanical tunneling through the gate oxide, short-channel effects (SCEs) such as drain-induced barrier lowering (DIBL) and threshold voltage (V_{th}) roll-off, surface scattering, hot-carrier effects, and excessive power dissipation [8, 9]. In addition, the rising cost of advanced lithography below the diffraction limit of visible light has further complicated the path forward, as projected by the International Technology Roadmap for Semiconductors (ITRS) [10].

To overcome these challenges, several alternative device structures and channel materials have been proposed by researchers worldwide, such as multi-gate MOSFETs, Silicon-on-Insulator (SOI) FETs, Tunnel FETs (TFETs), High Electron Mobility Transistors (HEMTs), Carbon Nanotube FETs (CNTFETs) and Nanowire FETs (NWFETs) [11-13]. Among these, carbon-based materials have been the most recently studied because of their better electrical, thermal and mechanical properties with respect to silicon at the nanoscale. One of the candidates from carbon-based materials for silicon replacement is a graphene.

Graphene is the two-dimensional allotrope of carbon. It was experimentally discovered by Geim and Novoselov in 2004 and they are awarded with the Nobel Prize in Physics in 2010 [14]. The discovery of graphene has emerged as a plausible option for beyond the CMOS silicon transistor era [14]. Graphene-based electrical devices have various benefits such as outstanding carrier mobility 8%%6 %~ 5d ±%ö≠%pozw≈wq%%oÅ±üö≠2%wv%qo≠w≠%üssr %ö≠%o±%~ wqvwÅu2%ö~ wqozz”% thin structure for efficient electrostatic control and great thermal conductivity .H%666% ~ U / [15, 16]. These features of graphene have the potential for transistor applications in devices that could switch faster, use less power and provide better electrostatic control than Si-based devices.

Graphene has great electrical characteristics but absence of bandgap restricts its direct applications in electronics applications [17]. Researchers are attempting to create a gap in graphene by employing techniques such as quantum confinement in one dimension, resulting in Graphene Nanoribbons (GNRs) [18]. Graphene nanoribbons serve as the fundamental component in the advancement of graphene-based nanoelectronics technology. Graphene nanoribbons are possible alternatives for transistor channels in next-generation integrated circuits. Armchair graphene nanoribbons (AGNRs) and zigzag graphene nanoribbons (ZGNRs) are the two primary types of graphene nanoribbons, which are classified according to their edge geometry [19]. Previously reported study reveals that AGNRs can be categorized into three separate subfamilies depending on the number of carbon atoms along AGNR width, N (N = 3p, 3p + 1, and 3p + 2), where p is the positive integer [20]. Among the three AGNR families 3p, 3p+1, and 3p+2 family, the 3p and 3p+1 family is known to exhibit the semiconducting nature, which makes them particularly attractive for applications in nanoelectronics where a substantial bandgap is essential [20].

However, promising properties and several challenges related to the GNR based device performance like edge passivation, temperature sensitivity, reliability, and sensing applications remain insufficiently explored in the literature. Also, the simulation of the atomic-scaled graphene nanoribbon FETs (GNRFET) devices requires accurate modeling approaches. Further, to address these gaps, in this thesis, a systematic atomic-scale investigation of Gate-Stack Armchair Graphene Nanoribbon FETs (GS-AGNRFETs) is carried out using Semi-empirical DFT-based approaches, specifically the Slater Koster tight-binding model and the Extended Hückel formalism, integrated with the Non-O¨ .wp≠w.~ %Q≠sÅ±ºP.Åq≈öÅ%XOQP/%ö≠ ozw~ 4%vs% proposed device uses a gate-stack dielectric architecture to achieve better electrostatic control and leakage suppression. Overall, this thesis provides a comprehensive framework for low-power

nanoelectronics and sensing applications by addressing various DFT based approaches, width engineering, edge passivation using Icosagens group components, temperature-dependent reliability analysis, and extension of the proposed device toward toxic gas sensing.

1.2 LITERATURE SURVEY

A review of the existing literature is important to understand the context and motivation for the present work. The following subsections discuss scaling in conventional MOSFET, the associated short-channel effects, the engineering schemes proposed to mitigate them, and the gaps that point toward GNRFETs as a possible solution.

1.2.1 Scaling in Conventional MOSFETs

The development of MOSFET technology has closely followed the concept of device scaling. In 1974, Dennard et al. [6] proposed a constant field scaling, which states that if all device dimensions oÅr %öz≈ous±%≠s %qozsr %ö—Åp”%%oq~ö≠%t%%H72%vs %Ås≠Åoz%zsq≈q%wzr %—wz%ps% owÅ~owÅsr % constant. The advantage of this is that the transistor density doubles every generation, the speed wÅq≠so±s±%p”%%oq~ö≠%t%2%År %vs %ö—s≠%s≠%s–wqs %≠öü±%p”%%oq~ö≠%t%[2]. The benefit of this approach is that transistor density doubles with each generation and the transistors speed improves p”%2%År %ö—s≠%s≠%s–wqs %sq≠so±s±%p”% 4%vw≠%≠Åqwüzs %≠ö–s %sor ”%≠öu≠s±±%≠ö..uv%vs %CB6±% oÅr %CC6±2%–vo≈%≠%t≈sÅ%qozzsr %vs %özr sÅ%≠o%t%Wöö≠s ±%Vo—[21]. During this era, the lengths of gate (L_g) decreased from tens of micrometers in the early 1970s to below by 1 µm in the late 1980s, and then further into the deep sub-100 nm regime through the 1990s and 2000s [22, 23]. The shift from aluminum to copper gates interconnects in the late 1990s also helped reduce resistive losses and improve circuit speed. Each successive technology node reliably delivered better performance, higher density, and lower power consumption. However, by the early 2000s,

as L_g crossed below 100 nm, the assumptions of Dennard scaling started to break down. The reason is that the supply voltage could not be scaled proportionally because of Boltzmann statistics governing carrier transport, which led to a sharp rise in power density. Also, as gate oxide thickness was reduced to maintain electrostatic control over the channel, quantum mechanical tunneling through the dielectric became a dominant leakage mechanism [24]. Moreover, the heavy channel doping needed to suppress SCEs at short channel lengths degraded carrier mobility due to impurity scattering, increased BTBT, and introduced random dopant fluctuations that worsened device-to-device variability [25]. These aforementioned limitations made it clear that continued down scaling of silicon MOSFETs could not go on indefinitely, and new solutions in materials and device architecture were required.

1.2.2 Short-Channel Effects

30 As channel length of the MOSFET is reduced to the nanoscale, the gate over the channel loses its ability to fully control the channel potential, and the source and drain electric fields start to influence the channel. This leads to a group of parasitic effects collectively called SCEs. These effects degrade transistor switching performance, increase static power dissipation, and reduce device reliability. Five main SCEs are discussed below.

49 1.2.2.1 Drain-Induced Barrier Lowering

DIBL occurs when the drain electric field penetrates into the channel and lowers the source-to-
122 channel potential barrier, as shown in Figure 1.3 [26, 27]. Ideally, this potential barrier should be controlled only by the gate voltage. But when the length of channel in devices becomes shorter, the depletion region extends toward the source and reduces this barrier even when the gate voltage is below the threshold. As a result, leakage current flows from drain to source even in the OFF

state (when no V_{gs} is applied). This increases the I_{off} and degrades the SR ratio. DIBL becomes more severe as the channel length shrinks below 10 nm, and it is calculated by the change in threshold voltage per unit change in drain-source voltage [28].

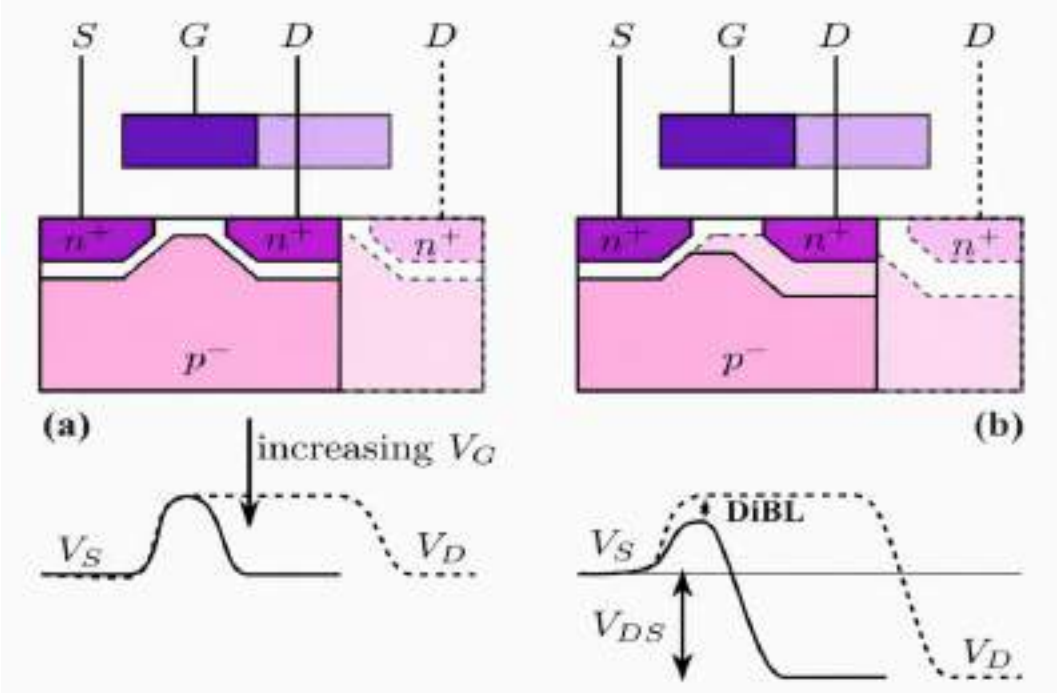

Figure 1.3: Drain-induced barrier lowering [27]

1.2.2.2 Surface Scattering

Figure 1.4 shows the surface scattering which is a mobility reducing effect and is more dominant in the MOSFETs having shorter channel [27]. When the carriers are in transit through the channel, the transverse electric field from the gate pulls them toward the semiconductor-oxide contact. The roughness of this interface results in several collisions which limits the effective mobility of the carriers as opposed to the bulk mobility [26]. As devices are reduced to very small dimensions, the gate oxide thickness is reduced in order to maintain gate control. This reduction raises the

transverse field and aggravates surface scattering. The reduction in carrier mobility directly lowers the drive current and switching speed of the transistor.

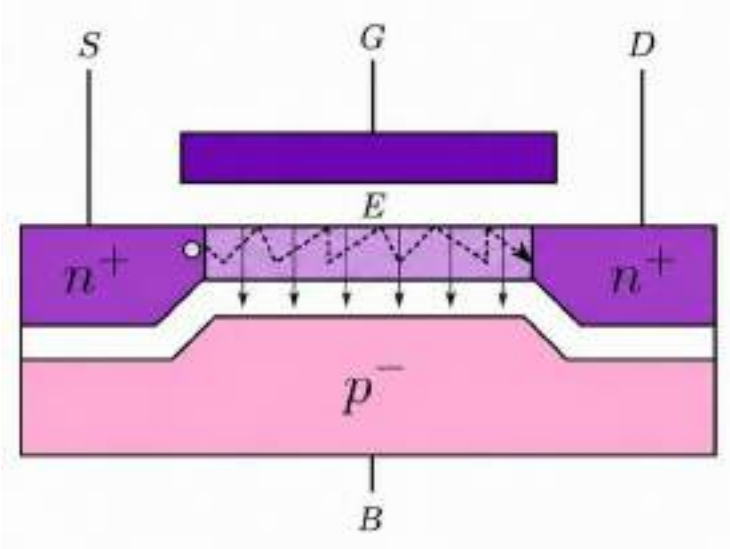

Figure 1.4: Surface Scattering [27]

47

1.2.2.3 Threshold Voltage Roll-off

Threshold voltage roll-off is the reduction in the value of V_{th} as the length of the channel in MOSFET is reduced. In a long-channel device, the gate has good control of the channel and V_{th} is

12 steady. However, at the nanoscale regime the source and drain electric fields begin to share the

38 control of the channel potential with the gate [29]. This results in a lower threshold voltage for the short-channel device compared to the long-channel one. A lower V_{th} turns the transistor on earlier, which increases the subthreshold leakage and decreases the circuit performance. Mathematically, V_{th} roll-off is the difference between the threshold voltage of a short-channel MOSFET and a long-channel MOSFET [8].

1.2.2.4 Impact Ionization

Impact ionization is related to the significant lateral electric fields inherent in short channel devices, as shown in Figure 1.5. These high electric fields accelerate the channel carriers to

significant kinetic energies and produce so-qozzsr %vö≈%qo#vs≠ [8]. These heated carriers smash with the atoms in the silicon lattice near the drain with enough energy to break covalent bonds and create electron-hole pairs [30]. The produced holes flow to the substrate causing a substrate current and the electrons flow to the drain. In extreme circumstances, the holes flowing in the bulk resistance can forward bias the source-bulk junction, switching on the parasitic BJT created by the source-bulk-drain regions. This may result in a self-sustaining avalanche current that is uncontrollable with the gate voltage and may lead to device failure. The magnitude of impact ionization is measured by the substrate current. This process results in an increase in current, beyond what is controlled by the gate voltage, and can lead to several adverse effects, such as:

- **Increased leakage current:** Unwanted current due to the creation of extra charge carriers.
- **Hot carrier injection:** Damage to the gate oxide as high-energy carriers are injected into it.
- **Device reliability issues:** Long-term degradation of the MOSFET.

Impact ionization becomes more significant as MOSFETs are scaled-down and electric fields intensify.

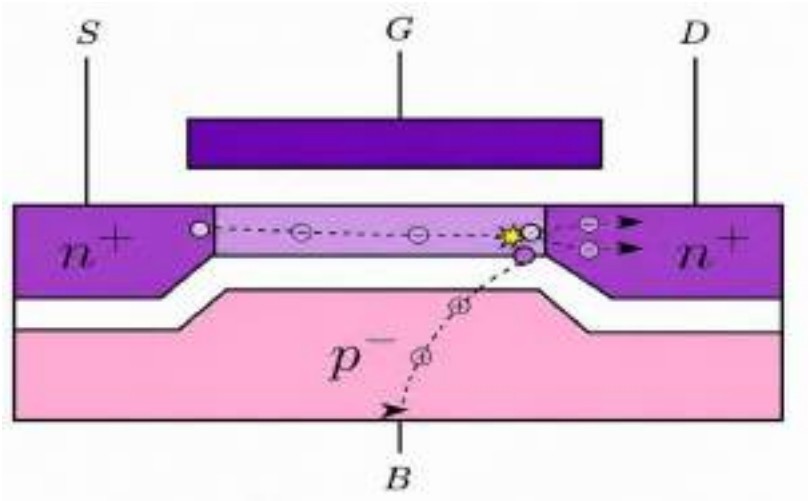

Figure 1.5: Impact Ionization [27]

1.2.2.5 Hot-Carrier Effects

Hot-carrier effects are a long-term reliability concern in short-channel MOSFETs, as shown in Figure 1.6 [30]. When carriers are accelerated by the strong lateral electric field near the drain, some of them gain enough energy to enter the gate oxide and get trapped in it. These trapped charges alter the local electrostatics of the device, causing a shift in V_{th} and degradation of subthreshold swing over time. Hot carriers can also create interface states at the Si-a w Y %ö. År o≠'2% which further reduces carrier mobility and transconductance. To reduce hot-carrier effects, Lightly Doped Drain (LDD) implants are used to spread the peak electric field over a larger region near the drain [31]. However, this also increases the parasitic source/drain resistance, which has to be carefully managed [31].

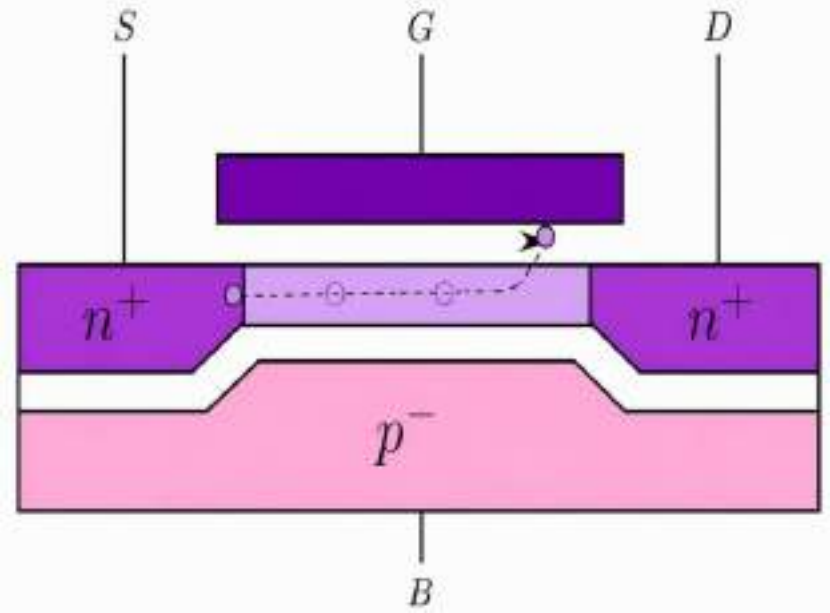

Figure 1.6: Hot Carrier Effects in NMOS [27]

1.3 WAYS TO OVERCOME SHORT-CHANNEL EFFECTS

The above discussed SCEs are the primary obstacles to continued MOSFET scaling. To preserve long-channel electrical behavior in physically short-channel devices, researchers have developed various device engineering strategies and new device architectures aimed at improving gate electrostatic control and suppressing leakage. As shown in Figure 1.7, these approaches cover gate engineering, channel engineering, dielectric engineering, and advanced device topologies.

Figure 1.7: Different ways to overcome SCEs in nano-scale MOSFET

1.3.1 Types of Engineering Schemes

Researchers have developed various engineering schemes to mitigate the impact of SCEs on transistor performance. Here are some types of engineering schemes to address the SCEs.

1.3.1.1 Junctionless Engineering

A Junctionless Field-Effect Transistor (JLFET) is a transistor that operates without any conventional p-n junction in the channel region as shown in Figure 1.8 [32]. In a JLFET, the entire device source, channel, and drain are uniformly doped with the same type of dopant (either p type or n type). The gate controls current flow by modulating the depletion or accumulation of carriers in this uniformly doped body. When a positive gate voltage is applied, carriers accumulate near the gate dielectric interface, forming a conducting path. When the gate voltage is made sufficiently negative, the channel is fully depleted and no current flows. The elimination of p-n junctions simplifies the fabrication process, lowers contact resistance variability, and reduces SCEs like DIBL and V_{th} roll-off that are worsened by the steep doping gradients of conventional junctions [33].

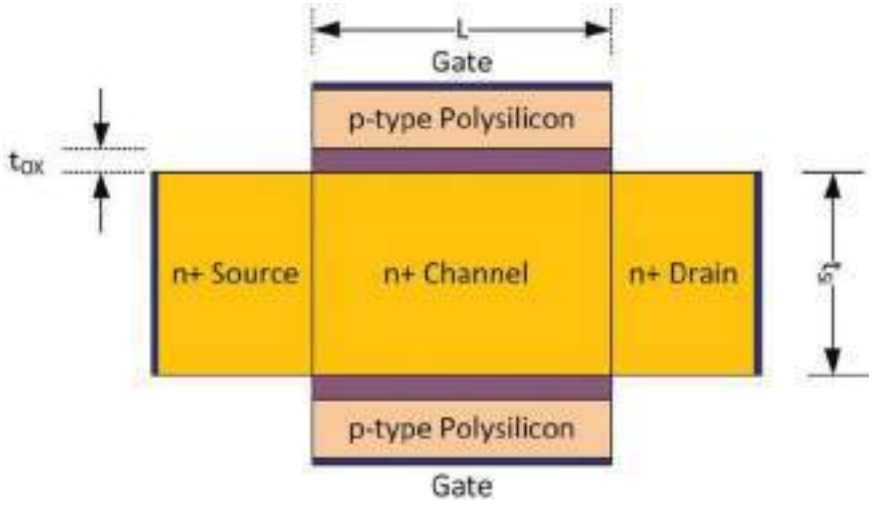

Figure 1.8: Cross-sectional view of junctionless double gate MOSFET [32]

1.3.1.2 Gate Engineering

Gate engineering includes changes to the gate structure or gate material to provide better electrostatic control over the channel. One of the most commonly investigated methods is the Dual Material Gate (DMG) MOSFET proposed by Long et al. in 1999. In this structure the gate is

separated into two parts with distinct work functions. One gate with higher work function is placed near the source and one with lower work function is placed near the drain, as shown in Figure 1.9 [34]. This will result in a step in the channel potential profile screening the source from the drain electric field, which further minimizing the DIBL and hot-carrier effects. The asymmetric potential distribution also enhances the efficiency of carrier transmission. The reason is that it improves the carriers in the source-to-gate region and provides the maximum electric field at the drain.

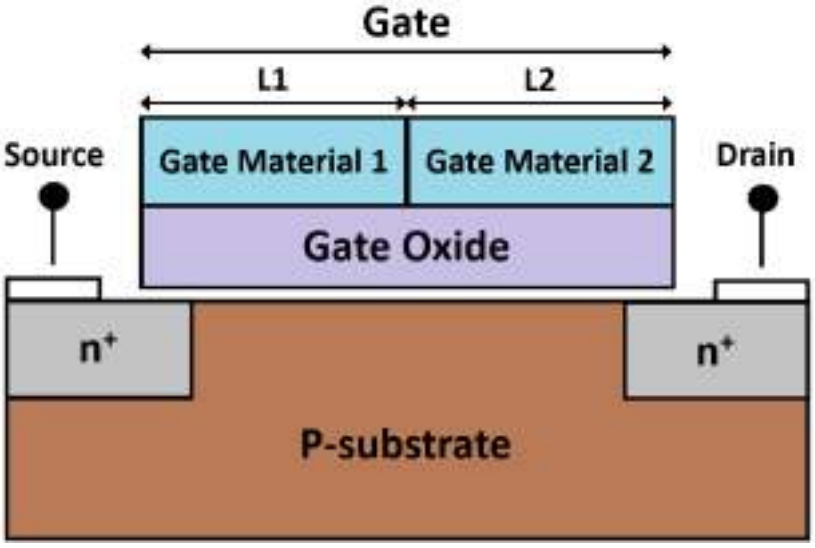

Figure 1.9: Schematic structure of dual material gate MOSFET [34]

1.3.1.3 Dual-k Spacer Engineering

Dual-k spacer engineering uses two gate spacer materials with different dielectric constants on either side of the gate electrode as shown in Figure 1.10 [35]. A high- %wzsq≈∧q%æ%zoqsr %Å%vs% vÅs≠∧ws2%qö±s%ö%vs%o≈s2%ö%sÅvoÅqs%vs%o≈s ±%szsq≈ö±o≈q%Åtz.sÅqs%ö–s≠%vs%qvoÅÅsz%År% suppress the SCEs. A low- %wzsq≈∧q%.qv%±%Y %æ%±sr %Å%vs%ö.≈s≠%ws%ö%sr.qs%vs%o≠±∧q% fringing capacitance between the gate and the source/drain contacts, which reduces capacitive loading and improves switching speed [35]. The combination of both gives better channel control

that suppresses V_{th} roll-off and DIBL, while also reducing the parasitic capacitances that slow down the circuit.

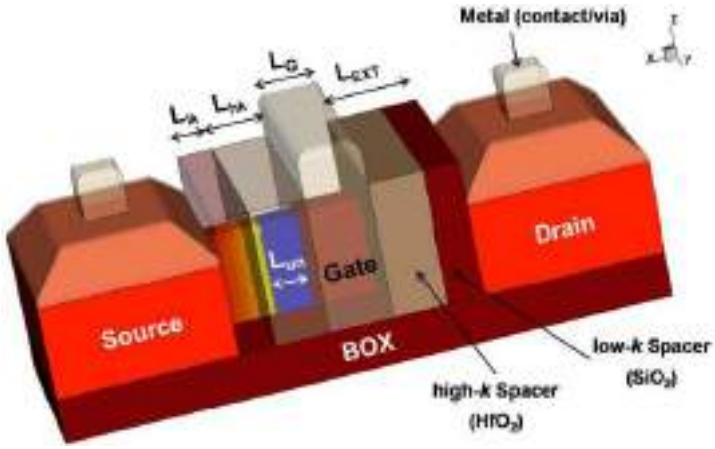

Figure 1.10: Schematic FinFET structure with dual-k underlap spacers [35]

1.3.2 Device Concepts

Researchers globally are now working to advance the speed of operation and packing density of ICs by developing novel devices. Here are some devices to address SCEs.

1.3.2.1 Silicon-on-Insulator MOSFET

Silicon-on-Insulator (SOI) technology uses a thin active silicon layer separated from the bulk substrate by a buried oxide (BOX) layer as depicted in Figure 1.11 [36]. The BOX prevents the extension of source and drain depletion regions into the substrate, which reduces the charge sharing responsible for V_{th} roll-off and DIBL. In a Fully Depleted SOI (FD-SOI) device, the thin silicon body is completely depleted under normal operating conditions, which gives very good gate control and a steep subthreshold slope. The BOX also eliminates latch-up, reduces junction leakage, and lowers the body-effect coefficient [36]. The reason for its better performance is that the reduced body doping minimizes random dopant fluctuation, which is a major source of V_{th} variability in ultra-scaled bulk devices.

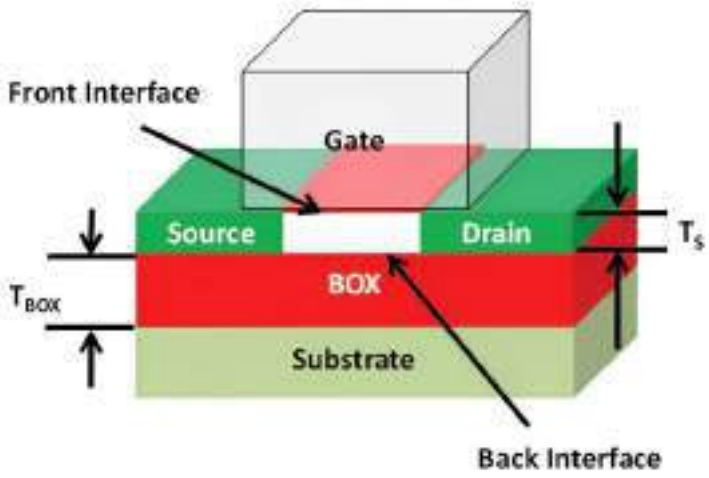

Figure 1.11: Schematic structure of FD-SOI MOSFET [36]

1.3.2.2 Tunneling Field Effect Transistor

TFETs control the drain current by quantum mechanical BTBT rather than by thermionic emission. The schematic structure of TFET is depicted in Figure 1.12 [37]. Also, the TFETs are not limited by the 60 mV/decade subthreshold swing which was the limitation of traditional MOSFETs. This enables the TFETs to work at lower supply voltages with reasonable driving currents and hence suitable for ultra-low-power applications. However, TFETs have lower ON-state current densities compared to MOSFETs which limits their application in high performance circuits [38]. Also, the accurate abrupt tunnel connections during fabrication still remains a great issue.

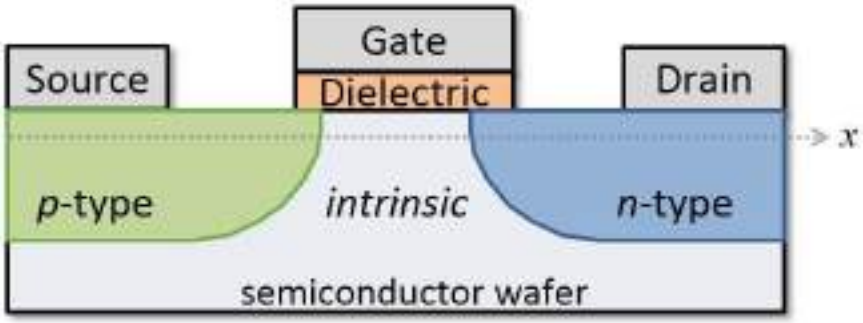

Figure 1.12: Schematic lateral structure of TFET [37]

81

1.3.2.3 Carbon Nanotube Field Effect Transistor

Carbon nanotubes field effect transistor (CNTFETs) use carbon nanotubes as the conducting channel material, as portrayed in Figure 1.13 [39]. The CNTs have carrier mobilities far exceeding than silicon, have large current-carrying capacity, and excellent thermal stability up to ~1700°C. The bandgap of a semiconducting CNT is inversely proportional to its diameter, which allows threshold voltage control. CNTFETs have shown sub-60 mV/decade subthreshold swing and SR s“qssr wÅu%76 4⁄Rö—s–s≠2⁄₀vs%qöÅ≤⁄özzsr%±”Å≈vs±w⁄öt%MXb±%–w%⁄₀üsqtwq%qvw⁄ozw”, which determines whether a CNT is metallic or semiconducting remains very difficult. Issues related to scalability, device-to-device variability, and high contact resistance have limited the practical deployment of CNTFETs in large-scale ICs [40].

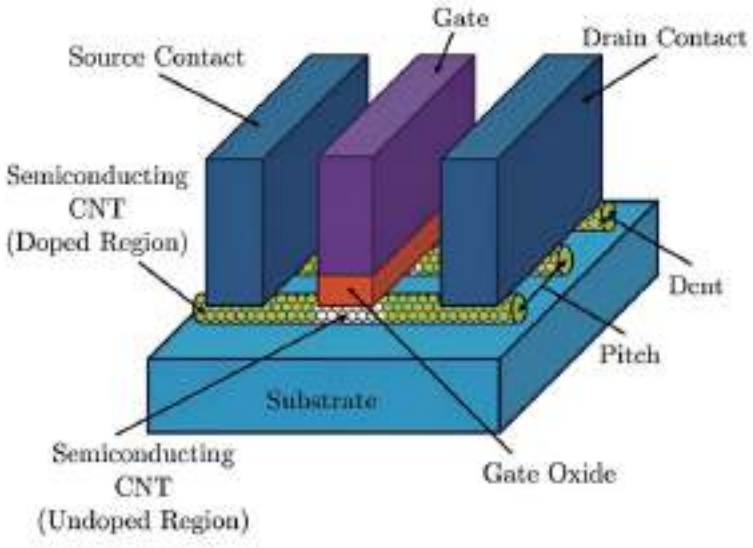

Figure 1.13: Schematic structure of CNTFET device [39]

1.4 RESEARCH GAPS

A detailed review of the existing literature reveals several important gaps that remain unaddressed. These gaps are summarized as follows.

- The continued miniaturization of silicon-based MOSFETs is fundamentally limited by SCEs, quantum tunneling through gate oxides, rising leakage currents, and excessive power dissipation. While various engineering schemes have been proposed, none of them offers a complete solution below the sub-5 nm regime, which makes the need for alternative channel materials very clear.
- Although CNTs have excellent electronic properties, the difficulty in controlling CNT chirality during synthesis results in a mixed population of metallic and semiconducting tubes. This severely limits device-to-device uniformity and makes large-scale integration unreliable.
- GNRs have emerged as a promising alternative to both silicon and CNTs, with their width-dependent bandgap tunability and compatibility with planar fabrication. However, the performance of GNRFETs is very sensitive to edge structure, channel width, gate dielectric configuration, and temperature. A systematic atomic-scale study of these design parameters together remains unexplored in the existing literature.
- The reliability of GNRFETs under varying temperature conditions, which is critical for real-world applications, has received very limited attention. A detailed temperature-dependent study of DC and analog performance metrics is needed to identify the suitable operating range for GNRFET devices.
- Edge passivation of AGNR channels using group-13 and group-15 elements is a powerful but underexplored approach for modifying the electronic structure and transport properties of GNRFETs. A systematic study of Icosagens (Boron, Aluminum, Gallium, and Indium) as

edge passivation elements and their effect on device performance has not been comprehensively reported.

- Due to their many benefits, GNRFET-based electronic devices are widely utilized as bio-sensors, gas-sensors, radiation-sensors, etc. With the advancement of technology towards compact devices, there is a need for new GNRFET-based gas sensors that cater to different specialized applications.

These gaps together define the scope and motivation of the present research work.

1.5 Possible Solution - Graphene Nanoribbon FET

The research gaps identified above point clearly toward GNRFETs as a promising solution for next-generation nanoelectronics. Among the various GNR configurations, AGNRs from the 3p and 3p+1 families show semiconducting behavior with a tunable bandgap, making them suitable for use as channel materials in nanoscale transistors. Combining AGNRs with a gate-stack dielectric architecture improves the electrostatic performance of the device and addresses many of the limitations found in conventional MOSFET and GNRFET research. The following subsections cover the development of GNRFETs, experimental evidence, operation, classification, advantages, and fabrication challenges.

1.5.1 Development and Prospects of GNRFET

The idea of GNRFET came from two parallel developments: the experimental discovery of graphene by Geim and Novoselov in 2004, and the theoretical understanding that confining graphene laterally into narrow ribbons induces a semiconducting bandgap [14]. Early theoretical studies in the literature showed that AGNRs from the N = 3p and N = 3p+1 families exhibit semiconducting behavior with bandgaps inversely proportional to ribbon width, while ZGNRs and

N = 3p+2 AGNRs are metallic. The first graphene-based transistor structure to be proposed in both theoretically and experimentally ways was the Schottky Barrier type GNRFET (SB-GNRFET), where metallic contacts form Schottky barriers with the GNR channel [41]. In 2007 Chen et al. [42] experimentally fabricated SB-GNRFETs by designing narrow graphene ribbons between metal source and drain contacts, confirming that GNRs can behave as a semiconducting channel with a width-dependent bandgap, as illustrated in Figure 1.14. This experimental work demonstrated the practical practicality of GNR-based transistors. However, the work moved toward MOS-type GNRFETs with doped source and drain reservoirs, which showed much better SR and fast switching behavior compared to the SB-GNRFET.

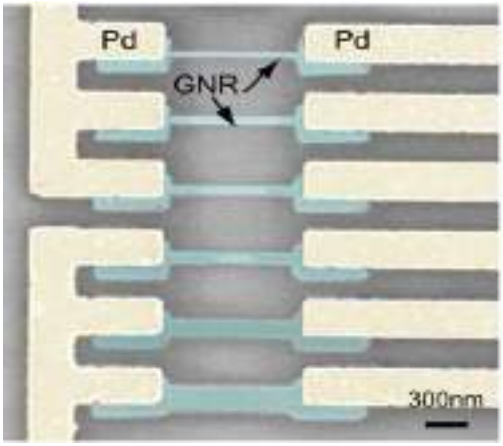

Figure 1.14: SEM picture of GNR devices fabricated on a 200nm SiO_2 substrate. The widths of the GNRs from top to bottom are 20, 30, 40, 50, 100 and 200nm [42]

In 2008, Yoon et al. [43] reported the first detailed atomistic simulation study of MOS-type GNRFET, where the source and drain are formed by heavily doped GNR extensions instead of metal contacts, as depicted in Figure 1.15. Using a self-consistent solution of the 3-D Poisson and Schrödinger equations within the NEGF formalism, the authors confirms that the ideal MOS-type GNRFET showed ~50% increase in I_{on}, ~30% higher cut-off frequency, and ~20% faster switching speed compared to the SB-GNRFET. The reason is that the SB at the source side of the SB-GNRFET introduces a tunneling barrier that limits the on current, while the MOS-type device transport is governed by the top of the channel barrier. The MOS-type device also showed a much

higher SR because of the absence of ambipolar conduction. Further, the Yien-Yu Chen et al. [44] in 2015 developed the first parameterized SPICE-compatible compact model of MOS-type GNRFET, which allowed circuit-level simulation of GNRFET-based ICs. This work confirmed that GNRFETs offer either lower delay or lower power than equivalent Si-CMOS, depending on the operating condition.

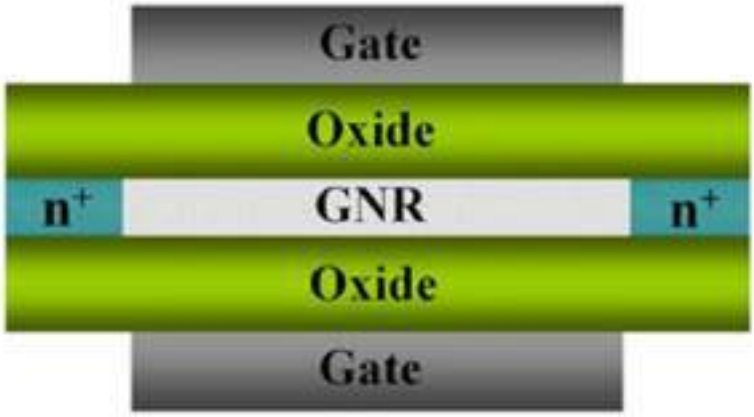

Figure 1.15: MOS type GNRFET with doped source and drain extensions [43]

1.5.2 Experimental Evidence of GNRFET

The practical fabrication feasibility of GNRFET has been demonstrated through several experimental works over the past decade. The earliest demonstrations were of the SB-GNRFET type in 2007, where graphene ribbons of a few nanometers width were patterned and contacted with metal electrodes, as discussed in section 1.5.1. Also, the experimental evidence of the MOS type GNRFET mechanism has been provided by Dinh et al. [45], where short-channel field-effect transistors are fabricated using AGNR (N = 9) as the channel material. The AGNR (N = 9) are synthesized through a bottom-up on-surface synthesis approach using the 3,6-diiodo-1,1:2,1-terphenyl (DITP) precursor on Au (111)/mica substrate, which yields atomically precise ribbons with an average length of ~70 nm and a width of ~0.95 nm as shown in Figure 1.16 [45].

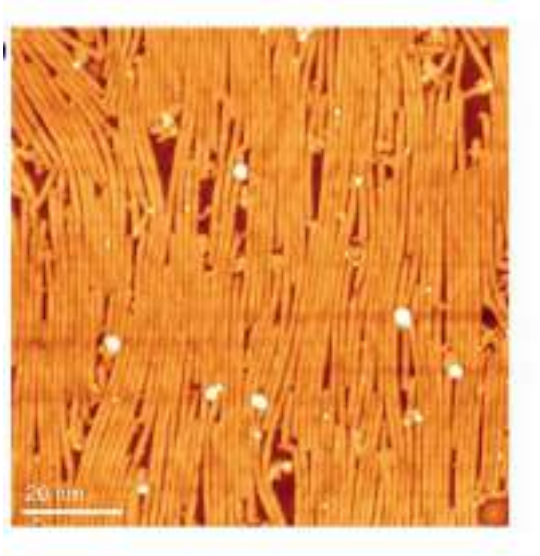

Figure 1.16: A typical scanning tunneling microscope (STM) image of a AGNR (N = 9) sample grown on Au (111) surface [45]

The synthesized A QX] ±‰⁄s%vsÅ‰oÅ±ts⁄≠sr %ÅÖö‰%‰⁄süo≈s≠Åsr %wY 5a w‰qvwü‰o–wÅu‰%‰ .Åu±≈sÅ% back-uo≈s%qoüüsr %-w‰v%‰%=4–%Å~ %RtY %‰wzsq≈≠w‰%”s≠2‰Ár %7=%Å~ %‰vwqy%‰ozzor w.~ %qöÅ≈oq≈±‰⁄s% formed using electron beam lithography to complete the device, as shown in Figure 1.17. The fabricated AGNR (N = 9) FET show p-type behavior with an I_{on} exceeding 1 µA and an SR of ~10^3 at Vds = -1 V. However, the authors observed that the device performance degrades over consecutive measurement cycles, which is attributed to the degradation of contact resistance. To orr ⁄s±±%vw‰w±. s2‰%76Å~ %KzY %Åqoü±. z≈o≈wÖÅ‰%”s≠‰w±‰sü±ited using atomic layer deposition, after which the devices are shown to operate stably for several thousand cycles without any Åö≈wqsopzs%su≠or o≈wÖÅ‰%vs%s±soöÅ‰w±‰vo~%‰vs%KzY %‰”s≠‰wözo≈s±‰vs%qöÅ≈oq~% s≈oz‰Ár %qvoÅÅsz% surface from environmental exposure, which prevents oxidation and water absorption at the Pd-GNR interface. These experimental results clearly confirm that GNR-FETs can be practically fabricated with reliable long-term operation, which strengthens the feasibility of GNR-based devices for future nanoelectronics applications.

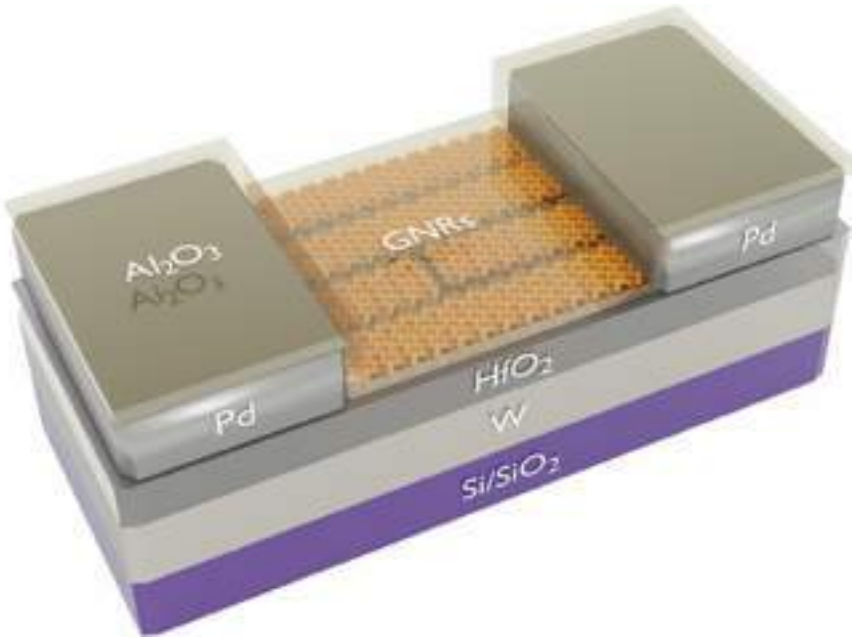

Figure 1.17: Schematic diagram of short-channel AGNR (N=9) FET [45]

1.5.3 GNRFET Classification

Since the first GNRFET was proposed, many device topologies have been reported in literature. Each offers different advantages in terms of electrostatic control, switching performance, fabrication complexity, and SCEs suppression. The main types of GNRFET are described below.

1.5.3.1 Schottky Barrier Type GNRFET

In SB-GNRFETs, metals contacts are employed instead of doped source and drain contacts, the contacts are known as Schottky contacts and GNR is used as channel material [41]. The schematic view of SB GNRFET is depicted in Figure 1.18. Also, in SB-GNRFETs, the fabrication process is simplified by the absence of further doping at the contacts. The charge transport is driven by the Schottky barrier tunneling phenomenon where the gate voltage regulates the width of the Schottky barrier and hence the tunneling probability [43]. This device configuration is composed of two parts, in first part the injection regions at the ends of the GNR, and in second part, a middle region

where the ballistic transport occurs. However, the ambipolarity feature of the SB-GNRFETs, where both electrons and holes contribute to the current based on the polarity of the gate bias, is a significant disadvantage as it hinders total suppression of the OFF-state current.

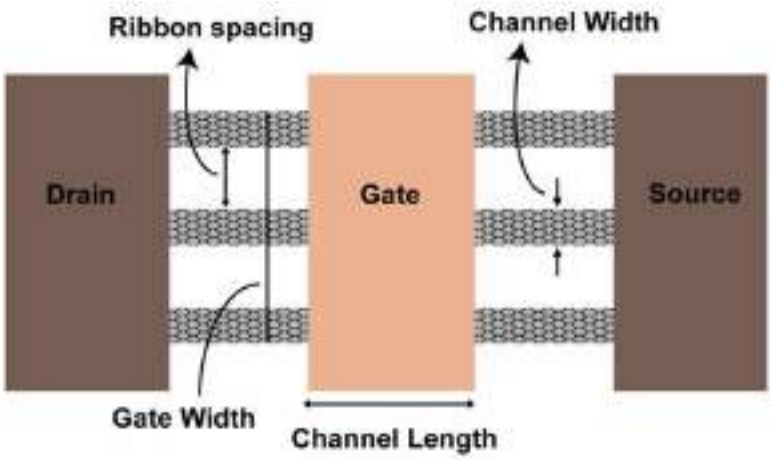

Figure 1.18: Schematic diagram of SB type GNRFET [41, 43]

1.5.3.2 Metal Oxide Semiconductor Type GNRFET

In MOS type GNRFET, the source and drain are formed by heavily doped GNR extensions instead of metal contacts, as depicted in Figure 1.15. The MOS type GNRFET has several advantages over the SB type, such as a greater SR due to the absence of ambipolarity, higher transconductance, better saturation behavior and faster switching. However, the MOS-type GNRFET requires doping to the source and drain GNR areas, which is technically problematic at nanoscale and increases the fabrication complexity [43].

1.5.3.3 Lightly Doped Drain and Source GNRFET (LDDS-GNRFET)

In the LDDS-GNRFET, a lightly doped transition areas are introduced between the intrinsic GNR channel and the strongly doped source and drain contacts, as shown in Figure 1.19. The introduction of LDDS between the channel and the contacts will reduces the probability of band to band tunneling (BTBT) in the OFF state and suppresses the ambipolar conduction [46]. Also, the LDDS

architecture has been proven to improve the subthreshold swing, switching ratio and power delay product over the standard GNRFETs.

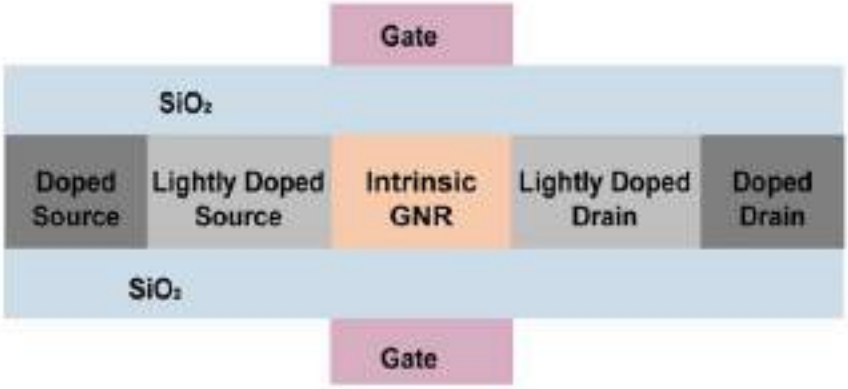

Figure 1.19: Schematic diagram of LDDS-GNRFET [41, 46]

1.5.3.4 Single Gate GNRFET (SG-GNRFET)

150 The SG-GNRFET uses a single metal gate electrode on the top side of the GNR channel to control the current flow as depicted in Figure 1.20. This device configuration is structurally simpler but has less electrostatic control over the channel which means it is employed largely in low frequency applications. The gate capacitance is lower, resulting in lower transconductance [41].

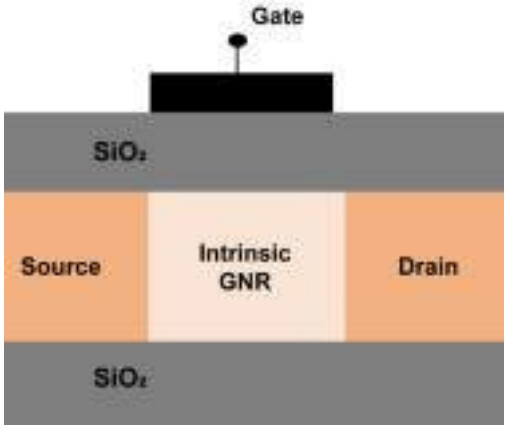

Figure 1.20: Schematic view of SG -GNRFET [41]

1.5.3.5. Double Gate GNRFET (DG-GNRFET)

In the DG-GNRFET, gate electrodes are placed symmetrically on both sides of the GNR channel, one on the top and one at the bottom. Both gate metals work functions are identical in this configuration. The representation of DG -GNRFET architecture is shown in Figure 1.21 [41]. This configuration provides much better electrostatic control over the channel compared to a single gate, which significantly suppresses DIBL and improves the subthreshold swing. One gate controls carrier injection from the source, and the other gate makes the band edge profile near the drain nearly flat, reducing BTBT. The device has a high cut-off frequency and small delay because of the very short channel length. The DG-GNRFETs are suitable for high-frequency and digital applications.

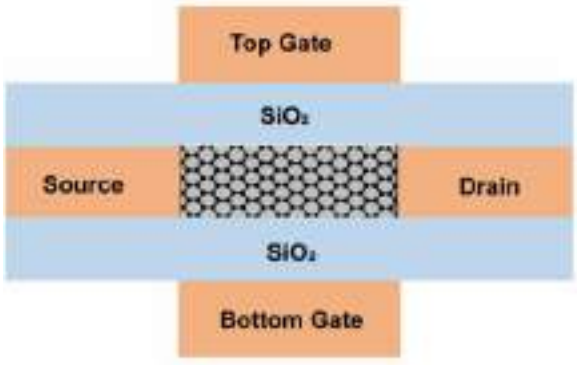

Figure 1.21: Representation of the DG -GNRFET [41]

1.5.3.6. Dual Material Gate GNRFET (DMG-GNRFET)

Unlike the DG-GNRFET, the gate in DMG-GNRFET is separated into two parts with different work functions as shown in Figure 1.22 [47]. The difference in work function provides a potential step in the channel which acts as a barrier to the drain electric field to reach the source and lowers DIBL and hot-carrier effects. An extra peak of electric field is also generated at the interface of the two gate materials, which extends the lifetime of the device by suppressing the hot-carrier

injection near the drain [47]. The DMG-GNRFET exhibits a greater saturation current and a better SR than a standard single material gate GNRFET.

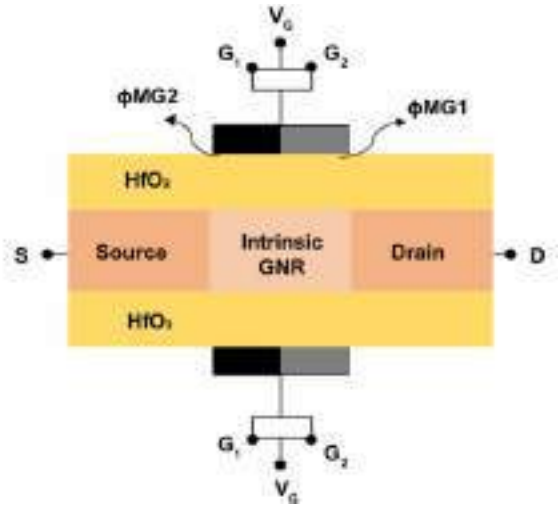

Figure 1.22: Diagrammatic illustration of the DMG -GNRFET [41, 47]

1.5.3.7. Two Different Gate Insulators GNRFET (TDI-GNRFET)

The TDI-GNRFET is a dual-gate device with two dielectric materials with different dielectric constants, as depicted in Figure 1.23. A high- % o~s≠wz%Å%vs%ö.≠qs%wvs%År %%ö—- % o~s≠wz%Å% the drain side is used in this architecture. The high- % o~s≠wz%Å%vs%ö.≠qs%w ü≠ö–s±%uo~s% electrostatic control and suppresses SCEs, while the low- % o~s≠wz%Å%vs%ö≠owÅ±wvs%sr.qs±% üo≠o±wwq%qoüoqwoÅqs±%År %zw- w±%vs%ö≠owÅ±%Åtz.sÅqs%Å%vs%qvoÅÅsz [48]. Overall, the TDI-GNRFET shows improved SR and reduced DIBL compared to single-dielectric GNRFET structures.

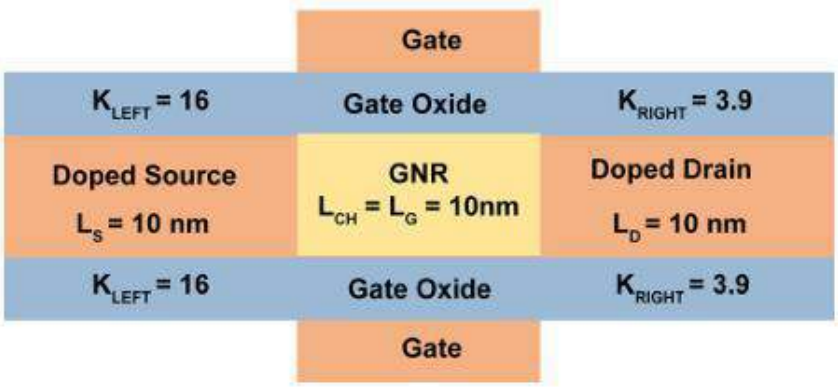

Figure 1.23: Structural layout for the TDI -GNRFET [41, 48]

1.5.3.8. Asymmetric Gate GNRFET (AG-GNRFET)

The AG-GNRFET is proposed as a simpler alternative to the double gate structure for suppressing the parasitic tunneling current in the SB-GNRFET. In this device architecture, the gate covers only the part of the channel close to the source, instead of the entire channel, as shown in Figure 1.24 [49]. The reason for this asymmetric placement is that the gate voltage has only a mild effect on the Schottky barrier thickness at the drain side, which reduces the hole tunneling through the drain SB. As a result, the parasitic carrier current is suppressed without the need to fabricate an extra gate. The AG-GNRFET shows a better subthreshold swing and a higher SR ratio compared to the conventional SB-GNRFET. Also, this device can be operated as either p-type or n-type by simply reversing the polarity of the drain voltage, which adds flexibility in circuit design.

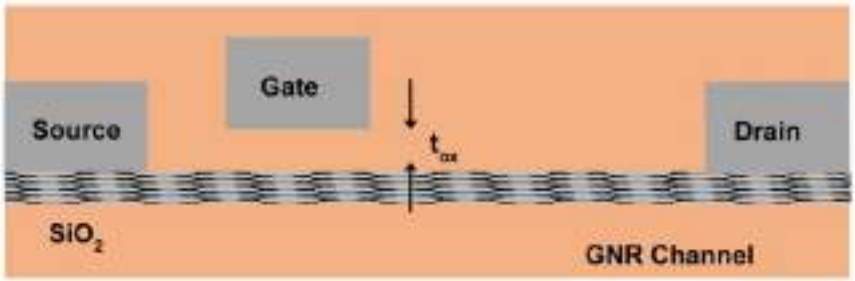

Figure 1.24: Asymmetric gate graphene nanoribbon field effect transistor [41, 49]

1.5.3.9. Electrically Activated Source Extension GNRFET

In this device configuration, the metal gate is divided into two parts, a main gate which regulates the channel potential and a side gate which works as an electrically operated source extension [50]. The pictorial representation of the ESE GNRFET is depicted in Figure 1.25. The use of sufficient voltage on the side gate, a step in the potential profile is induced, which acts as a source region without any physical doping. This design is based on the fact that the screening effect at the source extension lowers the change of the potential profile while increasing the drain bias, suppressing DIBL and improving SS [50]. Also, the increase in the length of the ESE region will reduces the ambipolar conduction.

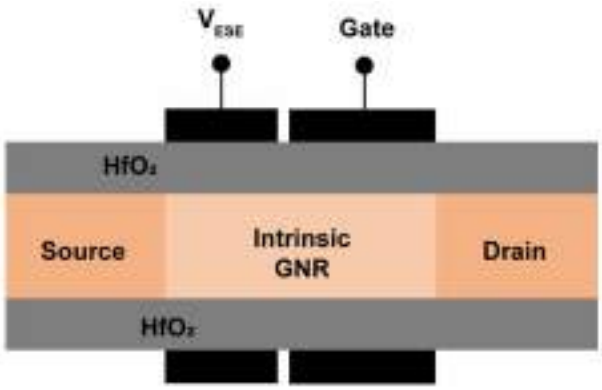

Figure 1.25: Electrically activated source extension (ESE)- GNRFET [41, 50]

1.5.3.10. Extra Peak Electric Field GNRFET (EPF-GNRFET)

The EPF-GNRFET is another dual-gate device that uses an original gate (OG) and a virtual gate (VG) with a fixed control voltage (VCS) applied between them, as shown in Figure 1.26. The VG forms an inversion channel under gate and this leads to an additional peak of electric field in the channel. This is an electric field induced source extension. This device configuration is designed in such a way that the surface potential under the OG remains consistent, whereas the surface

potential under the V_G declines abruptly, which improves the gate control of the potential barrier height [51]. The barrier height is reduced by increasing the VG voltage, which improves the thermionic emission and the on current. The carrier flow in EPF-GNRFET is created by three transport processes, thermionic emission over the channel barrier, source-to-drain tunneling and BTBT between the conduction and valence bands. The EPF-GNRFET has one of the best subthreshold swings among all the published GNRFET structures and is a promising candidate for ultra-low-power applications.

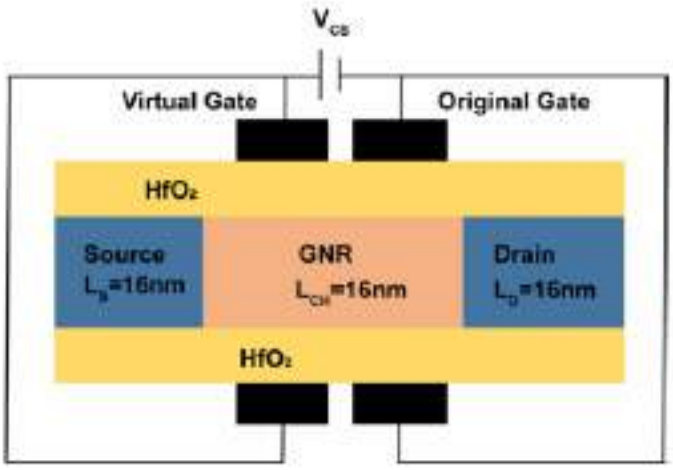

Figure 1.26: Schematic view of the EPF-GNRFET [41, 51]

1.5.4. GNRFET Operation

133 The basic structure of a GNRFET is comparable to a standard MOSFET. It comprises of a GNR channel with metallic source and drain contacts at both ends and a gate dielectric layer and a gate electrode to control the carrier density in the channel. In MOS-type GNRFETs, the source and drain regions consist of strongly doped GNR sections, providing ohmic contacts and well-defined ON and OFF states. The GNRFET has two working conditions as explained below.

ON Condition: $V_{gs} > V_{th}$, V_{ds}d(D ((at a constant value)

When the value of gate voltage is higher than the V_{th}, it creates a capacitive coupling between the gate and GNR channel resulting in the attraction of minority carriers towards the gate. This induces an inversion layer immediately below the dielectric interface which creates a conducting channel between the source and drain through which current can flow from drain to source. The on-state performance is superior than silicon MOSFETs primarily because of substantially higher mobility in GNRs due to ballistic transport and linear dispersion of Dirac electrons, so higher drive current for the same gate overdrive.

OFF Condition: $V_{gs} < 0V$, V_{ds} = D ((at a constant value)

When the gate voltage is below zero, carriers are repelled from the channel region. Under this condition, the device is in the OFF state and no current ideally flows from drain to source. The finite bandgap of the AGNR channel provides a potential barrier that suppresses carrier injection in the OFF state, which gives a high value of SR that is essential for various applications.

1.5.5. Advantages of GNRFET

GNRFET has significant material and device advantages over the regular silicon MOSFET and CNTFET which makes it a strong candidate for future generation nanoelectronics. These benefits are listed below:

High carrier mobility: Graphene has the highest carrier mobility with values up to 2×10^5 cm ^{2} /Vs. The reason is that the carriers in graphene behave as massless Dirac fermions and propagate along the lattice with a long mean free path. This high mobility is often maintained even after patterning of graphene into GNRs.

Tunable Bandgap: GNRs have a finite bandgap due to lateral quantum confinement, while pristine graphene is a zero-bandgap semimetal. For AGNRs, the bandgap is inversely proportional to the ribbon width, which makes AGNR to tune the bandgap by adjusting the value of N. Such design flexibility is not possible in silicon where the band gap is set and also is problematic in CNTFETs because control of the CNT chirality during synthesis requires very high technologically.

Reduced Short-Channel Effects: The atomically thin body of GNR provides better control to the metal gate over the channel. In Si - MOSFETs, the downscaling increase the DIBL and threshold voltage roll-off. However, this problem is mostly eliminated in GNRFETs due to the one-atom-thick channel, which improves the overall electrostatic performance of the device.

Low leakage current: The thin channel of AGNR is strongly controlled by the gate, which reduces the off-state leakage of GNRFETs than that of silicon MOSFETs with similar dimensions. This ensures high switching ratio even for a small channel length, which is very significant for low power digital applications**.**

Compatibility with High- (n The atomically smooth surface of GNR does not have any dangling bonds from normal to the basal plane and they can be readily integrated with high- % gate dielectrics such as HfO_2, $LaAlO_3$ and Al_2O_3. The reason is that GNR lacks with the interface trap density as observed at the silicon-oxide contact. The use of high- %dielectric material not only enhances the gate capacitance, but also minimizes the effective oxide thickness (EOT), which directly improves the switching properties.

High thermal conductivity: Graphene has a thermal conductivity of ~5000 $Wm^{-1}K^{-1}$ at room temperature, which is much higher than silicon (~150 $Wm^{-1}K^{-1}$). GNRFETs also have better heat

dissipation, which is critical for high-density ICs where self-heating effects can degrade the reliability.

CMOS Process Compatibility: GNR has a flat lattice structure which is compatible with traditional wafer scale CMOS production procedures, and GNRFETs may be integrated into the current semiconductor manufacturing infrastructure with minor adjustments. This gives a major practical benefit over alternative beyond-CMOS options, which need entirely new fabrication processes.

Power Efficiency: The values of Power-Delay Product (PDP) and Energy- Delay Product (EDP) of GNRFETs are significantly lower than those of Si-CMOS devices. This signifies the fact that GNRFETs require lower supply voltage, which leads to lower leakage current and lower cost of energy for the same logic function.

Wide Application Range: Apart from digital switching, GNRFETs have applications in high frequency analog circuits, gas and bio-sensors, optoelectronic devices and flexible electronics due to the versatile characteristics of graphene. GNR has excellent surface sensitivity, and this makes it particularly effective for sensing applications.

1.5.6. Challenges Confronted by GNRFET

However, the GNRFETs shows excellent but there are several manufacturing issues which need to be addressed before practical implementation in large scale ICs.

1. **Precise Width Tuning:** The bandgap of a GNR is highly sensitive to its width, and sub nanometer differences can have a dramatic effect on its electrical properties. The exact value of width on an atomic scale during GNR patterning by lithography is extremely challenging, and any width variation gives rise to undesired variability in threshold voltage and switching performance.

2. **Line Edge Roughness (LER):** If GNRs are derived from bulk graphene, atomic size roughness develops at the edges of the ribbon. This LER introduces localized states into the band gap, reduces the carrier mean free path and increases the scattering states which degrades the SR. The LER is one of the most crucial practical limits of GNRFET performance.
3. **Edge Passivation:** The dangling bonds at the edges of GNRs are chemically active and can generate electronic states that interfere with the inherent bandgap. The edge passivation of GNR using hydrogen or other elements like group 13 or group 15 atoms, is essential for stable and predictable electronic properties.
4. **Contact Resistance:** The formation of low resistance ohmic connections between the metallic source/drain electrodes and the GNR channel still remains a challenge. The Schottky barrier at the metal-GNR interface in SB-GNRFETs limits the drive current and switching speed. At the nanoscale, a technical challenge arises in obtaining substantial doping of source and drain GNR areas to form ohmic contacts for MOS-GNRFETs.
5. **Controlled doping:** The precise doping of the GNRs at the nanoscale is extremely challenging as compared to silicon, where ions implantation procedures are widely known. The dopant variability at the atomic scale causes significant threshold voltage fluctuation.
6. **High- (n (t Y(** Although the GNR surface has no out-of-plane dangling bonds, still the uniform and defect-free deposition of high- %ó“ws±%like HfO_2, $LaAlO_3$) on GNR without causing interfacial traps or chemical contamination is still challenging.

1.5.7. Role of Density Functional Theory in This Present Work

Density Functional Theory is one of the most used quantum mechanical approaches to explore the electrical structure of materials at the atomic scale [52]. It is widely used in research areas like material science, nanotechnology, condensed matter physics, chemistry and semiconductor device, due to the ability of giving accurate results with relatively low computational cost. Using the DFT scheme, researchers can study the structural, electrical, magnetic, optical and transport properties of atoms, molecules, solids and nanoscale devices. DFT was developed because to the limitation in solving the Schrödinger equation for many-electron systems [52]. The Schrödinger equation gives an accurate theoretical explanation of quantum systems and is very useful for simple single-electron systems such as the hydrogen atom. In a multi-electron system, all the electrons interact with each other through the Coulombic forces. Hence, the accurate solution of the many-body wave function is analytically complex and computationally expensive using the Schrödinger equation. Also, in the real systems involving hundreds or thousands of atoms, it is practically impossible to solve the full many-electron issue using traditional quantum mechanical methods. To overcome this limitation, DFT approach was introduced as an alternative approach. The DFT based approach used electron density as a central quantity instead of working with the complicated many-electron wave function. The reason is that the electron density depends only on three spatial coordinates, no matter how many electrons are present in the system. Because of this, the complexity of the calculations is significantly reduced. At the same time, the important quantum mechanical information of the material is still preserved. The basis of DFT comes from the Hohenberg Kohn theorems [53], which showed that the ground-state properties of a system are fully decided by its electron density. Later, the Kohn and Sham [54] proposed a practical scheme that made DFT usable for the actual calculations. The working of DFT scheme is based on a basic

principle. The problem of many electrons in a system is replaced by a system of noninteracting particles moving in an effective potential. In this form, the total energy of the system is expressed as a functional of the electron density. Then, the electron density is iteratively updated to arrive at the lowest energy state, which is called the ground state. The technique is self-consistent and is used to derive various parameters of the material such as total energy, band structure, density of states, charge distribution and electron transport behavior. The major advantage of DFT approaches is the perfect balance between computational expense and accuracy. Compared to wave-function based methods such as Hartree Fock and post-Hartree Fock techniques, DFT requires far less computer resources yet still achieves credible findings for large systems [52]. This is because DFT deals with electron density rather than the whole many electrons wave function which reduces the number of variables. This makes DFT very suitable for the study of realistic nanoscale materials and semiconductor devices. DFT allows scientists and researchers to predict the properties of novel materials before they are experimentally created. Furthermore, DFT also helps to understand the physical genesis of experimentally observed phenomena. In recent years, the DFT has been emerged as a significant method for the atomistic modeling in computational research. The Quantum ATK simulation tool includes a large set of DFT based methodologies for the study of molecules, surfaces, crystalline structures and nanoscale electrical devices [55]. This tool provides calculations of electrical, optical, magnetic, thermal and transport properties. In addition to the classic DFT methods, Quantum ATK offers semi-empirical and force-field based methods for effective treatment of systems with higher number of atoms [55].

In this thesis, the Semi-empirical DFT-based calculator (ATK-SE) is used to carried out all the device-level simulations. The reason for choosing this approach is the size of the proposed GS-AGNRFET device. The simulated structure contains several hundred of carbon atoms in the

AGNR channel, along with the metallic gate, ZGNR source and drain electrodes, and the bilayer of a wY 5VoKzY %as dielectric stack. A full first-principles DFT treatment of such a system would require very high computational resources and long simulation times. This becomes more difficult when multiple parameters like temperature, channel width, and edge passivation need to be studied. The semi-empirical approach reduces the computational cost by several orders of magnitude. At the same time, it provides accurate quantum effects parameters like tunneling, ballistic transport, and band structure modulation.

1.6. THESIS OBJECTIVES

The entire work in the present thesis is divided into seven chapters based on the following objectives listed below:

1. To investigate the role of junction-less channel architecture and gate-stack dielectric engineering on the electrical characteristics of Armchair Graphene Nanoribbon Field Effect Transistors using Semi empirical DFT-based approach.
2. To analyze the impact of temperature on the performance of proposed Gate-Stacked AGNRFET using Semi-empirical DFT based approach.
3. To analyze the effect of edge passivation and width variation of the AGNR channel in the proposed GS AGNRFET for low-power applications.
4. To study the impact of Semi empirical DFT based models on the performance of the proposed Gate Stacked Armchair Graphene Nanoribbon Field Effect Transistors.
5. To develop a toxic gas sensor using the proposed device for environment monitoring applications.

1.7. SCHEME OF CHAPTERS

This thesis is organized into seven chapters to accommodate all the research objectives. Each chapter is organized to be fundamentally self-contained.

Chapter 1. Introduction

This chapter summarize the basics of nanoscale MOSFET, scaling issues, and short-channel effects. After that, the ways to overcome the short-channel effects are discussed. In this regard, the different engineering schemes and the advanced FET structures, such as SOI MOSFET, TFETs and CNTFET, reported in different research articles, have been presented. Further, the research gaps found during the literature survey have been explored. Then, the chapter progresses toward the architecture of GNRFET, the basic working principle of GNRFET, and its potential advantages and drawbacks. Then, the thesis objective and overall organization of the thesis, and the importance of the research work presented in this thesis are discussed.

Chapter 2. Gate - Stack Engineering, Temperature Effects, and Edge Passivation in Graphene Armchair Nanoribbon FET

In this chapter, the GS-KQX] POb %s~ üzö”wÅu%%pwo”s≠%aW 5VoKzY %nwzsq≈Aq%≠qvwsq≈.≠s%w% proposed and benchmarked against conventional GNRFET, demonstrating a ~73% suppression in off-state leakage current and a ~46 times improvement in switching ratio. The gate-stack configuration enhances on-state current by ~30% and peak transconductance from 24.71 to 27.76 µS, confirming superior electrostatic control and amplification capability over conventional GNRFET. Then, the temperature-dependent analysis of proposed GS AGNRFET within 250 350 K reveals that rising temperature causes ~48% reduction in I_{on}, ~98% degradation in SR, and ~56% increase in SS, with DIBL increasing ~138 times, establishing the device as best suited for

low-temperature and low-power applications. The novel empirical exponential fitting functions for I_{on} and I_{off} as functions of temperature are proposed, enabling drain current estimation without additional simulations and offering utility in compact circuit modelling. Further, the edge passivation of the AGNR channel is performed using 13th group element Boron and 15th group element Nitrogen to investigate their impact on electronic structure and transport properties of the proposed GS-AGNRFET. Boron edge passivation of the AGNR channel reduces I_{off} p”%A4B%%6 % times and increases Ion by ~139 times compared to pristine AGNR FET, yielding an exceptional ± —wqvwÅu%o~wö%ot%74 =%%6 4%Mb~ üo≠sr %ö%oz%qöÅtw. ≠o~wöÅ±2%-AGNR FET demonstrates the optimal balance between bandgap (1.48 eV), PDOS enhancement, and leakage control, confirming its strong candidacy for ultra-low-power and high-performance nanoscale electronic applications.

Chapter 3. Impact of Channel Width Engineering on Electronic and Quantum Transport Properties of Gate-Stack Armchair Graphene Nanoribbon FET

In this chapter the electronic and quantum transport properties for the bulk configuration of AGNRs with varied number of carbon atoms along AGNRs width (N) are investigated. The semi-empirical DFT based approach is used to calculate the band structure, DOS, and transmission spectrum for the bulk configuration of AGNRs. The AGNRs are used in channel material to analyse the performance of field-effect transistors with Gate Stack architecture. The GS-AGNR (N = 4) FET demonstrates significantly reduced off-state current and a markedly improved switching ratio compared to wider ribbons having N = 7, 10 and 13. Overall, this chapter establishes channel width as a critical design parameter and highlights GS - AGNR (N = 4) FET as promising candidates for low-power and nanoscale electronic applications.

Chapter 4. Reliability performance analysis of Gate-Stack Armchair Graphene Nanoribbon FET using Extended Hückel DFT model

The Extended Hückel model with SCF iterations is employed in this chapter to investigate the reliability and performance of the GS-AGNRFET. The EH model demonstrates strong agreement with benchmark first-principles DFT methods including PBE, HSE06, DFT½, and tight-binding approaches in both bandgap trend and transmission coefficient values for AGNR (N = 4 and 7), validating its physical credibility and computational efficiency for nanoscale device modelling. The A7 device (GS-AGNRFET with AGNR N = 7 as channel material) demonstrates superior performance over the A4 device across all key reliability metrics including I_{on}, I_{off}, SR, V_{th}, DIBL, device efficiency, and static power dissipation under the EH-SCF framework. Advanced transport analyses including DDOS, PLDOS, transmission spectrum, transmission pathways, and EDD collectively confirm enhanced gate electrostatic control, stronger electron tunneling, and more efficient carrier transport in the A7 device. Overall, the A7 device achieves a remarkably low static üö–s≠%t%4=B%%6 % 2%vwqv%≠%wuÅtwqoÅ≈’%ö–s≠%voÅ%vs%K: %s–wqs%84=%%6 % /%År % substantially lower than all previously reported GNRFET configurations available in the literature, making it highly reliable for low-power applications such as biomedical devices, gas sensors, and signal amplification circuits.

Chapter 5. Performance enhancement of Gate - Stack Armchair Graphene Nanoribbon FET through Icosagens edge passivation

The EH model with SCF iterations is employed in this chapter to investigate the effect of edge passivation by Icosagens elements (B, Al, Ga, and In) in the channel material of GS - AGNRFET. The passivation of Icosagen group elements at the edge of bulk-configured P AGNR decreases the bandgap, and the DOS analysis confirms that passivated AGNRs provide more accessible states for

electrons in the conduction band as compared to P AGNR. It is also observed that the passivation of Al, Ga, and In at the edges of AGNR (N = 7) results in complete bandgap closure (E_g = 0 eV), making it metallic in nature and unsuitable for transistor operation. Therefore, AGNR (N = 4) is selected as the channel material for the present chapter. The effect of Icosagen group element passivation in the channel material of GS-AGNRFET shows a significant increase in I_{on} from 1.06 K%ö%B4 %K%wÅ%Kz AGNRFET, a reduced value of I_{off} t≠ö~ %4 C 76 %K%ö%4 9 76 %K%wÅ%vs%‰ In KQX] POb 2%Ar %%ps≈s≠%oz.s%ot%] %ö~ %4A7 76 %ö%49= 76 %ö≠%o±±wo~sr%KQX] POb±%±% compared with P AGNRFET. The transconductance and device efficiency analysis shows the higher value of g_m and DE in Al AGNRFET and Ga AGNRFET, which signifies stronger electrostatic control and better electron transport. The PLDOS and transmission pathway analysis further confirms that the possibility of electron tunneling is higher in Al AGNRFET and Ga AGNRFET as compared with other passivated AGNRFETs.

Chapter 6. Aluminium-passivated Gate-Stack Armchair Graphene Nanoribbon FET as a gas sensor for toxic gases

In this chapter, the Al-AGNRFET is investigated as a nanoscale sensor for toxic gas molecules, ±üsqwwqoz”%~ ~ öÅw%XR /%Ar %Åw≠ösÅ%wö“ws%XY /. A two-step simulation methodology is employed in the present study, the linear combination of atomic orbitals framework with generalized gradient approximation is used for bulk configured analysis, while the Extended Hückel model with NEGF formalism under a self-consistent field framework is used for device-level simulation. The bulk configured analysis demonstrates that Al-AGNR exhibits stable üv”±wö≠ü~wÅ%-ww%r±ö≠ü~wÅ%sÅs≠uws±%t%64-8%sd %Ar %6478%sd %ö≠%XY %Ar %XR 2%s±üsq~wsz’4% bvs%sÅ±wwv”%oz.s±%/s%A9>+ %ö≠%XY %Ar %77>+ %ö≠%XR 2%-vwqv%/s%49>%Ar %4>%w s±%wuvs≠% than the pristine AGNR. The device analysis of the proposed Al-AGNRFET shows I_{on}-based

sensitivities of 85.14% for NO_2 and 7.03% for NH_3, and SR-based sensitivities of 99.86% for NO_2 and 99.47% for NH_3. Also, the proposed device also shows opposite V_{th} shifts of +0.15 V and 64̸76%d %ö≠2XY$_2$ and NH_3, respectively, which further confirms the selectivity response of the device. Moreover, the selectivity coefficient is calculated using I_{on}-based sensitivity that reaches 12.12 when NO_2 is treated as the target gas, which confirms the strong selective detection of NO_2 in the presence of NH_3. Owing to these results, the proposed Al-AGNRFET is a promising candidate for applications in environmental air quality monitoring, industrial safety systems, ~ sr wqozp%≠so~v%owuÅö±wq±2%u≠wq. z≈≠oz%XR % öÅwö≠wÅu%oÅr %o. ≈ö~ ö≈w s%~ w±wöÅ%qöÅ≈öz

Chapter 7. Conclusion, Social Impact and Future Scope

This chapter summarizes the overall research work illustrated in this thesis, along with the concrete conclusions drawn from the results presented in this thesis. This chapter also discusses the social impact and future scope of the present work and how this work can be extended and used in future research directions.

1.8 References

[1] A. N. Saxena, *Invention of integrated circuits: untold important facts*. World Scientific, 2009.

[2] G. E. Moore, "Cramming more components onto integrated circuits," ed: McGraw-Hill New York, 1965.

[3] Y. H. Chen *et al.*, "Ultra high density SoIC with sub-micron bond pitch," *IEEE*, pp. 576-581, 2020.

[4] R. U. Ayres, "The transistor transition: 1945 1969," in *The History and Future of Technology: Can Technology Save Humanity from Extinction?*: Springer, 2021, pp. 425-466.

[5] W. Cao *et al.*, "The future transistors," *Nature*, vol. 620, no. 7974, pp. 501-515, 2023.

[6] R. H. Dennard, F. H. Gaensslen, H.-N. Yu, V. L. Rideout, E. Bassous, and A. R. LeBlanc, "Design of ion-implanted MOSFET's with very small physical dimensions," *IEEE Journal of solid-state circuits*, vol. 9, no. 5, pp. 256-268, 2003.

[7] M. Lundstrom, "Moore's law forever?," *Science*, vol. 299, no. 5604, pp. 210-211, 2003.

[8] C. Hu, S. C. Tam, F.-C. Hsu, P.-K. Ko, T.-Y. Chan, and K. W. Terrill, "Hot-electron-induced MOSFET degradation-model, monitor, and improvement," *IEEE Journal of Solid-State Circuits*, vol. 20, no. 1, pp. 295-305, 1985.

[9] S. A. Parke, J. E. Moon, H. j. C. Wann, P. K. Ko, and C. Hu, "Design for suppression of gate-induced drain leakage in LDD MOSFETs using a quasi-two-dimensional analytical model," *IEEE Transactions on Electron Devices*, vol. 39, no. 7, pp. 1694-1703, 1992.

[10] M. Neisser and S. Wurm, "ITRS lithography roadmap: 2015 challenges," *Advanced Optical Technologies*, vol. 4, no. 4, pp. 235-240, 2015.

[11] M. J. Kumar *et al.*, "Special issue on nanowire transistors: Modeling, device design, and technology," *IEEE Transactions on Electron Devices*, vol. 55, no. 11, pp. 2813-2819, 2008.

[12] R. Martel, T. Schmidt, H. R. Shea, T. Hertel, and P. Avouris, "Single-and multi-wall carbon nanotube field-effect transistors," *Applied physics letters*, vol. 73, no. 17, pp. 2447-2449, 1998.

[13] K. Biswas and A. Sarkar, *Advanced Nanoscale MOSFET Architectures: Current Trends and Future Perspectives*. John Wiley & Sons, 2024.

[14] K. S. Novoselov *et al.*, "Electric field effect in atomically thin carbon films," *Science*, vol. 306, no. 5696, pp. 666-669, 2004.

[15] H.-Q. Wu, C.-Y. Linghu, H.-M. Lu, and H. Qian, "Graphene applications in electronic and optoelectronic devices and circuits," *Chinese Physics B*, vol. 22, no. 9, p. 098106, 2013.

[16] K. S. Novoselov *et al.*, "Two-dimensional gas of massless Dirac fermions in graphene," *Nature*, vol. 438, no. 7065, pp. 197-200, 2005.

[17] F. Schwierz, "Graphene transistors: status, prospects, and problems," *Proceedings of the IEEE*, vol. 101, no. 7, pp. 1567-1584, 2013.

[18] L. Yang, C.-H. Park, Y.-W. Son, M. L. Cohen, and S. G. Louie, "Quasiparticle energies and band gaps in graphene nanoribbons," *Physical review letters*, vol. 99, no. 18, pp. 186801, 2007.

[19] Anshul and R. Chaujar, "Semi-empirical DFT Based Investigation of Electronic and Quantum Transport Properties of Novel GS-AGNR (N) FET," *IEEE Transactions on Nanotechnology*, vol. 23, pp. 400-407, 2024.

[20] S. Lone, A. Bhardwaj, A. K. Pandit, S. Gupta, and S. Mahajan, "A Review of Graphene Nanoribbon Field-Effect Transistor Structures: Lone, Bhardwaj, Pandit, Gupta, and Mahajan," *Journal of Electronic Materials*, vol. 50, no. 6, pp. 3169-3186, 2021.

[21] P. K. Chatterjee, W. R. Hunter, T. C. Holloway, and Y. T. Lin, "The impact of scaling laws on the choice of n-channel or p-channel for MOS VLSI," *IEEE Electron Device Letters*, vol. 1, no. 10, pp. 220-223, 1980.

[22] H. Majima, Y. Saito, and T. Hiramoto, "Impact of quantum mechanical effects on design of nano-scale narrow channel n-and p-type MOSFETs," *IEEE Xplore proceedings*, pp. 33-3. 2001.

[23] H. H. Radamson et al., "Miniaturization of CMOS," *Micromachines*, vol. 10, no. 5, 2019

[24] J. Robertson, "High dielectric constant oxides," *The European Physical Journal-Applied Physics*, vol. 28, no. 3, pp. 265-291, 2004.

[25] D. J. Frank, R. H. Dennard, E. Nowak, P. M. Solomon, Y. Taur, and H.-S. P. Wong, "Device scaling limits of Si MOSFETs and their application dependencies," *Proceedings of the IEEE*, vol. 89, no. 3, pp. 259-288, 2001.

[26] S. G. Chamberlain and S. Ramanan, "Drain-induced barrier-lowering analysis in VSLI MOSFET devices using two-dimensional numerical simulations," *IEEE transactions on electron devices*, vol. 33, no. 11, pp. 1745-1753, 1986.

[27] http://www.onmyphd.com/?p=mosfet.short.channel.effects.

[28] Anshul and R. Chaujar, " Investigation Temperature variation on DC and Analog performance of Gate Stack GNRFET using DFT-based atomic scale Modelling," *in Proc. 2025 Devices for Integrated Circuit (DevIC), Kalyani, India, IEEE*, pp. 337-342, 2025.

[29] A. Srivastava, Y. M. Banadaki, and M. S. Fahad, "Dielectrics for graphene transistors for emerging integrated circuits," *Electrochemical Society Transactions 225*, vol. 61, no. 2, pp. 351-361, 2014.

35 [30] E. Takeda, C. Y. W. Yang, and A. Miura-Hamada, "Hot-carrier effects in MOS devices," *Academic Press*, 1995.

[31] H. Wong and H. Iwai, "On the scaling issues and high- %süzoqs~ sÅ%t%z≠o~vwÅ%o~s%wszq≠w±% for nanoscale MOS transistors," *Microelectronic Engineering*, vol. 83, no. 10, pp. 1867-1904, 2006.

[32] A. Nowbahari, A. Roy, and L. Marchetti, "Junctionless transistors: State-of-the-art," *Electronics*, vol. 9, no. 7, pp. 1174, 2020.

[33] S. Sahay and M. J. Kumar, "Junctionless field-effect transistors: design, modeling, and simulation," *Wiley-IEEE Press* 2019.

[34] W. Long, H. Ou, J. M. Kuo, and K. K. Chin, "Dual-material gate (DMG) field effect transistor," *IEEE Transactions on Electron Devices*, vol. 46, no. 5, pp. 865-870, 1999.

[35] P. K. Pal, B. K. Kaushik, and S. Dasgupta, "Investigation of symmetric dual-k spacer trigate FinFETs from delay perspective," *IEEE Transactions on Electron Devices*, vol. 61, no. 11, pp. 3579-3585, 2014.

[36] J.-Y. Cheng, C. W. Yeung, and C. Hu, "Extraction of front and buried oxide interface trap densities in fully depleted silicon-on-insulator metal-oxide-semiconductor field-effect transistor," *ECS Solid State Letters*, vol. 2, no. 5, pp. Q32-Q34, 2013.

[37] C. P. Kumar and K. Sivani, "A tunnel field effect transistor is a substitute for ultra-low power applications," *Proc. of IEEE," International Conference on Advances in Human Machine Interaction (HMI)*, pp. 1-4, 2016.

[38] A. C. Seabaugh and Q. Zhang, "Low-voltage tunnel transistors for beyond CMOS logic," *Proceedings of the IEEE*, vol. 98, no. 12, pp. 2095-2110, 2010.

[39] M. H. Moaiyeri, R. F. Mirzaee, K. Navi, and O. Hashemipour, "Efficient CNTFET-based ternary full adder cells for nanoelectronics," *Nano-Micro Letters*, vol. 3, no. 1, pp. 43-50, 2011.

[40] K. Tamersit, M. K. Q. Jooq, and M. H. Moaiyeri, "Analog/RF performance assessment of ferroelectric junctionless carbon nanotube FETs: A quantum simulation study," *Physica E: Low-dimensional Systems and Nanostructures*, vol. 134, pp. 114915, 2021.

[41] S. Lone, A. Bhardwaj, A. K. Pandit, S. Gupta, and S. Mahajan, "A review of graphene nanoribbon field-effect transistor structures," *Journal of Electronic Materials*, vol. 50, pp. 3169-3186, 2021.

[42] Z. Chen, Y.-M. Lin, M. J. Rooks, and P. Avouris, "Graphene nano-ribbon electronics," *Physica E: Low-dimensional Systems and Nanostructures*, vol. 40, no. 2, pp. 228-232, 2007.

[43] Y. Yoon, G. Fiori, S. Hong, G. Iannaccone, and J. Guo, "Performance comparison of graphene nanoribbon FETs with Schottky contacts and doped reservoirs," *IEEE Transactions on electron devices*, vol. 55, no. 9, pp. 2314-2323, 2008.

[44] Y.-Y. Chen *et al.*, "A SPICE-compatible model of MOS-type graphene nano-ribbon field-effect transistors enabling gate-and circuit-level delay and power analysis under process variation," *IEEE Transactions on Nanotechnology*, vol. 14, no. 6, pp. 1068-1082, 2015.

[45] C. Dinh *et al.*, "Atomically precise graphene nanoribbon transistors with long-term stability and reliability," *ACS nano*, vol. 18, no. 34, pp. 22949-22957, 2024.
[46] H. Sarvari and R. Ghayour, "Design of GNRFET using different doping profiles near the source and drain contacts," *International Journal of Electronics*, vol. 99, no. 5, pp. 673-682, 2012.
[47] A. Naderi, "Theoretical analysis of a novel dual gate metal graphene nanoribbon field effect transistor," *Materials Science in Semiconductor Processing*, vol. 31, pp. 223-228, 2015.
[48] M. A. Eshkalak, R. Faez, and S. Haji-Nasiri, "A novel graphene nanoribbon field effect transistor with two different gate insulators," *Physica E: Low-dimensional Systems and Nanostructures*, vol. 66, pp. 133-139, 2015.
[49] M. Gholipour, N. Masoumi, Y.-Y. C. Chen, D. Chen, and M. Pourfath, "Asymmetric gate Schottky-barrier graphene nanoribbon FETs for low-power design," *IEEE Transactions on Electron Devices*, vol. 61, no. 12, pp. 4000-4006, 2014.
[50] A. Naderi and P. Keshavarzi, "Electrically-activated source extension graphene nanoribbon field effect transistor: novel attributes and design considerations for suppressing short channel effects," *Superlattices and Microstructures*, vol. 72, pp. 305-318, 2014.
[51] M. A. Eshkalak and M. K. Anvarifard, "A novel graphene nanoribbon FET with an extra peak electric field (EFP-GNRFET) for enhancing the electrical performances," *Physics Letters A*, vol. 381, no. 16, pp. 1379-1385, 2017.
[52] M. Orio, D. A. Pantazis, and F. Neese, "Density functional theory," *Photosynthesis research*, vol. 102, no. 2, pp. 443-453, 2009.
[53] P. Hohenberg and W. Kohn, "Inhomogeneous electron gas," *Physical review*, vol. 136, no. 3B, pp. B864, 1964.
[54] W. Kohn and L. J. Sham, "Self-consistent equations including exchange and correlation effects," *Physical review*, vol. 140, no. 4A, pp. A1133, 1965.
[55] S. Smidstrup *et al.*, "QuantumATK: an integrated platform of electronic and atomic-scale modelling tools," *Journal of Physics: Condensed Matter*, vol. 32, no. 1, pp. 015901, 2019.

2

CHAPTER

Gate - Stack Engineering, Temperature Effects, and Edge Passivation in Armchair Graphene Nanoribbon FET

In this chapter, the GS-Tb i maYo(’β μəη ³γ ×(–(—³ε– ’⁴(n³j ?g–Tgj (’”³’ε’“⁶⁴³“(architecture is proposed and benchmarked against conventional GNRFET, demonstrating a ~73% suppression in off current and a ~46 times improvement in switching ratio.

The gate-stack configuration enhances on-state current by ~30% and peak transconductance from 24.71 to 27.76 μS, confirming superior electrostatic control and amplification capability over conventional GNRFET.

Temperature-dependent analysis of proposed GS AGNRFET within 250 350 K reveals that rising temperature causes ~48% reduction in I_{on}, ~98% degradation in SR, and ~56% increase in SS, with DIBL increasing ~138 times, establishing the device as best suited for low-temperature and low-power applications.

Novel empirical exponential fitting functions for I_{on} and I_{off} as functions of temperature are proposed, enabling drain current estimation without additional simulations and offering utility in compact circuit modelling.

Edge passivation of the AGNR channel is performed using 13th group element Boron and 15th group element Nitrogen to investigate their impact on electronic structure and transport properties of the proposed GS-AGNRFET. Boron edge passivation of the AGNR channel reduces the I_{off} —(HH((BA (⁶³β ’⁵(–γ ”(³γ “⁴ ’–⁵ ’⁵ the I_{on} by ~139 times compared to pristine AGNR FET, yielding an exceptional switching ratio of ~1.45 × BA 9(

Compared to all configurations, the B-AGNR FET demonstrates the optimal balance between bandgap (1.48 eV), PDOS enhancement, and leakage control, confirming its strong candidacy for ultra-low-power and high-performance nanoscale electronic applications.

2.1 INTRODUCTION

The rapid miniaturization of semiconductor transistor ±‰w sÅ±wöÅ± has been both the engine and the emblem of the modern electronics era. For nearly six decades, the guiding principle governing this miniaturization has been Moore's Law4‰vs‰Wöö≠s ±‰o—‰~s±‰o~the number of transistors on an integrated circuit doubles approximately every two years [1]. This remarkable advancement has been maintained through ongoing enhancements in lithographic accuracy, materials science, and device design. But as channel lengths decrease below 10 nm, the traditional silicon-based CMOS transistors begin to degrade in both fundamental and practical aspects [2]. The challenges that emerge at the nanoscale are collectively referred to as SCEs. Among these, DIBL reduces the gate's ability to control the channel potential in the presence of high drain voltages, threshold voltage roll-off produces unpredictable device-to-device variability, surface scattering degrades carrier mobility, and hot-carrier effects introduce reliability concerns. Perhaps most critically, quantum mechanical tunneling through the gate oxide and from drain to source dramatically increases leakage currents. These challenges have made it clear that silicon, the material on which the modern electronics industry is built, may be approaching the limits of what miniaturization can achieve through conventional approaches [3]. Graphene, the two-dimensional allotrope of carbon discovered experimentally by Geim and Novoselov in 2004 and recognized with the Nobel Prize in Physics in 2010, has emerged as a promising candidate for beyond - CMOS silicon transistor era [4]. Graphene-based electronic devices offer several advantages, including exceptional mobility for ballistic transport, high carrier speed for rapid switching, an atomically thin structure for optimal electrostatic control, and excellent thermal conductivity [5]. For transistor

applications, these advantages of graphene promise devices that could switch at higher speeds, with lower power consumption, and with better electrostatic control than the silicon-based devices. Although graphene has outstanding electrical properties, but lack of bandgap limits its application in electronics [6]. However, researchers have reported many bandgap engineering approaches so that graphene can be used in electronics. One bandgap engineering approach includes the making of graphene nanoribbons by quantum confinement, which creates a bandgap in graphene [7]. AGNRs and ZGNRs are the two primary types of graphene nanoribbons, which are classified according to their edge geometry [8]. Previously reported study reveals that AGNRs can be categorized into three separate subfamilies depending on N = 3p, 3p + 1, and 3p + 2 [9]. Among the three AGNR families 3p, 3p+1, and 3p+2 family, the 3p+1 family is known to exhibit the largest bandgaps, which makes them particularly attractive for applications in nanoelectronics where a substantial bandgap is essential [6]. Although N = 3 and N = 9, which belong to 3p family, these AGNRs also exhibit semiconducting behaviour but their bandgaps are smaller than those in the 3p+1 family [10]. AGNR (N = 4) from the 3p + 1 family offers a wider bandgap and stronger electrostatic control, leading to enhanced transistor performance metrics such as switching ratio, subthreshold swing, and transconductance. Also, it is experimentally feasible through bottom-up synthesis techniques [11]. Thus, AGNR (N = 4) stands out as a promising choice for high-performance and low-power graphene-based FET applications. Without the spin degree of freedom, tight-binding computations reveal that ZGNRs and AGNRs with N = 3p+2 show metallic behavior [12]. AGNRs electrical properties are heavily influenced by their width and edge structure, making them very adaptable to specific applications [13]. Although, developing a transistor using graphene nanoribbons is only the initial phase of the engineering challenge. The gate dielectric,

the insulating substance that separates the metallic gate electrode from the semiconducting channel, is equally crucial in influencing transistor performance [14]. Conventional SiO_2 layer shows challenges at ultra-thin dimensions due to the direct tunneling of electrons through the oxide layer. The high %wzsq≈≠wq%materials (like $LaAlO_3$. %G%%6/ provide a solution to this challenge [15]. By employing a material with a high value, the gate oxide capacitance increases which can improve the performance of transistor but r w≠sq~%sü±wwÅ%t%oKzY %o±% a high- %wzsq≈≠wq%o≠s±Å≈±%s–s≠oz%.Ar o~ sÅ≈oz%qvozsÅus±[16]4%oKzY 2%-vwz%ott s≠zÅu%%wv% r wzsq≈≠wq%qöÅ±≈oÅ≈% %%%6/2%ot≈sÅ%.tts≠±%ö~ %ööö≠%Å≈s≠toqs%..ozw”%-vsÅ%sü±ws r %w≠sq~z”% on semiconductor channels such as silicon or graphene nanoribbons [17]. This poor interface can result in a high density of interfacial defects, increased charge trapping, and degraded carrier mobility, all of which negatively impact device performance. Additionally, the r sü±wwÅ%o≠öqs±±%ö≠%oKzY %qoÅ%s or %ö%±. s±%.qv%±%q≠”±≈ozw≈wÅo%%ö—s≠%s~ üs≠o≈.≠s±2% instability in thin film form, and difficulties in achieving uniform, pinhole-free layers over large areas. The gate-stack architecture addresses this trade-off elegantly [18]. By combining a thin low- %oW %Ås≠toqwz%o”s≠%s≈—ssÅ%vs%qvoÅÅsz%Ar %%wv- %wzsq≈≠wq%o”s≠%.qv%±% zoÅ≈voÅ.~ %z.~ wÅo≈s%VoKzY 2% %G%%6/2%vs%uo≈s%±≈oqy%±w- .z≈oÅsö.±z”%- ovÅ≈ovÅ±%%o≠us% effective gate capacitance, preserves a high barrier at the channel-dielectric interface, and avoids the direct tunneling limitation of ultra-thin single-layer oxides [19]. This GS approach has been validated in conventional MOSFET architectures and, as this chapter demonstrates, produces analogous benefits in the conventional GNRFET context. The operational environment of a transistor adds another essential aspect to device performance. When the device size is less than 20 nm, a high value of temperature can greatly affect or even ruin the device operation. For better reliability, it is essential to investigate the impact of temperature

variation on performance of the proposed device. Several studies highlight how temperature impacts transistor performance. Eshkalak [20] found that GNRFETs perform best at low temperatures. Caridad et al. [21] showed that graphene FETs maintain stable plasmonic behavior across a wide range (10 K 300 K) due to weak electron phonon interactions. Illarionov et al. [22] reported strong thermal stability and minimal hysteresis up to 448 K, while Wang et al. [23] demonstrated consistent performance from 4.2 K to 300 K. Overall, both graphene-based devices and conventional FinFET/NCFET technologies tend to perform better at lower temperatures. However, the effect of temperature on GNRFET at atomic scale is still elusive in literature. Understanding this temperature sensitivity is especially important for applications ranging from biomedical implants operating near body temperature, to space-based electronics, to industrial systems exposed to elevated thermal stresses. The width and edge structure of AGNRs play pivotal roles in determining their electrical characteristics, making them highly customizable for specific applications [24]. The literature survey led to the observation that most studies focus on passivated ZGNR, while there have been few investigations on passivated AGNR [25]. By fine-tuning the width and passivation of edges in configuration of AGNRs, researchers aim to unlock their full potential for realizing high-performance, low-power electronic devices that can transcend the limitations of existing semiconductor technologies. Hydrogen passivation is the most studied baseline case. Substituting hydrogen with atoms from different chemical groups such as Boron (B, from Group 13) or Nitrogen (N, from Group 15) can fundamentally alter the edge electron density, the density of states, the bandgap, and ultimately the transistor's on-state conductance and off-state leakage. To address these issues, this chapter presents a detailed DFT based atomistic study of a GS- AGNRFET, examining how the gate-stack design, temperature, and edge

passivation influence key performance metrics, with the goal of improving high-performance, low-power graphene transistor technology beyond conventional silicon limits. The study primarily focuses on the effect of gate stacking in the conventional GNRFET. The electronic properties such as drain current, transmission spectrum and peak transconductance are analyzed, followed by temperature and edge passivation analysis of proposed GS AGNRFET in terms of switching ratio, off-state current, DIBL, V_{th} and subthreshold swing. The proposed GS architecture effectively mitigates short-channel effects and enhances device performance.

18 This chapter is organized as follows: Section 2.2 presents the device design and physical models, Section 2.3 describes the model calibration, Section 2.4 discusses the fabrication feasibility, Section 2.5 discuss the results obtained from simulations and finally, Section 2.6 concludes the findings of the current chapter.

2.2 DEVICE DESIGN AND PHYSICAL MODELS

The proposed device, Gate-Stack Armchair Graphene Nanoribbon Field-Effect Transistor architecture is depicted in Figure 2.1. It consists of a semiconducting AGNR channel flanked by metallic ZGNR source and drain contacts, all enclosed by a bilayer gate dielectric stack and a metallic gate electrode on top. This basic topology is shared across all device configurations studied in this thesis, with variations in channel width, edge passivation chemistry, and oxide thickness. The device is schematically organized into three distinct spatial

165 regions: the source electrode, the central scattering region (which contains the channel and the gate stack), and the drain electrode. The Pristine AGNR (P AGNR with N = 4) is used as a channel material in the proposed device and the conventional GNRFET to compare the electrical characteristics of both devices.

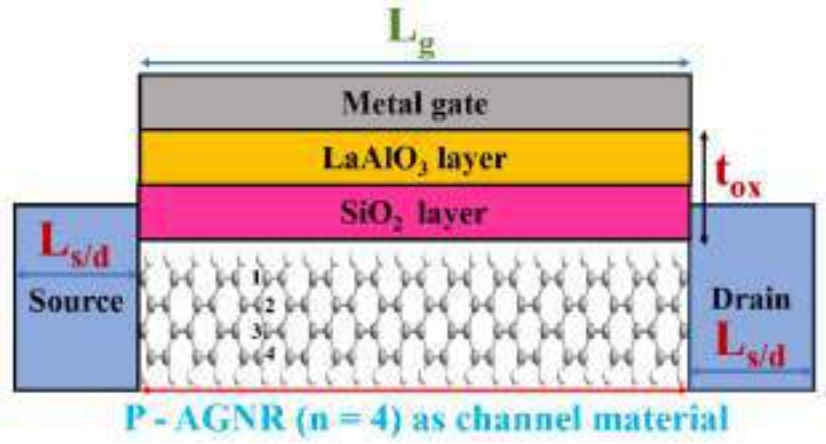

Figure 2.1: Cross sectional view of proposed GS AGNRFET [26]

Further, to study the impact of edge passivation on the channel material of proposed device, the pristine AGNR channel is independently passivated with the 13th group element Boron and the 15th group element Nitrogen, yielding the Boron-passivated AGNR (B-AGNR) and Nitrogen-passivated AGNR (N-AGNR), respectively, as illustrated in Figure 2.2 (a c). These passivated AGNRs are subsequently employed as channel materials in a separate set of gate-stacked device configurations named as boron passivated GS -AGNRFET (B-AGNR FET) and nitrogen passivated GS -AGNRFET (N-AGNR FET).

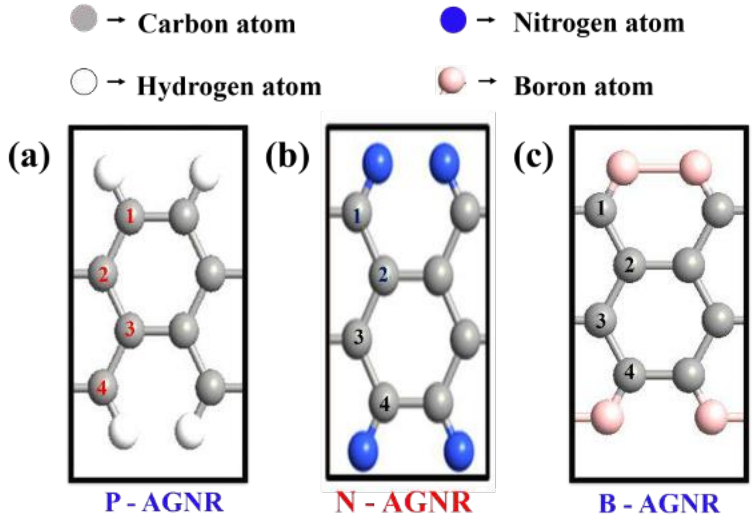

Figure 2.2: Atomic view of (a) P AGNR, (b) N AGNR, and (c) B AGNR [26]

The source and drain contacts are made using the ZGNR configuration with N = 6, as ZGNR exhibits metallic behavior due to its zero bandgap, making it suitable for use as a metallic contact. To reduce the circuit complexities, the drain, source, and channel regions are all n-type doped, with the doping concentration of the channel region (N_{Ch}) maintained at 3×10^{16} e/cm^3 and the doping concentration of the source and drain region ($N_{s/d}$) maintained at 5×10^{18} e/cm^{3}2%Å±.≠wÅu%vo~%vs%ö≠öüö±sr%s–wqs ±%s≠tö≠~ oÅqs%w≠%w üö≠–sr%p"%ö–s≠wÅu%vs% parasitic capacitance through heavy n-type doping of the source and drain as compared to the channel. A metallic gate is employed over the dielectric layers in all device configurations. As the uo≈s%öö≈Å≈woz%zo"±%%≠.qwoz%ö≈zs%Å%s≈s≠~ wÅvÅu%%s–wqs ±%zs q≈wqoz%vo≠oq≈s≠w≈wq±2%År% metal gates additionally provide several advantages, including excellent thermal stability, high purity, and compatibility with CMOS processing [27]. The gate length (L_g) and source/drain length ($L_{s/d}$) are fixed at 7 and 5 nm, respectively, for all device configurations studied in this chapter, and the oxide layer thickness (t_{ox}) is maintained at 0.50 nm. The key distinction between the conventional GNRFET and the proposed GS - AGNRFET lies in the gate dielectric architecture. While the conventional GNRFET employs only a single dielectric layer, the GS - AGNRFET implements a gate stack architecture comprising a low- %wzs q≈wq%o"s≠% of silicon dioxide ($SiO_2$2%%G%4C/%År—wqvsr%s≈–ssÅ%s%wv- %Å≈voÅ.~ %z.~ wÅo≈s%o"s≠% ($LaAlO_3$2%%G%6/%År%s%QX] %voÅÅsz2%vs≠s%s%wqyÅs±±s±%t%s%wY$_2$ and $LaAlO_3$ layers are each 0.25 nm. The motivation behind adopting the GS configuration arises from the fundamental trade-off between the high- %wzs q≈wq%öÅ±oÅ%År%%.wopzs%oÅr uoü%ö≠% transistor applications, where raising the dielectric constant induces a decrease in the bandgap. This problem is resolved through GS implementation, which maintains the effective oxide thickness while simultaneously benefiting from the improved electrostatic control offered by

the high- ‰ o≈s≠wz4 Also, the t_{ox} is inversely related to the gate oxide capacitance (C_{ox}), i.e., reducing t_{ox} will increase the C_{ox}, which provides better control of the gate over the channel as ≈vs%ö≈sÅ≈wz%≠öü%Å‰o≈s%“wvs% $_{ox}$) decreases. Further, the parameters can be co-related by a mathematical expression as follows [15]:

(2.11)

(2.12)

Now, putting the value of C_{ox} from Eq. (2.11) in Eq. (2.12)

(2.13)

where,

gate oxide potential

surface charge density

thickness of the oxide layer

gate oxide capacitance

permeability coefficient

the dielectric constant of the gate insulation

All the electronic properties and quantum transport simulations in this thesis are performed using the Quantum Atomistic Toolkit software platform developed by Synopsys, which provides an integrated environment for atomic-scale device modeling [28]. In this chapter, Semi-empirical (SE) calculator in ATK referred to as ATK-SE which implements tight-binding models in the Linear Combination of Atomic Orbitals basis is used to carried out all the simulations [29]. The tight-binding model employed throughout this work is the Slater-

Koster (SK) model within the Density-Functional Tight-Binding (DFTB) parametrization framework, without the self-consistent field iteration step. The decision to use the SK-based ATK-SE calculator rather than a full first-principles DFT approach is deliberately motivated by the nature of the proposed device systems [30]. The GNR transistors considered here involve simulation cells containing several hundred carbon atoms, a metallic gate, and a dielectric stack. A full DFT treatment of such systems at multiple bias points would be computationally prohibitive and can be cost effective, whereas the SK model reduces the computational cost by several orders of magnitude while retaining the quantum mechanical character of electron transport. However, the SK model has been extensively validated for carbon-based systems in the literature and has been shown to reproduce DFT-level bandgaps, transmission spectra, and current-voltage characteristics for GNR devices to a level of accuracy that is fully adequate for the device engineering comparisons carried out in this work. Also, this work is extended using Extended Hückel model in the ATK aO%ö%qvsqy%vs%s–ws ±% reliability with different DFT models in **Chapter 4.**

The Slater-Koster tight-binding model, originally formulated by J. C. Slater and G. F. Koster in their seminal 1954 Physical Review paper [31]. This model is built on the LCAO approximation in which the electronic wavefunction of the crystal is expressed as a linear combination of atomic orbitals localized at each atomic site. In QuantumATK, the LCAO basis functions are written as products of a radial function $R_{nl(r)}$ and a real spherical harmonic $Y_{lm(\hat{r})}$, i.e., $_{nlm(r)} = R_{nl(r)} \cdot Y_{lm(\hat{r})}$, where n, l, m are the principal, azimuthal, and magnetic quantum numbers respectively [31]. For the AGNRs studied here, the relevant atomic orbitals of the carbon atoms are the 2s, $2p_x$, $2p_y$, and $2p_z$ atomic orbitals. The full tight-binding Hamiltonian of the device is then constructed from the on-site energies ($_i$) and the inter-site hopping

integrals (t_{ij}) between neighboring orbitals in which in the SK model are treated through the two-center approximation. The Hamiltonian matrix element between any two orbitals on neighboring sites depends only on the types of orbitals involved and on the direction cosines (l, m, n) of the inter-atomic bond vector, independently of any third atom. The Hamiltonian and overlap matrix elements between basis functions on sites i and j are evaluated from these tables as functions of the inter-atomic distance $|R_i - R_j|$, following the standard Slater-Koster transformation rules. The equation for the matrix elements of the tight-binding Hamiltonian in the Slater-Koster model is given as [30]:

G (2.14)

where,

matrix element of the Hamiltonian between atoms i and j

Slater-Koster transfer integral

creation operators for atomic orbitals

annihilation operator for atomic orbitals

In QuantumATK, the band structure is computed using a 9 × 9 × 1 k-point sampling with the for bulk configuration analysis for edge passivated structures, and a 1 × 1 × 100 k-point sampling along the periodic transport direction (the C-direction) for device-relevant transmission calculations. The Hartree density mesh cutoff is set to 40 Ha throughout, providing a sufficiently fine real-space grid to accurately resolve the electrostatic potential across the thin dielectric layers of the gate stack. For the device-level transport calculations in which the AGNR channel is sandwiched between two ZGNR electrodes held at different electrochemical potentials by the applied drain voltage (V_{ds}), the Non-Equilibrium Green's

Function (NEGF) formalism is employed. The NEGF method is the natural and rigorous quantum mechanical framework for computing steady-state transport in open systems at the nanoscale, where quantum coherence, tunneling, and ballistic transport are dominant and classical drift-diffusion equations are no longer applicable. In QuantumATK, the NEGF method is implemented in the SE calculator, which couples the SK Hamiltonian of the central scattering region (the channel) to the self-energies of the source and drain electrode regions.

b vs%XOQP%ys”%. .oÅ~w”%w⁴%ö%qozq. .z~s%vs%s~o≠r sr%Q≠ssÅ±%. .Åq~wöÅ±%ö≠%vs%qsÅ≠oZ%suwöÅ%

Using Hamiltonian from equation 2.1: %oÅr %ö–s≠zoüüwÅu% o~≠w2%vs%Q≠ssÅ±%. .Åq~wÅ%±vÅu%

NEGF is mathematically expressed as [32]:

$$G \quad G\ G \qquad G \qquad G \qquad ^{-1} \tag{2.15}$$

where,

≠s~o≠r sr%Q≠ssÅ±%. .Åq~wöÅ

infinitesimal positive number

Overlapping matrix

Hamiltonian matrix

self-energies for the left electrode

self-energies for the right electrode

After the calculation of *G(E)*, the transmission coefficient for a device configuration is obtained by the without self-consistent solution of the Schrodinger equation and 3-N%Zöw⁴öÅ±% equations using the Slater-Koster model with NEGF method and it can be mathematically expressed as [33]*:*

(2.16)

where,

transmission coefficient

1 ≠s≈o≠r sr %Q≠ssÅ±‰ .Åq≈ẅÅ%
or –oÅqsr %Q≠ssÅ±‰ .Åq≈ẅÅ%
broadening function of the left electrode
broadening function of the right electrode

= i (-

The drain current is calculated after the calculation of T(E) and mathematically expressed by Landauer-Büttiker Formalism as [34]:

—

where,

drain current
Fermi-Dirac distribution
1 chemical potential of the left electrode
chemical potential of the right electrode

Further, these simulations models are calibrated with the previous findings in the literature in next section 2.3.

2.3 MODEL CALIBRATION

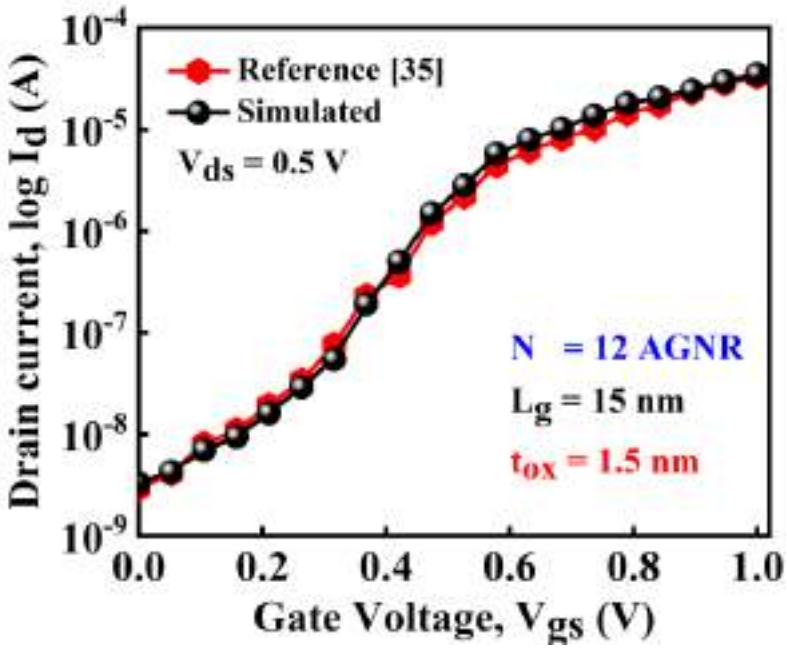

Figure 2.3: Transfer characteristics calibration of simulated and reference data [35]

The simulations models are validated by previously reported research findings in the literature [35]. To calibrate the simulation models, the MOSFET has been designed using AGNR (N = 12) material in the entire channel region and fixed device dimensions (L_g = 15 nm, t_{ox} = 1.5 nm), the source and the drain are doped extensions of GNRs, and SiO_2 . %o%4C/%o±%o~s%o“ws% as shown in reference [35]. The NEGF approach with a self-consistent tight-binding function is used to solve the Schrödinger equation to obtain device characteristics for MOSFET. Figure 2.3 depicts the transfer characteristics at V_{ds} = 0.5 V, of the extracted data from the reference [35] and results obtained from the simulations. Figure 2.3 shows the change in I_d on the logarithmic scale with gate voltage (V_{gs}). The logarithmic scale of I_d with V_{gs} depicts leakage current (I_{off}) in the device, aiding in the prediction of subthreshold slope. It can be observed from the Figure 2.3 that the results of the simulations are consistent with previous findings.

The near concordance between the simulated and reference data sets validates the choice of simulation models. Once the credibility of the simulation with the approach is established, a GS architecture is employed in the conventional GNR-FET. The detailed simulation process of the present study for GS-AGNRFET is already discussed in section 2.2.

2.4 FABRICATION FEASIBILITY

Figure 2.4: Fabrication flow chart for GS AGNRFET device [36]

92 The process flow chart for the fabrication process of GS - AGNRFET is displayed in Figure 2.4. This flowchart depicts a systematic overview of the fabrication process, emphasizing critical fabrication and material deposition phases required to produce a high-performance GS-AGNRFET [37]. The first step is to synthesis of GNRs using STM lithography. The STM lithography provides atomic-level precision in patterning graphene with well-defined widths and predetermined crystallographic orientations, which directly determines the edge type, armchair or zigzag GNRs and hence the confinement-induced bandgap of the GNR [38] . In

Step 2, these ±”Å~vs±ẃsr %QX] ±%ẃs%ẃoÅ±ts≠sr %ẃÅ~ö%ẃÅ%ẃÅ±. zo~ẃÅu%ẃ .p±≈ẃo~s%ẃ .qv%ẃ±%ẃaẃY %±ẃÅu% dry or wet transfer techniques [39]. The substrate selection significantly affects device performance, as epitaxial graphene on SiC substrate shows much lower residual potential tz .q≈ .o~ẅöÅ±%–78%ẃ sd /%ẃ±%ẃqö~ üoẃ≠sr %ẃ~ẃv%ẃoÅ±ts≠sr %ẃ≠oüvsÅs%ẃÅ%ẃaẃY %–=C 77 meV), which supports conventional band-transport rather than hopping and localization effects [40]. Next, device patterning is performed using photolithography or Electron Beam Lithography (EBL) techniques. EBL uses hydrogen silsesquioxane (HSQ) as a negative-tone electron-beam resist and has been demonstrated to produce GNR channel widths down to ~10 nm, with edge roughness less than ~0.35 nm [40]. In Step 4, the source and drain contacts are deposited using electron beam evaporation, typically employing a Cr/Au bilayer that forms ohmic contacts with the zero-bandgap two-dimensional graphene regions on either side of the GNR channel. In Step 5, a dielectric layer is deposited over the channel. However, the direct deposition of high- %ẃwzsq~≠ẃu±%ẃ .qv%ẃ±%ẃoKzY %ẃÅ%ẃQX] %ẃ .p±≈ẃo~s±%ẃ≠%ẃÅẃö~%ẃ≈%ẃowuv~tö≠ o≠r 2%ẃ±%ẃ%ẃsor ±%ẃö%ẃöö≠% interface quality, increased charge trapping, high density of interfacial defects, and degraded carrier mobility. To overcome these challenges, GS architecture is adopted in Step 6, where ~vs%ẃo~s%ẃö“ẃvs%ẃ≠%ẃüzẃ%ẃÅ~ö%ẃö%ẃvÅ%ẃaẃY %ẃÅs≠toqẃvz%ẃ”s≠%ẃÅr %ẃ%ẃoKzY %ẃas high- %ẃwzsq~≠ẃu%ẃ”s≠% bvs%ẃaẃY %ẃ”s≠%ẃoq~±%ẃ±%ẃ%ẃqvs~ ẃqozz”%ẃ≈opzs%ẃüo±±ẃo~ẅöÅ%ẃÅr %Å .qzso~ẅöÅ%ẃ”s≠%ẃvo~%ẃoqẃzẃo~s±% .Åẃtö≠~ %ẃoKzY %ẃsüö±ẃẃöÅ2%ẃsr .qs±%ẃvs%ẃsÅ±ẃ”%ẃöt%ẃÅs≠toqs%ẃ≈o~s±2%ẃÅr %ẃ ovÅ≈owÅ±%ẃ%ẃqöÅ±≈oÅ~% EOT [18]. In Step 7, the metal gate electrode is formed using a metal decomposition process, completing the top-gate structure of the device [39]. Finally, at Step 8, the GS-AGNRFET is fully formed and continues into subsequent processing stages. The fabrication sequence discussed above integrates well-established nanofabrication techniques at each step and is

consistent with fabrication approaches reported in the literature. This fabrication feasibility flow chart summary confirms that GS-AGNRFET is practically feasible.

2.5 RESULTS AND DISCUSSIONS

This section is divided into three subsections corresponding to the studies that constitute this chapter: (i) performance comparison between conventional GNRFET and proposed GS AGNRFET device (ii) effect of temperature variation on the performance of proposed device (iii) the impact of Boron and Nitrogen edge passivation on the electronic structure and transport properties of the proposed device

2.5.1 Performance comparison between conventional GNRFET and proposed GS -AGNRFET device

Figure 2.5(a) depicts a comparison between the drain current (I_d) of the GNRFET and GS-AGNREFT with gate voltage (V_{gs}) varying from 0 to 1 V at V_{ds} = 0.5 V. The simulations are performed on the same dimension, and results are compared within the output obtained from numerically varied layer parameters. The main challenge in nanoscale devices is the high value of I_{off}. The high leakage current is raised by carrier tunneling, which causes high power dissipation in IC. Hence, it is observed that the use of gate-stacking provides a reduction in off current (I_{off}) from 3.26 to 0.91 pA as compared with conventional GNRFET. Also, the on current (I_{on}) increases from 6.39 to 8.34 μA in the case of GS - AGNRFET. The use of gate stacking reduced the I_{off} by 72% and gave an increment in I_{on} by 30%. Also, the switching ratio for both devices is shows in Figure 2.5(b). The SR is an important factor that determines the performance of a device. A high SR ratio indicates that the device can reliably and rapidly switch between conducting (on) and non-conducting (off) states, enabling it to amplify and

process electrical signals with minimal power consumption. From Figure 2.5, it can be observed that the value of SR is 91.3 $\times 10^6$ for GS AGNRFET, and for GNRFET it is 1.46 $\times 10^6$. The value of SR for the proposed device is 46 times higher than the conventional GNRFET. The higher value of SR in proposed device signifies the high switching speed and low power consumption. The reason for the better SR and, reduction in I_{off} is that the high-k material in gate stacking helps to improve the strength of fringing electric fields, which significantly minimized the height of potential barrier in off state, and a reduction in I_{off} has been achieved, which cause increment in SR.

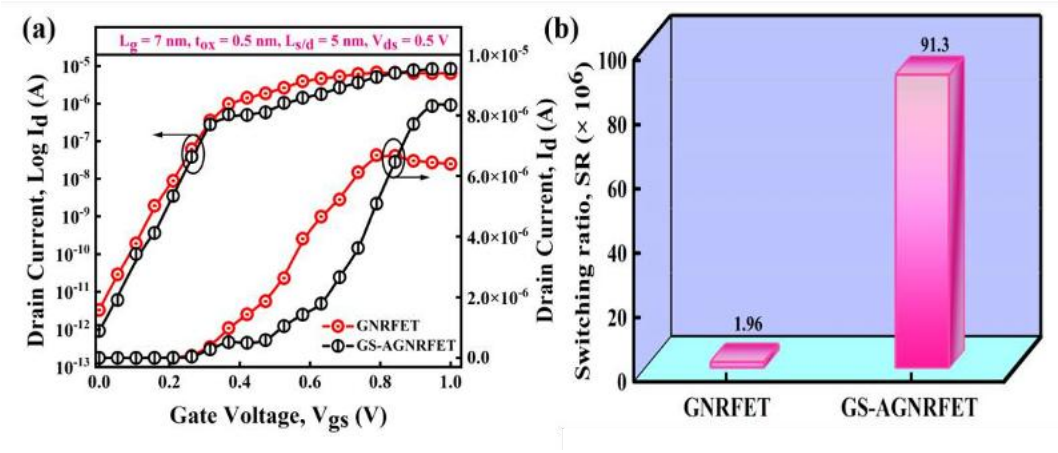

Figure 2.5: (a) Transfer characteristics of conventional GNRFET and proposed GS AGNRFET, (b) switching ratio for GNRFET and GS AGNRFET [41]

Figure 2.6 (a) illustrates the comparison of both devices in terms of peak transconductance (g_m) at V_{gs} = 0.75 V. The g_m of a device describes its ability to alter the barrier height in the saturation mode using the applied gate voltage [41]. It is observed that the value of peak conductance increased from 24.71 to 27.76 μS in GS - AGNRFET. The transistor amplification is directly related to the g_m. The rise in the g_m of a device governs amplification applications. The reason is that the value of I_d increases with gate stacking and significantly improves the g_m. Mathematically, g_m can be expressed as [17]:

(2.18)

where,

change in drain current

change in gate voltage

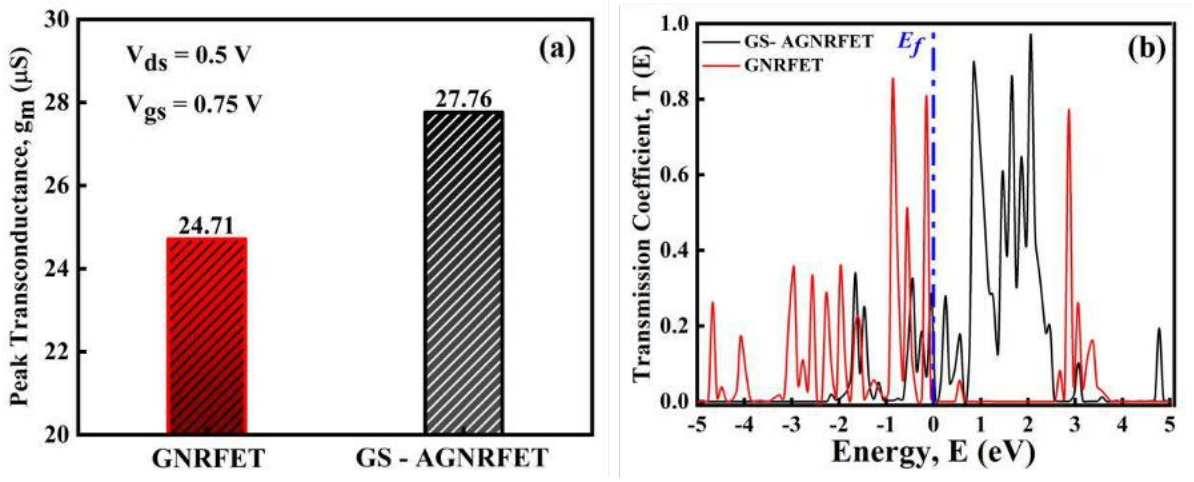

Figure 2.6: (a) Bar plot of peak transconductance of GNRFET and GS - AGNRFET, (b) Variation of transmission spectrum with energy for both devices [41]

The variation of the transmission spectrum in terms of transmission coefficient, T(E) with energy (E), is shown in Figure 2.6 (b). The T(E) has been calculated using Eq. (2.16). The value of E has been varied from -5 to +5 eV to observe the behavior of T(E). From Figure 2.6, it is observed that the number of peaks available for conduction in the valance band (VB) in GS-AGNRFET is greater than GNREFT. Due to the electric field generated by the V_{gs} and the device's Z-shaped design, the transmission spectrum of GNRFETs is not anticipated to be symmetrical. A higher value of T(E) means that a higher number of electrons can tunnel the nanoribbon's energy barrier between its conduction and valance bands. Also, proposed device shows stronger and more frequent peaks around E_f which leads more electron transport, better

conductivity and higher current as compared to the conventional GNRFET. Further, the analysis led to a conclusion that the proposed device GS AGNRFET shows improved results in terms of I_{on}, I_{off}, SR, peak transconductance and T(E) as compared with the conventional GNRFET.

2.5.2 Effect of temperature variation on the performance of proposed device

In this section, the effect of temperature on analog parameters like I_{on}, I_{off}, SR, SS, and DIBL have been studied. The authors have examined the performance of GS-AGNRFET at five different temperatures, T = 250, 275, 300, 325, and 350K. The temperature range of 250 to 350 K was chosen because it represents realistic working conditions for a device, from slightly low temperatures (for cryogenic and space applications) up to moderately high temperatures (for automotive and industrial environments), including room temperature (300 K). Studying this range helps us clearly understand how temperature affects the device, especially in terms of carrier movement, mobility changes, and leakage currents in GNRFETs. Figure 2.7(a) depicts the I_d -V_{gs} characteristics curves for GS - AGNRFET at different temperatures. As, the temperature increases, the value of the I_{on} decreases, which is shown in Figure 2.7(b). Also, the I_{off} increases with an increase in temperature. The reason is that the stronger control of the gate voltage on the channel near the source at low temperatures results in a higher emission of thermal current.

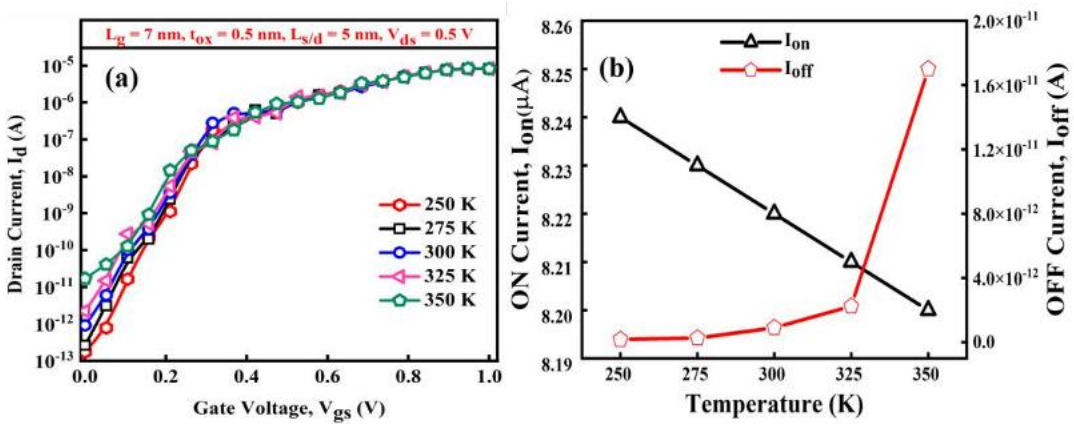

Figure 2.7: (a) I_d-V_{gs} characteristics curves for GS - AGNRFET at varied temperatures (b) Change in I_{on} and I_{off} with a range of temperatures [41]

It is observed that I_{on} has an exponential decay with temperature, and I_{off} shows an exponential increase with temperature as shown in Figure 2.7 (b). Based on the behaviour of I_{on} and I_{off} currents at varied temperatures, novel empirical fitting exponential functions have been proposed in the present chapter. These parameters can be mathematically expressed as follows:

(2.19)

(2.20)

where, 7 7 7and are empirical fitting parameters as given below:

G	on current
	8.3409
	5×10^{-5}
	1×10^{-18}
	0.452
T	temperature

The above empirical equations provide a simple way how the value of I_d changes with temperature. Also, using these equations we can find out estimated values of I_d without performing further simulations. Further, these empirical equations can be useful in circuit modeling and design.

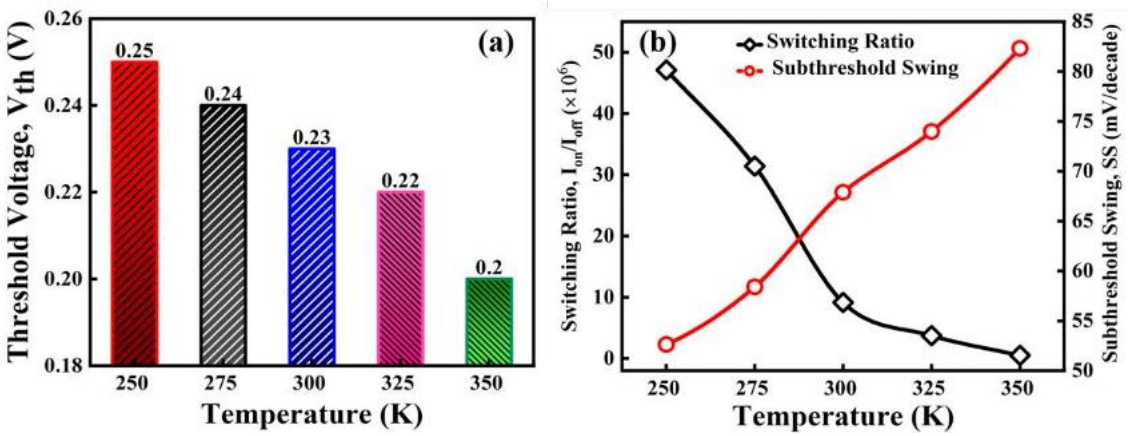

Figure 2.8: (a) Threshold voltage variation with temperature (b) switching ratio and subthreshold swing at different temperatures [41]

Figure 2.8(a) portrays the change in V_{th} with temperature. The V_{th} is the lowest value of V_{gs} required to create conduction between the source and drain terminals. The value of V_{th} decreased from 0.25 to 0.20 V as the temperature increased from 250 to 350 K. The reason is that at higher temperature the intrinsic carrier concentration increases, so lower value of V_{gs} is required to form the channel. Variation of SR and subthreshold swing (SS)for a range of temperature adopted in the present work as shown in Figure 2.8(b). From the simulated results, we analyzed that the value of SR decreases with an increase in temperature depending on the behavior of I_{on} and I_{off}. An important variable in transistor miniaturization is the SS The SS signifies how much value of V_{gs} required to increase the I_d by one decade in the subthreshold region. It can be mathematically expressed in terms of temperature as [42]:

$$G \qquad (2.21)$$

From Eq. (2.21), with a rise in temperature, the value of SS increases, which degrades the device's performance. The reason is that the rise in temperature increases carrier leakage and reduces the effectiveness of gate control over the channel. The values of I_{on}/I_{off} and SS at different temperatures are tabulated in Table 2.1.

TABLE 2.1

Values of Switching Ratio and Subthreshold Swing [41]

Temperature (K)	SR (× 10^6)	SS (mV/decade)
250	47.1	52.62
275	31.4	58.41
300	9.13	67.88
325	3.72	73.99
350	0.49	82.31

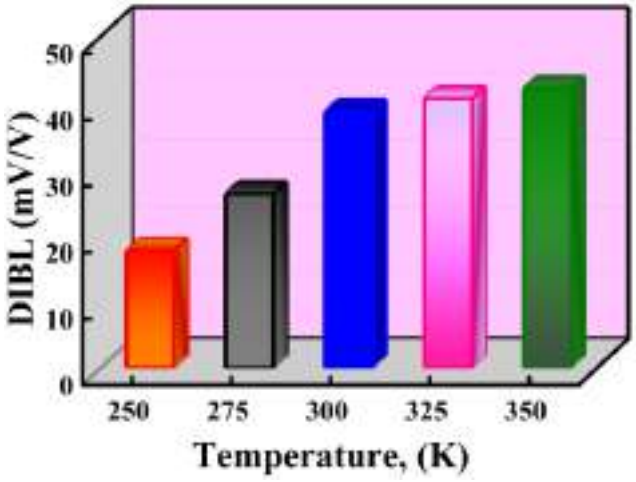

Figure 2.9: Dependence of DIBL at various temperatures [41]

Figure 2.9 depicts the dependence of DIBL for a range of temperatures adopted in the present study. DIBL is a short-channel effect that occurs in transistors. A higher value of V_{ds} increases the drain depletion zone as the channel gets shorter, and lowering the potential barrier. Even though the V_{gs} is less than the threshold voltage, the potential barrier is reduced, allowing

electrons to pass between the source and drain. This phenomenon has been referred to as DIBL [43]. It is calculated at V_{ds} (high) = 1.0 V, V_{ds} (low) = 0.1 V, using the mathematical formula [43]:

$$\frac{G}{G} \quad (2.22)$$

From Figure 2.9, it is observed that the value of DIBL is decreasing with temperature. The increase in the value of DIBL with rise in temperature signifies that the performance of the proposed device degrades with temperature. From the above results, it is concluded that the proposed device shows better performance at lower temperature and can be suitable for low power applications. Thus, the temperature analysis shows that our proposed device GS AGNRFET is reliable at low and room temperature.

2.5.3 Impact of Boron and Nitrogen edge passivation on the electronic structure and transport properties of the proposed device

In this section, the edges of AGNRs are passivated with the 13th group element Boron and the 15th group element Nitrogen. Initially, the electronic properties of bulk passivated AGNR are studied in terms of bandgap and projected density of states. Further, the B/N passivation used in the channel material of the proposed Gate Stacked pristine AGNR-FET (P AGNR FET). Moreover, parameters like I_{off}, V_{th}, and I_{on} have been calculated from the I_d V_g characteristics of all proposed device configurations. Also, the t_{ox} is taken 1 nm for this study. Bar plot of the bandgap is shown in Figure 2.10. Figure 2.10 shows that the value of bandgap after passivation at edges in P AGNR is significantly reduced from 1.77 to 0.34 eV. The bandgap is basically

the energy difference between the VB, where electrons normally reside, and the conduction band, where electrons need to reach to produce current [44].

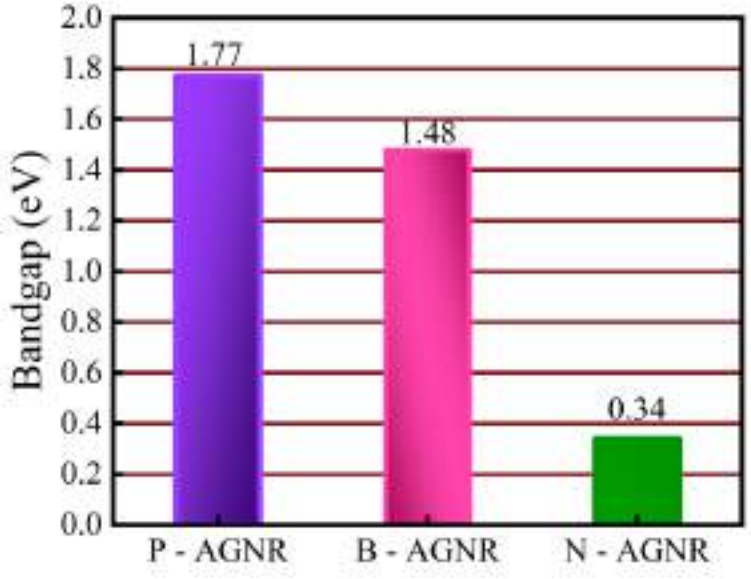

Figure 2.10: Bar plot of bandgap for all three-bulk configured AGNRs [26]

In the context of present work, the P-AGNR has a bandgap of 1.77 eV, which is quite wide, meaning electrons find it relatively harder to jump across and contribute to the on current. When we passivate the edges with B and N, this bandgap gets modified, it reduces to 1.48 eV for B-AGNR and further down to 0.34 eV for N-AGNR. A reduced value of bandgap does not inherently indicate superior performance; it presents a dual challenge. However, it supports greater electron participation in conduction and enhances I_{on}, but it simultaneously poses the risk of raising the I_{off}, as some electrons may thermally leak across the narrow gap even when the device is supposed to be in an off state. The superior performance of B-AGNR over N-AGNR in switching ratio is attributable to its bandgap of 1.48 eV, which effectively balances conduction and leakage control. Further, the analysis of PDOS provides a more detailed, microscopic explanation of the behaviour of the bandgap as shown in Figure 2.11.

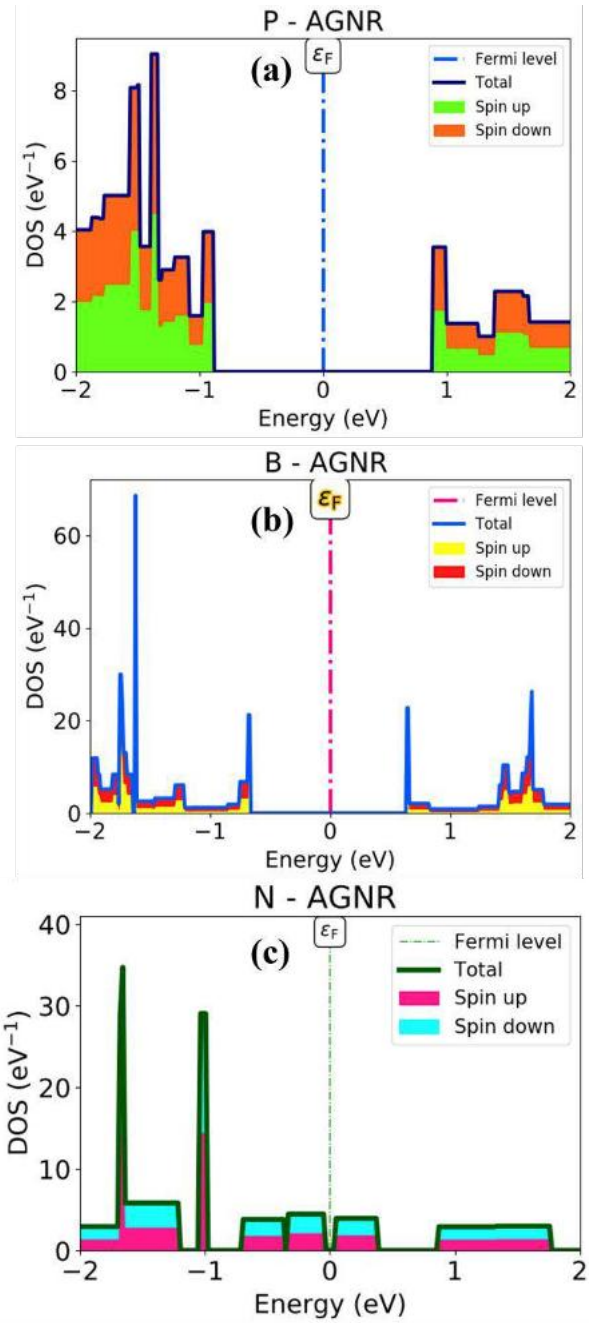

Figure 2.11: Projected Density of states analysis of (a) P AGNR, (b) B AGNR, and (c) N AGNR [26]

The PDOS indicates the quantity of quantum electronic states accessible at each energy level within the material, precisely projected onto the relevant atoms or orbitals. In simplest terms, PDOS shows the density of states in the energy range, an increased number of states at the

Fermi level signifies a greater availability of electrons for conduction, which directly correlates with enhanced device performance [45]. From Figure 2.11(a), it can be observed that in P AGNR, the PDOS is very low and minimal dense around fermi level, which is consistent with its bandgap value. However, the use of boron at the edge of the AGNR results in a significant wÅq⁄so±s%Å%⁄vs%ZNYa%ouÅw.r.s%ö%üü⁄ö“w˜o~sz”%o%sd 2%±%qö~üo⁄sr%ö%pö.~%b%sd %Å%⁄vs P AGNR as shown in Figure 2.11 (b). The reason is that B belongs to the 13th group element and electron deficient element, which generates acceptor like states VB. From Figure 2.11 (c), in the N-AGNR, nitrogen, as an electron-rich element from group 15, donates additional electrons, hence elevating states toward the conduction band, resulting in a bandgap reduction to 0.34 eV and a PDOS approaching 40 eV^{-1}. Although this may be remarkable but the challenge lies in the minimal bandgap, which complicates the complete shutdown of the device. Further, the SR of N-AGNRFET despite being superior to that of P-AGNRFET but still, it is less than the SR of B-AGNRFET.

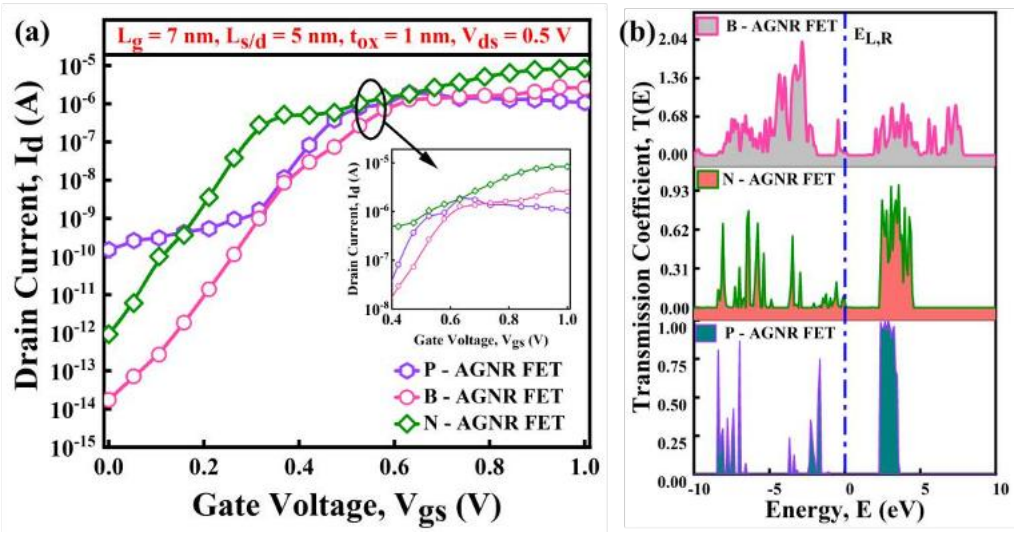

Figure 2.12: (a) I_d V_g characteristics for the proposed devices and (b Transmission spectrum analysis of proposed devices [26]

Figure 2.12 (a) depicts the I_d V_g characteristics for P AGNR FET, B AGNR FET, and N AGNR FET. From the I_d V_g characteristics, it is observed that the I_{off} of B - AGNR FET is reduced by 7.8×10^5 times as compared to the P AGNR FET, which improved the SR for the B AGNRFET. The reason is that when boron atoms are added to the edges, they can passivate the dangling bonds. This reduces defects and edge roughness, which can serve as carrier leakage routes and reduce I_{off}. Also, the value of I_{on} in B AGNRFET is 139 times better than P-AGNR FETs due to the higher DOS by boron passivation, which is evident in the PDOS analysis. The increase in I_{on} and decrease in I_{off} in B AGNRFET provides significant increment in SR. All values of I_{on}, I_{off} and SR are tabulated in Table 2.2. In contrast, the N-AGNR FET exhibits an intermediate behaviour. Although the value of SR i.e., 9.16×10^6 is clearly superior to P-AGNR FET, it is unable to match B-AGNR FET. The reason is already discussed in bandgap and PDOS analysis.

TABLE- 2.2

Values of I_{on}, I_{off}, and SR for the proposed devices [26]

Parameter	Proposed devices		
	P -AGNRFET	B AGNRFET	N AGNRFET
I_{on}	1.02×10^{-6}	2.54×10^{-6}	8.37×10^{-6}
I_{off}	1.49×10^{-10}	1.74×10^{-14}	9.13×10^{-13}
SR	7.11×10^3	1.45×10^8	9.16×10^6

Figure 2.12 (b) depicts the transmission spectrum analysis for all proposed devices. As discussed in section 2.2, NEGF formalism is used to determine the T(E), which signifies the quantum mechanical probability that an electron at a specific energy E would successfully transmit over the channel from the source to the drain. A broader and higher transmission

spectrum indicates that a greater number of electrons flow through the channel efficiently, which directly correlates with enhanced conductance and improved current flow. It is observed from 2.12(b) that the B -AGNRFET shows broader and higher transmission spectrum is as compared with other device configurations, which concludes will be the conductance. Also, the N- AGNRFET shows better TS as compared to P AGNRFET. However, N AGNRFET has inferior edge passivation efficiency relative to B results in a lower peak transmission compared to the B-AGNR FET.

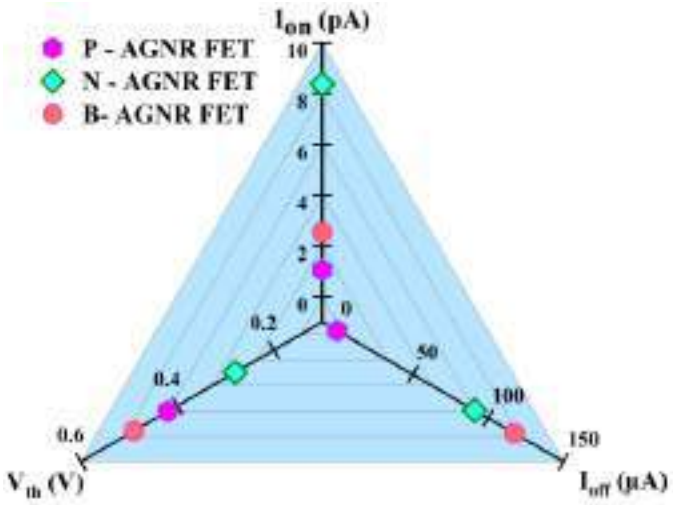

Figure 2.13: Variation of I_{on}, I_{off} and V_{th} for P AGNR FET, N AGNR FET, and B AGNR FET [26]

The parameters like I_{off}, V_{th}, and I_{on} are calculated from the I_d V_g characteristics as displayed by the spider chart (Figure 2.13). From Figure 2.13, it is observed that the passivation of B/N enhances the value of V_{th} and I_{on} as compared with the P AGNR FET. The value of I_{on} increased in B AGNR FET by 139 times to the P AGNR FET. From the V_{th} analysis in Figure 2.13, the authors concluded that the passivation of B atoms at the edges of P AGNR increased the value of V_{th} by 15%, whereas the passivation of N atoms at the edges of P AGNR decreased it by 33%. The reason is that B/N atom passivation can alter the electronic

structure and carrier mobility, both of which have an impact on V_{th}. Overall, the enhanced results in terms of PDOS, TS, I_{on}, I_{off} and SR for B AGNR FET with B - passivation in the channel material confirms its potential for applications in low-power electronics and signal amplification areas.

2.6 SUMMARY

In this chapter, DFT based atomistic study of a GS- AGNRFET examining how the gate-stack design, temperature, and edge passivation influence key performance metrics are studied. First, the impact of gate stacking using a low- %aẁY 5vwuv- %VoKzY %i wzsq≈wq%qö~ pwÅo≈wöÅ%w±% analyzed, demonstrating significant suppression of I_{off} by ~73% , and ~213 times enhancement in the SR. Additionally, the improved electrostatic control offered by gate stacking leads to a ~12% reduction in SS, indicating lower leakage and sharper switching behavior, along with an increase in threshold voltage that suppresses short-channel effects. Further, temperature dependent analysis of GS - AGNRFET reveals that increasing temperature from 250 K to 350 K causes a ~ 48% reduction in I_{on}, a ~98% degradation in SR, and a ~ 56% increase in SS, attributed to enhanced phonon scattering and weakened gate control at elevated temperatures. Furthermore, DIBL increases by ~138 times, confirming that GS - AGNRFET is best suited for low-temperature and low-power applications, such as cryogenic electronics and biomedical sensors. Additionally, the performance enhancement is achieved through edge passivation engineering of AGNR channel with 13_{th} and 15^{th} group elements. Boron passivation reduces the bandgap significantly and increases the PDOS near the Fermi level, resulting in a ~ 7.8 × 76 %w s±%sr . q≈wÅ%wÅ%I_{off} and an exceptional ~139 times increase in I_{on} compared to P - AGNRFET4%MöÅ±s¨ . sÅ≈z’2%vs%±—w≈qvwÅu%o≈w%w ü≠ö–s±%t≠ö~ %A47% %76 %ö%74 =% %76 2%

representing an improvement of more than four orders of magnitude, making the B AGNRFET highly promising for ultra-low-power and high-performance nanoelectronics applications.

In summary, this chapter systematically demonstrated that gate stack dielectric engineering, temperature-dependent analysis, and edge passivation play a crucial role in governing the electrostatic behavior, transport efficiency, and leakage characteristics of armchair graphene nanoribbon FET at atomic scale. However, the proposed GS-AGNRFET with AGNR (N = 4) demonstrated exceptional switching performance but the systematic influence of varying the value of N belongs to 3p + 1 family on the electronic band structure, density of states, and quantum transport properties within the GS architecture remains unexplored. Therefore, to address this gap. the width engineering in channel material will be the primary focus of the next chapter.

2.7 REFERENCES

[1] M. Lundstrom, "Moore's law forever?," *Science,* vol. 299, no. 5604, pp. 210-211, 2003.
[2] W. Cao *et al.*, "The future transistors," *Nature,* vol. 620, no. 7974, pp. 501-515, 2023.
[3] T. Radsar, H. Khalesi, and V. Ghods, "Graphene nanoribbon field effect transistors analysis and applications," *Superlattices and Microstructures,* vol. 153, pp. 106869, 2021.
[4] V. M. Tyutyunnik, "Graphene breakthrough into future technology: the 2010 Nobel Prize in Physics Laureate Sir Konstantin Sergeevich Novoselov," *Journal of Advanced Materials and Technologies,* vol. 6, no. 1, pp. 6-9, 2021.
[5] K. S. Novoselov *et al.*, "Electric field effect in atomically thin carbon films," *science,* vol. 306, no. 5696, pp. 666-669, 2004.
[6] H. Luo and G. Yu, "Preparation, bandgap engineering, and performance control of graphene nanoribbons," *Chemistry of Materials,* vol. 34, no. 8, pp. 3588-3615, 2022.
[7] M. R. Maamoon *et al.*, "A tight binding study of electron transport in notched graphene nanoribbons," *Scientific Reports,* vol. 15, no. 1, pp. 19218, 2025.

[8] M. Mehdi Pour *et al.*, "Laterally extended atomically precise graphene nanoribbons with improved electrical conductivity for efficient gas sensing," *Nature communications*, vol. 8, no. 1, pp. 820, 2017.

[9] Y. Zhang *et al.*, "Carbon nanotube-dependent synthesis of armchair graphene nanoribbons," *Nano Research*, vol. 15, no. 3, pp. 1709-1714, 2022.

[10] T. Radsar, H. Khalesi, V. Ghods, and A. Izadbakhsh, "Effects of channel dimension and doping concentration of source and drain contacts on GNRFET performance," *Silicon*, vol. 13, no. 10, pp. 3337-3350, 2021.

[11] N. Merino-Díez *et al.*, "Width-dependent band gap in armchair graphene nanoribbons reveals Fermi level pinning on Au (111)," *ACS nano*, vol. 11, no. 11, pp. 11661-11668, 2017.

[12] S. Lou, B. Lyu, X. Zhou, P. Shen, J. Chen, and Z. Shi, "Graphene nanoribbons: current status, challenges and opportunities," *Quantum Frontiers*, vol. 3, no. 1, pp. 3, 2024.

[13] Anshul and R. Chaujar, "Numerical evaluation of the gate stacked GNR FET for improved device switching," *in Proc. 2022 Int. Conf. Recent Trends Microelectronics, Automation, Computing and Communication Systems (ICMACC), IEEE* , pp. 88 91, 2022.

[14] S. Yang, K. Liu, Y. Xu, L. Liu, H. Li, and T. Zhai, "Gate dielectrics integration for 2D electronics: challenges, advances, and outlook," *Advanced Materials*, vol. 35, no. 18, pp. 2207901, 2023.

[15] J. Robertson, "High dielectric constant oxides," *The European Physical Journal-Applied Physics*, vol. 28, no. 3, pp. 265-291, 2004.

[16] J. M. Marmolejo-Tejada and J. Velasco-Medina, "Review on graphene nanoribbon devices for logic applications," *Microelectronics Journal*, vol. 48, pp. 18-38, 2016.

[17] T. Radsar, H. Khalesi, and V. Ghods, "Improving the performance of graphene nanoribbon field-effect transistors by using lanthanum aluminate as the gate dielectric," *Journal of Computational Electronics*, vol. 19, no. 4, pp. 1507-1515, 2020.

[18] B. H. Lee, J. Oh, H. H. Tseng, R. Jammy, and H. Huff, "Gate stack technology for nanoscale devices," *materials today*, vol. 9, no. 6, pp. 32-40, 2006.

[19] B. Kumar, M. Sharma, and R. Chaujar, "Gate electrode work function engineered JAM-GS-GAA FinFET for analog/RF applications: Performance estimation and optimization," *Microelectronics Journal*, vol. 135, pp. 105766, 2023.

[20] E. M. Akbari, "Graphene nano-ribbon field effect transistor under different ambient temperatures," 2016.

[21] J. M. Caridad *et al.*, "Room-temperature plasmon-assisted resonant THz detection in single-layer graphene transistors," *Nano Letters*, vol. 24, no. 3, pp. 935-942, 2024.

[22] Y. Y. Illarionov *et al.*, "Variability and high temperature reliability of graphene field-effect transistors with thin epitaxial CaF2 insulators," *npj 2D Materials and Applications*, vol. 8, no. 1, pp. 23, 2024.

[23] M#% oÅu2% 4%RöÅu2%W4%n voÅu2%oÅr %R4%TwÅu2%(Qs po±sr %u≠oüvsÅs%POb %ö≠%ö— temperature electronics," *Electronics Letters*, vol. 60, no. 13, pp. e13261, 2024.

[24] H. Raza and E. C. Kan, "Armchair graphene nanoribbons: Electronic structure and electric-field modulation," *Physical Review B Condensed Matter and Materials Physics*, vol. 77, no. 24, pp. 245434, 2008.

[25] M. Gupta, N. Gaur, P. Kumar, S. Singh, N. K. Jaiswal, and P. N. Kondekar, "Tailoring the electronic properties of a Z-shaped graphene field effect transistor via B/N doping," *Physics Letters A*, vol. 379, no. 7, pp. 710-718, 2015.

[26] Anshul and R. Chaujar, "DFT based analysis of Boron and Nitrogen passivation at the edge of Armchair Graphene Nanoribbon for low power applications," *in Proc. 2024 IEEE 19th Int. Conf. Nano/Micro Engineered and Molecular Systems (NEMS), IEEE*, pp. 1-4, 2024.

[27] B. Kumar and R. Chaujar, "Analog and RF performance evaluation of junctionless accumulation mode (JAM) gate stack gate all around (GS-GAA) FinFET," *Silicon*, vol. 13, no. 3, pp. 919-927, 2021.

[28] S. Smidstrup *et al.*, "QuantumATK: an integrated platform of electronic and atomic-scale modelling tools," *Journal of Physics: Condensed Matter*, vol. 32, no. 1, pp. 015901, 2020.

[29] K. Stokbro, D. E. Petersen, S. Smidstrup, A. Blom, M. Ipsen, and K. Kaasbjerg, "Semiempirical model for nanoscale device simulations," *Physical Review B Condensed Matter and Materials Physics*, vol. 82, no. 7, pp. 075420, 2010.

[30] D. A. Papaconstantopoulos and M. J. Mehl, "The Slater Koster tight-binding method: a computationally efficient and accurate approach," *Journal of Physics: Condensed Matter*, vol. 15, no. 10, pp. R413-R440, 2003.

[31] J. C. Slater and G. F. Koster, "Simplified LCAO method for the periodic potential problem," *Physical review*, vol. 94, no. 6, pp. 1498, 1954.

[32] T. Ono, Y. Egami, and K. Hirose, "First-principles transport calculation method based on real-space finite-difference nonequilibrium Green's function scheme," *Physical Review B Condensed Matter and Materials Physics*, vol. 86, no. 19, pp. 195406, 2012.

[33] A. Sampaio-Silva, D. F. Ferreira, C. A. B. Silva Jr, and J. Del Nero, "Hydrogenation, width and strain effect in Me-graphene devices," *Computational Materials Science*, vol. 210, p. 111456, 2022.

[34] S. Datta, "Exclusion principle and the Landauer-Büttiker formalism," *Physical Review B*, vol. 45, no. 3, pp. 1347, 1992.

[35] Y. Yoon, G. Fiori, S. Hong, G. Iannaccone, and J. Guo, "Performance comparison of graphene nanoribbon FETs with Schottky contacts and doped reservoirs," *IEEE Transactions on electron devices*, vol. 55, no. 9, pp. 2314-2323, 2008.

[36] Anshul and R. Chaujar, "Extended Huckel DFT-based study of Icosagens passivation at the edge of armchair graphene nanoribbon for next generation nanoelectronics applications," *Micro and Nanostructures*, vol. 207, pp. 208263, 2025.

[37] L. Tapasztó, G. Dobrik, P. Lambin, and L. P. Biro, "Tailoring the atomic structure of graphene nanoribbons by scanning tunnelling microscope lithography," *Nature nanotechnology*, vol. 3, no. 7, pp. 397-401, 2008.

[38] A. A. Tseng, A. Notargiacomo, and T. P. Chen, "Nanofabrication by scanning probe microscope lithography: A review," *Journal of Vacuum Science & Technology B: Microelectronics and Nanometer Structures Processing, Measurement, and Phenomena*, vol. 23, no. 3, pp. 877-894, 2005.

[39] W. Xu and T.-W. Lee, "Recent progress in fabrication techniques of graphene nanoribbons," *Materials Horizons*, vol. 3, no. 3, pp. 186-207, 2016.

[40] W. S. Hwang *et al.*, "Graphene nanoribbon field-effect transistors on wafer-scale epitaxial graphene on SiC substrates," *APL materials*, vol. 3, no. 1, 2015.

[41] Anshul and R. Chaujar, "Investigation Temperature variation on DC and Analog performance of Gate Stack GNRFET using DFT-based atomic scale Modelling," *in Proc. 2025 Devices for Integrated Circuit (DevIC), Kalyani, India*, *IEEE*, pp. 337-342, 2025.

[42] R. Saha, B. Bhowmick, and S. Baishya, "Temperature effect on RF/analog and linearity parameters in DMG FinFET," *Applied Physics A*, vol. 124, no. 9, pp. 642, 2018.

[43] M. R. Moslemi, M. H. Sheikhi, K. Saghafi, and M. K. Moravvej-Farshi, "Electronic properties of a dual-gated GNR-FET under uniaxial tensile strain," *Microelectronics Reliability*, vol. 52, no. 11, pp. 2579-2584, 2012.

[44] R. Jyoti, M. Chauhan, R. Kashyap, M. Singh, B. C. Choudhary, and R. K. Sharma, "A DFT modulated analysis of manganese doped graphene nanoribbons as a potential material for sensing of highly toxic gases CO, PH3 and SbH3," *Physica Scripta*, vol. 98, no. 4, pp. 045803, 2023.

[45] R. Mann and R. Chaujar, "DFT-based Atomic Calculation of Si-doped HfO2 and Effect of its Negative Capacitance on Analog/RF, and VTC Parameters of MOSFET," *Silicon*, vol. 16, no. 3, pp. 1237-1252, 2024.

3

CHAPTER

Impact of Channel Width Engineering on Electronic and Quantum Transport Properties of Gate-Stack Armchair Graphene Nanoribbon FET

In this chapter the electronic and quantum transport properties for the bulk configuration of AGNRs with varied number of carbon atoms along AGNRs width are investigated.

52 *The Semi-empirical Density Functional Theory based approach is used to calculate the band structure, DOS, and transmission spectrum for the bulk configuration of AGNRs.*

The AGNRs (N = 4, 7, 10 and 13) are used in channel material to analyse the performance of field-effect transistors with Gate Stack architecture.

The GS-AGNR (N = 4) FET demonstrates significantly reduced off-state current and a markedly improved switching ratio compared to wider ribbons having N = 7, 10 and 13.

Overall, this chapter establishes channel width as a critical design parameter and highlights GS - AGNR (N = 4) FET as promising candidates for low-power and nanoscale electronic applications.

The advantage of the GS architecture with AGNR (N = 4) over the conventional GNRFET is discussed in **Chapter 2**. To further enhance the performance of the proposed device, the effect of channel width variation and scaling down in AGNR channel material is explored in this chapter. Additionally, the performance analysis is carried out in terms of projected local density of states, transmission spectrum at different values of V_{ds}, and electrostatic difference potential, which provides a unique approach to analyze the electronic and quantum transport characteristics of the proposed device.

3.1 INTRODUCTION

As discussed in **Chapter 2**, to increase the functionality of electronic gadgets the new technology tries to shrink more components on IC. The co-founder of Intel, Gordon Moore, in 1965 predicted that the number of electronic devices would double every 18 months, i.e., the size of the devices would be reduced [1]. The scaling down in ICs will bring significant hurdles in the electronic industry. The majority of electronic devices are built using silicon technology, which has been widely used in the semiconductor industry. According to the International Roadmap for Devices and Systems (IRDS), transistor channel lengths will reach 5 nm by 2021 [2]. However, as the physical limits of silicon transistors are being approached, there is a growing demand for alternative materials and device architectures that can offer superior performance, energy efficiency, and scalability [3]. The GNRFETs have emerged as potential candidates for revolutionizing IC technology in this context. Due to its outstanding electrical properties, graphene, a 2D carbon allotrope, has drawn much attention [4]. This unique material possesses amazing qualities, including outstanding electrical conductivity, excellent mechanical strength, great thermal conductivity, and gas impermeability [5]. As graphene possesses exceptional electrical characteristics, the absence of bandgap limits its employment

in electronics. However, it is possible to create a bandgap in graphene through quantum confinement to make GNRs [6]. The generally utilized edge configurations for GNRs are the zigzag and armchair edges. ZGNR shows a near-zero bandgap and exhibit metallic nature [7]. In the AGNR category, there are three groups, N = 3p, N = 3p + 1, and N = 3p + 2, where N is the number of carbon atoms along AGNR width and p is a positive integer [8]. The 3p+1 and 3p groups in AGNR exhibit a direct energy gap and are semiconducting in nature, while the 3p+2 group is metallic in nature [9]. Semiconducting AGNRs are ideal materials for channels in GNRFET [10]. The materials with a high- ‰wzsq≈Åq‰ôÅ±≈oÅ‰ó/s‰ssr sr ‰ö≠‰s‰oÅ±w≈ö≠‰ gate oxide to upgrade the performance of nanoscale transistors and prevent SCEs [11]. While choosing a high- ‰wzsq≈Åq‰ o≈s≠wz2‰‰r s-off must be made between the high- ‰wzsq≈Åq‰ and an appropriate bandgap for a transistor. There is an adverse relationship between the bandgap and dielectric constant. Implementing a high- ‰wzsq≈Åq‰o"s≠‰Å‰s‰KQX] ‰voÅsz‰ can generate undesirably strong fringing fields at the source and drain contacts, which can cause various issues like bandgap degradation, threshold voltage instability, and mobility degradation [12]. The issues above, like bandgap degradation, threshold voltage instability, and mobility degradation, can be overcome using gate stack architecture. In GS architecture, a combination of two dielectric layers has been used. Specifically, a low-dielectric layer of SiO_2. ‰Ô94C/‰o±‰ssÅ‰oÅr—wqvsr ‰s≈–ssÅ‰s‰wv- ‰wzsq≈Åq‰o"s≠‰År ‰s‰QX] ‰voÅsz [13]. The narrow SiO_2 layer in GS stabilizes the high- ‰wzsq≈Åq‰VoKzY$_3$) layer and AGNR ±p±≠o≈s‰wvö.≈‰ttsq≈Åu‰s‰s–ws ±‰ttsq≈s‰"ws‰vqyÅs±±. The high- ‰wzsq≈Åq‰ÅQa‰ will permit the increase in physical oxide thickness to prevent gate tunneling and thus improves the carrier efficiency, reduce off current, and enhance the device performance [14, 15]. Although several studies have investigated the electronic properties of AGNRs and their

application in nanoscale transistors, limited attention has been given to the systematic impact of channel width engineering in combination with gate stack architecture using a semi-empirical DFT framework. In particular, the correlation between AGNR width (N), electronic band structure, and quantum transport properties remains insufficiently explored for optimized device performance.

In this chapter, a Gate Stack Armchair Graphene Nanoribbon Field Effect Transistor is proposed, where the impact of channel width on the electronic and quantum transport properties is systematically investigated using a Semi-empirical Density Functional Theory approach. The study primarily focuses on AGNR configurations belonging to the 3p+1 family (N = 4, 7, 10, and 13), owing to their superior semiconducting behavior. The electronic properties such as band structure, density of states, and transmission spectrum are analyzed, followed by device-level performance evaluation in terms of switching ratio, off-state current, and transport characteristics using the NEGF formalism. The proposed GS architecture effectively mitigates short-channel effects and enhances device performance. This chapter is organized as follows: Section 3.2 presents the device design and structural configuration, Section 3.3 describes the simulation methodology, Section 3.4 discusses the results and analysis, and finally, Section 3.5 concludes the findings of the study.

3.2 DEVICE DESIGN AND DESCRIPTION

The simulated proposed device architecture and optimized atomic structure of AGNRs with varied N are shown in the Figure 3.1. An AGNR layer of 50 Å is used as channel material considering the fact of scaling down. The value of N in the AGNR varies for different types of device configurations. From the above Figure 3.1(c-f), it can be observed that the periodic direction of all widths is kept the same. The highlighted box in Figure 3.1(c-f) shows one atom

–w—2‰Åqz.r.wÅu‰ws‰Å.~ ps≠‰t‰ö~ ±‰zöÅu‰KQX] ‰w≈v4P.≠vs≠2‰ws‰KQX] ‰≠‰ö≈sr‰6 ö‰

make a perfect interface with the ZGNR-type contacts, as shown in Figure 3.1 (b). The length of the drain and source is also taken 50 Å. A gate stacking architecture is used after a metallic gate. Step-increasing doping profile of n-type is used in all regions to make a junctionless configuration having a concentration of 3×10^{16} in the channel region and 5×10^{18} in the source and drain region. Gate potential plays an important role in calculating the electronic properties of a device, and hence, a metallic gate is employed over the dielectric layers. Here, the t_{ox} is taken as 1 nm (0.50 nm $LaAlO_3$ layer + 0.50 nm SiO_2 layer). The t_{ox} is inversely related to the C_{ox}, i.e., reducing t_{ox} will increase the C_{ox}, which provides better control of the gate over the channel as the potential drop on gate oxide decreases.

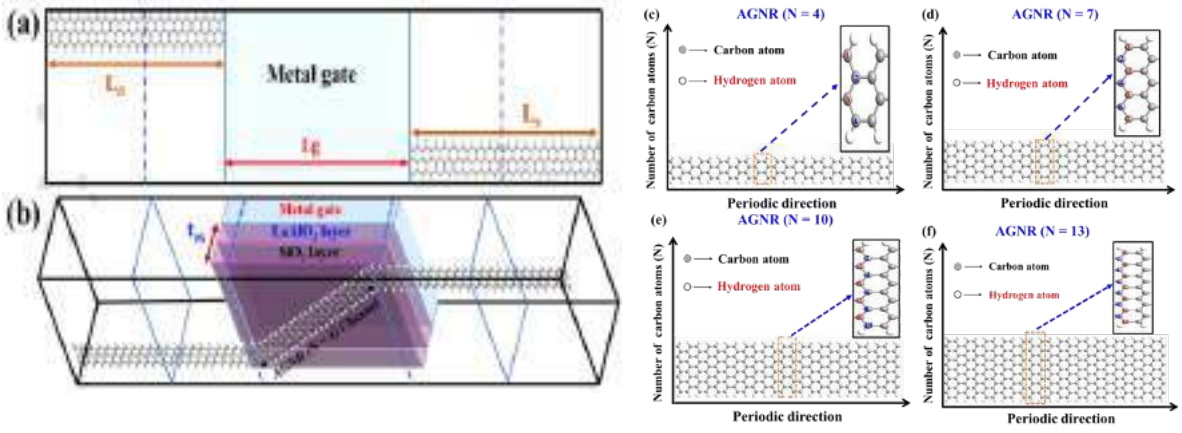

Figure 3.1: (a) Front view, (b) rotated view of the proposed device taken from the ATK Simulator, and (c-f), optimized atomic structure of AGNR having different number of atoms along its width used as channel material in proposed device [13]

3.3 SIMULATION METHODOLOGY

The Quantum ATK tool is used to carry out all the simulations. The SE calculator uses the Slater-Koster model with the DFTB parameter group in ATK to perform all the analyses in this chapter. The Slater-Koster model is frequently used to create the tight-binding Hamiltonian matrix for a given system [16]. This includes determining the matrix elements of the Hamiltonian between orbitals of atoms [17]. The equation for the matrix elements of the tight-binding Hamiltonian in the Slater-Koster model is already defined **Eq. 2.14 in Chapter 2.** The NEGF method without a self-consistent tight-binding function is adopted in this chapter. The non-self-consistent portion of the tight-binding Hamiltonian is parametrized in SE using a two-center approximation, meaning that the matrix components are independent of the positions of the other atoms and only depend on the distance between two atoms. The Hartree potential is kept constant at 40 Ha, and the K-point sampling is taken 1×1×100. The electrode temperature is kept at 300 K. Bulk configured AGNR electronic properties are calculated using the Fast Fourier Transform Poisson solver, whereas device properties are calculated using the multi-grid type Poisson solver. Firstly, all structures are optimized using the Brenner_CH_2002 with a force tolerance of 0.05 eV/Å. Further, the electrical properties of a fully optimized structure are computed using DFT and NEGF formalisms. Also, the simulation models are calibrated with the previous findings as discussed in **Chapter 2, Section 2.2.**

3.4 RESULTS AND DISCUSSIONS

In this section, the DFT analysis of AGNR with varied N belonging to the (3p+1) family is studied in terms of band structure, DOS, and transmission coefficient. Further, the AGNR is used as a channel material in GS- AGNR FET with the varied number of carbon atoms along

AGNR width, and then the performance analysis of the proposed devices has been carried out using the DFT and NEGF approach.

3.4.1 DFT based Investigation of electronic properties of AGNR with different values of N

In this section, the band structure, DOS and TS for AGNR (N = 4, 7, 10, 13) is analyzed. The band structure and DOS for AGNR (N = 4, 7, 10, 13) is depicted in Figure 3.2. The band structure is used to compute the band gap, which shows the number of energy levels that an electron can have as illustrated in Figure 3.2 (a, c, e, and g). High symmetric k-points, are plotted on the x-axis, and energy (eV) is plotted on the y-axis to represent band structures. The values of bandgap are 1.98, 1.21, 0.87, and 0.68 eV for AGNR (N = 4), AGNR (N = 7), AGNR (N = 10), and AGNR (N = 13), respectively. From the bandgap analysis, it is observed that the 3p+1 family of AGNR, i.e., N = 4, 7, 10, and 13 having values of p = 1, 2, 3, and 4, are semiconductor in nature and can be used as a channel material in FETs. It is also observed that the value of the bandgap decreased as the widths of AGNR increased. The width of AGNR is given by [18]:

$$\text{[illegible]} \qquad \text{[illegible]} \qquad (3.11)$$

where,

- - width of AGNR
- G - bond length of carbon-carbon atom in AGNR
- N - number of carbon atoms along AGNR width

The width of AGNR is 1.8, 2.88, 3.96, and 4.2 nm for N = 4, 7, 10, 13 respectively. From the bandgap analysis, we observed that Width of AGNR and bandgap have an adverse relationship.

The number of available electronic states (both occupied and unoccupied) that are accessible for electrons to fill at a given energy level determines the DOS, as illustrated in Figure 3.2 (b, d, f, and h). From these figures, the authors observed that there is no peak at the Fermi level in DOS. Also, in accordance with the energy states that are available, DOS exhibits similarities to band structure. The semiconducting nature of the AGNR is verified by the fact that there is no peak at the Fermi level in DOS. Further, the number of DOS peaks increases as the value of width (W_{AGNR}) increases. In AGNR (N = 4), the DOS peaks in the CB are observed at 1.46 eV and in the VB at -0.68, -1.68 eV. In AGNR (N = 7), the peaks in CB are at 0.80 and 1.30 eV, while in VB, peaks are observed at -0.84 and -1.22 eV. In the case of AGNR (N = 10) and AGNR (N = 13), DOS peaks in CB are observed at 1.94 and 1.68 eV, and in VB peaks are observed at -1.74 and -1.48 eV. From the above analysis, the authors observed that as the value of N in AGNR increased, the large number of peaks shifted in CB. Further, an increase in electron energy opens more states to occupy an electron in the CB. The relation between DOS and energy is given by [19]:

G G G (3.12)

where,

D (E) - The density of states for the available energy range

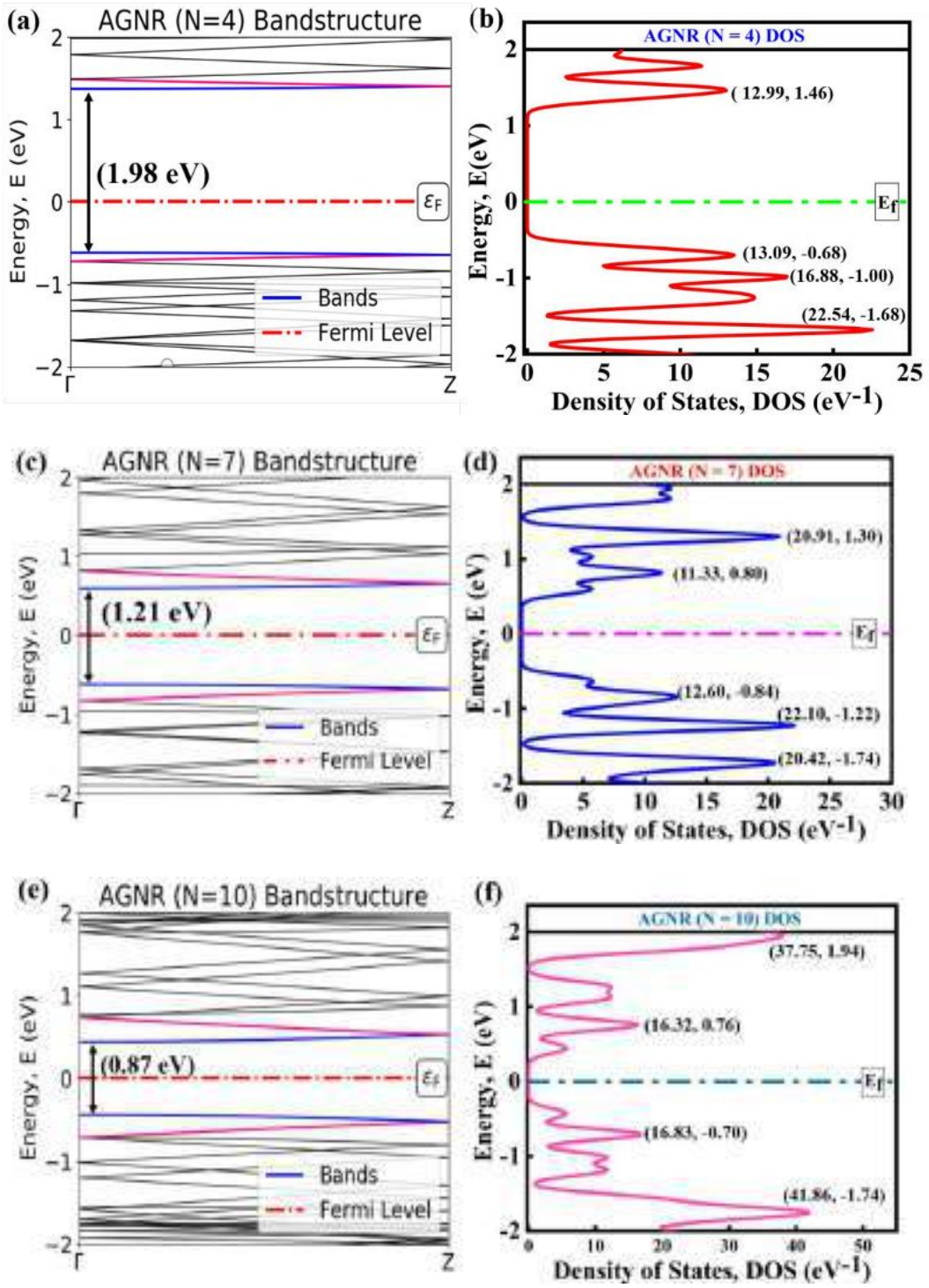
(a)
AGNR (N=4) Bandstructure
Energy, E (eV)
(1.98 eV)
Bands
Fermi Level
Γ
Z
(b)
AGNR (N = 4) DOS
(12.99, 1.46)
(13.09, -0.68)
(16.88, -1.00)
(22.54, -1.68)
Energy, E(eV)
Density of States, DOS (eV-1)
(c)
AGNR (N=7) Bandstructure
(1.21 eV)
(d)
AGNR (N = 7) DOS
(20.91, 1.30)
(11.33, 0.80)
(12.60, -0.84)
(22.10, -1.22)
(20.42, -1.74)
(e)
AGNR (N=10) Bandstructure
(0.87 eV)
(f)
AGNR (N = 10) DOS
(37.75, 1.94)
(16.32, 0.76)
(16.83, -0.70)
(41.86, -1.74)

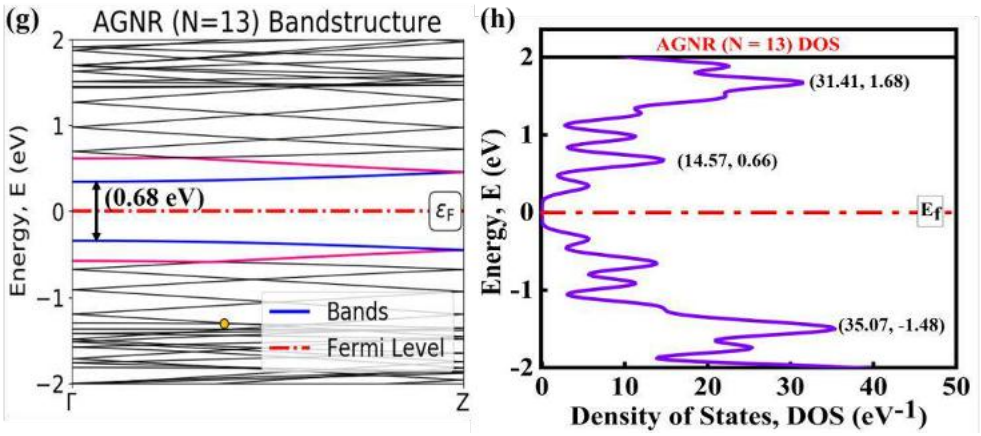

Figure 3.2: Quantum transport properties for bulk configuration of AGNR with different N that are used as a channel material (a) AGNR (N = 4) band structure, (b) AGNR (N = 4) DOS, (c) AGNR (N = 7) band structure, (d) AGNR (N = 7) DOS, (e) AGNR (N = 10) band structure, (f) AGNR (N = 10) DOS, (g) AGNR (N = 13) band structure and, (h) AGNR (N = 13) DOS [13]

The analysis of the transmission spectrum for different N in AGNR is illustrated in Figure 3.3. The transmission spectrum of a GNR describes how the transmission of electrons changes as their energy varies while passing through the nanoribbon. This transmission is affected by the GNR structure, which in turn depends on its width and other structural features. The energy range for the transmission coefficient is taken from -10 to +10 eV. It is observed from Figure 3.3 that the peaks of the transmission spectrum increased as the value of N in AGNR increased. Also, no peak is observed at Fermi energy (i.e., for E = 0 eV), which points out the semiconducting nature. From Figure 3.3, it is observed that the AGNR (N = 4) has no peaks in the energy range of - 0.5 to + 1.5 eV, which describes that an electron can easily tunnel through VB to CB. From the above discussions, the authors lead to an observation that the AGNR (N = 4) has improved transmission spectrum peaks around Fermi energy and has a better value of bandgap.

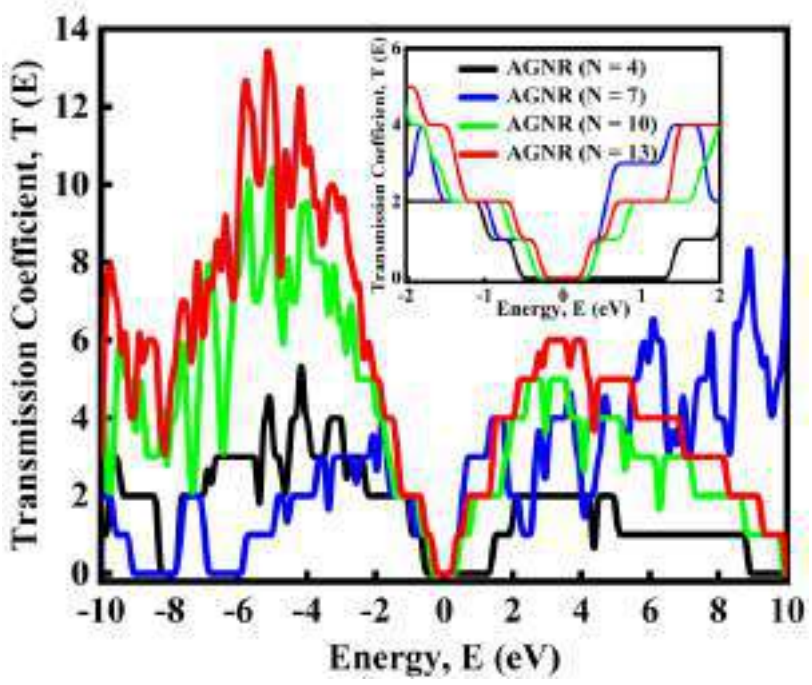

Figure 3.3: Transmission spectrum for varied N in the AGNRs [13]

3.4.2 Performance analysis of the proposed devices using the DFT approach

From the DFT analysis of AGNR, as discussed in Figure 3.2 and 3.3, it is observed that the AGNR (N = 4) shows improved results in terms of band structure and transmission spectrum. Further, the transport properties for different device configurations with varying values of N in AGNR for the channel material are calculated. The authors have analyzed the impact of the V_{ds} on the transmission spectrum for each device configuration as depicted in Figure 3.4. The transmission coefficient for a device configuration is obtained by the without self-consistent solution of the Schrodinger equation and 3-N%Zöw±öÅ±%s¨..o~wöÅ±%.±vÅu%ws% Slater-Koster model with NEGF method as discussed in **Eq. 2.16**. The value of V_{ds} is changed from 0 to 1 V in 0.5-step increments. A new without self-consistent calculation needs to determine the associated transmission spectrum for every drain voltage. Once the transmission spectrum is calculated, it is observed that the Fermi level shift at the VB and CB edges is the

primary distinction between the various spectra calculated from the parameters $_L(E)$ and $_R(E)$. The terms E_L and E_R in Figure 3.4 denote the shift in the Fermi level corresponding to the left and right electrodes, respectively. From Figure 3.4(a), it is observed that the GS-AGNR (N = 4) FET at 0 V shows a minimum resonance peak. The width and electrical characteristics of the GNR would determine the number of resonance peaks and their specific positions. The reason can be understood by the Fermi levels shift in the left and right electrodes. The Fermi level shown in the presented work governs the range of electron transport inside a GS-AGNR (N) FET. The electron transmission inside the GNR channel increases with the value of the Fermi level range in GNR. It can be clearly observed from Figure 3.4 (a-d) that for 0.5 V, the range of Fermi level shift for both electrodes are higher in GS-AGNR (N = 4) FET as compared to the other three device configurations.

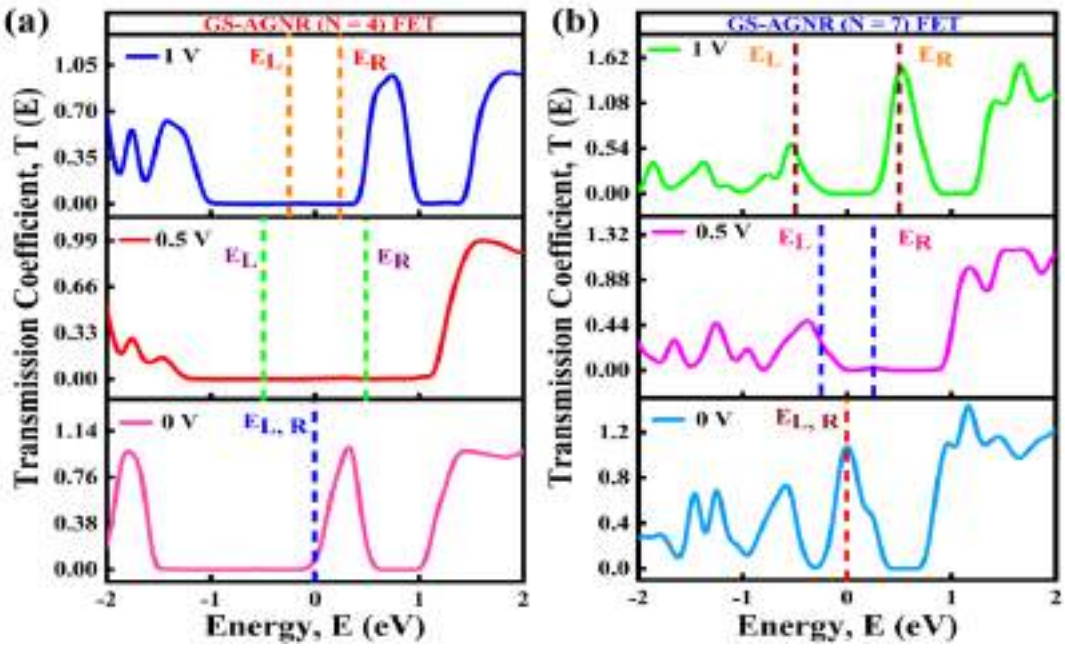

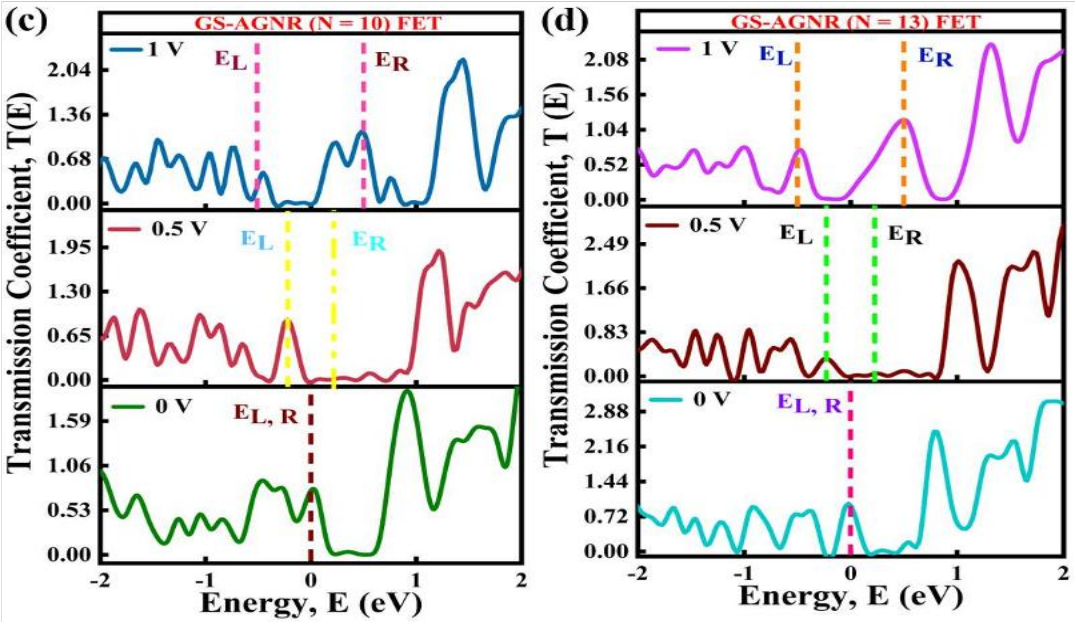

Figure 3.4: Transmission spectrum at input voltages 0 V, 0.5 V, and 1 V for (a) GS-AGNR (N = 4) FET, (b) GS-AGNR (N = 7) FET, (c) GS-AGNR (N = 10) FET, (d) GS-AGNR (N = 13) FET [13]

It is evident from Figure 3.4(a) that the possibility of electrons tunneling for 0.5 V in GS-AGNR (N = 4) FET is greater than the other device configurations at this voltage (0.5 V). Also, in Figure 3.4(a) at 0.5 V, there is no peak present in the barrier of E_L and E_R, which points out the higher possibility of conductance as compared to the transmission spectrum, as shown in Figure (b-d). The values of T(E) at 0 V and 0 eV are 1.09 in GS-AGNR (N = 7) FET, which is higher than in other device configurations. When the drain voltages change from 0 to 1 V, it is observed that the value of T(E) decreases, and the area under the curve also decreases. In GS-AGNR (N = 10) FET and GS-AGNR (N = 13) FET, as depicted in Figure 3.4(c) and (d), the values of T(E) at 0 V and 0 eV are 0.76 and 0.97. Also, as the V_{ds} change from 0 to 0.5 V, the resonance peak value decreases. Further, the authors observed that the variation of the transmission spectrum for GS-AGNR (N) FET having different values of N in channel material

shows the transport of electrons and its dependence on external voltage. Moreover, the DFT based analysis of GS-AGNR FET in terms of T(E) gives a unique approach to explain the device performance, which can be very useful in many applications. The transfer characteristics of GS-AGNR (N) FETs with different values of N are shown in Figure 3.5 (a). The drain current is calculated after using the without self-consistent solution of tight-binding Hamiltonian matrix after the calculation T(E) and mathematically expressed by Landauer-Büttiker Formalism as disussed in **Eq. 2.17.**

The **Eq. 2.17** depicts the dependence of I_d on T (E). Also, the GS-AGNR (N = 4) FET shows improved value of I_{off} as compared to other device configurations. The value of I_{off} changed from 1.75 nA to 5.42 µA for GS-AGNR (N = 4) FET and GS-AGNR (N = 13) FET. The narrower width of AGNR shows improved results in terms of I_{off}, switching ratio, and other parameters like transmission probability and conductance, which can be easily understood by analyzing the transmission spectrum for each device configuration. The transmission spectrum and transfer characteristics of a GNRFET are related through the electronic properties of the GNR and the operation of the FET. The discussion about the variation of transmission spectrum in terms of T(E) for different device configurations led to an observation that the transfer characteristics, as shown in Figure 3.5 (a), have been improved significantly for GS-AGNR (N = 4) FET. From the transfer characteristics, the switching ratio and the off current are calculated.

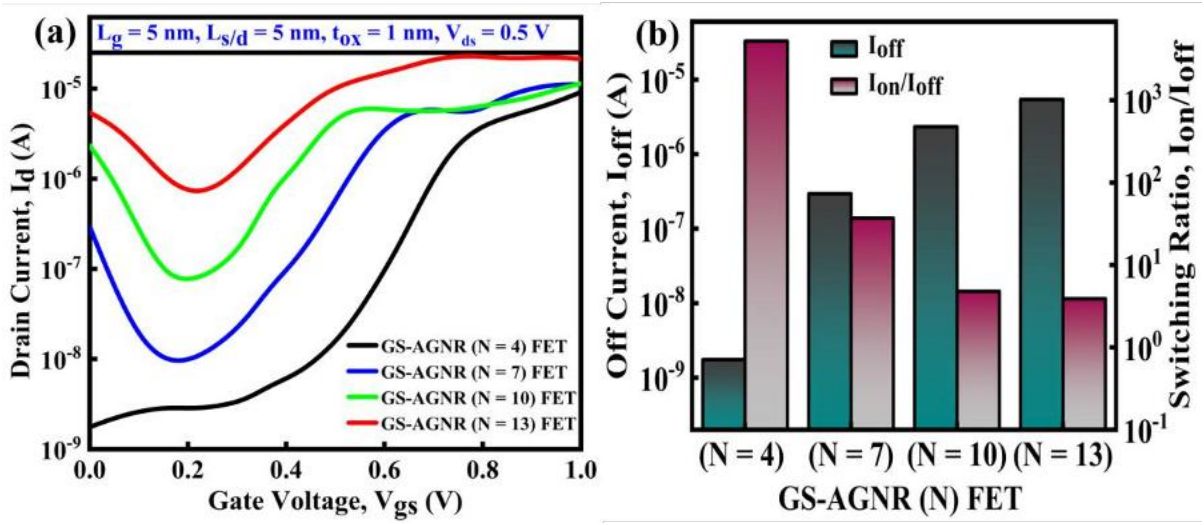

Figure 3.5: (a) Transfer characteristics of GS-AGNR (N) FETs with different values of N in the channel material, and (b) Variation in off current and switching ratio for GS-AGNRFET [13]

The variation in I_{off} and SR ratio for all purposed device configurations is illustrated in Figure 3.5(b). The switching ratio is an important factor that determines the performance of a device. A high SR ratio indicates that the device can reliably and rapidly switch between conducting (on) and non-conducting (off) states, enabling it to amplify and process electrical signals with minimal power consumption. In this present study, the GS-AGNR (N = 4) FET shows a higher switching ratio value than other device configurations. Based on the SR parameter, the authors have observed that the GS-AGNR (N = 4) FET can be used in high-speed electronics and low-power integrated IC.

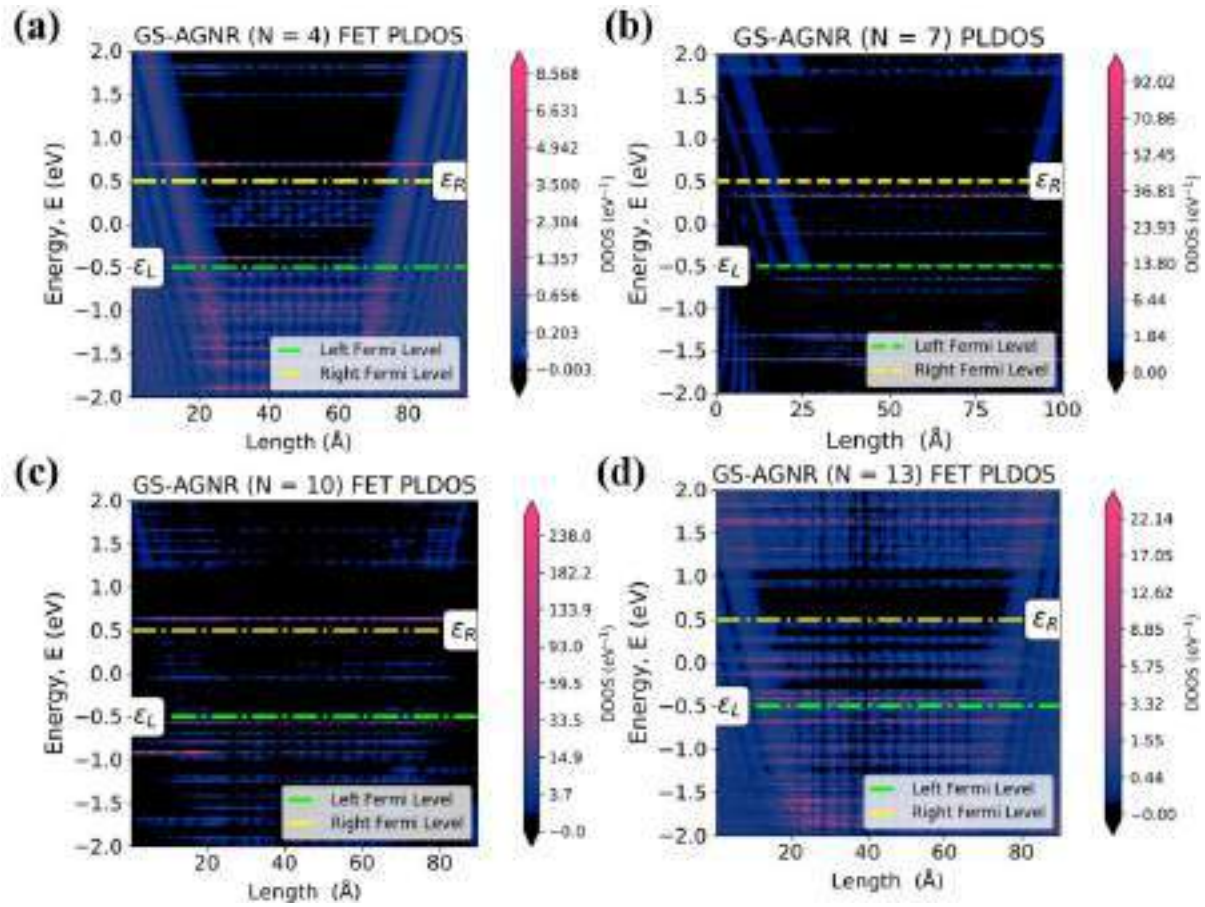

Figure 3.6: Projected local density of states for (a) GS-AGNR (N = 4) FET, (b) GS-AGNR (N = 7) FET, (c) GS-AGNR (N = 10) FET and, (d) GS-AGNR (N = 13) FET [13]

Figure 3.6 portrays the contour plot of the projected local density of states (PLDOS) for all device configurations. These contour plots of PLDOS in GS-AGNR (N) FETs provide crucial insights into the electronic structure and behavior of these atomic-scale devices. In Figure 3.6, the PLDOS is typically represented as a function of energy and position within the GNR. Each contour line in the graph corresponds to a specific energy level, and the intensity or color bar of the contour lines reflects the density of electronic states at that energy level. The magnitude of these contour lines associated with device density of states (DDOS) varies from -0.03 to 238 eV^{-1}.

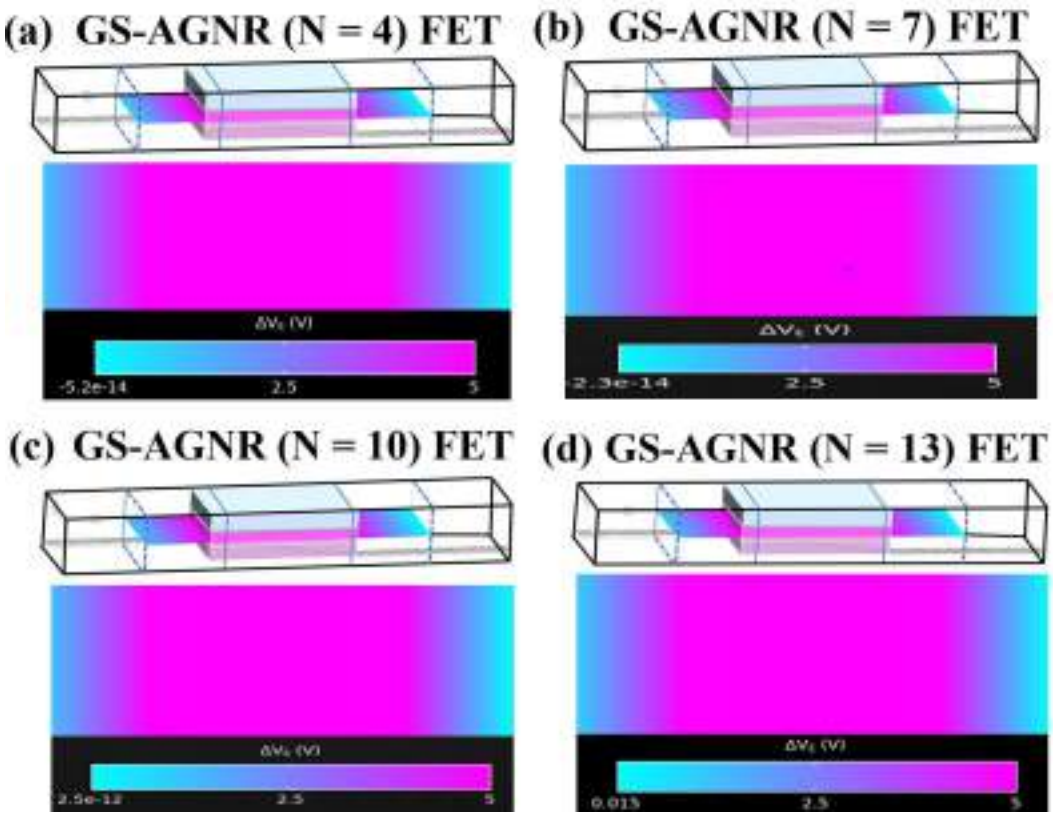

Figure 3.7: Electrostatic difference potential profile for (a) GS-AGNR (N = 4) FET, (b) GS-AGNR (N = 7) FET, (c) GS-AGNR (N = 10) FET, and (d) GS-AGNR (N = 13) FET [13]

The contour plots of electrostatic difference potential in Figure 3.7 show crucial insights into the distribution of electric charges within different device configurations. The contour plots qzso≠z”%s~ öÅ±≈/o~s%-vs≠s%szsq~≠wq%qvo≠us±%/s%qöÅqsÅ≈/o~sr%ÅÅr%ö—%/s”%ttsq~%/s%s–wqs ±% overall performance. The blue color contour depicts the electronic distribution near the electrodes, whose magnitude ranges from 0.015 to 5.2×10^{-14} V, while the pink color illustrates the distribution of electric charges inside the channel. These contour plots can be used by scientists and engineers to improve the design of GNR FETs. They can fine-tune the devices having a narrower number of carbon atoms along AGNR width (like N = 4, as presented in this work) for certain uses, like high-speed computing or low-power electronics, by adjusting the charge distribution and electric field with exact atomic-level modifications.

For GS AGNR (N = 4) FET, both PLDOS and EDD are highly confined within the channel region, indicating strong carrier localization and minimal interaction with the source and drain regions. This behavior arises due to enhanced quantum confinement and a larger bandgap, which restrict the spatial extension of electronic states and charge distribution. Table 3.1 summarizes the comparison among proposed GS-AGNR(N) FETs with previously reported GNRFETs. The variation of N from 4 to 13 in GS-AGNR (N) FETs brings down the magnitude of the on current (9.14 µA to 0.21 µA) and increases the off current (1.75×10^{-3} to 5.4 µA). These variations in the on and off currents due to a varied N value in GS-AGNR(N) FETs imparts a switching ratio of 3.9 to 5.22×10^{3} corresponding to bandgap in the range of 0.68 to 1.98eV.

Table 3.1
COMPARISON AMONG PROPOSED GS-AGNR(N)FETs WITH PREVIOUSLY REPORTED GNRFETs [13]

n	(A B	l (h r µ κ (Aµ B	t (A h B	t (A h B	t Hl	i (A B
Qa 3KQX] %X%G%/% POb 0	64=	X%G%	C47:	74A=%76^{39}	=488%% 76^{9}	74CB
Qa 3KQX] %X%G%A/% POb 0	64=	X%G%A	6477	648C=	9A	7487
Qa 3KQX] %X%G% 76/%POb 0	64=	X%G%6	6478	849:	: 4B	64BA
Qa 3KQX] %X%G% 79/%POb 0	64=	X%G%9	6487	=4 8	94C	64>B
aL3QX] POb%k	64=	X%G%8	3	3	994A	3
KQ3QX] POb%%6k	64=	X%G%8	3	3	96:	3
NWQ3QX] POb% i87k	64>	X%G%9	3	3	=B89	3
aVN3QX] POb%8k	64	X%G%8	94>>	7=4A%%6^{3}	849%% 76^{9}	3

***Present work**

3.5 SUMMARY

This chapter investigates the influence of channel width engineering on the electronic and quantum transport properties GS-AGNR FET using a semi-empirical density functional theory framework combined with Slater Koster DFT based model. AGNRs belonging to the 3p+1 family (N = 4, 7, 10, and 13) are systematically analyzed to correlate ribbon width with bandgap, density of states, transmission spectrum, and device-level transport characteristics. The results reveal a strong inverse relationship between AGNR width and bandgap, with the narrowest ribbon (N = 4) exhibiting the largest bandgap (~1.98 eV), suppressed density of states near the Fermi level, and enhanced transmission control. When the AGNR (N = 4) implemented as the channel material in a gate-stack architecture, the GS-AGNR (N = 4) FET demonstrates significantly reduced off-state current and a markedly improved switching ratio compared to wider ribbons having N = 7, 10 and 13. Transmission spectra under varying drain bias, along with projected local density of states and electrostatic potential profiles, further confirm superior gate control and reduced leakage for narrower channels. Overall, this chapter establishes channel width as a critical design parameter and highlights GS - AGNR (N = 4) FET as promising candidates for low-power and nanoscale electronic applications.

Following a comprehensive analysis of the gate-stack engineering, temperature-dependent analysis, and edge passivation of the GNRFET device in **Chapter 2**, it is imperative to address the width engineering associated with this proposed device. In this chapter the proposed device with width engineering is studied with SK model. The SK model is used with non-SCF iteration in this chapter. Therefore, to ensure the device s reliability, it is crucial to explore its device modelling with different simulation approaches and the SCF iteration methods, which will be the primary focus area of the next chapter.

3.6 REFERENCES

[1] T. Radsar, H. Khalesi, and V. Ghods, "Graphene nanoribbon field effect transistors analysis and applications," *Superlattices and Microstructures*, vol. 153, pp. 106869, 2021.

[2] B. Hoefflinger, "Irds international roadmap for devices and systems, rebooting computing, s3s," *NANO-CHIPS 2030: On-Chip AI for an Efficient Data-Driven World*, pp. 9-17, 2020.

[3] B. Kumar and R. Chaujar, "Numerical simulation of analog metrics and parasitic capacitances of GaAs GS-GAA FinFET for ULSI switching applications," *The European Physical Journal Plus*, vol. 137, no. 1, pp. 110, 2022.

[4] Y.-Y. Chen *et al.*, "A SPICE-compatible model of MOS-type graphene nano-ribbon field-effect transistors enabling gate-and circuit-level delay and power analysis under process variation," *IEEE Transactions on Nanotechnology*, vol. 14, no. 6, pp. 1068-1082, 2015.

[5] K. S. Novoselov *et al.*, "Electric field effect in atomically thin carbon films," *science*, vol. 306, no. 5696, pp. 666-669, 2004.

[6] H. Shen, Y. Shi, and X. Wang, "Synthesis, charge transport and device applications of graphene nanoribbons," *Synthetic Metals*, vol. 210, pp. 109-122, 2015.

[7] A. Hazra and S. Basu, "Graphene nanoribbon as potential on-chip interconnect material A review," *C*, vol. 4, no. 3, pp. 49, 2018.

[8] F. Schwierz, "Graphene transistors," *Nature nanotechnology*, vol. 5, no. 7, pp. 487-496, 2010.

[9] F. Schwierz, "Graphene and beyond: two-dimensional materials for transistor applications,", *SPIE*, vol. 9467pp. 144-152, 2015.

[10] J. H. Choi, J. Lee, M. Byeon, T. E. Hong, H. Park, and C. Y. Lee, "Graphene-based gas sensors with high sensitivity and minimal sensor-to-sensor variation," *ACS Applied Nano Materials*, vol. 3, no. 3, pp. 2257-2265, 2020.

[11] B. Kumar, M. Sharma, and R. Chaujar, "Junctionless-accumulation-mode stacked gate GAA FinFET with dual-k spacer for reliable RFIC design," *Microelectronics Journal*, vol. 139, p. 105910, 2023.

[12] N. Gupta and R. Chaujar, "Optimization of high-k and gate metal workfunction for improved analog and intermodulation performance of Gate Stack (GS)-GEWE-SiNW MOSFET," *Superlattices and Microstructures*, vol. 97, pp. 630-641, 2016.

[13] Anshul and R. Chaujar, "Semi-empirical dft based investigation of electronic and quantum transport properties of novel gs-agnr (n) fet," *IEEE Transactions on Nanotechnology*, vol. 23, pp. 400-407, 2024.

[14] S. Valasa, S. Tayal, L. R. Thoutam, J. Ajayan, and S. Bhattacharya, "A critical review on performance, reliability, and fabrication challenges in nanosheet FET for future analog/digital IC applications," *Micro and Nanostructures*, vol. 170, pp. 207374, 2022.

[15] B. H. Lee, J. Oh, H. H. Tseng, R. Jammy, and H. Huff, "Gate stack technology for nanoscale devices," *materials today*, vol. 9, no. 6, pp. 32-40, 2006.

[16] K. Stokbro, D. E. Petersen, S. Smidstrup, A. Blom, M. Ipsen, and K. Kaasbjerg, "Semiempirical model for nanoscale device simulations," *Physical Review B Condensed Matter and Materials Physics*, vol. 82, no. 7, pp. 075420, 2010.

[17] D. A. Papaconstantopoulos and M. J. Mehl, "The Slater Koster tight-binding method: a computationally efficient and accurate approach," *Journal of Physics: Condensed Matter*, vol. 15, no. 10, pp. R413-R440, 2003.

[18] D. Gunlycke and C. T. White, "Tight-binding energy dispersions of armchair-edge graphene nanostrips," *Physical Review B Condensed Matter and Materials Physics*, vol. 77, no. 11, pp. 115116, 2008.

[19] R. Jyoti, M. Chauhan, B. C. Choudhary, and R. K. Sharma, "Density functional theory study of manganese doped armchair graphene nanoribbon for effective carbon dioxide gas sensing," *ES Energy and Environment*, vol. 18, no. 9, pp. 47-55, 2022.

[20] M. Gholipour, N. Masoumi, Y.-Y. C. Chen, D. Chen, and M. Pourfath, "Asymmetric gate Schottky-barrier graphene nanoribbon FETs for low-power design," *IEEE Transactions on Electron Devices*, vol. 61, no. 12, pp. 4000-4006, 2014.

[21] A. Naderi, "Theoretical analysis of a novel dual gate metal graphene nanoribbon field effect transistor," *Materials Science in Semiconductor Processing*, vol. 31, pp. 223-228, 2015.

[22] H. Sarvari and R. Ghayour, "Design of GNRFET using different doping profiles near the source and drain contacts," *International Journal of Electronics*, vol. 99, no. 5, pp. 673-682, 2012.

4

CHAPTER

Reliability performance analysis of Gate-Stack Armchair Graphene Nanoribbon FET using Extended Hückel DFT model

The Extended Hückel model is employed in this chapter to investigate the reliability and performance of GS-AGNRFET, offering a more physically complete treatment of device electrostatics compared to the non-self-consistent Slater-Koster approach used in Chapters 2 and 3.

The Extended Hückel model demonstrates strong agreement with benchmark first-principles DFT methods including PBE, HSE06, DFT½, and tight-binding approaches in both bandgap trend and transmission coefficient values for AGNR (N = 4 and 7), validating its physical credibility and computational efficiency for nanoscale device modelling.

The A7 device (GS-AGNRFET with AGNR N = 7 as channel material) demonstrates superior performance over the A4 device across all key reliability metrics including I_{on}, I_{off}, SR, V_{th}, DIBL, device efficiency (DE), and static power dissipation under the EH-SCF framework.

Advanced transport analyses including DDOS, PLDOS, transmission spectrum, transmission pathways, and EDD collectively confirm enhanced gate electrostatic control, stronger electron tunneling, and more efficient carrier transport in the A7 device.

o¹ ’(TH(”’⁻³“’(–“¹³’⁻’⁵(–(⁴’β–⁴α—ε (εη₂ (⁵⁶–⁶³“(μη₂ ’⁴(η–(B9FI((BA (s 7(₂ ¹³“¹ (³⁵(⁵³×γ³–³“–γ⁶ε (εη₂ ’⁴(⁶¹–γ(⁶¹’(TE(”’⁻³“’(3C9FF((BA (s 4(–γ”(⁵⁸—⁵⁶–γ⁶³–εε (εη₂ ’⁴(⁶¹–γ(–εε(previously reported GNRFET configurations available in the literature, making it highly reliable for low-power applications such as biomedical devices, gas sensors, and signal amplification circuits.

4.1 INTRODUCTION

As discussed in detail in **Chapter 2** and **Chapter 3**, the proposed GS-AGNRFET was systematically analyzed using the SK tight-binding model within a semi-empirical DFT based calculator. As electronic devices continue to shrink to atomic dimensions, it is crucial to consider the impact of individual atoms in device simulations. Several first-principles methods with ab initio and DFT based approaches have been used to investigate the optical, structural, and electronic properties of various materials [1, 2]. Also, atomic-scale electron-transport simulation methods built on the NEGF formalism have been developed in recent years. The methods can be broadly classified into two categories: Semi-empirical methods, which use a model with adjustable parameters fitted to experiments or first-principles calculations, and ab initio methods, which calculate the electronic structure of the system. Semi-empirical methods include SK and Extended Hückel models to calculate the electronic properties of the device [3, 4]. The advantage of using Semi-empirical methods over an ab initio approach is that their application domain allows them to provide extremely precise outcomes. Moreover, the models can be fitted to experimental data, which sometimes yields more accurate results than DFT-based technique [5, 6]. In **Chapter 2**, GS dielectric engineering, temperature analysis, and edge passivation were investigated using SK model to understand the fundamental electrostatic and transport characteristics of the proposed device [7-9]. In **Chapter 3**, this analysis is expanded by examining the effects of channel width engineering on AGNRs from the 3p+1 with N values of 4, 7, 10, and 13.The results demonstrated that the GS-AGNR (N = 4) FET, despite exhibiting the largest bandgap (~1.98 eV) and the lowest off-state current, was identified as the optimal channel configuration in the SK model-based study [10]. However, it is important to note that in **Chapter 2 and 3**, all simulations were carried out using a without

self-consistent solution of the tight-binding Hamiltonian matrix. Although this approach is computationally efficient and provides a reasonable first approximation of electronic and transport properties, it inherently lacks the self-consistent treatment of electrostatic potential, which can limit the accuracy of certain device-level parameters [11]. In particular, when the Slater Koster model is used without SCF iterations, the spatial redistribution of charge density in response to applied bias is not fully accounted for. As a result, several important parameters such as DE, TP, static power dissipation, and the accurate variation of DDOS under applied bias cannot be reliably computed or analyzed. Additionally, we attempted to conduct a simulation using the SK model with SCF iterations; however, some of the resulting parameters are contradictory. These limitations restrict the completeness of the reliability assessment of the proposed device. To address this gap, the present chapter used the Extended Hückel model with a SCF iteration scheme. The EH method, as implemented in Quantum ATK, employs a tight-binding Hamiltonian with parameters that are empirically derived or fitted to first-principles calculations [3]. This approach provides significant computational efficiency while maintaining reasonable accuracy for nanoscale device modelling over other methods. In contrast to first-principles DFT, which solves the Kohn-Sham equations and provides predictive power at the expense of computational intensity, the EH method solves for electronic structure and transport properties using parametrized Hamiltonian basis sets and the NEGF formalism with a self-consistent Hartree potential [6, 12]. Unlike the non-SCF approach used in **Chapter 3**, the EH-SCF method iteratively updates the Hamiltonian matrix until convergence is achieved. This enables reliable extraction of reliability parameters including DE, TP, and static leakage power. A significant difference that motivates the use of the Extended Hückel model over the Slater Koster tight-binding model in proposed device

simulations is their underlying spatial parametrization in Hamiltonian matrix. In the SK model, the overlap and Hamiltonian matrix elements are represented as numerical, pairwise tabular functions dsüsÅr sÅ~%ÅwÅs≠o~ö~ wq%w≈oÅqs%%ö≠%z%uÅwwqoÅ~%≠pw≈o%qö~ pwÅo~wöÅ±%z2%2% / [11]. Even though this tabular methodology provides significant numerical flexibility and the capacity to accurately replicate complex band structures when precisely fitted, but it needs a considerably greater quantity of fitting parameters namely distinct SK tables for each elemental üow≠%oÅu.zo≠%ö~ sÅ≈.~ %qö~ pwÅo~wöÅ2%oÅr%s”üs%ötvöüüwÅu%wÅ≈su≠oz% 2%2%%pöÅr±/. This renders the fitting process markedly more complex, computationally demanding, and less adaptable across various structural configurations. In contrast, the EH model constructs the complete Hamiltonian matrix from the physically grounded Slater orbital overlap integrals through a closed-form analytical expression, which needs merely four adjustable parameters üs≠%oÅu.zo≠%±vszz%üs≠%szs~ sÅ~% 2% 2%M2%M/%wÅ%or r w≈wöÅ%ö%vs%±wÅu.zo≠%szs~ sÅ~level Wolfsberg Hel~ vözˇ%qöÅ≈oÅ~%2%vwqv%%%s¨.sÅ≈z”%ÅwvsÅ≈ozz”%±±wÅsr%%oz.s%t%AÅ~%ö≠% organic and carbon-based systems [12-14]. Thus, the EH model is far simpler in its parameterization and offers greater physical clarity, as each matrix element can be explicitly linked to an orbital overlap integral with a distinct quantum mechanical meaning [15]. Moreover, the SK model considers the Hamiltonian and overlap matrices as independent tabular units, whereas the EH model imposes a direct algebraic proportionality between H_{ij} (Hamiltonian matrix element) and S_{ij} (overlap matrix element) via the Wolfsberg Helmholz relation [14, 16]. This algebraic proportionality between H_{ij} and S_{ij} in EH model will help in maintaining the fundamental physical relationship between orbital overlap and electron hopping, which is crucial to the chemistry of conjugated carbon systems like AGNRs. The Quantum ATK documentation clearly states that the Extended Hückel model is a Slater

Koster model as well, but with a unique fitting procedure for the Hamiltonian matrix elements, indicating that the EH model serves as a physically constrained, parameter-efficient specialization of the SK framework [13]. Furthermore, in this chapter the EH model has been validated against benchmark first-principles DFT methods, including the Perdew Burke Ernzerhof (PBE) functional, Heyd Scuseria Ernzerhof (HSE06) functional, Tight Binding (TB) method, and DFT-½ approach, confirming its physical credibility and computational efficiency for modeling AGNR-based devices. Also, from **Chapter 2,** it is concluded that B AGNRFET shows better performance when the edges of AGNR are passivated with 13^{th} group element boron. Considering the importance of edge effects in determining the performance of devices based on GNR, **Chapter 5** systematically extends this investigation to the remaining elements of the Icosagen group (Al, Ga and In), providing a comprehensive understanding of how Group 13 elements edge passivation influences proposed device characteristics.

In the present chapter, the study focuses specifically on AGNRs with N = 4 and 7, both belonging to the semiconducting 3p+1 family of AGNRs. The two proposed device configurations, namely the A4 device (GS-AGNRFET with AGNR N = 4 as the channel material) and the A7 device (GS-AGNRFET with AGNR N = 7 as the channel material), are systematically compared in terms of performance and reliability metrics. This chapter is organized as follows: Section 4.2 presents the device design and physical models, Section 4.3 discusses the results and analysis, and finally, Section 4.4 concludes the findings of the study.

4.2 DEVICE DESIGN AND PHYSICAL MODELS

The cross-sectional view of the proposed A4 device is illustrated in Figure 4.1. The AGNR (N = 4) and AGNR (N = 7) are used as channel material in proposed devices A4 and A7, respectively. Further, a GS architecture is employed below a metallic gate to overcome the SCEs. The device design is already **discussed in Chapter 2 and 3 in detail**. All the device parameters used for simulation are tabulated in Table 4.1.

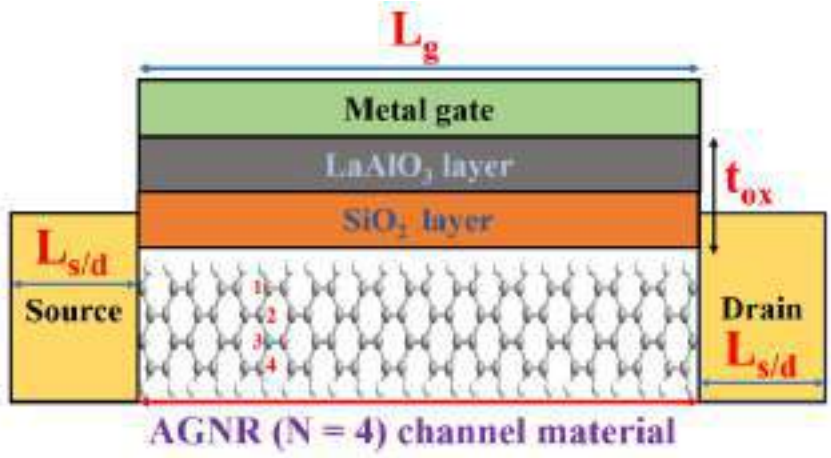

Figure 4.1: Cross-sectional view of the proposed A4 device [17]

Table 4.1
Proposed device parameters for the present chapter [17]

Parameters	Proposed Devices	
	A4 device	A7 device
N	4	7
Gate length, L_g (nm)	5	5
Oxide layer thickness, t_{ox} (nm)	1	1
Source and drain length, $L_{s/d}$ (nm)	5	5
The concentration of doping in the channel region, N_{Ch} (e/cm^3)	3×10^{16}	3×10^{16}
The concentration of doping in source and drain regions, $N_{s/d}$ (e/cm^3)	5×10^{18}	5×10^{18}

As previously discussed in previous chapters, the Quantum ATK tool is used to carry out all the simulations. In the previous chapters the SE calculator uses the Slater-Koster model with the non SCF iterations in ATK to perform all the analysis. In this chapter, the tight-binding Hamiltonian matrix approach with the EH model is employed in the SE calculator. To calculate spectral densities, we have used the NEGF methods with SCF iteration. The transmission spectra and current-voltage characteristics computed under NEGF formalism, used with the EH model in the SE calculator, do not consider electron-phonon interactions. All the simulation parameters, including the basis set, EH fitted parameters, temperature, k-point sampling, energy cut-offs, SCF criteria, and boundary conditions, are tabulated in Table 4.2. Also, the summarized process flow chart for the simulation approach is displayed in Figure 4.2.

Table 4.2
Simulation parameters used for the present work [17]

Parameters	Value/Description
Simulation tool	Quantum ATK 2019.12
Computational model	Extended Hückel model
Basis set	Hoffmann
Fitted parameters	Hückel Hamiltonian parameterization
Temperature and Fermi Dirac broadening	300 K
Boundary conditions	Multigrid type Poisson solver with Periodic ×Periodic × Dirichlet boundary conditions
K point sampling	1 × 1 × 100
Energy cut off	40 Hartree
Contact self-energies	calculated using the direct self-energy method

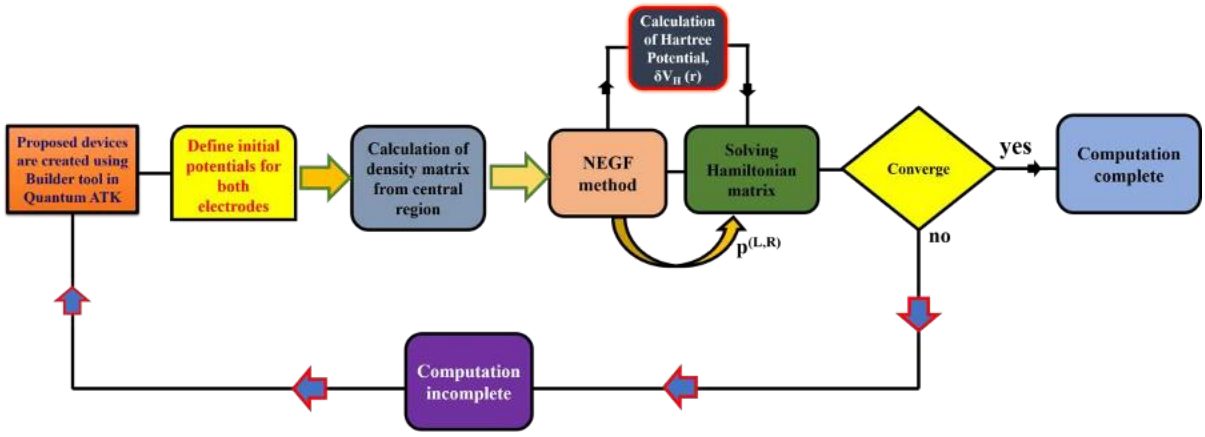

Figure 4.2: Simulation flow chart for the proposed work [17]

Firstly, the initial potentials for both electrodes are defined then the density matrix for the central region in the device using EH-SCF is calculated. This equation uses the Fermi-Dirac distribution to add up the contributions from both the left and right electrodes in the central region (channel region), which shows how electrons are spread out in the device energy levels when a bias voltage V_b is applied. Mathematically the density matrix is given as [18]:

, G G G G G(GGGGGGGGGGGGGGGGGGGGGGGGGGGG

where

partial spectral density of states in the left electrode

partial spectral density of states in the right electrode

external bias voltage

the chemical potential of the left electrode

the chemical potential of the right electrode

The partial spectral densities with the NEGF method discussed in Eq. 4.11 are given as [3]:

G—G| (4.12)

Where

spectral densities of states in the left and right electrodes

≠s≈o≠sr %Q≠ssÅ±‰ Åq≈ööÅ

broadening function

or–oÅqsr %Q≠ssÅ±‰ Åq≈ööÅ%

From the density matrix and partial spectral densities, the real-space density for the central region is calculated. This equation changes the density matrix into real space electron density by breaking it down into Gaussian orbitals that are centered on each atom. This shows the spatial distribution of electrons throughout the device. Mathematically, the real-space density is given as [3]:

G G% G — (4.13)

where

G induced electron density at position r

Mulliken population

width of the Gaussian orbital

üö±≈≈öÅ‰sq≈ö≠‰t%≈ö~ %

Once the real-space density matrix is calculated, the Hartree potential is calculated by solving Zöw±öÅ±‰¨ ..o≈öÅ±‰vs%R o≠≠ss%ö≈sÅ≈wz%w%w≈sÅ%" [3]:

G (4.14)

where

spatially dependent dielectric constant

Hartree potential

induced electron density

The Hartree potential is used to solve the one-electron Hamiltonian until a self-consistent solution is obtained. This is the core Extended Hückel Hamiltonian equation. The diagonal elements (i=j) represent the on-site energy of each orbital corrected by the local Hartree potential. The off-r wuöÅoz%szs~ sÅ±%wx/%%sü≠s±sÅ≈%vs%wÅ≈s≠oq≈wöÅ%ps≈—ssÅ%Åswuvpö≠wÅu% orbitals2%qö~ pwÅwÅu%%vs%ö≠%pw≈oz%Å≈s≠uws±%-swuv≈sr %p”%Å%or x.±≈opzs%ö≈o~ s≈s≠%%År %%vs%ö–s≠zoü% matrix S, corrected by the average Hartree potential at both atomic sites. Mathematically this is given as [14]:

G G G G (4.15)

G G– G GG (

where

Hamiltonian matrix element between atomic orbitals i and j

Orbital energy

β Wolfsberg-Helmholtz constant typically set to a value of 1.75 in the standard Hückel approximation

Hartree potential corresponds to the induced electron density on the atoms

G overlap matrix element between atomic orbitals i and j

Once the Self-consistent solution of the tight-binding Hamiltonian matrix from Eq. 4.15 is obtained, the transmission coefficient and the drain current are calculated. The expressions for the transmission coefficient and the drain current have already been discussed in detail in **Chapter 2** and are represented by **Eq. 2.16** and **Eq. 2.17** respectively.

4.3 RESULTS AND DISCUSSIONS

In this section, the DFT analysis of AGNR with varied N belonging to the (3p+1) family is studied in terms of band structure, DOS, and transmission coefficient. Further, the AGNR is used as a channel material in GS- AGNR FET with the varied number of carbon atoms along AGNR width, and then the performance analysis of the proposed devices has been carried out using the DFT and NEGF approach.

4.3.1 Investigation of bandgap, DOS and T(E) parameters in bulk-configured AGNRs using the EH model

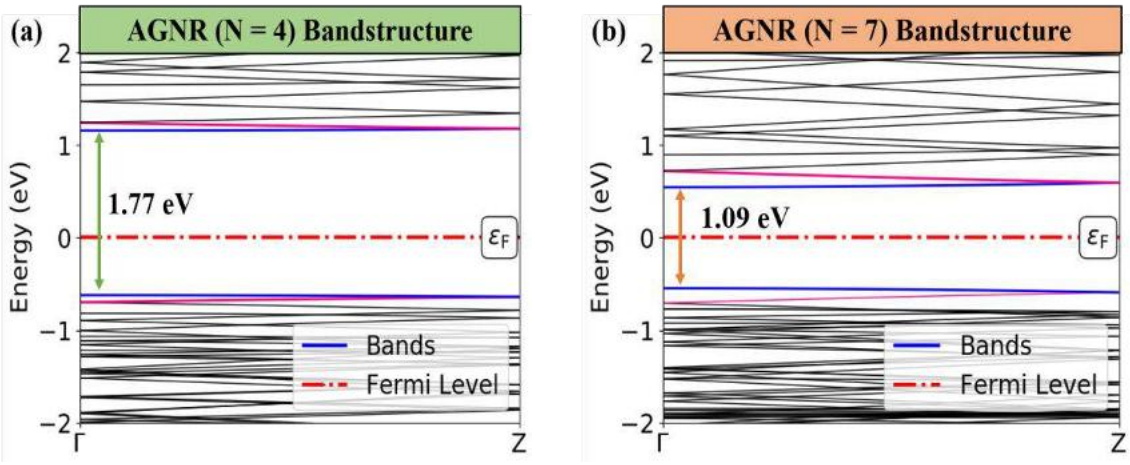

Figure 4.3: Bandgap analysis of bulk-configured (a) AGNR (N = 4) and (b) AGNR (N = 7) [17]

Figure 4.3 shows the bandgap analysis of bulk-configured AGNRs for different values of N = 4 and 7 using the EH model. The band gap, which displays the total number of possible energy levels for an electron, is calculated using band structure. The high symmetry k-üöwÅ±%%År%% are plotted on the x-axis, representing the boundaries of the one-dimensional Brillouin zone, while energy in eV is plotted on the y-axis. The values of the bandgap for AGNR (N = 4) and (N = 7) are 1.77 and 1.09 eV, respectively. The reduction in bandgap from 1.77 eV to 1.09 eV as N increases from 4 to 7 is a direct consequence of the reduced quantum confinement in the wider ribbon, which brings the conduction band minimum and valence band maximum closer together. While a larger bandgap is conventionally associated with better OFF state leakage suppression, the self-consistent Extended Hückel framework employed in this work captures additional electrostatic effects that influence device performance beyond what bandgap alone predicts, as elaborated in the device performance analysis presented in the subsequent sections.

P.≠vs≠2%vs±s%KQX] ±%-w%wts≠sÅ%oz.s±%t%N %≠s%±sr%±%qvoÅÅsz% o≈s≠wz%Å%≠öüö±sr% devices A4 and A7.

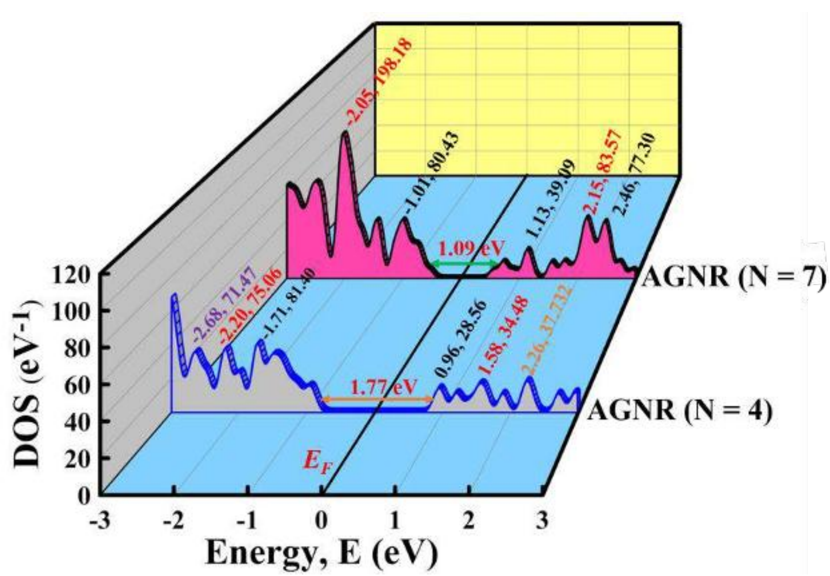

Figure 4.4: DOS analysis for bulk-configured AGNR (N = 4) and AGNR (N = 7) [17]

A higher DOS value signifies the availability of greater states for occupation. The mathematical expression of DOS is already defined with **Eq. 3.12** in **Chapter 3**. This equation demonstrates the interrelation between DOS and energy. The results of a DOS study on AGNR (N = 4) and AGNR (N = 7) are illustrated in Figure 4.4. From Figure 4.4, it is observed that DOS resembles the bandgap. The absence of a peak around the E_F signifies the semiconducting nature of both AGNRs which is consistent with their band structure analysis. In AGNR (N = 4), the DOS peak value in the CB is 37.73 eV^{-1} at an energy value of 2.26 eV. When the value öt%N %w=%qvoÅusr %ö~ %%ö%A%Å%K GNR, the DOS peak value in CB shifted to 83.57 eV^{-1} at an sÅs≠u”%oz.s%öt%47=%d 4%ovs%qvoÅus%Å%vs%oz.s%öt%N %ows±%ws%ö%vs%soy%oz.s±%öt%Ya % in CB. From this DOS study, it is observed that the bulk configuration of AGNR (N = 7) has more availability of states for occupation in CB than AGNR (N = 4).

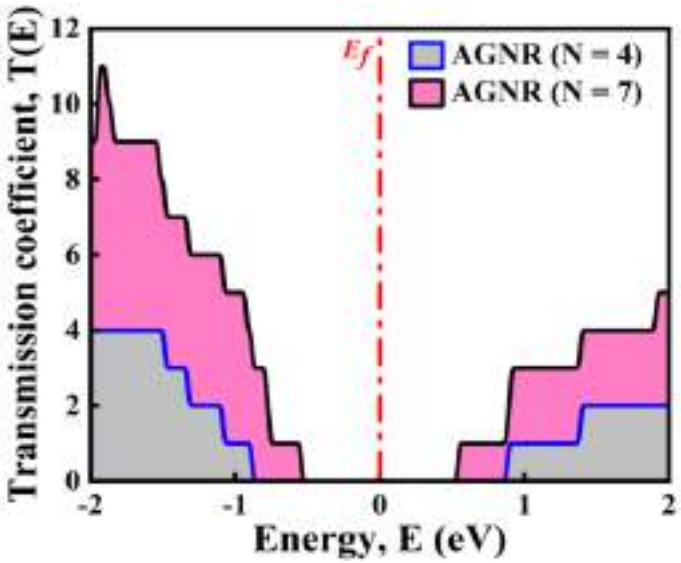

Figure 4.5: Transmission spectrum analysis for bulk-configured AGNR (N = 4) and AGNR (N = 7) [17]

The greater availability of conducting states combined with the closer proximity of the first DOS peak to the Fermi level in AGNR (N = 7) directly enhances electron injection into the

channel under applied gate bias, which is expected to contribute to improved I_{on} and DE in the A7 device configuration as discussed in the next sections. The transmission spectrum analysis for bulk-configured AGNR (N = 4) and AGNR (N = 7) is depicted in Figure 4.5. The transmission spectrum of a GNR explains how electrons change energy as they move through it. In the transmission spectrum, the number of transmission peaks and their positions are directly related to the energy levels of the AGNR. For semiconducting AGNRs, as the value öt%N %wÅq≠so±s±2%vs%poÅr uoü%sq≠so±s±2%sor wÅu%ö%%vv~%Å%vs%%oÅ~ w±vöÅ%soy±%qzö±s≠%ö% the Fermi level. From Figure 4.5, it can be observed that for AGNR (N = 7), transmission peaks shift closer to E_F, and the value of T(E) is higher than that of AGNR (N = 4). A smaller bandgap, more availability of states in DOS, and higher transmission spectrum in AGNR (N = 7) imply that less energy is required to move electrons from the VB to the CB, making the material more conductive. These improved parameters suggest that AGNR (N = 7) has improved electrical conductivity.

4.3.2 Comparison of the EH Model with other DFT models

In this section, we have compared and reported the value of bandgap and T(E) using the EH model against benchmark first-principles DFT methods, namely the PBE, TB methods, DFT ½ method, and HSE06 functionals in Table 4.3. The comparison focuses on parameters like the E_g and T(E) for bulk-configured AGNRs with N = 4 and 7, which are used in our device configurations. The reported data in Table 4.3 suggest that the value of E_g and T(E) for all the ~ örsz±%sq≠so±s±%År %wÅq≠so±s±2%s±üsq~wsz’2%±%vs%oz.s%öt%N %wÅq≠so±s±%ö~ %%ö%A%vs±s% findings confirm the reliability of the EH model used in calculating the bandgap and T(E). Although the EH model slightly underestimates E_g compared to PBE and HSE06, while the

trend and range are consistent with TB and DFT ½ results, supporting the physical credibility of our EH model for device modeling.

Table 4.3
Comparison table of the EH model with other DFT models [17]

Models	Parameters	AGNRs configurations	
		N = 4	N = 7
EH	E_g *(eV)*	1.77	1.09
	T (E)	1.99	4.99
PBE	E_g *(eV)*	2.38	1.47
	T (E)	3.99	6.99
HSE 06	E_g *(eV)*	3.05	1.91
	T (E)	--	--
DFT ½ method	E_g *(eV)*	2.25	1.38
	T (E)	2.99	6.99
TB	E_g *(eV)*	1.98	1.21
	T (E)	0.99	1.97

Additionally, we have calculated and compared the DOS using EH model with other DFT methods such as PBE, HSE06, TB, and DFT ½ for AGNRs with N = 4 and 7 as shown in Figure 4.6. From Figure 4.6(a), we can observe that for AGNR (N = 4), the PBE and DFT ½ methods shows no peaks in the energy range of ± 1.15 and ± 1.12 eV, indicating a bandgap of 2.38 and 2.25 eV respectively, which aligns with the values reported in Table 4.3. Similarly, HSE06 displays a wider no-peak energy range of ± 1.51 eV, which indicates a bandgap of 3.05 eV. The TB method shows peaks that are narrower and slightly shifted compared to PBE, with an energy range of ± 1.28 eV. The DOS suggests a bandgap close to 1.98 eV for the TB method. The EH model exhibits sharp and symmetric peaks near ± 1.11eV, corresponding to the VB and CB, yielding a bandgap of 1.77 eV. From Figure 4.6(b), we can observe that as the width increases to n = 7, the DOS peaks move closer to the E_F, resulting in a reduced bandgap for all the models. The EH model shows no peaks for energy range ± 0.66 eV, which indicates a decrease in the E_g for AGNR (N = 7) with a value of 1.09 eV. The PBE method shows a broader

zero DOS peaks range from about ± 0.71 eV (E_g %74 A%d /2%-vws%vs%Ra O6>% ör sz%vö—±%% wider gap from ± 0.99 eV (E_g %4C7%d /4%vs%NPb%% s≈vör %wzr±%Åö-peak region between ± 0.67 eV (E_g %49B%d /2%Ar %vs%L% ör sz%w#üzo”±%vs%~ ozs±%s≠ö%üsoy±%suwöÅ%ö~ %% 0.61 eV (E_g %487%d /4%vs%”~ ~ s≈”%Ar %-wr≈v%öt%vs%s≠ö%NYa%üsoy±%suwöÅ%oq≠ö±%oz% models consistently reflect the expected bandgap as tabulated in Table 4.3. Further, the trend and estimated band gaps from the DOS plot for AGNR (N = 4 and 7) with the EH model is consistent with other DFT models, which confirms the reliability of the EH model used in this work.

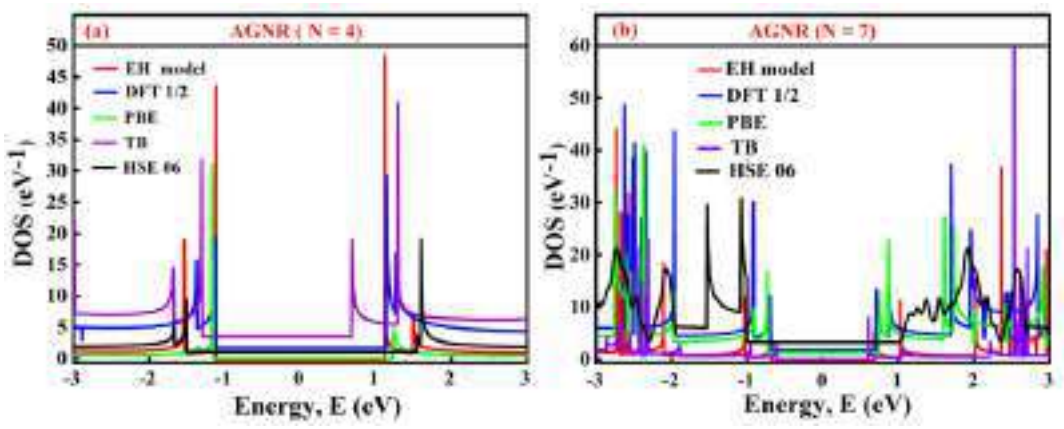

Figure 4.6: Density of state analysis comparison of EH model with other DFT models for (a) AGNR (N = 4) and (b) AGNR (N = 7) [17]

Also, the authors have tabulated the values of band gaps of the present work with other compounds based on DFT approaches available in the literature in Table 4.4. The Table 4.4 shows a direct comparison between our AGNR results (1.09 1.77 eV, using the EH model) and other materials studied using first-principles approaches. The comparison validates that the bandgap range of our AGNR configurations is competitive with several materials previously reported for optoelectronic applications.

Table 4.4
Comparison of band gaps of the present work with other compounds based on DFT approaches available in the literature [17]

Materials/Compounds	Simulation models	Reported bandgap value (eV)	References
AGNR (N = 4)	EH model	1.77	present work
AGNR (N = 7)	EH model	1.09	Present work
3C - SiC	General Gradient Approximation (GGA)	2.5	[19]
4C - SiC	GGA method	3.58	[19]
Graphene	DFT with FP LAPW formalism	0	[20]
8. 33 % Si doped graphene	DFT with FP LAPW formalism	1.022	[20]
12.50% Si doped graphene	DFT with FP LAPW formalism	1.35	[20]
25% Si doped graphene	DFT with FP LAPW formalism	1.95	[20]
50 % Si doped graphene	DFT with FP LAPW formalism	2.51	[20]
$BaHfO_3$	GGA	5.9	[21]
Mn_3GaC	Monte Carlo simulations	0	[22]
Chalcogens doped SHO	LDA method	6.07	[23]
Hydrogen boride	PBE method	0	[24]
$AlCMn_3$	Monte Carlo simulations	0	[25]

4.3.3 Proposed devices performance analysis using the EH model for low power applications

In this section, we have compared parameters for low-power application analysis like I_{on}, I_{off}, SR, V_{th}, DIBL, DE and other parameters like DDOS, TP, and EDD for both device configurations. Figure 4.7 (a) depicts the spider chart variation in the parameters I_{on}, I_{off}, and SR. The V_{gs} varies from 0 to 1 V at a constant V_{ds} = 0.5 V for the transfer characteristics of the devices. From the transfer characteristics, the parameters I_{on}, I_{off}, and SR are calculated.

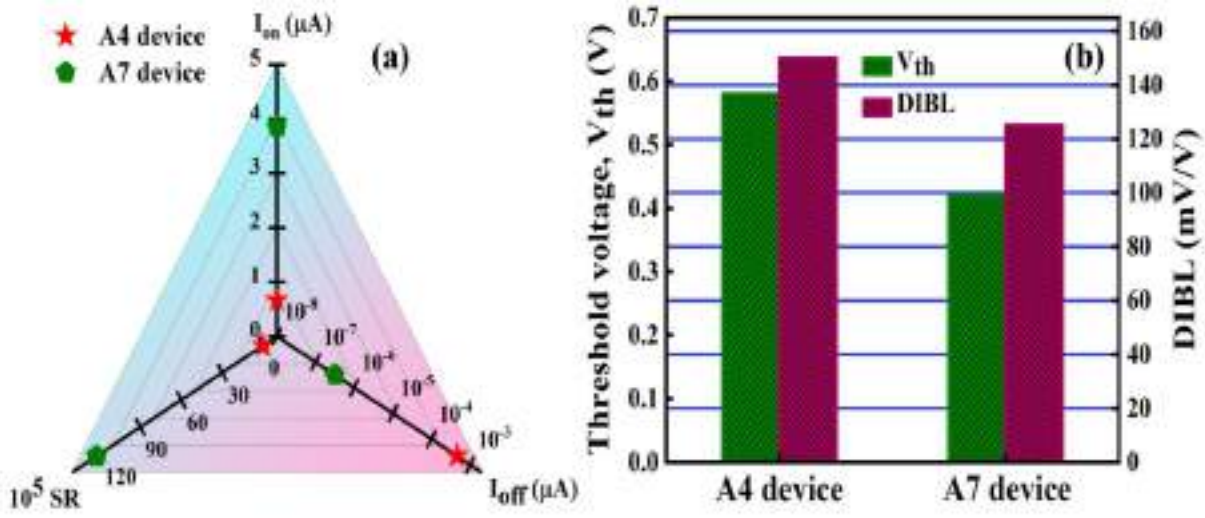

Figure 4.7: (a) Variation in I_{on}, I_{off}, and SR for proposed devices and (b) Variation in V_{th} and DIBL for proposed devices [17]

From Figure 4.7 (a), it is observed that the A7 device shows improved value of I_{on} and reduced value of I_{off}, which significantly improved the SR compared with the A4 device. The better the SR, the better the speed of the device and the lower the power consumption. The reason for the better performance of the A7 device is that the AGNR (N = 7) has a smaller bandgap, which improves its electrical conductivity. Also, in AGNR (N = 7), the increased availability of states in the DOS enhances the electron transition, while the higher transmission spectrum ensures efficient electron transport across the material. These factors improve the current flow in A7 devices as compared with A4 devices. Considering the effect of scaling down, we have also calculated the SCEs parameters like V_{th} and DIBL. The variation of V_{th} and DIBL is depicted in Figure 4.7 (b). The V_{th} for a device is defined as the minimum amount of V_{gs} required to switch on the device. From Figure 4.7 (b), we can observe that the value of V_{th} reduces by 27.59% in the A7 device compared with the A4 device. The DIBL is an SCE observed in FETs when the channel length reduces to the nanometer range. It refers to the reduction of the potential barrier in the channel near the drain region due to the influence of the V_{ds}. It is an

important parameter to check the device performance and power consumption. The higher value of DIBL signifies a lesser control of the gate over the channel, which leads to higher power consumption and degradation in device performance. The values of parameters calculated from the transfer characteristics of proposed devices such as I_{on}, I_{off}, SR, V_{th}, and DIBL are tabulated in Table 4.5. From Figure 4.7 (b), it can be observed that the A7 device has a lower value of DIBL, which signifies lower power consumption over the A4 device. The value of DIBL reduces from 150 to 125 mV/V in the case of the A7 device. The reason is that the A7 device has a smaller bandgap, lower threshold voltage, and better switching speed, which improves the control of the gate over the channel and reduces DIBL value as compared with the A4 device.

Table 4.5
Comparison table for proposed devices [17]

Parameters	Proposed Devices	
	A4 device	**A7 device**
I_{on} **(A)**	0.664×10^{-6}	3.86×10^{-6}
I_{off} **(A)**	4.51×10^{-10}	3.16×10^{-13}
SR **(× 10^5)**	0.0145	122
V_{th} **(V)**	0.58	0.42
DIBL (mV/V)	150	125

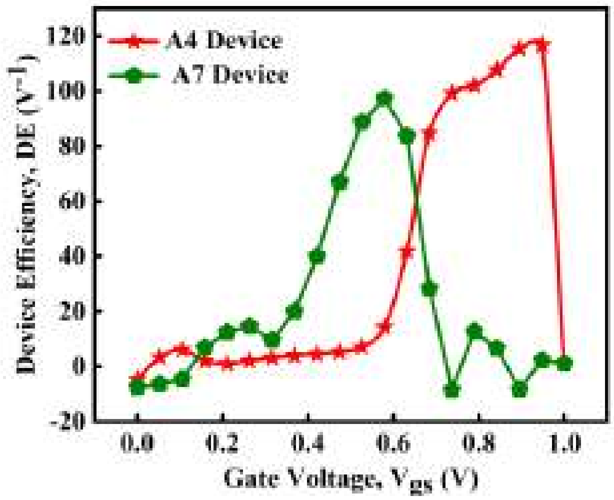

Figure 4.8: Device efficiency analysis of A4 and A7 devices [17]

Figure 4.8 depicts the DE analysis of the proposed A4 and A7 devices. DE is a critical parameter that measures how well a transistor converts V_{gs} modulation into I_d, reflecting the r s–wps ±‰Ås≠u”‰ttwqwsÅq”. Mathematically, DE is given as:

GGGG—GGGGGGGGGGGGGGGGGGGGGGGGGGGGGGGGGGGGG

where

- transconductance
- drain current

From Figure 4.8, it can be observed that the value of DE for the A7 device is higher at lower gate voltages as compared with the A4 device (~ 0.5V). The early peak and sharp increase in A7 device indicate that it has superior electrostatic control over the channel, g_m and enhances DE. The higher value of DE for the A7 device signifies that the A7 device operates more efficiently, requiring lower voltage to achieve significant current modulation and highly reliable in low power applications.

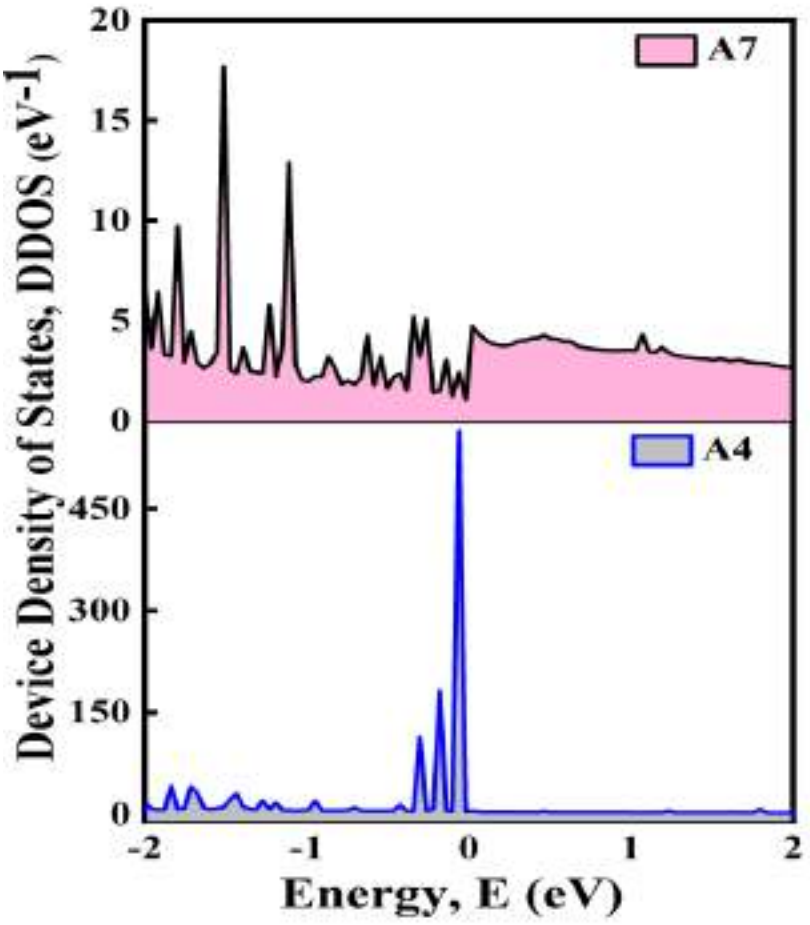

Figure 4.9: Device density of states analysis for A4 and A7 devices [17]

Figure 4.9 depicts the variation of DDOS in both devices at V_{ds} = 0.5 V. The DDOS presents the total number of electronic states that are obtainable (occupied + unoccupied), how they are distributed in terms of energy, and how important they are to the operation and behavior of the device. The VB (energy range from -2 to 0 eV) and the CB (energy range from 0 to 2 eV) are the two main sections that make the DDOS curve. From Figure 4.9, it is observed that the A4 r s–wqs%s“vvpw≠%vwvs≠%isoy%NNYa%~ ouÅw.r.s%t%üü≠ö“w~ o≈sz”%=6%sd %qö~ üo≠sr%ö% oüü≠ö“w~ o≈sz”%6%sd %ö≠%ve A7 device. However, it is important to note that the absolute magnitude of the DDOS alone does not determine the device transport performance. The

critical parameter to understand the device operation is the energy position of the DDOS peaks relative to the E_F (E = 0 eV). In the A4 device, the larger bandgap of 1.77 eV pushes the first DDOS peak further away from the Fermi level, meaning that under a moderate applied gate voltage, fewer states fall within the transport window available for electron conduction. In contrast, in the A7 device, the smaller bandgap of 1.09 eV positions the first DDOS peak closer to the Fermi level, enabling more efficient electron injection into the channel under the same applied bias conditions. This energetically favorable positioning of DDOS peaks in the A7 device, rather than the absolute peak magnitude, is responsible for the improved carrier transport and enhanced I_{on} observed in the A7 device compared to the A4 device.

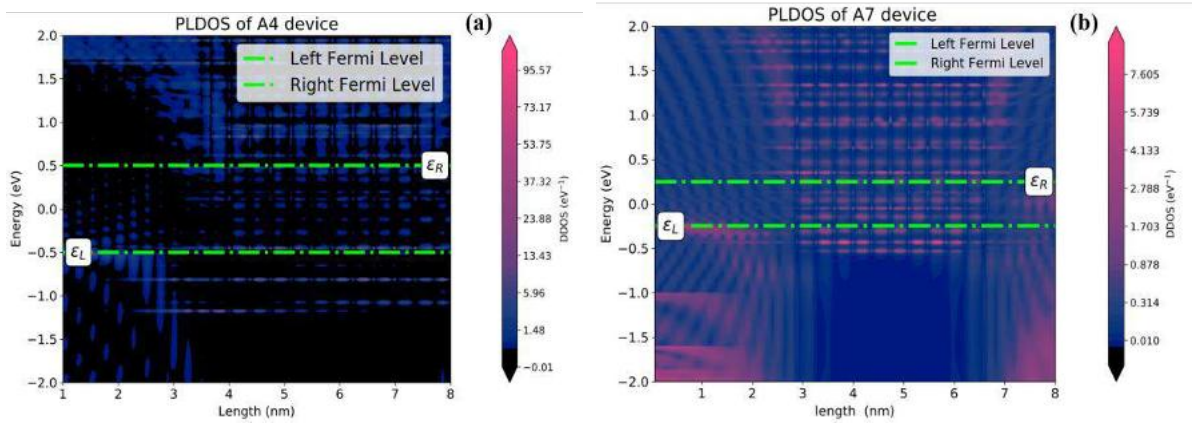

Figure 4.10: Projected local density of states analysis for (a) A4 and (b) A7 device [17]

Figure 4.10 shows the PLDOS plot at applied V_{ds} = 0.5 V. The PLDOS contour plots represent electron propagation through the channel. The horizontal axis typically corresponds to the device transport direction along the channel (from source to drain), while the vertical axis represents energy, often centered around the E_F. Color gradients indicate the availability of the NYa%o~%vo~%sÅs≠u”%s–sz#%vs%qözö≠%po≠%ö≠%vs%K: %s–ws%oÅus±%üö%6=4=A%sd %–vvs%ö≠%≈vs%KA%s–ws%%%soqvs±ºA4>6=%d 2%Ar wqo~vÅu that the absolute local DOS magnitude is higher

in the A4 device. However, the spatial and energetic distribution of states within the transport sÅs≠u”%-wÅr ö—%t%8%ö%Ⅼ8%d %≠ö. År %vs %s≠~ w%s–sz%s–soz±%% ö≠s%v”±wqozz”% soÅwÅut. z% distinction between the proposed devices. The pink, black and blue colors in the contour plot reflect the high, low, and moderate availability of DOS respectively. From Figure 4.10(a), we observe that there exists black colored region within the energy range from 2 to + 2 eV for A4 device whereas in case of A7 device there exist pink and blue colored regions within the energy range of 2 to + 2 eV as shown in Figure 4.10(b). These findings indicate that the availability of the DOS for the conduction electrons is very high in case of A7 device compared to A4 which can be the reason behind the observed lower I_{off} and better switching ratio for the A7 device.

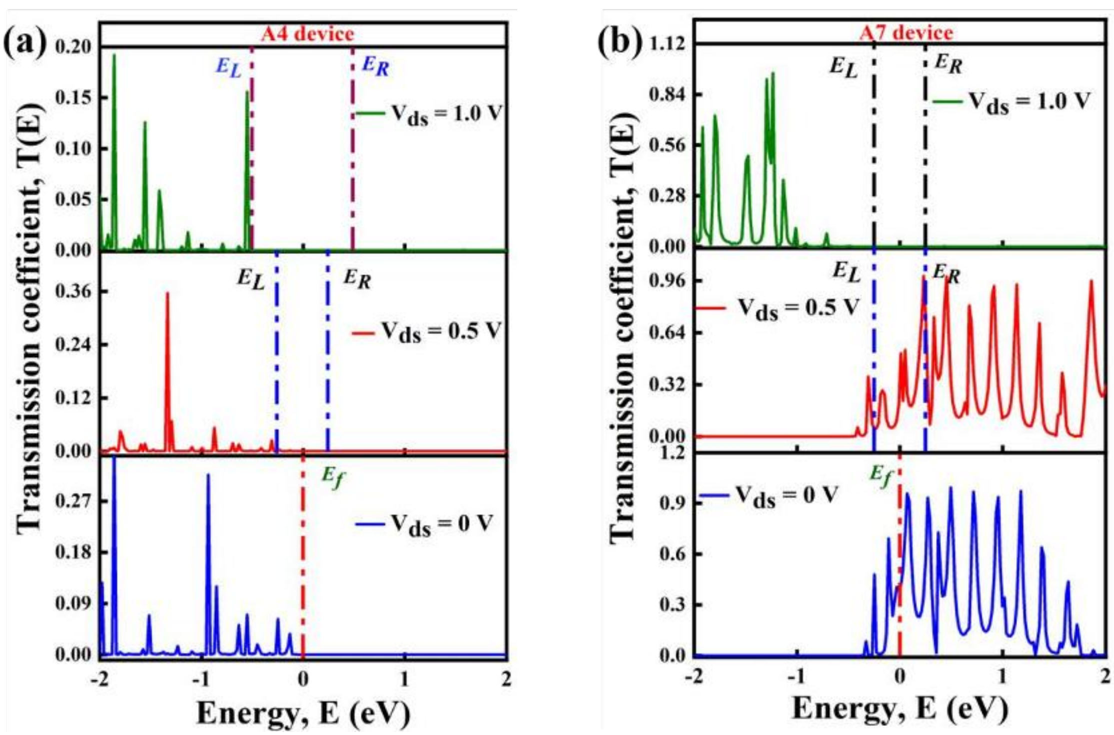

Figure 4.11: Transmission spectrum analysis for (a) A4 and (b) A7 device at different V_{ds} [17]

Anshul

Figure 4.11 presents the transmission spectrum analysis of A4 and A7 devices at varied drain voltages, revealing critical details about energy-dependent electron transport dynamics under applied bias. Once the transmission spectrum is calculated, it is observed that the shift in E_F shift at the VB and CB edges is the primary distinction between the various spectra calculated from the parameters $_d(E)$ and $_s(E)$. The terms E_L and E_R in Figure 4.11 denote the shift in the Fermi level corresponding to the left and right electrodes, respectively. From Figure 4.11(a), we can observe that at V_{ds} = 0 V, the A4 device exhibits few and weak transmission peaks in VB, particularly around the E_F = 0 eV, indicating an absence of transport channels which leads to greater resistance. From Figure 4.11 (b), for V_{ds} = 0 V, the value of transmission coefficient at E_F for the A7 device is found to be 0.54, while for the A4 device, the value of T(E) is zero. This confirms that the A7 device has more available conducting channels at the Fermi level. Also, the A7 device exhibits more obvious and sharper transmission peaks in the CB near E_F = 0 eV, allowing for greater carrier injection and a lower threshold for conduction, as shown in Figure 4.11(b). Further, at V_{ds} = 0.5 V, the trend remains similar, with the A7 device still showing a higher value of T (E) = 0.98, whereas the value of T (E) is zero for the A4 device. These findings suggest that the A7 device at V_{ds} = 0.5 V exhibits better transport performance, lower resistance, and higher output current. However, as V_{ds} increases to 1V, both devices exhibit a vanishing T (E) between E_L and E_R, indicating a suppression of conducting channels under higher bias conditions. Hence, based on our T (E) analysis, we observed that the A7 device is suitable for low-power applications, where minimal leakage current and fast switching are desirable. The above statement is confirmed by the device efficiency analysis, as discussed in Figure 4.8. To examine deeper insight into the spatial characteristics of electron transport, the transmission pathways were analyzed at V_{ds} = 0.5 V.

The transmission coefficient, T(E), is divided into local bond contributions, Tij, through the analysis option known as TP. The TP is correlated with the possibility of an electron tunneling from the source electrode to the drain electrode in the FET device.

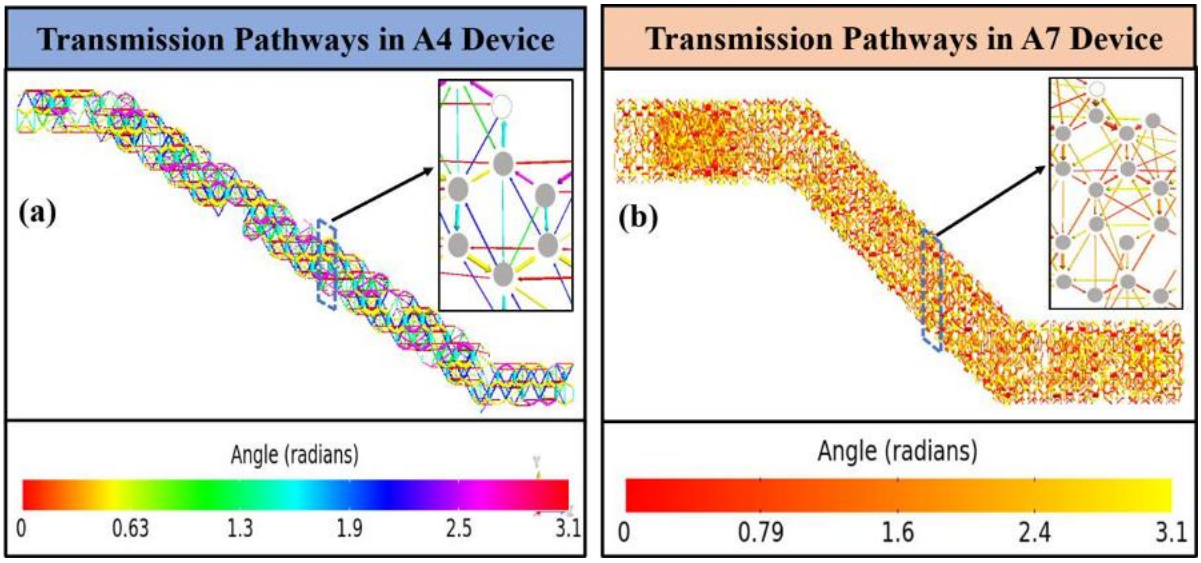

Figure 4.12: Transmission pathways in (a) A4 device and (b) A7 device [17]

The investigation of TP offers information about the conductance, optimization, and quantum mechanical effects of the device, which are important parameters in determining the performance. In TP analysis, arrows are frequently employed to indicate the direction of electron transmission. The volume of the arrow represents the magnitude of the TP, while the color indicates the direction of TP as illustrated in Figure 4.12. In Figure 4.12(a) for device A4, the yellow color shows the right direction, and the other color shows the left direction of electron transmission, while in Figure 4.12 (b), the red color shows the right direction and the yellow color shows the left direction of electrons. The inset view of Figure 4.12 (a) and (b) clearly shows that the device A7 has longer and thicker arrows, indicating a stronger transmission than the A4 device. The A7 device has a higher TP than the A4 device, indicating stronger conductance, faster switching.

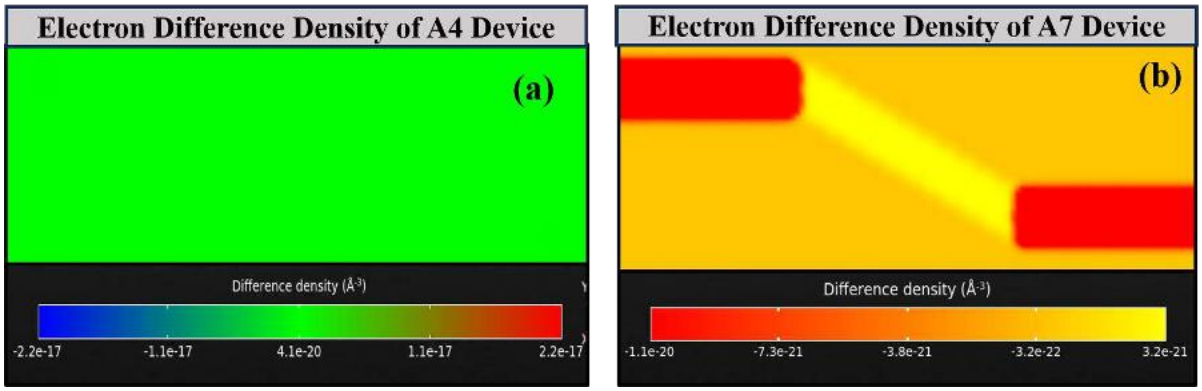

Figure 4.13: Contour plot of EDD in (a) A4 device and (b) A7 device [17]

The applied gate voltage causes a change in electron density, which is represented by the electron difference density. Figure 4.13 shows the contour plot of EDD for both proposed devices. Due to the applied gate voltage, the contour map will demonstrate areas of increased or decreased electron density within the devices. From Figure 4.13(a) and (b), the highest value of EDD for the A4 device is 4.1×10^{-20}, while for the A7 device, the value is 3.2×10^{-21} along the channel regions. The EDD analysis indicates that the A4 device demonstrates a greater sz≈öÅ‰wts≠sÅqs‰sÅ±w”‰t‰47‰76 % 2as compared to 948‰76 % ‰ö≠ws‰KA‰s–qs4‰ The higher EDD value in the A4 device signifies a higher and less regulated redistribution of electron density under the applied gate voltage, implying that the gate modulation in A4 results that creates a lot of charge variance across the device, but have unlocalized redistribution of electrons. The reduced EDD value in the A7 device indicates more accurate and regulated gate modulation, resulting in a more uniform and localized redistribution of electron density inside the designated channel region. The enhanced gate control of the A7 device leads to diminished electron density fluctuations throughout the channel, hence providing superior switching performance, a lower threshold voltage, and decreased leakage current relative to the A4 device. Further, for low-power applications, the static power (leakage power) of a device plays

an important role. The static power for a device is defined as the amount of power consumed by that device in the off state. It is an essential parameter to determine the thermal stability, battery life, and total power consumption for a device. A lower value of static power signifies low power consumption and long battery life for a device. Mathematically, it is given as [26]:

G GG GGGGGGGGGGGGGGGGGGGGGGGGGGGGGGGGGGGGGGGGGGGGGGGGGGGGGGGGGG

We have compared the static power of our proposed device with previously reported GNRFETs. Table 4.6 summarizes the comparison between the proposed devices and the previous devices available in the literature. From Table 4. 6, it can be observed that the A7 device has a very low value of static power (1.58 × 10^{-13} watt) as compared with other devices, which leads to the conclusion that the A7 device is a reliable device to use in low-power applications.

Table 4.6
Comparison table of proposed device configurations with previous devices available in the literature [17]

Device	V_{ds} (V)	Channel AGNR (N)	Bandgap (eV)	I_{on} (A)	I_{off} (A)	*SR*	P_s (W)	Reference
A4 device	0.5	N = 4	1.77	0.664 × 10^{-6}	4.51 × 10^{-10}	1.47 × 10^{3}	2.55 × 10^{-10}	Proposed work
A7 device	0.5	N = 7	1.09	3.86× 10^{-6}	3.16 × 10^{-13}	1.22 × 10^{7}	1.58 × 10^{-13}	Proposed work
SB-GNRFET	0.5	N= 12	-	7.77 × 10^{1}	5.51 × 10^{-1}	141.01	2.77 × 10^{-1}	[27]
MOS-GNRFET	0.5	N= 12	-	7.79 × 10^{1}	2.07 × 10^{-3}	3.76 × 10^{4}	1.035 × 10^{-3}	[27]
Si CMOS (LP)	0.9	-	-	6.67 × 10^{1}	1.40 × 10^{-5}	4.76 × 10^{6}	1.26 × 10^{-5}	[27]
AG-GNRFET	0.5	N = 12	-	-	-	304	-	[28]
DMG-GNRFET	0.6	N = 13	-	-	-	5823	-	[29]
SLD-GNRFET	0.4	N = 12	-	3.66	15.7 × 10^{-10}	2.3 × 10^{3}	6.28 × 10^{-4}	[30]

4.4 SUMMARY

This chapter provides a comprehensive analysis of the reliability and performance of the GS-AGNRFET using EH model with the SCF iteration scheme within the NEGF framework. The present study focuses specifically on AGNRs with N = 4 and 7, both belonging to the semiconducting 3p+1 family of AGNRs. The two proposed device configurations, namely the A4 device and the A7 device, are systematically compared in terms of performance and reliability metrics using the EH model. The band structure and DOS analysis for AGNRs (N = 4, 7) indwqo~s%vo~%vs%ül7%o~ wz"%t%KQX] ±%wv%N %oz.s±%ö~ %%ö%A%s%s~ wqöÅr.q~vÅu% in nature and validate their potential as an alternate channel material in FETs. Furthermore, the semiconducting characteristics of the AGNR are confirmed by the absence of a peak at the Fermi level in the DOS. The EH model demonstrates strong agreement with benchmark DFT methods in both bandgap and T (E) for AGNRs (N = 4 and 7), confirming its reliability over other models for device-level modeling. The DOS and bandgap comparisons validate the EH model as a computationally efficient alternative. Moreover, the obtained bandgap range of 1.09 1.77 eV highlights the potential of AGNRs for optoelectronic and low-power oüüzwqo~vöÅ±%vsÅ2%vs%ttsq~%t%o~Asr%N %n the channel material for the performance of GS-AQX] POb%æ%~r.wr4%vs%qvoÅus%Å%vs%oz.s%t%N %ö~ %%ö%A%~ ü±ö–s±%Sn by 481 times, reduces I_{off} by 99. 92%, improves the SR, reduces V_{th} by 27.59%, and reduces DIBL by 16% in the A7 device as compared to the A4 device. Also, the higher value of DE for the A7 device signifies that the A7 device requires low voltage to achieve significant current modulation and high reliable for low power applications as compared to the A4 device. Moreover, the transport properties, namely DDOS, PLDOS, T(E), TP, and EDD, were studied to analyze the performance of both devices. The PLDOS analysis reveals significantly higher electron state

availability in the A7 device, explaining its lower I_{off}, enhanced switching performance as compared with the A4 device. Further, the transmission spectrum analysis confirms that the A7 device offers superior transport characteristics with more available conduction channels, lower resistance, and higher current output under bias, making it highly suitable for low-power and fast-switching applications. Transmission pathway analysis further confirms that the A7 device has stronger conductance, faster switching, and lower power consumption due to its robust electron tunneling. Additionally, electron difference density analysis shows that the A7 device achieves more effective gate control with reduced electron density variations, leading to improved switching behavior. The comparison of static power with previously reported QX] POb±⁰⁄vwuvzwuv≈±⁰⁄vs⁰⁄KA⁰⁄s–wqs ±⁰⁄t..wopwzw"⁰⁄tö≠⁰⁄zö—-power applications, making it an excellent candidate for use in energy-efficient electronics, biomedical devices, signal amplification, and sensors. Overall, the A7 device emerges as a highly promising and reliable device for advanced electronic applications, combining superior performance with lower power consumption.

The results of **Chapter 3** and **Chapter 4** highlights that the optimal channel width of GS-AGNRFET is model-dependent. In **Chapter 3**, using the non-self-consistent Slater-Koster model, AGNR (N = 4) shows better performance due to its largest bandgap of 1.98 eV which suppresses leakage current most effectively within this framework where bandgap alone governs device behavior. In **Chapter 4**, using the Extended Hückel model with SCF iterations, AGNR (N = 7) shows better performance across all reliability metrics because the self-consistent treatment of the Hartree potential properly captures charge redistribution under applied bias, revealing that the wider ribbon with its first DDOS peak positioned closer to the Fermi level enables more efficient electron injection and superior gate electrostatic control.

Therefore, the two chapters are not contradictory but rather complementary, providing a complete performance understanding of GS-AGNRFET from both bandgap-dominated and charge-transport-dominated computational perspectives. As discussed in **Chapter 2**, the boron-passivated GS-AGNRFET demonstrates significantly improved device performance when the edges of P - AGNR are passivated with boron. However, the study of the remaining Icosagens group elements, namely Al, Ga and In, in the context of GS-AGNRFET edge passivation remains unexplored in the literature. To address this research gap, the performance investigation of all Icosagens group elements using the Extended Hückel model with self-consistent field formalism will be the primary focus of the next chapter.

4.5 REFERENCES

[1] N. Zographos, C. Zechner, I. Martin-Bragado, K. Lee, and Y.-S. Oh, "Multiscale modeling of doping processes in advanced semiconductor devices," *Materials Science in Semiconductor Processing*, vol. 62, pp. 49-61, 2017.

[2] A. Blom and K. Stokbro, "Atomic-Scale Modeling of Nanoscale Devices," *Nanoelectronic Device Applications Handbook*, pp. 867-877, 2017.

[3] K. Stokbro, D. E. Petersen, S. Smidstrup, A. Blom, M. Ipsen, and K. Kaasbjerg, "Semiempirical model for nanoscale device simulations," *Physical Review B Condensed Matter and Materials Physics*, vol. 82, no. 7, pp. 075420, 2010.

[4] S. Smidstrup *et al.*, "QuantumATK: an integrated platform of electronic and atomic-scale modelling tools," *Journal of Physics: Condensed Matter*, vol. 32, no. 1, pp. 015901, 2020.

[5] E. G. Emberly and G. Kirczenow, "Multiterminal molecular wire systems: A self-consistent theory and computer simulations of charging and transport," *Physical Review B*, vol. 62, no. 15, pp. 10451, 2000.

[6] D. Kienle, K. H. Bevan, G. C. Liang, L. Siddiqui, J. I. Cerda, and A. W. Ghosh, "Extended Hückel theory for band structure, chemistry, and transport. II. Silicon," *Journal of applied physics*, vol. 100, no. 4, 2006.

[7] Anshul and R. Chaujar, "Numerical evaluation of the gate stacked GNR FET for improved device switching," i*n Proc. 2022 Int. Conf. Recent Trends Microelectronics,*

Automation, Computing and Communication Systems (ICMACC), IEEE , pp. 88 91, 2022.

[8] Anshul and R. Chaujar, "Investigation Temperature variation on DC and Analog performance of Gate Stack GNRFET using DFT-based atomic scale Modelling," *in Proc. 2025 Devices for Integrated Circuit (DevIC), Kalyani, India, IEEE*, pp. 337-342, 2025.

[9] Anshul and R. Chaujar, "DFT based analysis of Boron and Nitrogen passivation at the edge of Armchair Graphene Nanoribbon for low power applications," *in Proc. 2024 IEEE 19th Int. Conf. Nano/Micro Engineered and Molecular Systems (NEMS), IEEE*, pp. 1-4, 2024.

[10] Anshul and R. Chaujar, "Semi-empirical dft based investigation of electronic and quantum transport properties of novel gs-agnr (n) fet," *IEEE Transactions on Nanotechnology*, vol. 23, pp. 400-407, 2024.

[11] D. A. Papaconstantopoulos and M. J. Mehl, "The Slater Koster tight-binding method: a computationally efficient and accurate approach," *Journal of Physics: Condensed Matter*, vol. 15, no. 10, pp. R413, 2003.

[12] D. Kienle, J. I. Cerda, and A. W. Ghosh, "Extended Hückel theory for band structure, chemistry, and transport. I. Carbon nanotubes," *Journal of applied physics*, vol. 100, no. 4, 2006.

[13] Quantum ATK. team, *QuantumATK T-2022.03 Documentation*, 2022, https://docs.quantumatk.com/manual/manual.html.

[14] M. H. Whangbo and R. Hoffmann, "Counterintuitive orbital mixing," *The Journal of Chemical Physics*, vol. 68, no. 12, pp. 5498-5500, 1978.

[15] J. N. Murrell and A. J. Harget, "Semi-empirical self-consistent-field molecular orbital theory of molecules," *Wiley-Interscience*, 1972.

[16] R. Hoffmann, "An extended Hückel theory. I. hydrocarbons," *The Journal of Chemical Physics*, vol. 39, no. 6, pp. 1397-1412, 1963.

[17] Anshul and R. Chaujar, "Towards Extended Hückel model-based reliability performance enhancement of gate stack graphene nanoribbon field effect transistor," *Microelectronics Reliability*, vol. 173, pp. 115869, 2025.

[18] T. N. Todorov, J. Hoekstra, and A. P. Sutton, "Current-induced forces in atomic-scale conductors," *Philosophical Magazine B*, vol. 80, no. 3, pp. 421-455, 2000.

[19] M. Houmad, O. Dakir, A. Abbassi, A. Benyoussef, A. El Kenz, and H. Ez-Zahraouy, "Optical properties of SiC nanosheet," *Optik*, vol. 127, no. 4, pp. 1867-1870, 2016.

[20] M. Houmad, H. Zaari, A. Benyoussef, A. El Kenz, and H. Ez-Zahraouy, "Optical conductivity enhancement and band gap opening with silicon doped graphene," *Carbon*, vol. 94, pp. 1021-1027, 2015.

[21] C. Azahaf, H. Zaari, A. Abbassi, H. Ez-Zahraouy, and A. Benyoussef, "Theoretical investigation of spontaneous polarization, electronic and optical properties of cubic

perovskite BaHfO3," *Optical and Quantum Electronics*, vol. 47, no. 8, pp. 2889-2897, 2015.

[22] N. Ennassiri, N. Tahiri, O. El Bounagui, H. Ez-Zahraouy, and A. Benyoussef, "Structural, electronic, magnetic, and magnetocaloric properties in metallic antiperovskite compound Mn3GaC," *Materials Research Bulletin*, vol. 98, pp. 335-339, 2018.

[23] S. Dahbi, N. Tahiri, O. El Bounagui, and H. Ez-hov≠oö..."2⁄(Mvozqöus Å± %w ü..≠ws±%Å r % a single F-center in perovskite SrHfO3 compound: Ab initio calculations," *Materials Science in Semiconductor Processing*, vol. 138, pp. 106271, 2022.

[24] A. El Aiboudi, A. Sibari, Z. Mansouri, O. Mounkachi, N. Masaif, and H. Ez-Zahraouy, "Enhanced electrochemical performance of 2D hydrogen boride under strain: A DFT study for lithium-ion batteries," *Physica B: Condensed Matter*, vol. 704, pp. 417041, 2025.

[25] N. Ennassiri, N. Tahiri, O. El Bounagui, H. Ez-Zahraouy, and A. Benyoussef, "Magnetic, magnetocaloric and transport properties in AlCMn3 antiperovskite compound," *Journal of Alloys and Compounds*, vol. 741, pp. 1196-1202, 2018.

[26] K. Brelsford, S. A. P. López, and S. Fernandez-Gomez, "Energy efficient computation: A silicon perspective," *Integration*, vol. 47, no. 1, pp. 1-11, 2014.

[27] M. Gholipour, Y.-Y. Chen, A. Sangai, N. Masoumi, and D. Chen, "Analytical SPICE-compatible model of Schottky-barrier-type GNRFETs with performance analysis," *IEEE Transactions on Very Large Scale Integration (VLSI) Systems*, vol. 24, no. 2, pp. 650-663, 2015.

[28] M. Gholipour, N. Masoumi, Y.-Y. C. Chen, D. Chen, and M. Pourfath, "Asymmetric gate Schottky-barrier graphene nanoribbon FETs for low-power design," *IEEE Transactions on Electron Devices*, vol. 61, no. 12, pp. 4000-4006, 2014.

[29] A. Naderi, "Theoretical analysis of a novel dual gate metal graphene nanoribbon field effect transistor," *Materials Science in Semiconductor Processing*, vol. 31, pp. 223-228, 2015.

[30] H. Sarvari and R. Ghayour, "Design of GNRFET using different doping profiles near the source and drain contacts," *International Journal of Electronics*, vol. 99, no. 5, pp. 673-682, 2012.

5

CHAPTER

Performance enhancement of Gate-Stack Armchair Graphene Nanoribbon FET through Icosagens edge passivation

The Extended Hückel model with self-consistent field iterations is employed in this chapter to investigate the effect of edge passivation by Icosagens elements (B, Al, Ga, and In) in the channel material of GS - AGNRFET.

The passivation of Icosagen group elements at the edge of bulk-configured P AGNR decreases the bandgap, and the density of states analysis confirms that passivated AGNRs provide more accessible states for electrons in the conduction band as compared to P AGNR. It is also observed that the passivation of Al, Ga, and In at the edges of AGNR (N = 7) results in complete bandgap closure (E_g = 0 eV), making it metallic in nature and unsuitable for transistor operation. Therefore, AGNR (N = 4) is selected as the channel material for the present chapter.

The effect of Icosagen group element passivation in the channel material of GS-AGNRFET shows a significant increase in on current ⁻⁴ηβ (B9AG(T(⁶η(BI 9E(T(³γ(Tε AGNRFET, a reduced value of off current ⁻⁴ηβ (B9EK BA (T(⁶η(F9ED BA (T(in the In AGNRFET, and a better value of switching ratio ⁻⁴ηβ (A9HB BA (⁶η(A9DF BA (⁻η⁴(passivated AGNRFETs as compared with P AGNRFET.

The transconductance and device efficiency analysis shows the higher value of g_m and DE in Al AGNRFET and Ga AGNRFET, which signifies stronger electrostatic control and better electron transport. The projected local density of states and transmission pathway analysis further confirms that the possibility of electron tunneling is higher in Al AGNRFET and Ga AGNRFET as compared with other passivated AGNRFETs.

5.1 INTRODUCTION

The findings of previous chapters highlight the effect of width variation and different simulation models reliability. However, simply choosing an appropriate AGNR width is not sufficient to realize a high-performance transistor that can truly overcome the challenges introduced by device scaling. As channel lengths shrink below 10 nm, the transistor performance becomes increasingly sensitive to every atomic detail of the device structure including the chemical state of the ribbon edges [1-3]. At this point, edge passivation becomes an essential and crucial engineering feature for the scaled GNRFETs. The electrical properties of GNRs are largely governed by the particular arrangement of their boundaries, which leads to the formation of edge states and localized electronic states that have a substantial impact on the overall electronic characteristics, such as conductivity, bandgap, and transport characteristics [4]. The carbon atoms at the ribbon boundaries of a fabricated or theoretically modelled AGNR have unoccupied dangling bonds which are chemically reactive and energetically unstable. If these dangling bonds are not passivated, they create localized mid-gap states in the AGNR energy bandgap. This localized mid gap will reduce the effective bandgap and switching performance of the FETs. Therefore, passivation of these edges states is essential to analyze the performance of proposed GNRFET. The type of edge passivating atom and its chemistry are very important in determining exactly how and where electronic changes happen in the AGNR channel [5, 6]. The widely used and thoroughly investigated edge passivation for GNRs is hydrogen, which establishes the traditional baseline configuration. Hydrogen passivation effectively removes dangling bond states, resulting in a pristine semiconducting AGNR (P AGNR). However, P AGNR offers limited control on the bandgap and DOS with variation only in the width of AGNR. To overcome this limit,

researchers used other group elements from the periodic table to enhance the performance of semiconducting AGNRs. The DFT based investigation in the literature has established that edge passivation using elements other than hydrogen can precisely alter the bandgap of AGNRs. Many significant studies have carefully examined edge passivation effects in GNR transistors, as mentioned in the available literature. Gupta et al. [7] conducted first-principles calculations on a Z-shaped double gate graphene FET, revealing that boron and nitrogen doping at the AGNR channel margins substantially alters the bandgap. Their research demonstrated that single nitrogen doping introduces an extra electronic state that overlaps with the Fermi level, suggesting semi-metallic characteristics. While, single B doping creates a dispersive state across the Fermi level owing to charge transfer from carbon to the electron-deficient boron atom. When B and N are co-doped at opposite edges of the channel ribbon, a direct bandgap of 1.84 eV is obtained which is approximately 20% lower than the P - AGNR. This arises from symmetry breaking and charge redistribution at the GNRs boundaries. These results clearly demonstrate that the electronic behavior of the AGNR is highly sensitive to the type, site, and concentration of the passivating atom at the edges. Further, Owlia [8] confirmed through studies on defect-engineered GNR FETs that different passivation types produce opposite channel conductivity behaviors. The study validates that edge passivation type is a critical determinant of the current-voltage characteristics, local density of states, and transmission pathways of the device. Kharwar et al. [9] recently investigated the impact of cadmium passivation on cove-edge GNRs and discovered a distinctive semiconductor-to-metal transition due to the interaction between cadmium atoms and the GNR edges. This led to modifications in the band structure and a notable change in conductance characteristics. The cadmium passivated devices exhibiting negative differential resistance and remarkably high

current ratios [9]. These collective findings from the literature establish a clear and compelling narrative that the choice of passivating atoms at the GNR edge can alter both the electronic structure and the device functionality of GNR-based transistors [7-9]. Also, from **Chapter 2**, boron passivation reduces the bandgap significantly and increases the PDOS near the Fermi [illegible]$_{off}$ and an exceptional ~139 times increase in I_{on} compared to P - AGNRFET. The boron-passivated GS-AGNRFET demonstrates significantly improved device performance when the edges of P - AGNR are passivated with boron [10]. However, the study of the remaining Icosagens group elements namely Al, Ga and In, in the context of GS-AGNRFET edge passivation remains unexplored in the literature. To address this issue the present chapter focuses specifically the study of edge passivation with Icosagens group element (B, Al, GA, and, In) at the edge of bulk configured P AGNR in terms of electronic and transport properties analysis. The subsequent sections of this chapter are organized as follows: Section 5.2 delineates the device design and physical models utilized, Section 5.3 articulates the results accompanied by their analysis and discussion, and Section 5.4 concludes the findings of the study.

5.2 DEVICE DESIGN AND PHYSICAL MODELS

Figure 5.1 shows the schematic representation of the boron-passivated GS - AGNRFET (B AGNRFET). Figure 5.1(a) depicts the 3D visual of the gate stack architecture in the proposed device consisting of a metal gate, $LaAlO_3$ layer, and SiO_2 layer. Figure 5.1 (b) depicts the top view of the proposed device, displaying the source and drain areas coupled via the AGNR (N = 4) channel with boron passivation. The source and drain are of ZGNR (N = 6) type and are doped with n-type dopant at a concentration of 5×10^{18} e/cm^3. The channel of B AGNR (N = : / [illegible]

Anshul

in Figure 5.1 (b). A metal gate is used over the dielectric layers. All the device parameters used for simulation are tabulated in Table 5.1.

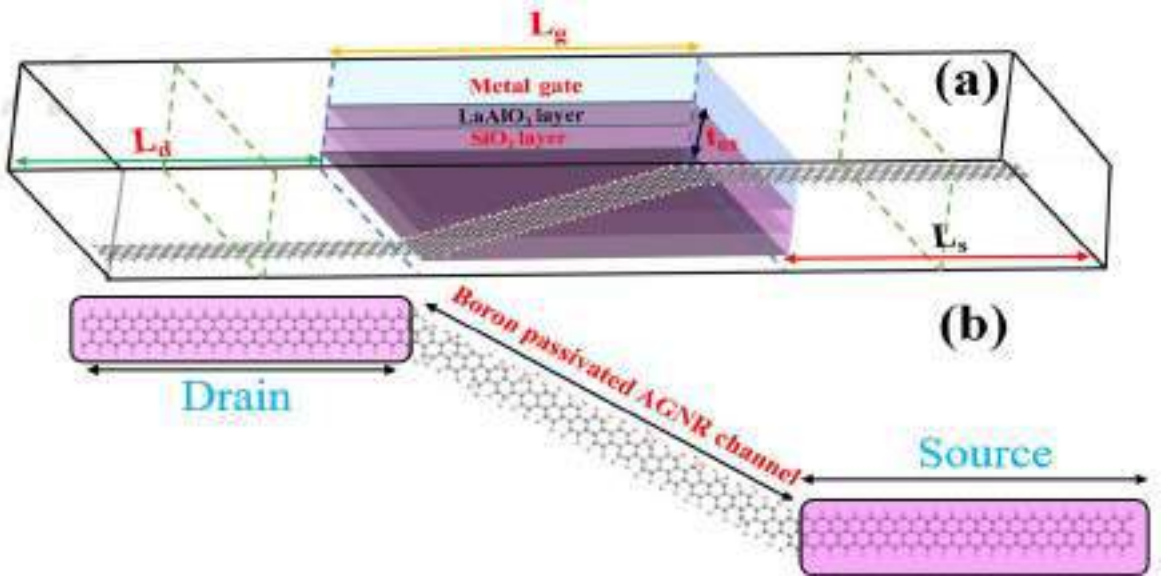

Figure 5.1: Schematic representation of (a) proposed device architecture with Boron passivated channel in 3D visuals, and (b) geometrical structures of drain, source, and channel in the proposed the B AGNRFET device [11]

Table 5.1
Proposed device parameters for the present chapter [11]

Parameters	Symbols	Value	Unit
No. of carbon atoms along AGNR width in the channel	N	4	
No. of carbon atoms along ZGNR width in source and drain	N	6	
Oxide thickness	t_{ox}	1	nm
Gate length	L_g	7	nm
Source length	L_s	5	nm
Drain length	L_d	5	nm

The Quantum ATK tool is used to carry out all the simulations. The tight-binding Hamiltonian matrix approach with the EH model is employed in the semi-empirical calculator. The spectral densities are calculated using the NEGF approach with self-consistent Formalism iteration in

order to prevent the scattering states in the practical computations. The density mesh cut-off value is 40 Hartree (Ha), and the K-point sampling is 100 along the C-direction. All the simulations are carried out at 300 K temperature. The details of EH simulation model is discussed in **Section 4.2** in **Chapter 4**.

5.3 RESULTS AND DISCUSSIONS

5.3.1 Electronic and transport properties analysis of bulk configured Icosagens group passivated AGNRs

Figure 5.2 depicts the comparative analysis of pristine AGNR with Icosagens group passivated AGNRs in terms of atomic structure, bandgap, and density of states. Figure 5.2 (a - e) shows the atomic structure of P AGNR, B AGNR, Al AGNR, Ga AGNR, and In AGNR respectively. Comprehending atomic structure is essential for device fabrication and modeling electronic properties. From Figure 5.2 (a e), we can observe that the passivation of the Icosagen element at the edge of AGNR changes the C C bond length at the ribbon edges by means of varying atomic radii and electronegativities of the Icosagen atoms. Higher atomic radii of heavier Icosagen elements (e.g., Ga, In) cause strain at the edges, which results in a minor buckling action in the lattice, while lighter elements like boron combine more naturally with the carbon structure and show less deformation. The reason is that the strain and buckling effect in heavier Icosagens (Ga, In) occurs due to size mismatch, weaker bonding, and reduced electronegativity, resulting in lattice distortions. Figure 5.2 (a) shows that hydrogen atoms passivate the dangling bonds at the edges of the ribbon with a C H bond length of around 1.09 Å [12-14]. This is significantly shorter than the C C bond length of 1.42 Å within the ribbon. This tightly bonded edge profile makes the ribbon physically stable and symmetrical, with no

distortion out of the plane. From Figure 5.2 (b), in B AGNR, boron atoms replace the hydrogen atoms at the ribbon edges. However, boron combines more naturally with carbon. The reason is that boron has the smallest atomic radius (87 pm) and the closest electronegativity (2.04) to carbon (2.55) among all studied Icosagen elements, which results in a stable and less distorted AGNR structure with a C B bond length of approximately 1.56 Å [12]. From Figure 5.2(c), in Al AGNR, aluminum atoms passivate the ribbon edges with a C Al bond length of approximately 1.97 Å. Due to the larger atomic radius (118 pm) and reduced electronegativity (1.61) of aluminum as compared to boron. The Al AGNR shows moderate edge distortion, which introduces a slight widening of the edge bond angle without significantly disrupting the overall planar geometry of the ribbon. From Figure 5.2(d), the gallium atoms passivate the ribbon edges with a C Ga bond length of approximately 1.96 Å. The larger atomic radius of gallium (136 pm) causes noticeable strain at the ribbon edges, resulting in a minor out-of-plane buckling of the edge atoms [12]. The reason for this buckling is that the larger Ga atom displaces slightly out of the ribbon plane to minimize steric repulsion with the neighboring carbon atoms. However, the symmetric distribution of this buckling along both edges partially compensates its effect, which explains why Ga AGNR retains a near-pristine bandgap of 1.75 eV despite the structural distortion. From Figure 5.2(e), the indium atoms passivate the ribbon edges with a C In bond length of approximately 2.15 Å. Indium has the largest atomic radius (167 pm) and the lowest electronegativity (1.78) among all studied Icosagen elements [12]. The reason is that this large size mismatch introduces the maximum lattice distortion and out-of-üzoÅs%p. qyzwÅu%~%ws%æppöÅ%sr us±2%-vwqv%as–s≠sz”%w≠.ü≈±%ws%qo≠pöÅ%%ås≈–ö≠y%oÅr %w%

responsible for the significant bandgap reduction to 0.93 eV in the In AGNR.

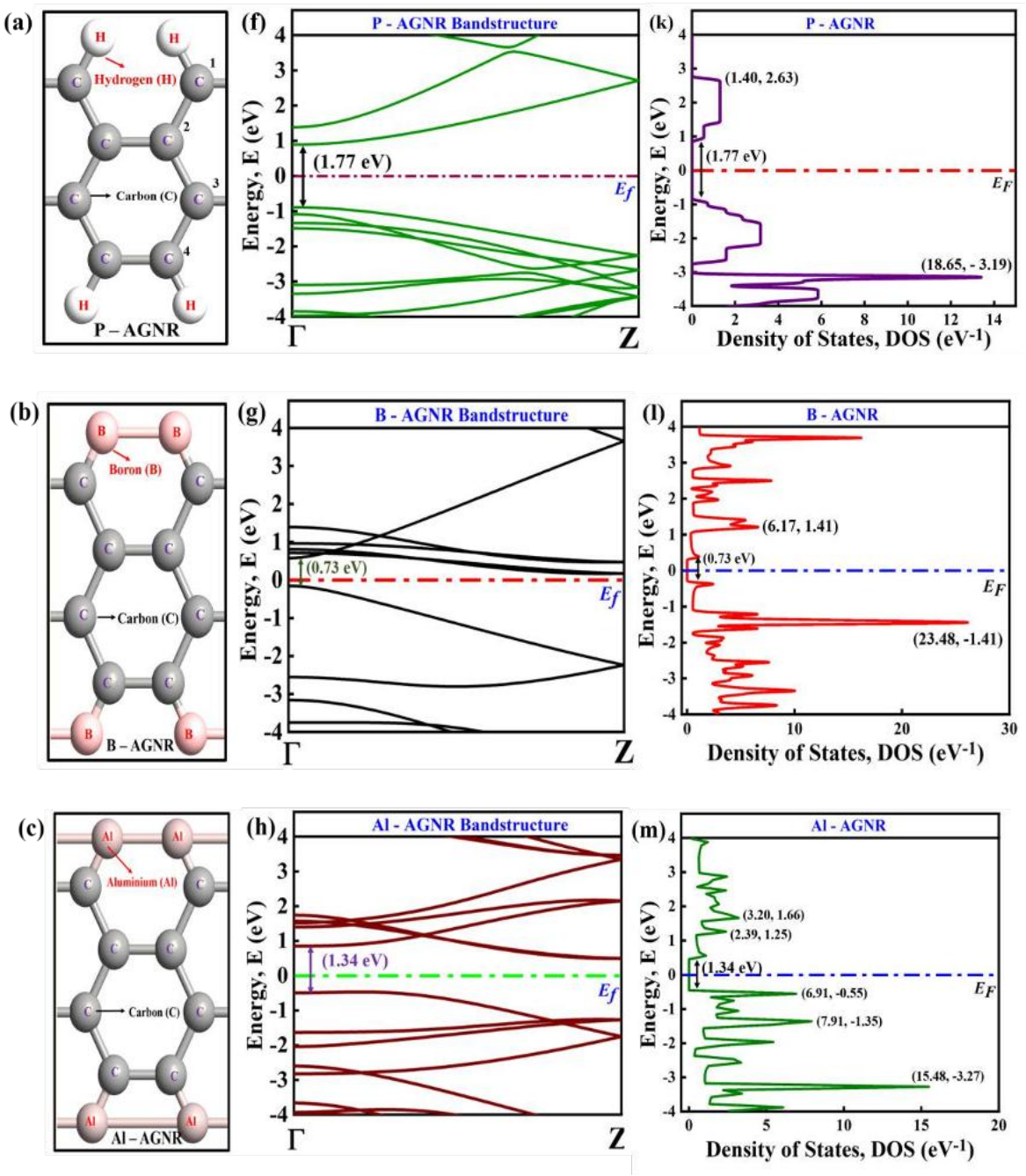

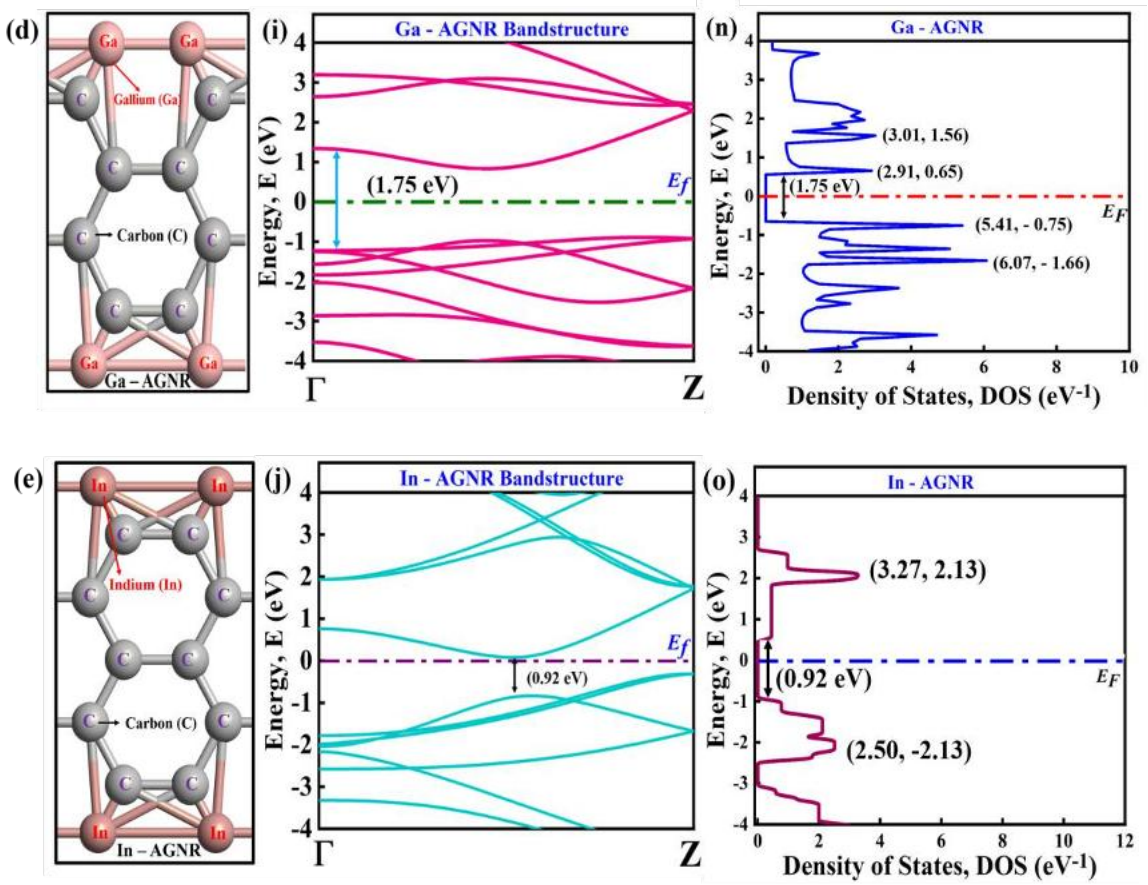

Figure 5.2: (a e) Atomic structure of pristine and Icosagens group passivated AGNRs, (f j) calculated band structure of pristine and passivated AGNRs, and (k o) density of states analysis of pristine and passivated AGNRs [11]

Figure 5.2 (f j) depicts the calculated band structure for all devices. The range of energy that an electron can possess is indicated by the bandgap. Band structures are shown by plotting energy (eV) on the y-axis and high symmetric k-points on the x-axis. The value of bandgaps is 1.77, 0.73, 1.34, 1.75, and 0.93 eV for P -AGNR, B- AGNR, Al AGNR, Ga AGNR, and In AGNR, respectively. From Fig. 5 (f j), we can observe that the bandgap of P AGNR decreased after the passivation of B, Al, Ga, and In at the edges of AGNR. The reason is that the passivation with Icosagen elements weakens the orbital hybridization, adding strain effects and altering the charge distribution. From the bandgap analysis, the authors conclude that the

passivation of Icosagens group elements in P AGNR is semiconducting in nature and also shows non monochromatic trend of bandgap after passivation. From Figure 5.2(g) the bandgap reduces most significantly to 0.73 eV for B - AGNR. The reason is that boron possesses an empty p_z orbital perpendicular to the ribbon plane. This empty p_z orbital actively wÅs≠oq≈±º⁄₀ wv⁰⁄₀s ⁰⁄₀q o≠pöÅ⁰⁄₀ ⁰Ås≈—ö≠y and pulling the conduction band edge closer to the E_F and causing the largest bandgap reduction among all passivated AGNRs. The bandgap Al-AGNR the bandgap is 1.34 eV, which is intermediate between B-AGNR and P-AGNR as depicted in Figure 5.2(h). The reason is that aluminum undergoes sp^2 hybridization with the carbon edge o≈ö~ ±2⁄₀ ör s≠o≈sz'⁰⁄₀s≠≈.≠pwÅu⁰⁄₀ vs ⁰⁄₀ ⁰Ås≈—ö≠y⁰⁄₀ wvö. ≈⁰⁄₀ vs ⁰⁄₀ ≠öÅu⁰⁄₀ p_z interaction like the boron. From Figure 5.2(i), the Ga-AGNR has bandgap of 1.75 eV, which is very close to that of P-KQX] ⁰⁄₀ 74ÅÅ⁰⁄₀ d /4⁰⁄₀ vs ⁰⁄₀ s o±öÅ⁰⁄₀ ±⁰⁄₀ wo⁰⁄₀ ozzw.~ ⁰⁄₀ o±⁰⁄₀ ⁰⁄₀ qö~ üzs≈sz'⁰⁄₀ wzsr ⁰⁄₀ r ⁰⁄₀ vszz⁰⁄₀ 9r /2⁰⁄₀ vwqv⁰⁄₀ ±vwszr ±⁰⁄₀ w±⁰⁄₀ ozsÅqs⁰⁄₀ ü⁰⁄₀ ö≠pwoz±⁰⁄₀ ≠ö~ ⁰⁄₀ sttsq≈wsz'⁰⁄₀ wÅs≠oq≈wÅu⁰⁄₀ wv⁰⁄₀ vs ⁰⁄₀ q o≠pöÅ⁰⁄₀ ⁰Ås≈—ö≠y4⁰⁄₀ Additionally, the structural buckling introduced by Ga at the ribbon edges is symmetric, which ü≠s±s≠ s±⁰⁄₀ vs ⁰⁄₀ qöÅx uo≈wÅ⁰⁄₀ sÅu≈v⁰⁄₀ År ⁰⁄₀ owÅ≈owÅ±⁰⁄₀ ⁰Ås o≠-pristine bandgap. In In-AGNR, the value of bandgap reduces to 0.93 eV as shown in Figure 5.2(j). The reason is that indium has the largest atomic radius among all studied Icosagen elements, which introduces the maximum lattice distortion and strain at the ribbon edges. This severe structural distortion significantly r w≠.ü≈±⁰⁄₀ vs ⁰⁄₀ q o≠pöÅ⁰⁄₀ ⁰Ås≈—ö≠y 2⁰⁄₀ ≠educing the bandgap despite the weak orbital interaction of indium with carbon. From the bandgap analysis, it can be concluded that the reduction in the value of bandgap for passivated AGNRs is not governed simply by atomic size, but by the combined effect of orbital interaction strength, d-shell shielding, and structural distortion at the ribbon edges. Figure 5.2(k o) illustrates the DOS analysis of pristine and Icosagens group passivated AGNRs. The number of states that are accessible for electrons at a particular energy

level defines the DOS [15, 16]. The DOS analysis shows a resemblance to the band structure for all devices, which confirms the consistency of the calculated results. From Figure 5.2 (k), the DOS of P-AGNR shows a clear zero-DOS region around the E_F, confirming its semiconducting nature with a bandgap of 1.77 eV. The sharp Van Hove singularity peaks are observed at (0.54, 1.00 eV) and (1.40, 2.63 eV) in the CB and at (18.65, -3.19 eV) in the VB. These sharp peaks are a characteristic feature of quasi 1D nanostructures, arising from the divergence of DOS at sub band onsets. The absence of any DOS at the Fermi level confirms the semiconducting nature of P-AGNR in the absence of gate modulation. From Figure 5.2(l), B-AGNR exhibits a narrower bandgap and a sharp DOS peak very close to the conduction band edge. The reason is that the empty p_z orbital of boron pulls the CB edge toward the E_F, creating a high density of accessible states for electron conduction. From Figure 5.2(m), the Al-AGNR shows a bandgap of 1.34 eV with two distinct CB peaks at (2.39, 1.25 eV) and (3.20, 1.66 eV), indicating that Al passivation introduces multiple accessible subbands near the CB edge and multiple VB peaks at (6.91, -0.55 eV), (7.91, -1.35 eV), and (15.48, -3.27 eV) These peaks reflecting a rich electronic structure arising from sp^2 hybridization between aluminum and carbon edge atoms, which is directly consistent with the highest I_{on} value of 7B4 %K%ðp±s≠sr%wÅ%aluminium passivated AGNRFET (Al AGNRFET). From Figure 5.2 (n), Ga-AGNR shows a bandgap of 1.75 eV with conduction band peaks at (2.91, 0.65 eV) and (3.01, 1.56 eV) and VB peaks at (5.41, -0.75 eV) and (6.07, -1.66 eV). The reason for the moderate DOS values is that the filled 3d shell of gallium shields its valence 4p orbitals from ±≈≠öÅuz’%Åcs≠oq≈wÅu%≈w%vs%qo≠pöÅ%Åstwork, which limits the introduction of new electronic states. However, the CB peak close to 0.65 eV from the E_F contributes to the high I_{on} of 17.6 K%ðp±s≠sr%wÅ%gallium passivated AGNRFET (Ga-GNRFET). From Figure 5.2(o), the In-

AGNR shows a bandgap of 0.93 eV with a CB peak at (3.27, 2.13 eV) and VB peak at (2.50, -2.13 eV). The symmetric positioning of peaks around the E_F confirms that In passivation shifts the band edges symmetrically due to the significant lattice distortion introduced by the large atomic radius of indium. Overall, from the DOS analysis it can be concluded that the passivation of Icosagens group elements at the edge of AGNR provides more accessible states for electrons in the conduction band as compared to P-AGNR. The Al-AGNR and Ga-AGNR demonstrating the most favorable DOS profiles, which directly contributes to their superior switching performance in the proposed passivated AGNRFETs.

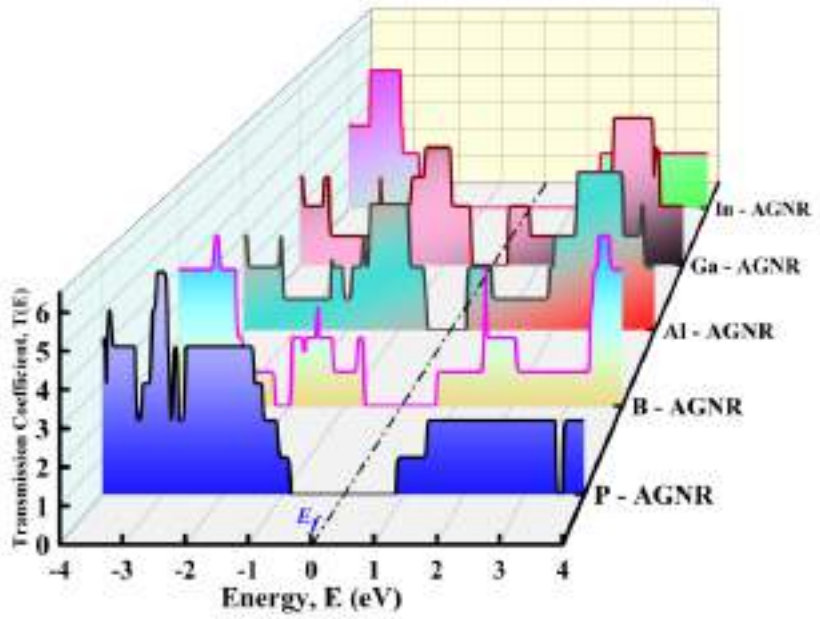

Figure 5.3: 3D visual of transmission spectrum analysis for pristine and passivated AGNRs [11]

Figure 5.3 depicts the 3D visuals of the transmission spectrum analysis for P AGNR and passivated AGNRs. The transmission coefficient represents the probability of electron transmission through the channel at a given energy level. A higher value of T(E) near the Fermi level indicates a greater number of open transmission channels, which directly contributes to

enhanced electron transport. From Figure 5.3, it can be observed that the P AGNR shows a zero T(E) region around the E_F, which is consistent with its semiconducting bandgap of 1.77 eV. The value of T(E) rises to approximately 0.96 just outside the gap region, indicating that electron transmission occurs only through the delocalized band states above the CB minimum. After the passivation of Icosagen elements at the edge of AGNR, the value of T(E) near the Fermi level increases as compared to P AGNR. From Figure 5.3, the B AGNR shows the highest T(E) value of approximately 2.61 among all studied AGNRs, with a sharp rise in transmission very close to the Fermi level. The reason is that the narrowest bandgap of 0.73 eV places the CB edge closest to the Fermi level, making more transmission channels available at lower energies, and also indicates that multiple transmission channels are simultaneously active near the band edge. From Figure 5.3, the value of T(E) is higher in Al AGNR and Ga AGNR as compared to P AGNR and In AGNR in the CB region. The reason is that Al and Ga passivation introduces additional transmission channels through p-orbital hybridization with the carbon edge states, which reduces backscattering at the ribbon edges and enhances the overall transmission probability. In Ga KQX] 2%vs%soy%%pöÅr vÅu%ps≈ ssÅ%vs%p_y orbital of gallium and the p_y orbital of carbon creates an additional parallel transmission pathway, which further enhances T(E) in the conduction band region. From Figure 5.3, In AGNR shows the lowest maximum T(E) of approximately 0.39 among all passivated AGNRs. The reason is that the lattice distortion introduced by the large atomic radius of indium increases the edge scattering, which reduces the transmission probability despite the reduced bandgap of 0.93 eV. This confirms that bandgap reduction alone does not guarantee higher transmission probability. From the TS analysis, it can be concluded that the passivation of Icosagen group elements improves T(E) as compared to P AGNR, with Al AGNR and Ga AGNR shows the most

favorable transmission profiles, which is directly consistent with the superior Ion and switching performance observed in Al GNRFET and Ga GNRFET as discussed in the subsequent sections.

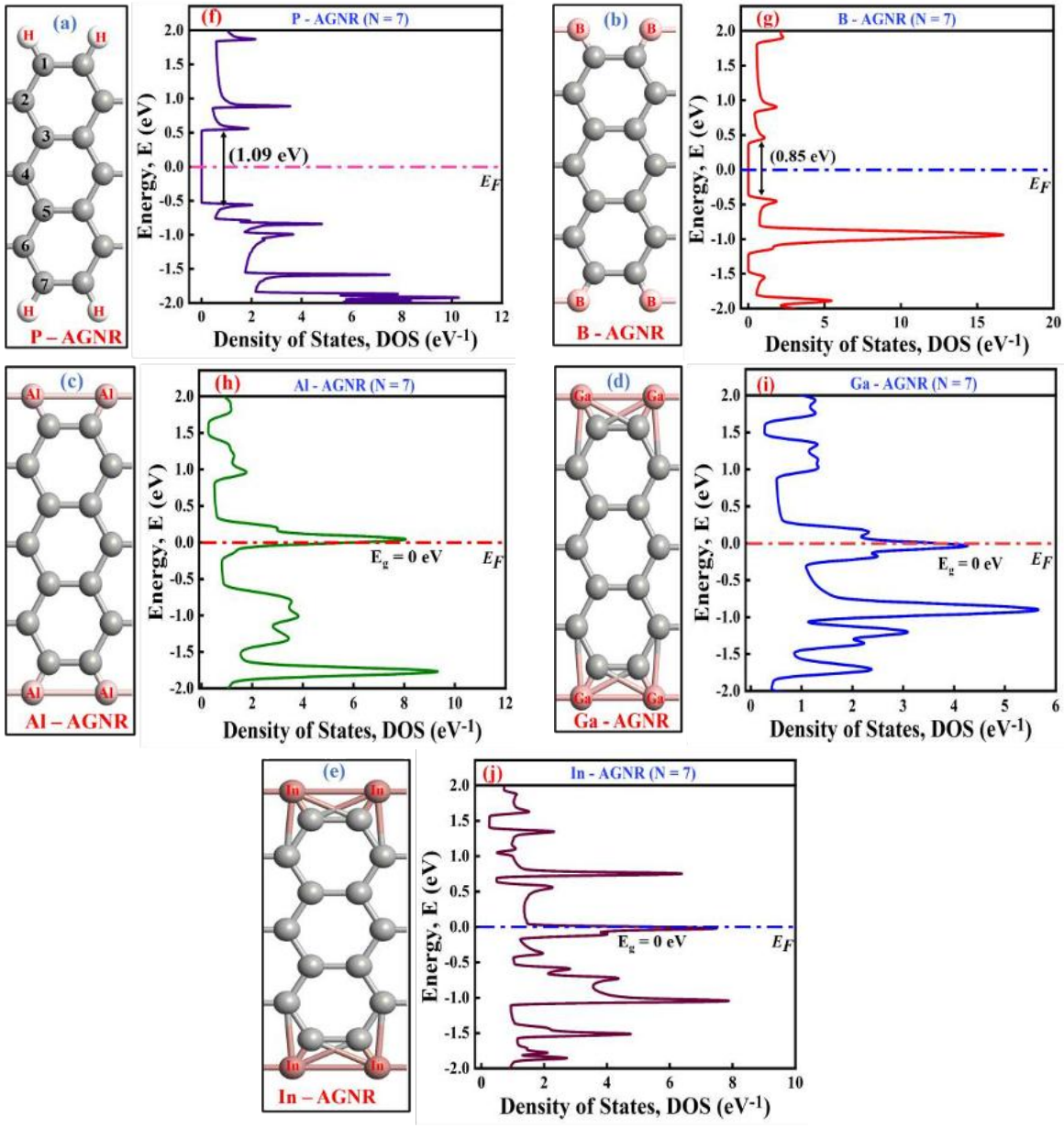

Figure 5.4: (a e) Atomic structure of pristine and Icosagens group passivated AGNRs with N = 7, (f j) calculated DOS of pristine and passivated AGNRs

As discussed in **Chapter 4**, the **A7** device (GS-AGNRFET with AGNR N = 7 as channel material) demonstrates superior performance over the A4 device under the EH-SCF framework. However, it is important to note that the superior performance of AGNR (N = 7) in **Chapter 4** is evaluated for the pristine hydrogen-passivated configuration. In the present chapter, the investigation is extended to examine the effect of Icosagen group element passivation at the edges of AGNR (N = 7), and the results reveal a critical limitation that prevents the use of AGNR (N = 7) as a channel material for Icosagen-passivated GNRFETs.

From the DOS analysis of Icosagen-passivated AGNR (N = 7), as illustrated in Figure 5.4 (f j), it can be observed that the passivation of Al, Ga, and In at the edges of AGNR (N = 7) results in a complete closure of the bandgap, with E_g = 0 eV for Al AGNR (N = 7), Ga AGNR (N = 7), and In AGNR (N = 7). This is confirmed by the presence of DOS peaks at the Fermi level in all the three cases. This indicates that Al, Ga, and In passivation makes AGNR (N = 7) metallic in nature, which completely eliminates the semiconducting behavior required for transistor operation. The reason for this metallic transition is that the P - AGNR (N = 7) has a smaller bandgap of 1.09 eV as compared to P - AGNR (N = 4) (1.77 eV) as shown in Figure 5.4 (f). The smaller bandgap means P AGNR (N = 7) has a weaker quantum confinement and a more fragile semiconducting gap. When heavier Icosagen elements with larger atomic radii (Al = 118 pm, Ga = 136 pm, In = 167 pm) passivate the edges of this wider ribbon, the combined effect of increased lattice distortion, edge strain, and orbital hybridization at the ribbon boundaries is sufficient to completely close the low bandgap and push electronic states into the gap region, resulting in metallic behavior. In contrast, for B AGNR (N = 7), a reduced but finite bandgap of 0.85 eV is retained due to the smaller atomic radius and closer electronegativity of boron to carbon, which introduces less structural distortion as depicted in

Figure 5.4(g). From the above analysis, it can be concluded that although AGNR (N = 7) shows superior device performance in the pristine configuration under the EH model as discussed in **Chapter 4**, the passivation of Icosagen group elements at its edges give rise to the metallic nature for Al, Ga, and In. This metallic nature is unsuitable as a channel material for Icosagen-passivated GNRFETs. Therefore, AGNR (N = 4) is selected as the channel material for the present chapter, as it retains a well-defined semiconducting bandgap across all Icosagen passivation cases, which is the fundamental requirement for AGNRFET operation.

5.3.2 Switching performance and Analog Characteristics of Pristine and Icosagen-Passivated AGNRFETs

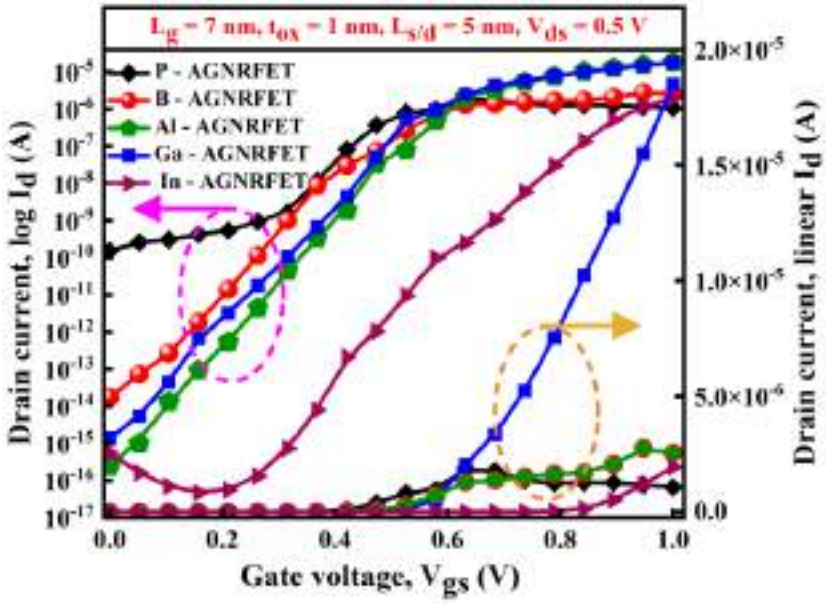

Figure 5.5: I_d V_{gs} characteristics of pristine and passivated AGNRFETs [11]

Figure 5.5 depicts the I_d V_{gs} characteristics of all proposed devices. The left side of Figure 5.5 illustrates the variation in the I_d on a logarithmic scale relative to V_{gs}, whereas the right side of Figure 5.5 presents the linear relationship between I_d and V_{gs}. The logarithmic representation of I_d against V_{gs} illustrates the I_{off} in the device, which is used to calculate the

SR, whereas the linear variation of I_d with V_{gs} determines the I_{on} and V_{th}. From the I_d V_{gs} characteristics, we can observe that the passivation of the Icosagens group improves the I_{on} and decreases the I_{off}. The reason is that the Icosagens group element passivation decreases the bandgap, which facilitates the passage of electrons and holes between energy levels and increases the I_d. Also, the passivation of the Icosagens group element increases the electrostatic control of the gate over the channel, allowing for a more efficient transition from OFF to ON states. From the I_d V_{gs} characteristics, we have calculated the important performance parameters for proposed devices, including I_{on}, I_{off}, SR, and V_{th}. The variation in I_{on}, I_{off}, SR, and V_{th} parameters is illustrated in Figure 5.6 using a spider chart.

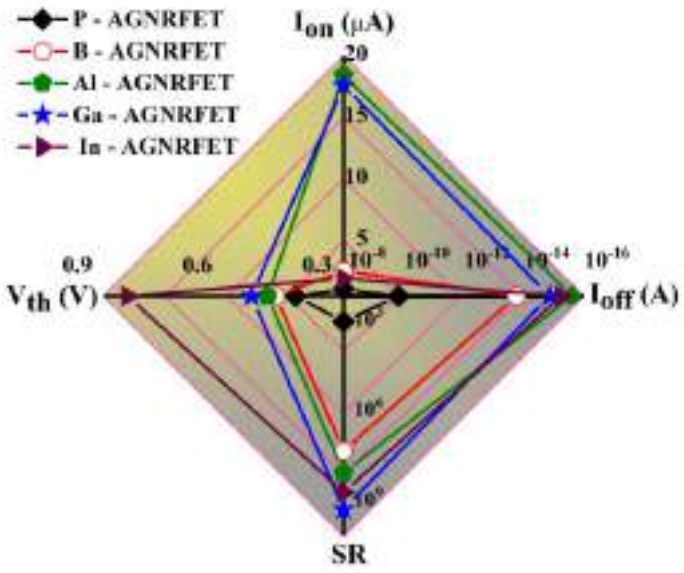

Figure 5.6: Comparative spider chart analysis of P AGNRFET and passivated GNRFETs. This chart depicts important performance parameters for devices, including I_{on}, I_{off}, SR, and V_{th} [11]

From Figure 5.6, it can be observed that the value of I_{on} is higher in the Al AGNRFET and Ga AGNRFET as compared with others. The higher value of I_{on} is 18.4 and 17.6 μA for Al AGNRFET and Ga AGNRFET, respectively, as compared with other device configurations. Also, the value of I_{off} reduced from 10-^{10} A to 10^{-15} A and 10^{-16} A for Al

AGNRFET, Ga AGNRFET, and indium passivated GS AGNRFET (In AGNRFET) as compared with P - AGNRFET. The improved value of I_{on} and reduced value of I_{off} provide a significant increase in SR. The switching ratio is a crucial transistor performance metric that shows how well a device can transition between its ON and OFF states. The higher value of SR indicates that the transistor can distinguish between ON and OFF states, which reduces I_{off} and increases energy efficiency [17]. A lower value of SR shows a weaker state distinction, which leads to increased I_{off} and poor switching performance [18]. A higher value of SR is observed in passivated AGNRFETs than in P AGNRFET. From Figure 5.6, we can observe that the Al AGNRFET, Ga AGNRFET, and In AGNRFET show higher values of SR as compared with P AGNRFET. The reason for the higher value of SR is that the presence of these dopants (Al, Ga, In) alters the electronic band structure of the AGNRFET. A key factor in transistor performance is the V_{th}, which defines the lowest value of V_{gs} needed to turn on the device. The higher value of V_{th} signifies the device requires more voltage to go ON, leading to reduced leakage current but slower operation. On the other hand, faster switching is made possible by a lower value of V_{th}, but power efficiency may suffer due to increased I_{off}. From Figure 5.6, it is observed that the value of V_{th} is higher in In GNRFET with a value of 0.84 V as compared with other passivated AGNRFETs. From the spider chart, it is observed that the Al AGNRFET and Ga AGNRFET show improved results in terms of I_{on}, I_{off}, SR, and V_{th}, while In AGNRFET shows improved results in terms of I_{off} and SR.

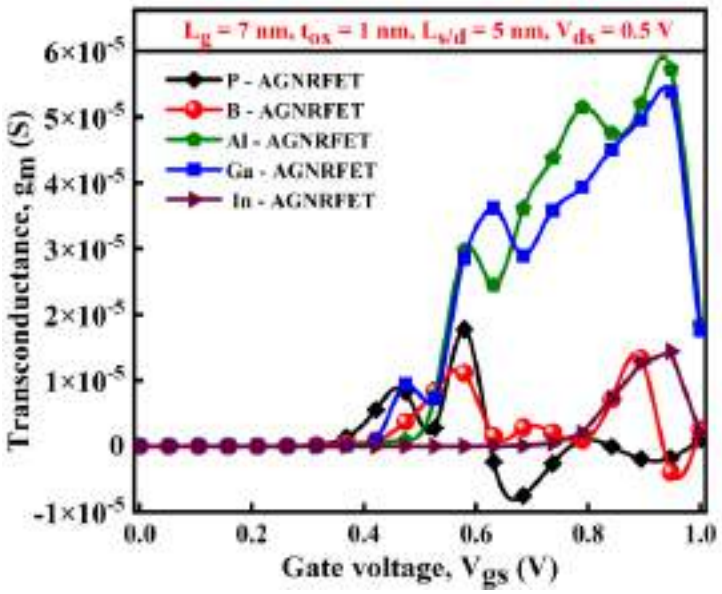

Figure 5.7: g_m versus V_{gs} analysis of AGNRFETs [11]

Figure 5.7 depicts the transconductance (g_m) as a function of V_{gs} for all device configurations. Transconductance defines the device's capacity to amplify signals and react to gate voltage changes. The higher value of g_m indicates better gate control over the channel, leading to enhanced current modulation and device efficiency [19, 20]. Further, g_m is derived from the derivative of the I_d-V_{gs} curve. From Figure 5.7, it can be observed that Al AGNRFET and Ga AGNRFET exhibit the highest transconductance values, particularly in the 0.6 1.0 V range of V_{gs}, suggesting that these devices have superior carrier transport characteristics and stronger electrostatic control. This is because Al passivation adds several available conduction band subbands near to the Fermi level, which is verified by the two unique DOS peaks at (2.39, 1.25 eV) and (3.20, 1.66 eV) in the DOS study of Al AGNR. This increases the rate of change of the drain current with the gate voltage which leads to a greater value of g_m. In Ga-AQX] POb 2⁄4vs%-soy%%pöÅr wÅu%ps≈-ssÅ⁰⁄4vs%ũ$_y$ orbital of gallium and p_y orbital of carbon opens an extra parallel conduction path at the borders of the ribbon. This lowers edge scattering

and increases the number of open transmission channels. It can be observed from the gm analysis that Al AGNRFET and Ga AGNRFET exhibit better carrier transport properties and electrostatic control than other device topologies. These results are in direct agreement with the higher I_{on} –oz.s±%t%B4 %K%År %A4>%K%År %ws%ps≈s≠%oÅ±~ w±wÅ%üsq≠.~ %s±.z±% reported in Al AGNRFET and Ga AGNRFET respectively, as discussed in the preceding section 5.3.3.

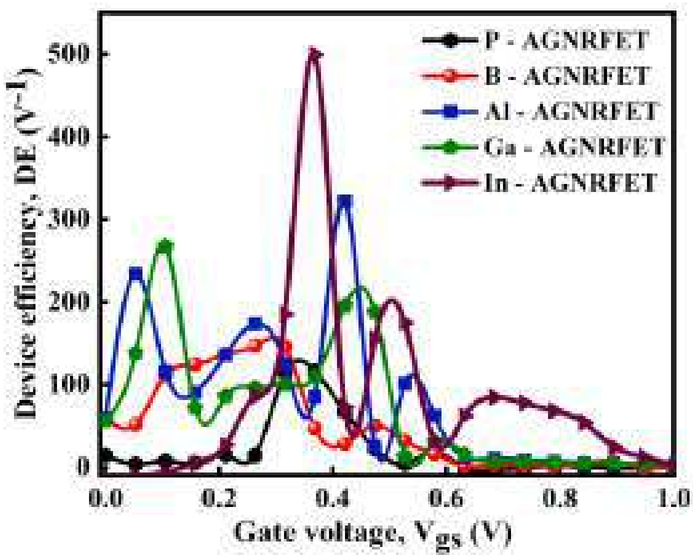

Figure 5.8: Device efficiency analysis of P AGNRFET and passivated AGNRFETs [11]

Figure 5.8 shows the device efficiency analysis of P AGNRFET and passivated AGNRFETs. DE is a critical parameter that assesses the efficacy with which a transistor transforms V_{gs} modulation into I_d, reflecting the device's performance regarding energy efficiency [19]. From Figure 5.8, it can be observed that the In AGNRFET exhibits the highest peak value of DE at a lower gate voltage (~0.4 V). However, it is important to note that the high value of DE value at low V_{gs} does not indicate that the In AGNRFET switches ON at a lower gate voltage. From the spider chart analysis discussed in the Figure 5.6, the value of V_{th} voltage of In GNRFET is 0.84 V, which is the highest among all passivated AGNRFETs. This higher value

of V_{th} in the In AGNRFET requires the highest gate voltage to turn ON as compared to other device configurations. The reason for the apparent high DE at ~0.4 V is that DE is mathematically expressed as DE = g_m/I_d, and in the subthreshold region where the value of I_d is exponentially small, even a small value of g_m produces a large g_m/I_d ratio, which results increase in the high DE value at low V_{gs}. This behavior is a well-known characteristic of the DE metric in the subthreshold regime and does not reflect the genuine energy efficiency of the device in its ON state. Further, P AGNRFET shows the lowest value of DE among all device configurations. The reason is that P AGNR has the largest bandgap of 1.77 eV, which requires a higher gate voltage before significant drain current flows, resulting in a slower I_d V_{gs} transition and therefore a lower g_m/I_d ratio across the entire V_{gs} range. The Al AGNRFET and Ga AGNRFET shows slightly lower peak of DE as compared to In AGNRFET. Also, Al AGNRFET and Ga- AGNRFET shows high value of DE from 0.6 1.0 V of V_{gs}.

5.3.3 Quantum Transport Properties Analysis of AGNRFETs: Transmission Spectrum, PLDOS, and Transmission Pathways under applied Bias

As discussed earlier, we have observed that Al AGNRFET and Ga AGNRFET show improved results. In this section, we have examined the quantum transport properties analysis for the proposed devices. These analyses provide crucial insight into device performance. Figure 5.9 depicts the transmission spectrum analysis for all proposed devices at V_{ds} = 0 V and 0.5 V. The T(E) represents the probability of electron transmission through the channel at a given energy level. A higher value of T(E) near the Fermi level indicates a greater number of open transmission channels, which directly contributes to enhanced electron transport. The transmission spectra shown in Figure 5.9 are based on a device-level configuration using a

finite-length AGNR channel and ZGNR electrodes. The observed transmission spectrum is larger than the bulk configured AGNRs due to contact effects, gate modulation, and applied bias, as modeled using the NEGF formalism.

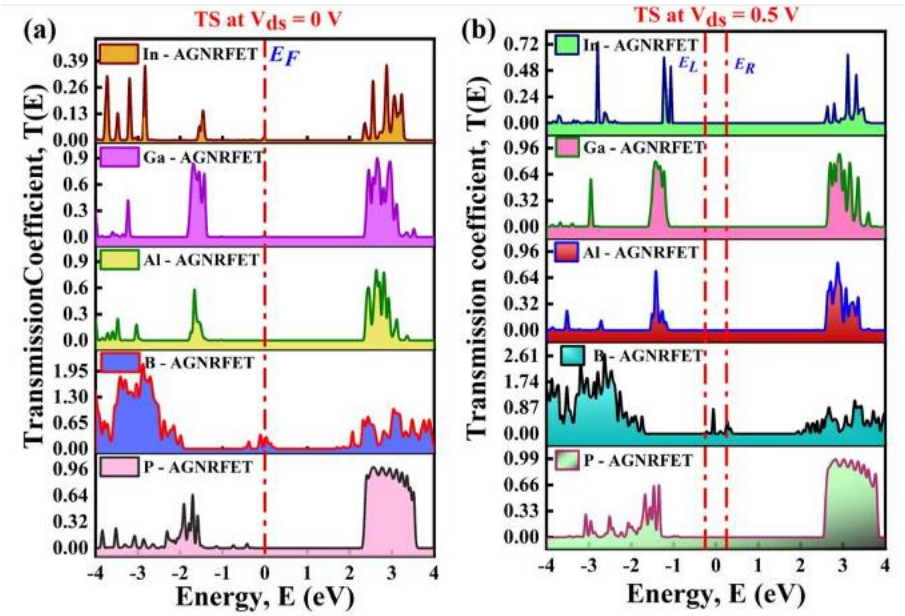

Figure 5.9: Transmission spectrum analysis for all proposed devices at (a) V_{ds} = 0 V and (b) V_{ds} = 0.5 V [11]

From Figure 5.9(a), it can be observed that all proposed devices show zero value of T(E) on the Fermi level for V_{ds} = 0 V. However, a distinction is observed in the proximity of transmission peaks to the Fermi level among different device configurations. In P AGNRFET, Al AGNRFET, and Ga AGNRFET, the first transmission peak appears further away from the Fermi level. The reason is that these devices have larger bandgaps of 1.77, 1.34, and 1.75 eV respectively, which place the conduction band edge further from the Fermi level, resulting in a wider zero T(E) region around E_F. In B AGNRFET and In AGNRFET, the first transmission peak appears very close to the Fermi level. The reason is that the narrower bandgaps of 0.73 eV and 0.93 eV respectively place the conduction band edge in much closer proximity to the Fermi level, so transmission channels become available at lower energies

above E_F as compared to other device configurations. This closer proximity of transmission peaks to E_F in B AGNRFET and In AGNRFET indicates that these devices require less energy to activate transmission channels, which is directly consistent with their lower bandgap values observed in the band structure analysis. When the V_{ds} is varied from 0 to 0.5 V, there is a shift in E_F corresponding to the left and right electrodes, denoted as E_L and E_R respectively. From Figure 5.9(b), it can be observed that there is no transmission peak available for Al AGNRFET, Ga AGNRFET, and In AGNRFET in the range of E_L and E_R at V_{ds} = 0.5 V. The reason is that the applied bias window falls within the bandgap region of these devices, confirming that current conduction is governed by band-edge transmission channels just outside this window rather than mid-gap states. Also, the value of T(E) and the number of transmission peaks are higher in the CB in Al AGNRFET, Ga AGNRFET, and In AGNRFET as compared to P AGNRFET. The reason is that the passivation of heavier Icosagen elements introduces additional transmission channels through p-orbital hybridization with the carbon edge states, which reduces backscattering at the ribbon edges and increases the number of open transmission channels in the conduction band. From the TS analysis, it can be concluded that the passivation of AGNR with Al, Ga, and In improves the transmission probability as compared to P AGNRFET.

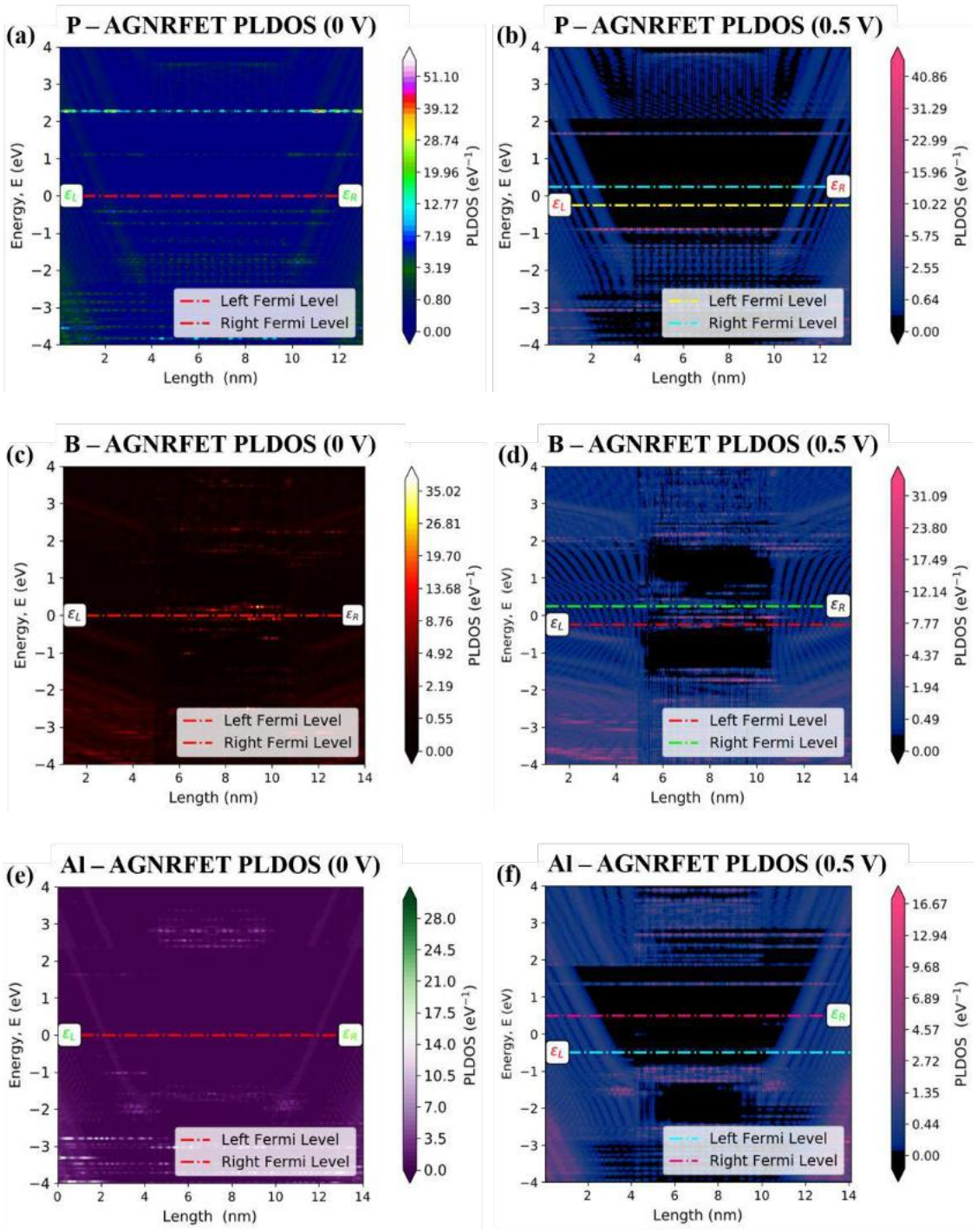
(a) P – AGNRFET PLDOS (0 V)
(b) P – AGNRFET PLDOS (0.5 V)
(c) B – AGNRFET PLDOS (0 V)
(d) B – AGNRFET PLDOS (0.5 V)
(e) Al – AGNRFET PLDOS (0 V)
(f) Al – AGNRFET PLDOS (0.5 V)
Energy, E (eV)
Length (nm)
PLDOS (eV⁻¹)
Left Fermi Level
Right Fermi Level

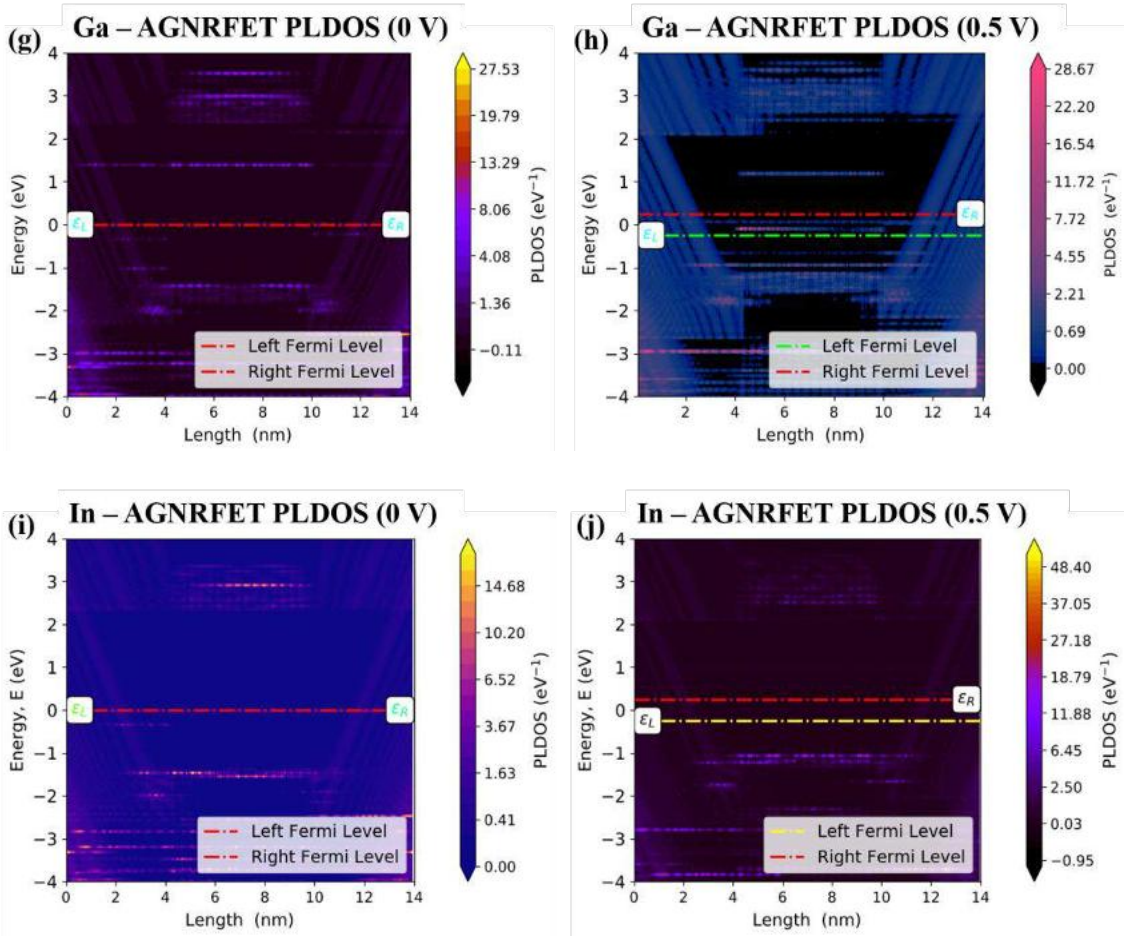

Figure 5.10: Projected density of states analysis at V_{ds} = 0 and 0.5 V for (a, b) P - AGNRFET, (c, d) B AGNRFET, (e, f) Al AGNRFET, (g, h) Ga AGNRFET, and (i, j) In AGNRFET [11]

Figure 5.10 shows the contour plot of the PLDOS at V_{ds} = 0 and 0.5 V. The contour plot of PLDOS at varied V_{ds} provides crucial insights into the transport properties of proposed devices. The PLDOS is generally depicted as a function of energy and position within the GNR. PLDOS is used to illustrate the contribution of various orbitals to the density of states. Each contour line in Figure 5.10 represents a distinct energy level, whereas the intensity or color gradient of the contour lines indicates the density of electronic states at that energy level. From Figure 5.10(a), we can observe that at V_{ds} = 0 V, P AGNRFET shows a uniform distribution of PLDOS in a single color (blue color), indicating minimal perturbation in the energy levels and

a balanced system. Also, the E_L and E_R are aligned on the same level at 0 eV. Further, when the V_{ds} are varied from 0 to 0.5 V, there is a shift in E_L and E_R, which evident the redistribution of electric charge as illustrated in Figure 5.10(b). The shift in E_L and E_R at V_{ds} = 0.5 V is equal for all device configurations as it is determined solely by the applied drain voltage Moreover, the contour plot of PLDOS in Figure 5.10(b) reveals a bandgap region with disrupted states, suggesting potential barrier formation and charge redistribution. Similarly, from Figure 5.10 (c), (e), (g), and (i), we can observe that at V_{ds} = 0 V, all passivated device configuration shows a uniform distribution of PLDOS, which evidences minimal perturbation in energy levels. From Figure 5.10(d), we can observe that the passivation of boron in the channel of AGNRFET provides more available states near E_L and E_R. The shift in E_L and E_R is higher in Al AGNRFET (- 0.5 eV and + 0.5 eV, respectively), as observed in Figure 5.10(f). the reason is that the stronger gate coupling arising from sp^2 hybridization between aluminum and carbon edge atoms. This shift makes it evident that the redistribution of electric charge is higher in Al - AGNRFET. Moreover, in Figure 5.10 (h) and (j), it can be observed that the In AGNRFET has uniform PLDOS distribution, while in Ga AGNRFET, the contour plot of PLDOS reveals potential barrier formation. From Figure 5.10, it has been observed that the contour plot of PLDOS explains the basis of device performance at different varied V_{ds}.

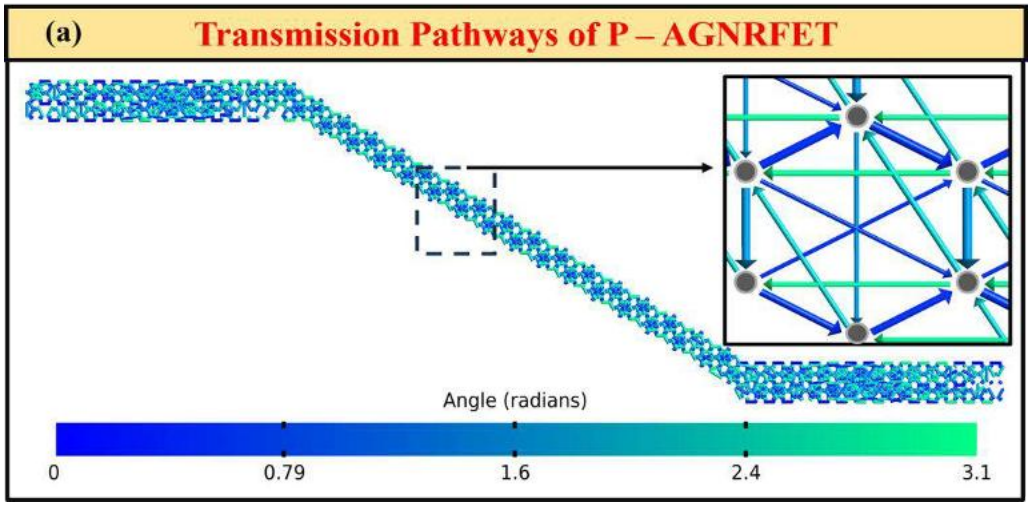

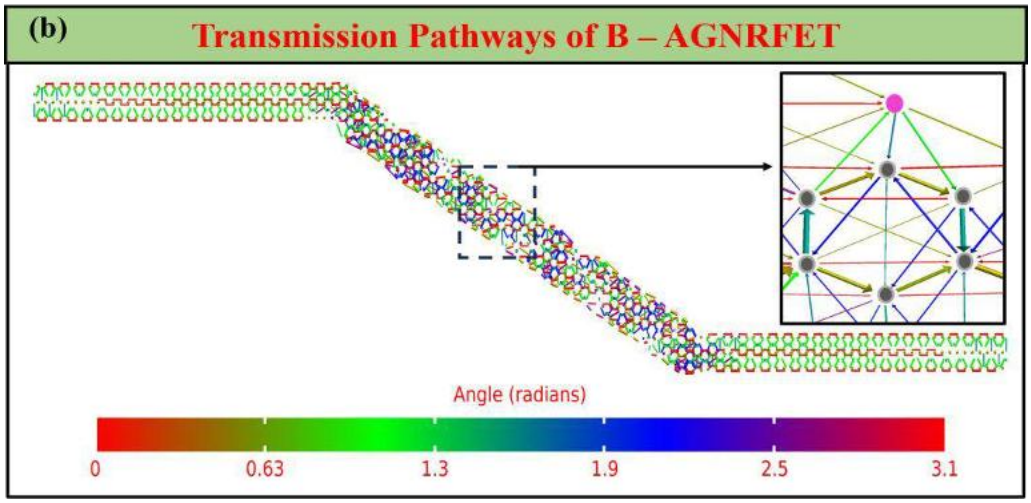

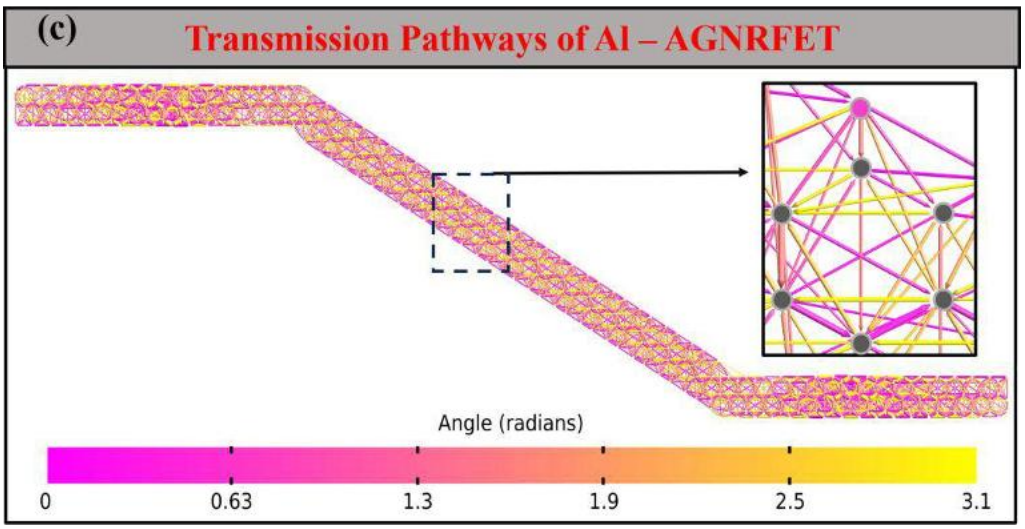

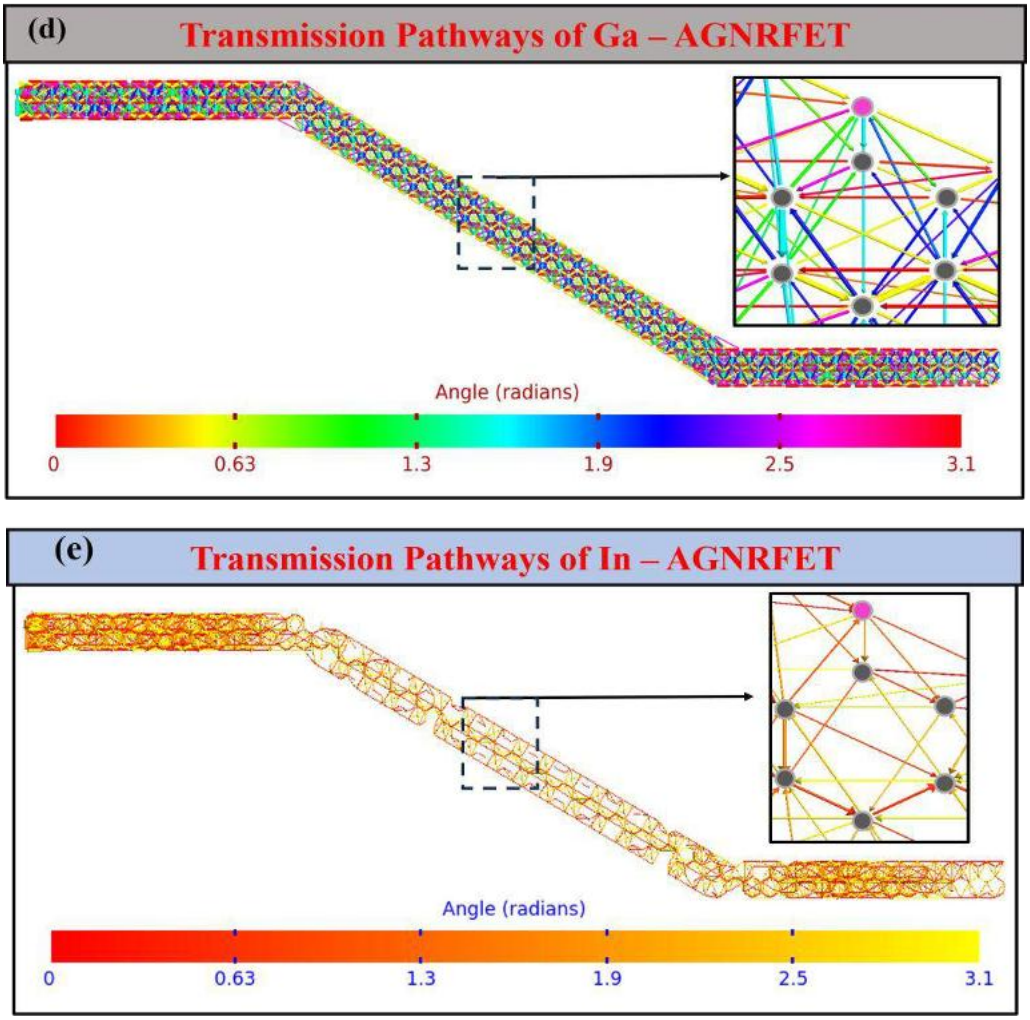

Figure 5.11: Transmission pathways analysis of (a) P AGNRFET, (b) B AGNRFET, (c) Al AGNRFET, (d) Ga AGNRFET, and (e) In AGNRFET [11]

Transmission Pathways is an analysis that divides the transmission coefficient into local bond contributions, Tij. The TP is correlated with the possibility of an electron tunneling from the source electrode to the drain electrode in the GNRFET device. Also, TP analysis is a crucial parameter that offers information about the conductance, optimization, and quantum mechanical effects of the device. In TP analysis, arrows are frequently employed to indicate the direction of electron transmission. The volume of the arrow represents the magnitude of

the TP, while the color indicates the direction of TP as illustrated in Figure 5.11. In the Figure 5.11(a), for the P AGNRFET device, the blue color shows the right direction of electron transmission while the green color shows the left direction of electron transmission. The inset view of Figure 5.11(a) shows that the volume of the blue and green color arrow is thinner, which indicates that the magnitude of TP is lower in P AGNRFET. From Figure 5.11 (b - e), it can observe that the passivation of Icosagens group elements increases the volume of TP arrows, which evident that the possibility of electron tunneling from source to drain is higher in passivated AGNR channel devices. Further, From Figure 5.11(c) and (d), it can be observed that Al AGNRFET and Ga AGNRFET show higher TP, indicating stronger conductance, faster switching, and lower power consumption. The reason is that Al and Ga passivation provides an optimal balance between bandgap reduction and structural integrity at the ribbon edges which is sufficient to open additional transmission channels without introducing excessive backscattering. In contrast, the In AGNRFET shows lower magnitude of TP despite its reduced bandgap, because the maximum lattice distortion introduced by indium's large atomic radius increases edge scattering and reduces the net electron tunneling probability from source to drain.

5.3.4 Comparative performance summary of all proposed GS-AGNRFET configurations in this thesis work

Table 5.2 presents the comparative performance summary of all proposed GS-AGNRFET configurations studied across **Chapters 2 to 5** in terms of L_g, t_{ox}, AGNR channel material (N), edge passivation atom, on-current, off-current, and switching ratio.

Table 5.2
Comparative Performance Summary of All Proposed GS-AGNRFET Configurations in this thesis work (Chapter 2 5)

Proposed Devices	L_g (nm)	t_{ox} (nm)	AGNR Channel Material (N)	Edge Passivating Atom	I_{on}	I_{off}	SR
P AGNRFET (Ch.2)	5	1	N = 4	Hydrogen	1.02 K	749> 76 % A	~5×10²
B AGNRFET (Ch.2)	5	1	N = 4	Boron	2. 54 K	74A= 76 % A	−=48: 76
N AGNRFET (Ch. 2)	5	1	N = 4	Nitrogen	8.37 K	9.13× 10^{-13}	9.16 × 10^{6}
GS-AGNR (N=4) FET (Ch.3)	5	1	N = 4	Hydrogen	9.14 K	74A= 76 ^{9}A	5.22×10³
GS-AGNR (N = 7) FET (Ch.3)	5	1	N = 7	Hydrogen	0.11 K	648C=%K	37
GS-AGNR (N = 10) FET (Ch.3)	5	1	N = 10	Hydrogen	0.12 K	849: %K	4.8
GS-AGNR (N = 13) FET N=13 (Ch.3)	5	1	N = 13	Hydrogen	0.21 K	=4 8%K	3.9
A4 Device (Ch.4)	5	1	N = 4	Hydrogen	0.66 K	: 4=7 76 % A	1.47×10³
A7 Device (Ch.4)	5	1	N = 7	Hydrogen	3.86 K	947> 76 % A	748 8 76

Proposed Devices	L_g (nm)	t_{ox} (nm)	AGNR Channel Material (N)	Edge Passivating Atom	I_{on}	I_{off}	SR
P AGNRFET (Ch.5)	7	1	N = 4	Hydrogen	1.06 K	1.49 × 76 % A	0.71×10^4
B AGNRFET (Ch.5)	7	1	N = 4	Boron	2.54 K	1.74 ×16 % A	1.45×10^8
Al AGNRFET (Ch.5)	7	1	N = 4	Aluminium	18.4 K	2.37×10^{-16} A	0.77×10^9
Ga AGNRFET (Ch.5)	7	1	N = 4	Gallium	17.6 K	1.36 ×76 % A	1.29×10^{10}
In AGNRFET (Ch.5)	7	1	N = 4	Indium	1.93 K	5.43 × 76 % A	0.35×10^{10}

The proposed device configurations are systematically compared to highlight the progressive improvement in device performance achieved through channel width engineering, variation in simulation model, and edge passivation optimization across the different chapters. From the comparison table 5.2, the most significant performance improvement is observed in the present chapter with Icosagen group element passivation. Among all proposed device configurations across **Chapters 2 to 5**, the Al AGNRFET demonstrates the highest value of I_{on} öt%B4 %K‰zöÅu%-w%‰uÅwqoÅ~z”%sr . qsr %$_{off}$ of 2.37×10 A and a SR of 0.77×10 Also, the Ga AGNRFET closely follows with an I_{on} öt%A4>%K2%$_{off}$ öt%49> 76 %K2‰Ar%] %öt% 748C 76 4‰vs%Å AGNRFET shows the lowest value of I_{off} öt%4 9 76 %K‰ut the value of

I_{on} is öt%4C9%K is relatively lower than Al AGNRFET and Ga AGNRFET. The reason for the superior performance of Icosagen-passivated devices is that the edge passivation with Group 13 elements decreases the bandgap, increases the electrostatic control of the gate over the channel, and introduces additional conduction-band sub bands near the Fermi level, which collectively improve the current switching performance of the proposed GS-AGNRFET. However, from the overall comparison of all proposed devices across **Chapters 2 to 5**, the Al AGNRFET emerges as the most balanced and promising device configuration in terms of the I_{on}, I_{off}, SR, transconductance and improved quantum transport properties. The improved findings of Al AGNRFET makes it a suitable choice to use as a toxic gas sensor. The reason is that a gas sensor requires a high value of I_{on}, a very low value of I_{off}, and a higher value of SR to ensure a large baseline current, a stable OFF-state, and a clear distinction between the ON and OFF states before and after gas molecule adsorption, which directly determines the sensitivity of the sensor. Further, the Al AGNRFET is used as a toxic gas sensor to extend this work as an application of gas sensor in the **Chapter 6.**

5.4 SUMMARY

163

In this chapter, the EH model with SCF iterations is employed to investigate the effect of edge passivation by Icosagens elements in the channel material of GS -AGNRFET. The passivation of Icosagens elements at the edge of bulk configured P AGNR significantly enhances electronic and transport properties. This includes a decrease in bandgap and improved DOS analysis that confirms the passivated AGNRs provide more accessible states for electrons in the CB and VB. Additionally, transmission spectrum analysis demonstrated that Al, Ga, and

In passivated GNRFETs have higher electron tunneling probability, further enhancing device performance. Also, the effect of Icosagens is analyzed in terms of bandgap and DOS on the AGNR (N = 7). The results states that the passivation with the heavier Icosagens elements like Al, Ga, and In makes AGNR (N = 7) metallic in nature which constraints its use in semiconducting applications. Further, the effect of Icosagens group element passivation in the channel material of the GS - AGNRFET with AGNR (N = 4) shows significantly increase in I_{on} (from 1.06 µA to 18.4 µA in Al AGNRFET), reduced I_{off} (from 1.49×10^{-10} A to 5.43×10^{-16} A in In AGNRFET), and better value of SR (from 0.71×10^{4} to 0.35×10^{10}) for passivated AGNRFETs as compared with P AGNRFET. The analysis of transconductance and device efficiency shows the higher value of gm and DE in passivation with heavier Icosagens group elements (Al, Ga), which signifies that Al AGNRFET and Ga AGNRFET have stronger electrostatic control and better electron transport. The quantum transport properties analysis in terms of TS and PLDOS at varied V_{ds} provides a unique idea for analyzing device performance. Further, the PLDOS contour plot analysis confirms that passivation of heavier Icosagens group elements shows better performance. Additionally, in transmission pathways, the magnitude of the arrow in heavier Icosagens group elements (Al, Ga) evidence that the possibility of electron tunneling from source to drain is higher. Owing to fast switching, low Ioff, and improved parameters like gm, DE, PLDOS, TP, and TS, Al GNRFET and Ga GNRFET are suitable candidates for high speed logic, low power memory devices, quantum computing in space exploration, and neuromorphic computing applications. These findings are likely to encourage industry experts to design electronic appliances for various applications ranging from space exploration to defense applications.

Additionally, on comparing all proposed devices from **Chapter 2 to 5**, the Al AGNRFET shows improved results in terms of I_{on}, I_{off} in Al AGNRFET And SR. Following a comprehensive analysis of all proposed device configurations, it is necessary to address the gas sensing application using the Al AGNRFET device. Therefore, to investigate the gas sensor application suitability, the present work will be extended to develop a toxic gas sensor, which will be the primary focus of the next chapter.

5.5 REFERENCES

[1] P. Kher *et al.*, "First-principles quantum transport investigation of Fe-functionalized phosphorene for high-sensitivity NO2 detection," *Next Materials*, vol. 12, pp. 102064, 2026.

[2] K. Stokbro, D. E. Petersen, S. Smidstrup, A. Blom, M. Ipsen, and K. Kaasbjerg, "Semiempirical model for nanoscale device simulations," *Physical Review B*, vol. 82, no. 7, pp. 075420, 2010.

[3] Anshul and R. Chaujar, "Towards Extended Hückel model-based reliability performance enhancement of gate stack graphene nanoribbon field effect transistor," *Microelectronics Reliability*, vol. 173, pp. 115869, 2025.

[4] T. Radsar, H. Khalesi, V. Ghods, and A. Izadbakhsh, "Effects of channel dimension and doping concentration of source and drain contacts on GNRFET performance," *Silicon*, vol. 13, pp. 3337-3350, 2021.

[5] S. S. Yu, W. T. Zheng, and Q. Jiang, "Electronic properties of nitrogen-/boron-doped graphene nanoribbons with armchair edges," *IEEE Transactions on Nanotechnology*, vol. 9, no. 1, pp. 78-81, 2009.

[6] S. Wang, N. T. Hung, H. Tian, M. S. Islam, and R. Saito, "Switching behavior of a heterostructure based on periodically doped graphene nanoribbon," *Physical Review Applied*, vol. 16, no. 2, pp. 024030, 2021.

[7] M. Gupta, N. Gaur, P. Kumar, S. Singh, N. K. Jaiswal, and P. N. Kondekar, "Tailoring the electronic properties of a Z-shaped graphene field effect transistor via B/N doping," *Physics Letters A*, vol. 379, no. 7, pp. 710-718, 2015.

[8] H. Owlia, "Effects of passivation type on electrical transport of a defect-engineered graphene nanoribbon FET," *Journal of Computational Electronics*, vol. 22, no. 2, pp. 626-633, 2023.

[9] S. Kharwar, F. Gity, P. K. Hurley, and L. Ansari, "Cadmium passivation induced negative differential resistance in cove edge graphene nanoribbon device," *Scientific Reports*, vol. 15, no. 1, pp. 8598, 2025.

[10] Anshul and R. Chaujar, "DFT based analysis of Boron and Nitrogen passivation at the edge of Armchair Graphene Nanoribbon for low power applications," *in Proc. 2024 IEEE 19th Int. Conf. Nano/Micro Engineered and Molecular Systems (NEMS), IEEE,* pp. 1-4, 2024

[11] Anshul and R. Chaujar, "Extended Huckel DFT-based study of Icosagens passivation at the edge of armchair graphene nanoribbon for next generation nanoelectronics applications," *Micro and Nanostructures*, vol. 20, pp. 208263, 2025.

[12] [illegible] 118," *Chemistry A European Journal*, vol. 15, no. 1, pp. 186-197, 2009.

[13] M. Rahm, R. Hoffmann, and N. W. Ashcroft, "Atomic and ionic radii of elements 1 96," *Chemistry A European Journal*, vol. 22, no. 41, pp. 14625-14632, 2016.

[14] B. Cordero *et al.*, "Covalent radii revisited," *Dalton transactions*, no. 21, pp. 2832-2838, 2008.

[15] R. Jyoti, M. Chauhan, B. C. Choudhary, and R. K. Sharma, "Density functional theory study of manganese doped armchair graphene nanoribbon for effective carbon dioxide gas sensing," *ES Energy & Environment*, vol. 18, pp. 47-55, 2022.

[16] Anshul and R. Chaujar, "Semi-empirical DFT Based Investigation of Electronic and Quantum Transport Properties of Novel GS-AGNR (N) FET," *IEEE Transactions on Nanotechnology*, vol. 23, pp. 400-407, 2024.

[17] R. Mann and R. Chaujar, "TCAD investigation of ferroelectric based substrate MOSFET for digital application," *Silicon*, vol. 14, no. 9, pp. 5075-5084, 2022.

[18] B. Kumar and R. Chaujar, "Analog and RF performance evaluation of junctionless accumulation mode (JAM) gate stack gate all around (GS-GAA) FinFET," *Silicon*, vol. 13, no. 3, pp. 919-927, 2021.

[19] R. Mann and R. Chaujar, "DFT-based Atomic Calculation of Si-doped HfO2 and Effect of its Negative Capacitance on Analog/RF, and VTC Parameters of MOSFET," *Silicon*, vol. 16, no. 3, pp. 1237-1252, 2024.

[20] Y. Machhiwar, D. Raja, G. Pahwa, P. Kushwaha, and H. Agarwal, "Anomalous Transconductance Behaviour in Mixed-Phase Negative Capacitance FETs," *IEEE Electron Device Letters*, 2025.

6

CHAPTER

Aluminium-passivated Gate-Stack Armchair Graphene Nanoribbon FET as a gas sensor for toxic gases

In this chapter an aluminium-passivated gate stack armchair graphene nanoribbon field-effect transistor is used as a nanoscale toxic gas sensor for the detection of nitrogen dioxide and ammonia gases.

A two-step simulation methodology is employed in the present study, the linear combination of atomic orbitals framework with generalized gradient approximation is used for bulk configured analysis, while the EH model with the NEGF formalism under a SCF framework is used for device-level simulation.

The bulk configured analysis shows that the Al-AGNR exhibits stable physisorption ₂ ³⁶¹ (–’’⁵η⁴μ⁶³ηγ(’γ’⁴×³’⁵(η–(A9FC(’r(–γ’’(A9BC(’r(–η⁴(i j (–γ’’(i c 7⁴’⁵μ’“⁶³–’ε 9o¹’(⁵’γ⁵363–36 (⁻–ε⁸’⁵(–⁴’(HDCO (–η⁴(i j (–γ’’(BBCO (–η⁴(i c 7₂ ¹³“¹ (–⁴’(D9DC(–γ’’(C9C(⁶³β’⁵(higher than the P - AGNR.

The device analysis of the proposed Al-AGNRFET shows I_{on}-based sensitivities of 85.14% for NO_2 and 7.03% for NH_3, and SR-based sensitivities of 99.86% for NO_2 and 99.47% for NH_3. Also, the proposed device also shows opposite V_{th} shifts of +0.15 V –γ’’(A9BA(r(–η⁴(i j ₂ and NH_3, respectively, which further confirms the selectivity response of the device.

Moreover, the selectivity coefficient is calculated using I_{on}-based sensitivity that reaches 12.12 when NO_2 is treated as the target gas, which confirms the strong selective detection of NO_2 in the presence of NH_3.

6.1 INTRODUCTION

The ≠oüwr%ŵr..±≈≠wzwo≈ẅÅ2%.≠poÅẃo≈ẅÅ%ŏÅr%o.≈ö~ ẃo≈ẅÅ%ŵÅ%ŏr o” ±%s≠o%wo±%≠wuÅẅwqoÅ≈z”% increased the emission of toxic and hazardous gases into the environment [1]. Harmful gases such as ammonia, nitrogen dioxide, carbon monoxide (CO), and volatile organic compounds (VOCs) pose serious risks to human health, industrial safety, and environmental sustainability [2]. Even exposure at low concentrations can lead to respiratory disorders, cardiovascular complications, and long-term systemic damage. The NO_2 is a reddish-brown gas. It is mainly produced through combustion processes [3]. The short- and long-term exposure to NO_2 can damages the cardiovascular and respiratory systems [4]. The NH_3 is a colorless gas with a pungent odor. It is produced from bacterial and organic processes. The inhalation of NH_3 can cause throat irritation and respiratory issues. At high blood concentrations, it can lead to brain damage and liver failure [5]. Therefore, there is an urgent need to develop the highly sensitive, selective, low-power, and miniaturized gas sensors has become a critical research priority. While conventional gas sensing technologies including resistive, optical, and electrochemical sensors have been demonstrated practical applicability but there are certain limitations with them [6]. The limitations include high-power consumption, limited scalability, bulky configurations, and reduced compatibility with integrated electronics [7]. On the other hand, the field-effect transistor - based gas sensors have emerged as promising alternatives due to their superior sensitivity, intrinsic signal amplification, CMOS compatibility, and nanoscale integration capability [8]. Unlike resistive sensors, FET-based sensors translate surface charge modulation directly into measurable variations in threshold voltage and drain current, enabling

enhanced detection performance at low concentrations. With the advancement of nanotechnology, low-dimensional materials such as carbon nanotubes (CNTs), graphene, and graphene nanoribbons (GNRs) have gained tremendous attention for sensing applications [9, 10]. Their high surface-to-volume ratio, exceptional carrier mobility, and tunable electronic properties make them ideal candidates for next-generation nano sensors. Among these materials, AGNRs are particularly attractive because of their width-dependent bandgap, which enables semiconducting behavior suitable for FET-based device architectures [11, 12]. However, pristine AGNR structures often exhibit limited sensitivity toward certain toxic gases due to weak physisorption interactions. To overcome this limitation, edge passivation strategies have been explored to improve the electronic and quantum transport properties of P AGNR. In our previous **Chapter 5**, the Al AGNRFET exhibits higher value of on current, significant reduction in off current, and better switching ratio among all Icosagens-passivated configurations [13]. The improved findings of Al AGNRFET makes it a suitable choice to use as a toxic gas sensor. The reason is that a gas sensor requires a high value of I_{on}, a very low value of I_{off}, and a higher value of SR to ensure a large baseline current, a stable OFF-state, and a clear distinction between the ON and OFF states before and after gas molecule adsorption, which directly determines the sensitivity of the sensor. Taking everything into consideration, in this chapter, we have proposed the Al AGNRFET as a nanoscale toxic gas sensor. Aluminium is selected due to its favorable electronic affinity, catalytic characteristics, and compatibility with semiconductor processing. The passivation of AGNR with aluminium atoms is expected to introduce localized states near the Fermi level as it belongs to the Icosagens group which enhances the charge transfer interaction between the adsorbed gas

molecules and the channel material. The sensing mechanism of the proposed device is based on adsorption-induced charge transfer between toxic gas molecules and the aluminium-passivated AGNR channel. In the present study, the key performance parameters such as adsorption energy, recovery time, bandgap, bulk configured sensitivity, conductivity, I_d V_{gs} response, transconductance and selectivity are analyzed to study the sensing performance. This chapter is organized as follows: Section 6.2 presents the device design and structural configuration, Section 6.3 describes the simulation methodology, Section 6.4 discusses the results and analysis, and finally, Section 6.5 concludes the findings of the study.

6.2 DEVICE DESIGN AND DESCRIPTION

Figure 6.1 shows the schematic representation of the proposed Al-AGNRFET as a toxic uo±%‰sÅ±ö≠%øzöÅu%~ ww%‰vs%~ özsq.zø≠%‰≈≠.q≈.≠s%ötXY %øÅr%XR %‰o±%~ özsq.zs±%øÅr%‰vsw≠% interaction with the Al-AGNR channel material. It is observed from Figure 6.1 that the toxic gas molecules are released from two major sources, namely vehicles and industries. These released gases interact with the Al-AGNR (N = 4) channel region of the proposed device. The bulk configured AGNRs was modelled by repeating the unit cell 4 times along the z direction. A vacuum layer of 20 Å was applied along the z direction in order to prevent from the interlayer interactions. The top inset view of Figure 6.1 r süwq≈±%‰vs%ø~ ö~ wq%ø≠.q≈.≠s%ötXY %~ özsq.zs4%XY %qöÅ±w≈±%ötÅs%Åw≠%usÅø~ ö~ %øÅr sr%~ ww%~ ö%“”usÅ%Y/%ø~ ö~ ±. The bottom inset of Figure 6.7%‰süwq≈±%‰vs%ø~ ö~ wq%ø≠.q≈.≠s%ötXR %~ özsq.zs4%XR %qöÅ±w≈±%ötÅs% nitrogen atom bonded with three hydrogen (H) atoms in a pyramidal configuration. The Al - AGNR (N = 4) is used as the channel material. The source and drain regions are made of ZGNR (N = 6). The source and drain contacts are doped with n-type impurities at a concentration of

5×10^{18} e/cm3. Further, the Al-AGNR channel is rotated by 30° to form a good interface with the source and drain ZGNR regions. The proposed device structure is a gate-stack armchair graphene nanoribbon field-effect transistor (GS - AGNRFET) employing an aluminium passivated armchair graphene nanoribbon (Al - AGNR) as the channel material. A metal gate electrode is placed above a dual-dielectric gate stack. The GS uses a $LaAlO_3$ high- ‰” s≠% %% 30) and a SiO_2 wÅs≠toqwz‰” s≠% %%4C/4‰vs‰wY$_2$ layer maintains the effective oxide thickness and improves device stability. The total oxide thickness is 1 nm. The gate length (L_g) is 7 nm and the length of source/drain length is 5 nm each. Overall, the Figure 6.1 shows the schematic representation of the proposed Al-AGNRFET gas sensor along with the graphical illustration of gas molecule interaction in the channel.

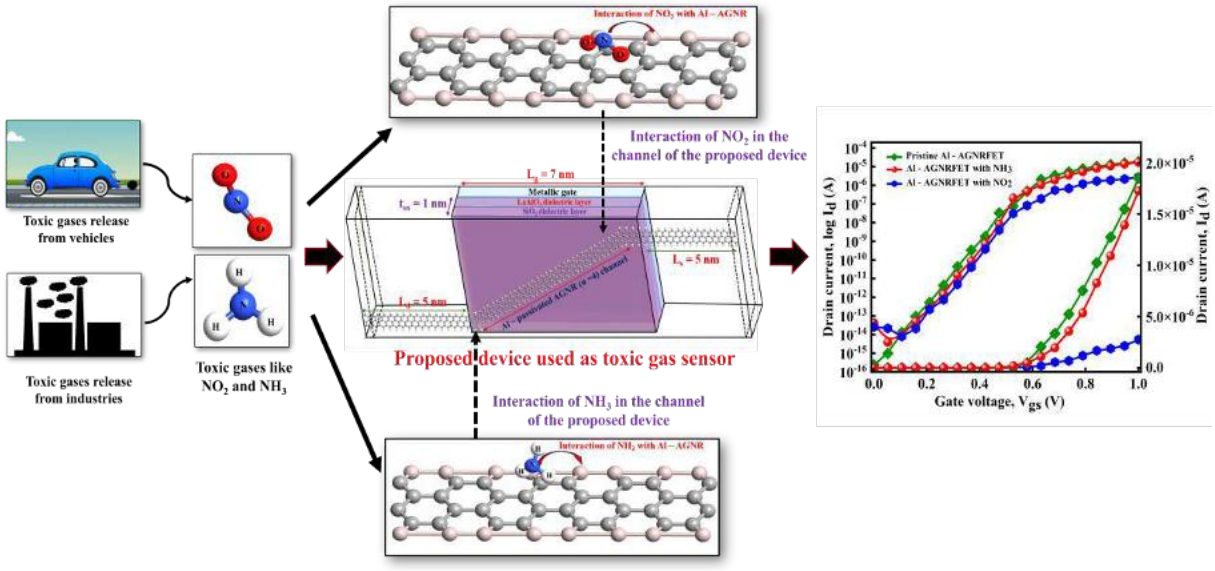

Figure 6.1: Schematic illustration of the proposed Al-AGNRFET as a nanoscale sensor for NO_2 and NH_3 toxic gas detection

6.3 SIMULATION METHODOLOGY

All the simulations are carried out in Quantum ATK (2019.12) simulator. The simulation methodology is divided into two parts. In the first part, density functional theory (DFT) based LCAO calculator with GGA and Perdew Burke Ernzerhof (PBE) exchange-correlation functional is used to find out the bandgap, adsorption energy, conductivity and recovery time for the bulk configured Al AGNR and its interactions with NO_2 and NH_3. The reason is that ≈vs%Q≠w ~ s%NPb - N9 ‰#%oysÅ%Å÷%qöÅ÷vs≠o≈wÅ%ö%qqö. Å÷%vs%Vander Waals interactions between the gas molecules and the targeted sensing material [14]. Also, all geometries with gases are optimized using LCAO PBE with Grimme DFT D3 model. The parameters that used in the LCAO-GGA framework are tabulated in Table 6.1.

Table 6.1
Computational Parameters for Bulk Configured AGNRs

Parameters	Values
Calculator	ATK DFT: LCAO
Exchange Correlation Function	GGA with PBE
Density Mesh Cut-off	40 Hartree
Occupation Method	Fermi Dirac
Broadening	100 K
K-Point Sampling	1×1×100
Maximum Steps	100
Step Size	0.01

In the second part, to perform the device-based analysis Extended Hückel model in Semi empirical calculator is used. These calculations are carried out using the EH model with the Non-Equilibrium Green's Function formalism under the SCF framework. The reason for using the EH model is that the full device configuration consists of a large number of atoms, including the source, drain, gate dielectric, and channel regions [15, 16]. The LCAO-GGA based calculations on such a large number of atoms may lead to significantly higher

computational cost [15]. Therefore, to overcome this problem we have adopted EH model with NEGF. All the parameters used in the EH based simulator is tabulated in Table 6.2.

Table 6.2
Computational Parameters for Proposed Device Configuration

Parameters	Values
Computational model	Extended Hückel model
Basis set	Hoffmann
Fitted parameters	Hückel Hamiltonian parameterization
Temperature and Fermi Dirac broadening	300 K
Boundary conditions	Multigrid type Poisson solver
K point sampling	1 × 1 × 100

6.4 RESULTS AND DISCUSSIONS

In this section, the sensing performance of the proposed Al-AGNRFET device is analyzed for NO_2 and NH_3 gas detection. The result and discussion are divided into three subsections. In the first section, the gas detection analysis for the bulk configured P-AGNR and Al-AGNR is performed. This includes the comparison of total free energy, adsorption energy, recovery time, bandgap, conductivity, and sensitivity upon NO_2 and NH_3 adsorption. Based on these results, it is concluded that the Al-AGNR shows superior sensing performance compared to the P-AGNR. Then, the Al-AGNR is used as the channel material in the proposed GS-AGNRFET device. The device-level analysis is performed in terms of I_d-V_{gs} transfer characteristics, transconductance, and projected local density of states, sensitivity and selectivity analysis in the other two subsections.

6.4.1 Comparison of bulk configured P -AGNR and Al – AGNR for NO_2 and NH_3 gas detection

The total free energy of all bulk configured AGNRs is tabulated in the Table 6.3. To investigate the interaction between NO_2, NH_3 gases and the AGNRs system, we assessed various orientations of these gases at the edge site as the initial geometry for optimization. The edge site is identified as the adsorption site owing to the molecular characteristics of gases that facilitate fast adsorption at this point. After optimization, the gases NH_3 and NO_2 are adsorbed at a distance of 2.17 and 2.67 Å, respectively from, the edge site. The most stable arrangements of gas molecules adsorbed on a material are determined by the minimum total energy of the system. The lower value of the total free energy indicates a more thermodynamically stable configuration. From Table 6.3, we can observe that the value of total free energy for Al AGNR with gases is significantly lower than the P-AGNR with gases. The negative value of free energy indicate that all the adsorbed systems are thermodynamically stable. Based on the comparison, we have found that the Al AGNR is more thermodynamically stable than the P AGNR.

Table 6.3
Total Free energy of all the systems

System	Total Free Energy, E (in eV)
P AGNR	-5478.26991
NO_2	-1179.01151
NH_3	-330.41409
P AGNR + NO_2	-6655.81461
P AGNR + NH_3	-5805.33081
Al AGNR	-21902.55453
Al AGNR + NO_2	-23082.086042
Al AGNR + NH_3	-22233.09111

Further, in order to determine the strength of the interaction between the gas and Al AGNR, P AGNR, we have calculated the adsorption energy (E_{ads}) using Eq. (6.11). The adsorption

energy is the amount of energy that is released or absorbed when a gas molecule contacts with the surface of a sensing material [17]. Mathematically, the E_{ads} is given as [18]:

$$E_{ads} = E_{material\ with\ gas} - E_{material\ without\ gas} - E_{gas} \tag{6.11}$$

where,

$E_{material\ with\ gas}$	-	total free energy of material in presence of gas molecule
$E_{material\ without\ gas}$	-	total free energy of material in absence of gas molecule
E_{gas}	-	total free energy of gas molecule

The values of adsorption energy and recovery time are tabulated in Table 6.4. The calculated positive value of E_{ads} suggested that the adsorption of NO_2 and NH_3 onto the P AGNR was chemisorption, whereas the adsorption of NO_2 and NH_3 onto the Al AGNR was physisorption. Based on the comparison of the adsorption energies values, we found that the NO_2 and NH_3 gases preferred to adsorbed on the Al AGNR rather than the P AGNR. Also, the Al -AGNR with NO_2 shows strong adsorption rather than the Al AGNR with NH_3. Kr r wwöÅozz'2⁄₀–s%o–s%ö. .År %ö. .≈⁄₀vs %⁄₀sqö–s≠'%w s%ö≠⁄₀vs%o±s±4%vs%⁄₀sqö–s≠'%w s% /%⁄₀% defined as the time required for the gas molecule to desorb from the surface of the sensing material after the source of gas is removed. It is calculated using the transition state theory and d oÅ≈Hoff Arrhenius equation, as follows [17]:

$$\tau = \nu_0^{-1} exp\left(\frac{-E_{ads}}{k_B T}\right) \tag{6.12}$$

where,

ν_0^{-1}	-	10^{12} s^{-1}, attempt frequency
k_B	-	Boltzmann constant, 8.617×10^{-5} eV
T	-	Temperature (300K)

From Table 6.4, we can observe that the values of recovery time are very small in case of the P - KQX] %84 %%76 %±%ö≠ºXY %oÅr %947%%76 %±%ö≠ºXR /2%–vwqv%wÅr wqo~s±%ùv”±wqozz”% unrealistic values. This confirms that no stable adsorption of gas molecules occurs on the P - AGNR surface. However, the values of recovery times in the Al-KQX] %–4 %%76 %%ö≠ºXY % oÅr %47%%76 %%ö≠ºXR /2%qöÅtw≠ %±opzs%wÅs≠oq~wÅ%t%o±% özsq.zs±%Å%vs%.≠toqs%t%Kz% KQX] 4%Kz±ö2%vs%sqö–s≠”%w s%t%4 %%76 %%ö≠ºXY %soÅ±%vo~%he Al-AGNR based sensor can be operate stably for a measurable duration, which is suitable for practical gas detection.

Table 6.4
Adsorption energy and Recovery time of all systems

System	Adsorption Energy, E_{ads} (eV)	Recovery Time (s)
P AGNR + NO_2	+ 1.47	2.4×10^{-37}
P AGNR + NH_3	+ 3.35	3.1×10^{-69}
Al AGNR + NO_2	- 0.52	5.4×10^{-4}
Al AGNR + NH_3	-0.12	1.1×10^{-10}

bvs%o≠w~wÅ%Å%vs%poÅr uoü2%qöÅr .q~w~v”% /2%År %sÅ±wwv”%a/%t%vs%Z% AGNR and Al AGNR with NO_2 and NH_3 gases are illustrated as spider chart in the Figure 6.2. From the Figure 6.2, we can observe that the P-AGNR has a bandgap of 0.17 eV. Upon NO_2 adsorption, the bandgap decreases to 0.11 eV. The reason is the acceptor nature of NO_2, which withdraws electrons from the AGNR. Also, the value of bandgap for P -AGNR increases to 0.18 eV with NH_3. This is due to the donor nature of NH_3, which adds electrons to the P- AGNR. The Al-AGNR shows a bandgap of 0.31 eV. The NO_2 adsorption in the Al AGNR deceases the bandgap to 0.20 eV and with NH_3 adsorption, it becomes 0.27 eV. The bandgap directly governs the conductivity of the AGNR material through the mathematical relation as follows [19]:

$$\sigma \propto exp\left(\frac{-E_g}{2k_BT}\right) \tag{6.13}$$

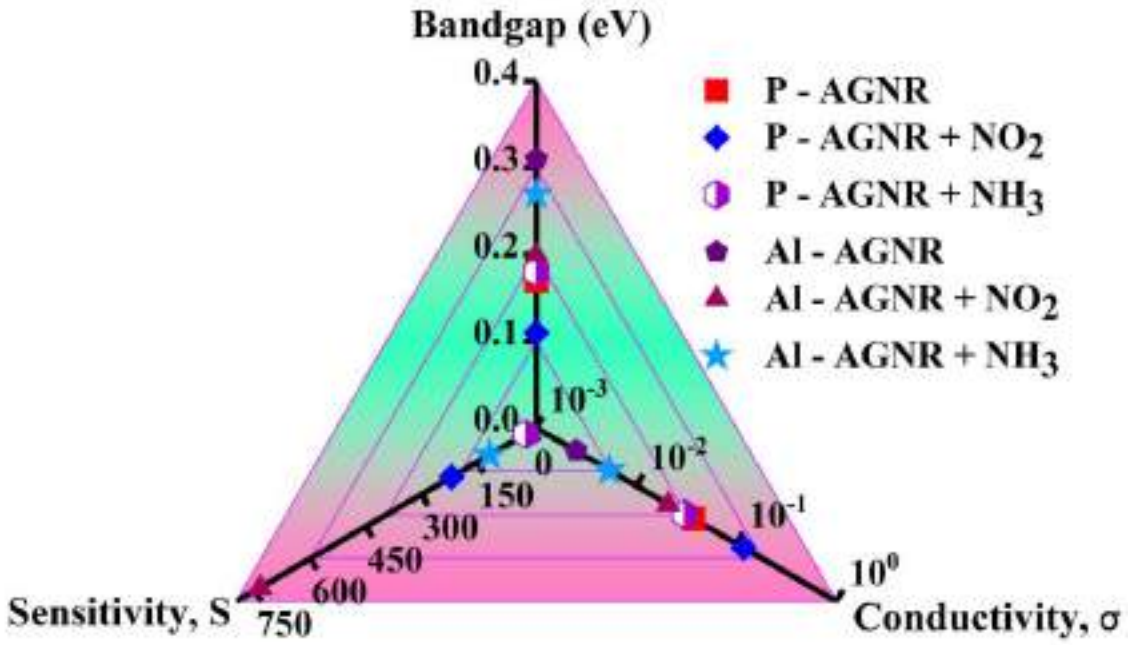

Figure 6.2: Spider chart for bandgap, conductivity and sensitivity analysis for all systems

From Eq. (6.13), we can say that, the small change in bandgap upon gas adsorption leads to change in conductivity. Using Eq. (6.13), the sensitivity is calculated. The sensitivity of a gas sensor is the ability of the sensing material to produce a measurable change in its electrical properties when in contact with a target gas molecule. The high value of sensitivity means that the sensing material has a larger change in electrical characteristics after adsorption of gas. This facilitates the detection of the target gas molecule even at low concentrations. The sensitivity of a gas sensor is shown to be directly dependent on the change in electrical conductivity of the detecting material following adsorption of gas. This is because adsorption of a gas molecule on the surface of the sensing material alters the electronic structure of the substance. This modification leads to a change in the bandgap, which leads to a change in the

electrical conductivity of the material. The change in conductivity is utilized to calculate the sensitivity of sensor and mathematically it is expressed as [19, 20]:

$$S = \left(\frac{\sigma - \sigma'}{\sigma'}\right) \times 100\% \tag{6.14}$$

where,

- Conductivity of system in presence of gas molecule
- - Conductivity of system in absence of gas molecule

Also from Figure 6.2, we can observe that the value of sensitivity of P-KQX] %æ#8%7C+ %ö≠%XY % oÅr %7AA+ %ö≠%XR 4%Rö—s–s≠2%vs%Kz-KQX] %vö—±%%sÅ±vw-w²”%t%A9>+ %ö≠%XY %År %7>+ % tö≠%XR 4%vs±s%oz.s±%s≠%94>%År %4>%w s±%wuvs≠%voÅ%Z-AGNR, respectively. From the above bulk configured analysis, the authors observed that the Al-AGNR performs better than the P-AGNR in all key sensing parameters. These include thermodynamic stability, adsorption energy, recovery time, bandgap modulation, and sensitivity. Therefore, the Al-AGNR is selected as the channel material for the proposed GS-AGNRFET device. In the next section, the gas molecules of NO_2 and NH_3 are adsorbed at the edge sites of the Al-AGNR channel material to analyse the device-level sensing performance.

6.4.2 Device characteristics analysis: Al-AGNRFET as a Gas Sensor

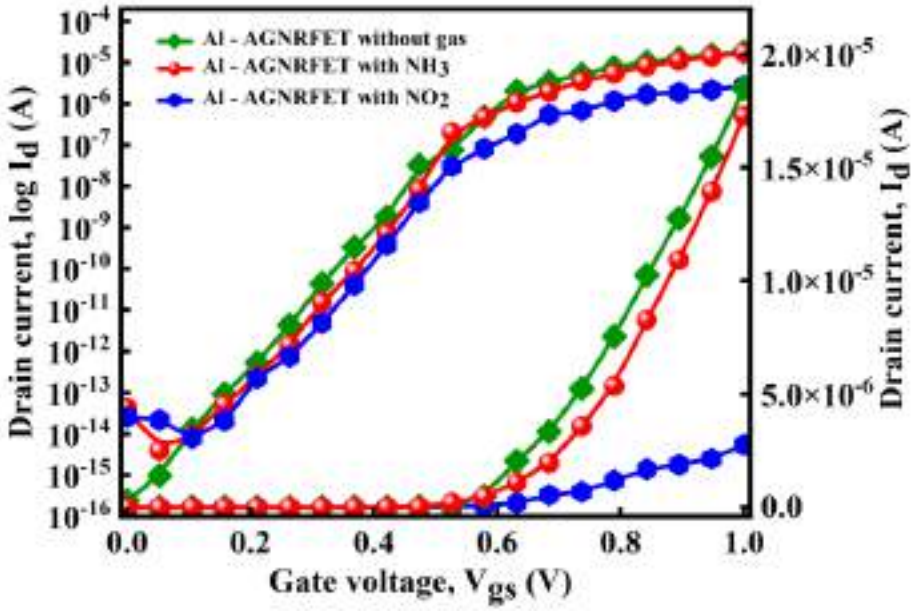

Figure 6.3: Transfer characteristics of the Al-AGNRFET without gas and with NO_2, and NH_3 gases at V_{ds} = 0.5 V

The transfer characteristics of the Al-AGNRFET without and with gas molecules are depicted in Figure 6.3. The V_{gs} is varied from 0 to 1 V at constant V_{ds} = 0.5 V. The left y-axis shows the logarithmic scale of I_d and the right y-axis shows the linear scale. The channel of the proposed device is an intrinsic (undoped) Al-AGNR. Therefore, the sensing mechanism is based on the modification of the threshold voltage and electrostatic potential of the intrinsic channel upon gas adsorption. From Figure 6.3, we observed that the value of I_{on} w¥%4B–%%6 % A, the I_{off} w¥%49A%%6 %K2%Ar%s%] %¥%4B%%6 %ö=%K2% AGNRFET without gas. The significance of the I_d-V_{gs} characteristic curve is that it provides direct evidence of how the gas molecules modify the threshold voltage of the device. From Figure 6.3, we can observe that the value of drain current changed, when gases are interacted with the channel material. Further, the change in the I_d-V_{gs} curve indicates a change in the V_{th}, which is the primary

sensing mechanism of the proposed device. From Figure 6.3, the authors calculated the shift in the V_{th} value.

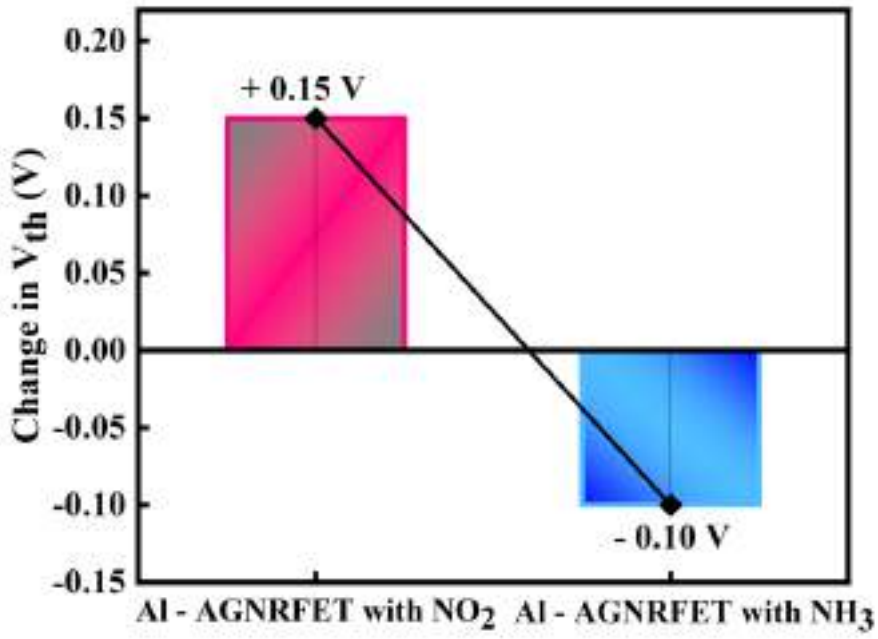

Figure 6.4: Change in the V_{th} value after NO_2 and NH_3 gas adsorption

The change in the V_{th} is illustrated in Figure 6.4. From the Figure 6.4, the value of V_{th} changes from 0.55 to 0.45 V and shows a shift of - 0.10 V, when NH_3 gas is adsorbed. The reason for the shift in V_{th} w#%vs%ö Åö≠Åo≈.≠s%ot%XR 4%o vsÅ%XR %#%or±ö≠psr%oÅ%vs%Å≈≠wÅ±wq%Kz-AGNR channel, it donates electrons to the channel material. This increases the electron density in the intrinsic channel and creates a net negative charge in the channel region. This negative charge lowers the value of threshold voltage of the device, which means the gate requires a lower voltage to ≈.≠Å%Å%vs%s–wqs4%o vwzs%vs%or±ö≠ü≈wöÅ%t%XY %Å%vs%Kz%AGNR channel material, increase the value of V_{th} to 0.70 V by a shift of + 0.15 V in V_{th}. The reason for the change in V_{th} w#%vo≈%vs%or±ö≠ü≈wöÅ%t%XY %Å%vs%Å≈≠wÅ±wq%Kz-AGNR channel withdraws electrons from the channel material. This creates a net positive charge in the channel region. This positive

charge increases the threshold voltage of the device, which means the gate requires a higher voltage to turn on the device. The opposite shifts in the value of V_{th} confirms the dual-direction sensing response of the device.

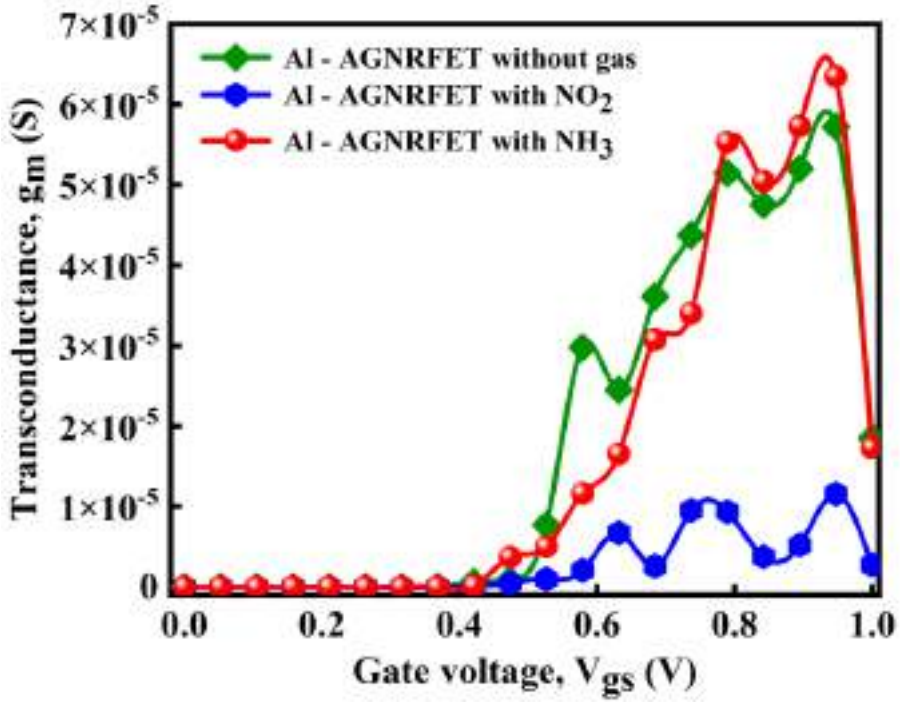

Figure 6.5: Transconductance analysis of the Al-AGNRFET without gas and with NO_2, and NH_3 gases

Figure 6.5 depicts the transconductance analysis for Al-KQX] POb%-wvö.~%o±%Ar%-wv%XY 2% oÅr%XR %uo±s±4%b≠oÅ±qöÅr.q~oÅqs%rstwÅs±%~vs%rs–wqs-±%qoüopwzw~”%ö%~ üzw~”%±wuÅoz±%Ar% respond to gate voltage changes. The higher value of gm indicates better gate control over the channel [21]. From Figure 6.5, we can observe that the Al-AGNRFET without gas molecules shows the highest value of g_m in the Vgs range of 0.6 1.0 V. The interaction of NO2 gas reduces the value of g_m significantly. The reason is that NO_2 withdraws electrons from the channel, reducing the charge carrier density and weakening the gate modulation. While, the adsorption of NH_3 shows a moderate change in the value the g_m. The donor nature of NH_3

slightly shifts the threshold voltage, which causes a shift in the g_m peak. From the above analysis, the authors observed that the change in g_m upon gas adsorption can also be used as an additional sensing parameter in the Al-AGNRFET. Figure 6.6 depicts the projected local density of states (PLDOS) analysis of the Al-AGNRFET (a) without gas, (b) with NH_3 and (c) with NO_2 at V_{ds} = 0.5 V.

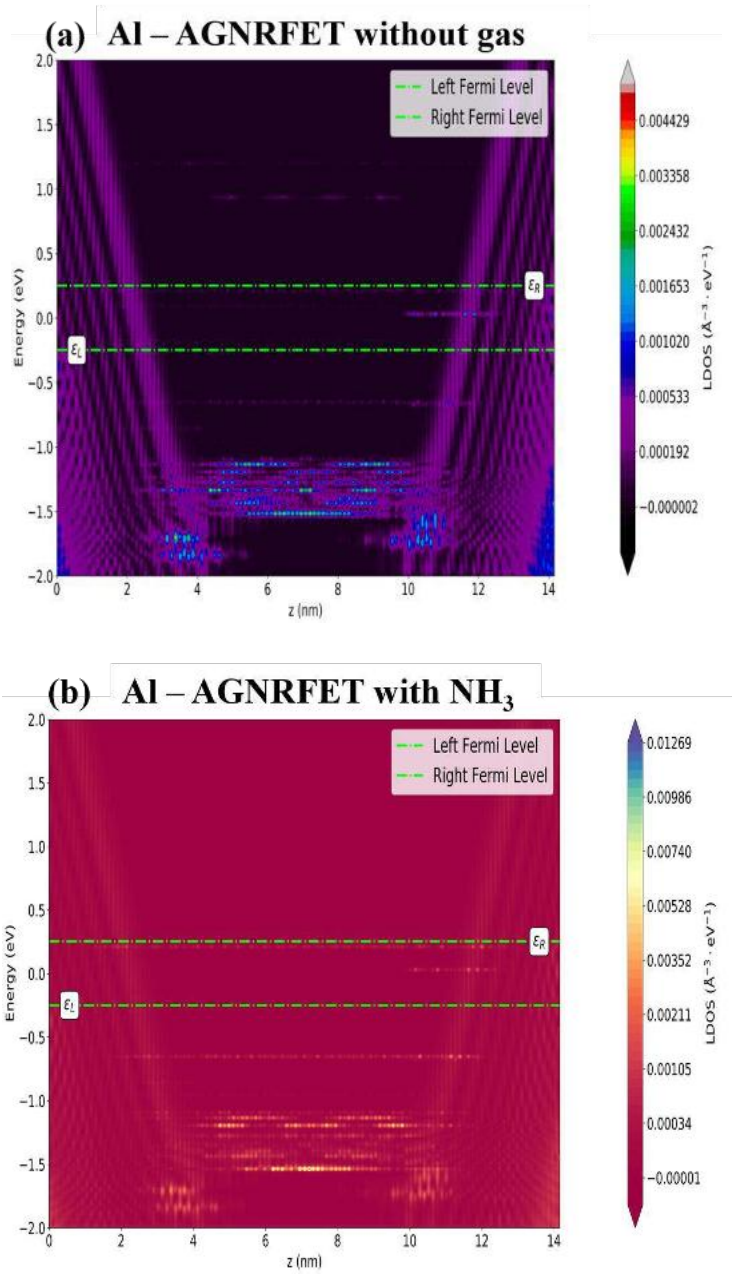

Anshul

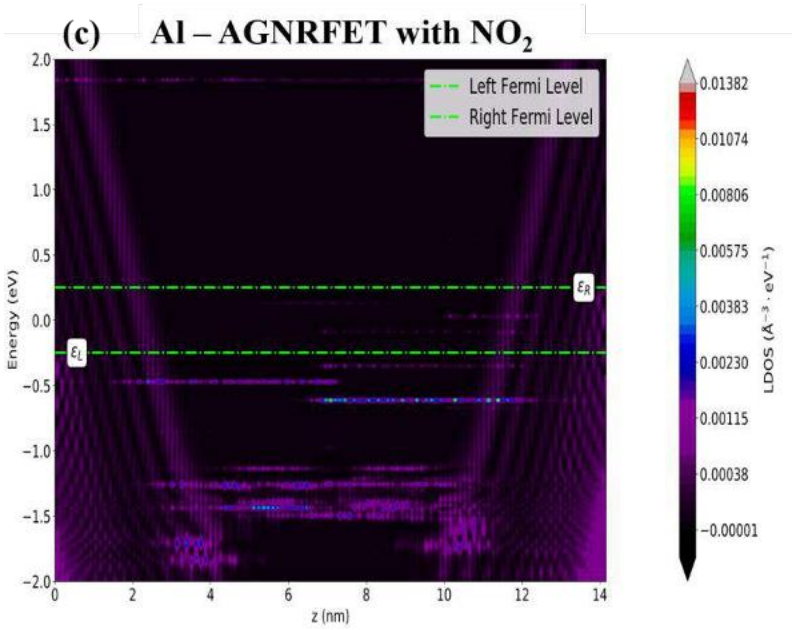

Figure 6.6: Projected local density of states analysis of the Al-AGNRFET (a) without gas, (b) with NH_3 and (c) with NO_2 at V_{ds} = 0.5 V

The contour plot of PLDOS at V_{ds} = 0.5 V offers the important information on the transport properties of the proposed device and its interaction with gas molecules. The PLDOS is usually plotted against energy and position in the AGNR. The PLDOS shows the contribution of different orbitals to the density of states. Each contour line in Figure 6.6 corresponds to a specific energy level, with the intensity or color of the contour lines indicating the density of electronic states at that energy level. From Figure 6.6 (a), we can observe that the contour lines are light and dispersed without gas, especially at the Fermi level. From Figure 6.6 (b) and (c), the intensity of color becomes stronger and also the magnitude of LDOS increases. This change in the color intensity and the LDOS signifies that the Al AGNRFET device is highly sensitive to the gas interactions. Also, the PLDOS analysis provides an alternate way to confirm the variation in the drain current when the gas is introduced. From the comprehensive analysis

presented in this section, the proposed Al-AGNRFET demonstrates superior gas sensing üs≠tö≠~ oÅqs%ö≠p¤ö≈v%XY %¤Ar %XR %¤o±%s≈sq≈wöÅ4

6.4.3 Sensitivity and Selectivity analysis of the Al – AGNRFET

In this section, the sensing performance of the proposed Al-AGNRFET evaluated through three sensitivity metrics defined in terms of the V_{th}, I_{on}, and SR, as presented in Figure 6.7. The sensitivity of a FET-based gas sensor is the relative change of a device parameter upon gas adsorption with respect to its baseline value in the absence of gas. Mathematically, the sensitivity is expressed as [22]:

$$S = \left(\frac{X_{(with\ gas)} - X_{(without\ gas)}}{X_{(without\ gas)}} \right) \times 100\% \quad (6.15)$$

Rs≠s2%vs%s≠~ %f %¤%vs%s–¤qs%¤o≠o~ s≈s≠%Å%s≠~ ±%t%d $_{th}$, I_{on}, or SR. From Figure 6.7, we can observe that the values of $S_{(Vth)}$, $S_{(Ion)}$, and $S_{(SR)}$ for NO_2 are 27.27%, 85.14%, and 99.86%, respectively.

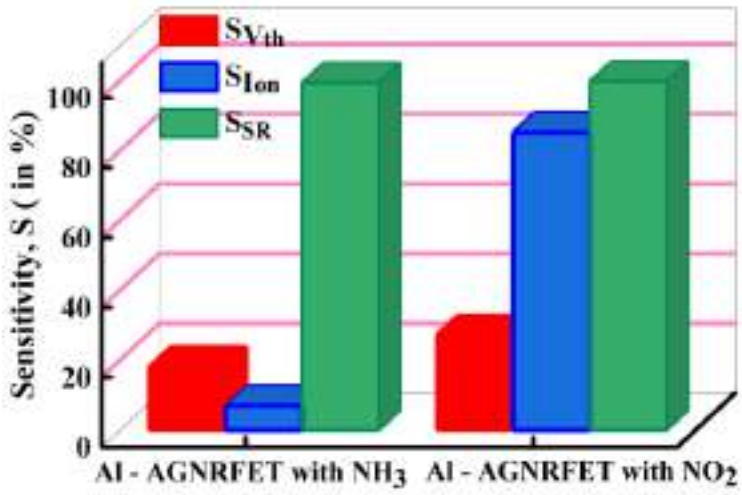

Figure 6.7: Bar plot representation of sensitivity analysis in terms of V_{th}, I_{on}, and SR for NO_2 and NH_3 gas adsorption at V_{ds} = 0.5 V

The reason for high $S_{(Ion)}$ and $S_{(SR)}$ is the acceptor nature of NO_2, which withdraws a significant number of electrons from the Al-AGNR channel and reduces the carrier density. This causes a large drop in I_{on} and a corresponding change in the SR. While in case of NH_3 adsorption, the values of $S_{(Vth)}$, $S_{(Ion)}$, and $S_{(SR)}$ are 18.18%, 7.03%, and 99.47%, respectively. The reason for low value of $S_{(Ion)}$ is the donor nature of NH_3 gas. It donates electrons into the channel and slightly increases I_{on} as compared to its baseline value (without gas), resulting in only a minor change in I_{on}. It is to be noted that the I_{off}-based sensitivity is not included in the present analysis. The reason is that the value of I_{off} changes by two orders of magnitude upon gas adsorption (from 2.37×10^{16} A to 2.58×10^{14} A for NO_2 and 4.14×10^{14} A for NH_3), which gives unphysically large sensitivity values exceeding 10000% for both gases. From the above analysis, the authors observed that the I_{on}-based sensitivity shows the largest contrast between NO_2 and NH_3, while the SR-based sensitivity saturates near 100% for both gases due to the dominant variation in value of I_{off}.

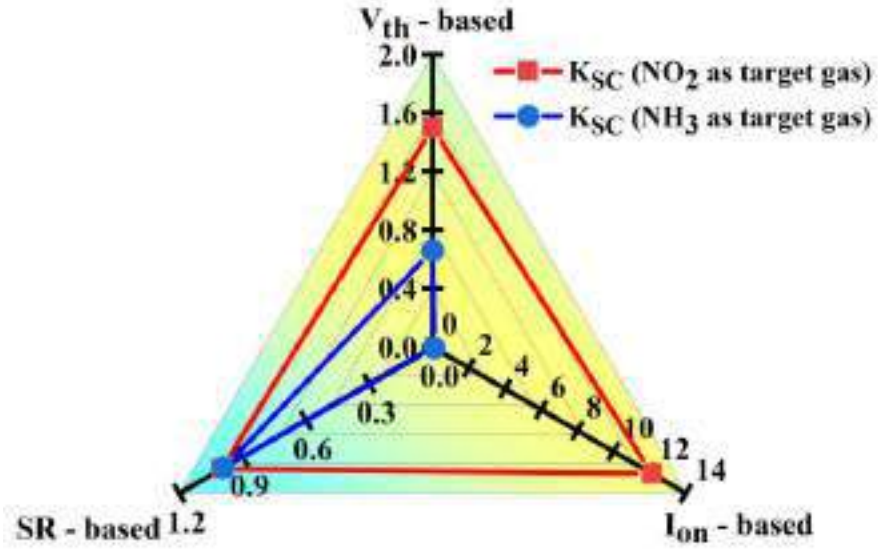

Figure 6.8: Selectivity analysis for NO_2 and NH_3 gas adsorption

Further, the selectivity of a gas sensor that defines the ability of the sensor to distinguish a target gas from an interfering gas is analyzed. The selectivity is quantified using the selectivity coefficient (K_{SC}), which is defined as the ratio of the sensitivity of the sensor to the target gas ($S_{target\ gas}$) to that of the interfering gas ($S_{interfering\ gas}$) [23, 24]. The value of $K_{SC} > 1$ confirms that the device selectively detects the target gas over the interfering gas, while $K_{SC} = 1$ indicates no selectivity between the two gases [23]. The selectivity analysis in the present work is performed only for V_{th}, I_{on}, and SR-based sensitivities as shown in Figure 6.8. From the Figure 6.8, we can observe that when NO_2 is treated as the target gas, the values of K_{SC} are 1.50, 12.12, and 1.00 for V_{th}, I_{on}, and SR-based sensitivities, respectively. The highest value of K_{SC} is obtained for I_{on}-based sensitivity, which means that the proposed Al-AGNRFET is 12.12 times more sensitive to NO_2 than NH_3 in terms of on current variation. The reason for this large value of K_{SC} is the opposite nature of charge transfer between NO_2 and NH_3 with the Al-AGNR channel. The NO_2 withdraws electrons from the channel and reduces I_{on} drastically, while the NH_3 donates electrons to the channel and keeps the value of I_{on} close to its baseline. This opposite effect on I_{on} forms the physical basis of the selectivity. While in case of NH_3 as the target gas, the values of K_{SC} are 0.67, 0.08, and 1.00 for V_{th}, I_{on}, and SR-based sensitivities, respectively. The low value of the K_{SC} of 0.08 in I_{on}-based sensitivity also confirms that the device cannot selectively detect NH_3 over NO_2 using on current as the selectivity parameter. The K_{SC} value of approximately 1.00 in SR-based selectivity for both directions is the consequence of the SR saturation behavior reported in the sensitivity analysis. Therefore, the SR-based selectivity does not provide useful information about discrimination of the two gases. From the above analysis, the authors observed that the I_{on}-based selectivity coefficient of

12.12, along with the opposite threshold voltage shift confirms the strong selective response of the proposed Al-AGNRFET towards NO_2 gas. From the above comprehensive analysis, the authors observed that the proposed Al-KQX] POb %vö—±%.üs≠ö≠%s≈sq≈öÅ%t%XY %–s≠%XR % oq≠ö±±%zz%sÅ±Åu%o≠o~ s≈s≠±%Y—Åu%ö%s%v”±ö≠i≈öÅ%t%XY %–v%Oor±%G% 0.52 eV), higher bulk sensitivity (736%), larger positive threshold voltage shift (+0.15 V), higher I_{on}-based sensitivity (85.14%), reduction in peak value of transconductance, and the I_{on}-based selectivity coefficient of 12.12. These results confirms that the Al-AGNRFET as a highly ±szsq≈s%År %sÅ±s%oÅö±qozs%sÅ±ö≠%ö≠%XY %s≈sq≈öÅ%Å%s%i≠s±Åqs%t%XR %±%Å% interfering gas.

6.5 SUMMARY

This chapter investigates the performance of the proposed Al-AGNRFET as a nanoscale gas ±sÅ±ö≠%ö≠%s%s≈sq≈öÅ%t%XY %År%XR 4%In this chapter, the two-step simulation methodology is employed, the LCAO-GGA for bulk configured analysis and the EH model with NEGF-SCF formalism for device-level simulation is used. The bulk configured analysis confirmed that the P-AGNR shows chemisorption with positive or±ö≠i≈öÅ%Ås≠uw±%t%174 A%d %ö≠%XY %År % 194=%d %ö≠%XR 2%–v%v”±qozz”%Å≠sozw≈q%sqö–s≠”%v s±%t%4 %%6 %%År %47%%6 %2% respectively. This confirms that P-AGNR is not suitable for practical gas sensing. In contrast, the Al-KQX] %vö—±%opzs%v”±ö≠i≈öÅ%–v%Åsuo≈s%r±ö≠i≈öÅ%Ås≠uw±%t%64=8%d %ö≠% XY %År%6478%d %ö≠%XR 2%–v%v”±qozz”% soÅÅut.z%sqö–s≠”%v s±%t%4 %%6 %%År %47% %6 %2%s±üsq≈sz”4%vs%sÅ±vw”%oz.s±%t%9>+ %ö≠%XY %År %7>+ %ö≠%XR %–vqv%≠s% 3.36 and 6.6 times higher than the P-AGNR, respectively. Based on these superior bulk configured results, Al-AGNR is selected as the channel material for the proposed GS-

AGNRFET device. In the device-level analysis, the intrinsic Al-AGNR channel of the proposed GS-KQX] POb%‰vö—±%o%ŵ=wÅq~%‰sÅ±wÅu%‰±üöÅ±s%‰üöÅ%‰uo±%‰r±ö≠ü≈wöÅ4%‰bvs%‰XR % adsorption causes a left shift in the I_d-V_{gs} curve with V_{th} decreasing from 0.55 V to 0.45 V. bvs%‰XY %‰r±ö≠ü≈wöÅ%‰qo.±s±%‰%‰uv~%‰vwv~%‰ww%‰1 $_{th}$ increasing to 0.70 V. These opposite threshold –öz~ous%‰wvwv~±%‰ot%‰6476%‰d %‰Ar %‰1647=%‰d %‰qöÅtw≠~ %‰vs%‰n..oz-direction sensing response of the proposed device. The I_{on}-based sensitivity is 85.14% for NO_2 and 7.03% for NH_3, while the SR-based sensitivity is 99.86% for NO_2 and 99.47% for NH_3. The value of K_{SC} using I_{on}-based sensitivity reaches 12.12 with NO_2 as the target gas, which confirms that the device responds 12.12 times more strongly to NO_2 than to NH_3 in terms of on current. Further, the ≠‰oÅ±qöÅr..q~oÅqs%‰oÅoz’±w%‰vö—±%‰o~%‰XR %‰Åq≠so±s±%‰vs%‰m üsoy%‰ö~ %‰B%‰6 %‰ö%‰4=%‰6 % a2%‰–vws%‰XY %‰≠o±~wqoz’”%‰sr..qs±%‰%‰ö%‰üü≠ö“w~ o~sz’”%‰6%‰6 %‰a4%‰bvs%‰ZVNYa%‰Åoz’±w% qöÅtw≠~ ±%‰vo~%‰XR %.Åwö≠~ z’”%‰owws±%‰vs%‰qvoÅÅsz%‰VNYa%‰ö%‰64678>C% sd 2%‰–vws%‰XY % introduces a new localized acceptor band at approxw~ o~sz’”%‰64=%‰d %‰wv%‰VNYa%‰öt%‰4679B8% [1] sd 4%‰Kzz%‰s–wqs-level results are fully consistent with each other and with the bulk configured analysis. The opposite response of the Al-AGNRFET to NO_2 and NH_3 across all sensing parameters along with the high I_{on}-based K_{SC} of 12.12 confirms that the proposed device can not only detect both gases but also distinguish between them with high selectivity. From the above analysis, the authors conclude that the proposed Al-AGNRFET is a highly sensitive, selective, and reliable naÅö±qozs%‰sÅ±ö≠%‰ö≠%‰vs%‰s≈sq~wöÅ%‰t%‰XY %‰Ar %‰XR toxic gases at room temperature. Overall, this chapter establishes the Al-AGNRFET as a promising candidate for next-generation low-power nanoscale toxic gas sensing applications like

environmental air quality monitoring, industrial safety systems, medical breath diagnostics, and automotive emission control.

6.6 REFERENCES

[1] A. Dixit, N. Gupta, and N. Chaturvedi, "Ab initio study of carbon nanotube field effect transistor gas sensor for detection of ammonia and nitrogen dioxide gas," *IEEE Transactions on Nanotechnology*, vol. 21, pp. 564-574, 2022.

[2] A. Valera-Medina *et al.*, "Ammonia, methane and hydrogen for gas turbines," *Energy Procedia*, vol. 75, pp. 118-123, 2015.

[3] M.-L. Fang *et al.*, "Chemical adsorption of nitrogen dioxide with an activated carbon adsorption system," *Aerosol and Air Quality Research*, vol. 19, no. 11, pp. 2568-2575, 2019.

[4] T. W. Hesterberg, W. B. Bunn, R. O. McClellan, A. K. Hamade, C. M. Long, and P. A. Valberg, "Critical review of the human data on short-term nitrogen dioxide (NO2) exposures: evidence for NO2 no-effect levels," *Critical reviews in toxicology*, vol. 39, no. 9, pp. 743-781, 2009.

[5] J. J. Renard, S. E. Calidonna, and M. V. Henley, "Fate of ammonia in the atmosphere a review for applicability to hazardous releases," *Journal of hazardous materials*, vol. 108, no. 1-2, pp. 29-60, 2004.

[6] Y. Santiago-Rodriguez, J. A. Herron, M. C. Curet-Arana, and M. Mavrikakis, "Atomic and molecular adsorption on Au (111)," *Surface science*, vol. 627, pp. 57-69, 2014.

[7] N. Mishra, B. P. Pandey, D. Kumar, V. K. Tomar, A. Dasgupta, and S. Kumar, "Investigating the infrared absorption and optoelectronic properties of Mn-doped MoSe 2 ML by adsorption of NO x gas molecules," *IEEE Sensors Journal*, vol. 22, no. 23, pp. 22564-22570, 2022.

[8] V. R. Kumbhare, P. P. Paltani, C. Venkataiah, and M. K. Majumder, "Analytical study of bundled MWCNT and edged MLGNR interconnects: impact on propagation delay and area," *IEEE Transactions on Nanotechnology*, vol. 18, pp. 606-610, 2019.

[9] F. Schwierz, "Graphene transistors," *Nature nanotechnology*, vol. 5, no. 7, pp. 487-496, 2010.

[10] M4W4‰o±2V4‰UoÅu2[‰ 4Y…".oÅu2‰År ‰U4‰4g öÅu2(Kr –oÅqsr ‰ö—r w- sÅ±wöÅoz‰φ≠pöÅ‰ materials for flexible devices," *InfoMat*, vol. 2, no. 4, pp. 698-714, 2020.

[11] Anshul and R. Chaujar, "Semi-empirical DFT Based Investigation of Electronic and Quantum Transport Properties of Novel GS-AGNR (N) FET," *IEEE Transactions on Nanotechnology*, vol. 23, pp. 400 - 407, 2024.

[12] T. Radsar, H. Khalesi, and V. Ghods, "Graphene nanoribbon field effect transistors analysis and applications," *Superlattices and Microstructures,* vol. 153, pp. 106869, 2021.

[13] Anshul and R. Chaujar, "Extended Huckel DFT-based study of Icosagens passivation at the edge of armchair graphene nanoribbon for next generation nanoelectronics applications," *Micro and Nanostructures,vol. 207, pp*. 208263, 2025.

[14] A. Bhandari, N. K. Puri, and P. Dua, "Adsorption of Cyanogen Chloride Gas Onto the Pristine and Copper-Decorated hBN Monolayer: A Comparative DFT Study," *IEEE Sensors Journal*, 2025.

[15] S. Smidstrup *et al.*, "QuantumATK: an integrated platform of electronic and atomic-scale modelling tools," *Journal of Physics: Condensed Matter,* vol. 32, no. 1, pp. 015901, 2019.

[16] K. Stokbro, D. E. Petersen, S. Smidstrup, A. Blom, M. Ipsen, and K. Kaasbjerg, "Semiempirical model for nanoscale device simulations," *Physical Review B Condensed Matter and Materials Physics,* vol. 82, no. 7, pp. 075420, 2010.

[17] R. Rahimi and M. Solimannejad, "Gas-sensing performance of BC 3 nanotubes for detecting poisonous cyanogen gas: a periodic DFT approach," *New Journal of Chemistry,* vol. 45, no. 26, pp. 11574-11584, 2021.

[18] J. T. Mazumder and R. K. Jha, "Theoretical insights into gas sensing properties of MXene," *Sensors and Actuators Reports,* vol. 6, pp. 100174, 2023.

[19] L. Chhana *et al.*, "Theoretical study of ZnS monolayer adsorption behavior for CO and HF gas molecules," *ACS omega,* vol. 7, no. 44, pp. 40176-40183, 2022.

[20] A. Bhandari, N. K. Puri, P. Dua, and R. Chaujar, "A deep insight into the adsorption mechanisms of lithium-ion battery thermal runaway gases onto Cu-decorated hBN for gas sensing applications using DFT," *Journal of Materials Chemistry A,* vol. 13, no. 43, pp. 37138-37155, 2025.

[21] R. Mann and R. Chaujar, "TCAD investigation of ferroelectric based substrate MOSFET for digital application," *Silicon,* vol. 14, no. 9, pp. 5075-5084, 2022.

[22] B. Kumar and R. Chaujar, "Fin field-effect-transistor engineered sensor for detection of MDA-MB-231 breast cancer cells: A switching-ratio-based sensitivity analysis," *Phys Rev E,* vol. 108, no. 3, pp. 034408, 2023.

[23] K. Kalantar-Zadeh, *Sensors: an introductory course*. Springer Science & Business Media, 2013.

[24] M. Tonezzer, S. C. Izidoro, J. P. A. Moraes, and L. T. T. Dang, "Improved gas selectivity based on carbon modified SnO2 nanowires," *Frontiers in Materials,* vol. 6, pp. 277, 2019.

7

CHAPTER

Conclusion, Social Impact and Future scope

This chapter summarizes the research contributions discussed in the previous chapters of this thesis.

Also, the societal implications and practical importance of the proposed devices and gas sensors are explored.

Finally, this chapter describes the possible future work that could be carried out based on this present study.

7.1 CONCLUSION

This thesis presents an atomistic-scale investigation of armchair graphene nanoribbon field-effect transistors under a gate-stack architecture, with the objective of identifying device configurations that are suitable for ultra-low-power logic and toxic gas sensing. The present work dielectric engineering, channel-width engineering, computational-model reliability, and edge-passivation chemistry. Each chapter builds on the device understanding established before it, and the final chapter applies the optimized device to a real sensing problem.

Chapter 1 summarizes the basics of nanoscale MOSFET, scaling issues, and short-channel effects. After that, the ways to overcome the short-channel effects are discussed. In this regard, the different engineering schemes and the advanced FET structures, such as SOI MOSFET, TFETs and CNTFET, reported in different research articles, have been presented. Further, the research gaps found during the literature survey have been explored. Then, the chapter progresses toward the architecture of GNRFET, the basic working principle of GNRFET, and its potential advantages and drawbacks. Then, the thesis objective and overall organization of the thesis, and the importance of the research work presented in this thesis are discussed. **Chapter 2** carries out a DFT-based atomistic study of a GS-AGNRFET, examining how the gate stack itself, ambient temperature, and edge chemistry effect the device performance. With GS architecture, the off-state current drops by ~73 % and the SR goes up by a factor of about 213 over conventional GNRFET. When the temperature is raised from 250 K to 350 K, I_{on} reduced by ~48 %, SR degrades by 98 %, SS rises by ~ 56 %, and DIBL increases by138 times. This makes the proposed device is most useful at low temperature applications like cryogenic electronics, biomedical sensors applications. Additionally, the performance enhancement is

achieved through edge passivation engineering of AGNR channel with 13th and 15th group elements. Boron passivation reduces the bandgap and raises the PDOS near the Fermi level, I_{off} reduced by ~ 7.8 × 10^5 times and I_{on} goes up by ~ 139 times relative to P-AGNRFET, and the SR improves from ~ 7.1 × 10^3 to ~ 1.45 × 10^8. Overall, **Chapter 2** systematically demonstrated that gate stack dielectric engineering, temperature-dependent analysis, and edge passivation play a crucial role in governing the electrostatic behavior, transport efficiency, and leakage characteristics of armchair graphene nanoribbon FET at atomic scale. However, the proposed GS-AGNRFET with AGNR (N = 4) demonstrated exceptional switching performance but the systematic influence of varying the value of N belongs to 3p + 1 family on the electronic band structure, density of states, and quantum transport properties within the GS architecture remains unexplored. Therefore, to address this gap. the width engineering in channel material is analyzed in **Chapter 3.** The **Chapter 3** investigates the influence of channel width engineering on the electronic and quantum transport properties GS-AGNR FET using a semi-empirical density functional theory framework combined with Slater Koster DFT based model. AGNRs belonging to the 3p+1 family (N = 4, 7, 10, and 13) are systematically analyzed. The results reveal a strong inverse relationship between AGNR width and bandgap, with the narrowest ribbon (N = 4) exhibiting the largest bandgap (~1.98 eV), suppressed DOS near the Fermi level, and enhanced transmission control. When the AGNR (N = 4) implemented as the channel material in a gate-stack architecture, the GS-AGNR (N = 4) FET demonstrates significantly reduced off-state current and a markedly improved SR compared to wider ribbons having N = 7, 10 and 13. Also, Transmission spectra under varying drain bias, along with PLDOS and electrostatic potential profiles, further confirm superior gate control and reduced leakage for narrower channels. Overall, this chapter establishes channel

width as a critical design parameter and highlights GS - AGNR (N = 4) FET as promising candidates for low-power and nanoscale electronic applications. In this chapter the proposed device with width engineering is studied with SK model. The SK model is used with non-SCF [illegible] device modelling with different simulation approaches and the SCF iteration methods, which are studied in **Chapter 4.** This **Chapter 4** provides a comprehensive analysis of the reliability and performance of the GS-AGNRFET using EH model with the SCF iteration scheme within the NEGF framework. The two proposed device configurations, namely the A4 device and the A7 device, are systematically compared in terms of performance and reliability metrics using the EH model. The EH model demonstrates strong agreement with benchmark DFT methods in both bandgap and T (E) for AGNRs (N = 4 and 7), confirming its reliability over other models for device-level modeling. The DOS and bandgap comparisons validate the EH model [illegible] for the performance of GS-KQX] POb [illegible] improves I_{on} by 481 times, reduces I_{off} by 99. 92%, improves the SR, reduces V_{th} by 27.59%, and reduces DIBL by 16% in the A7 device as compared to the A4 device. Also, the higher value of DE for the A7 device signifies that the A7 device requires low voltage to achieve significant current modulation and high reliable for low power applications as compared to the A4 device. The comparison of static power with previously reported GNRFETs highlights [illegible]-power applications, making it an excellent candidate for use in energy-efficient electronics, biomedical devices, signal amplification, and sensors. Overall, the A7 device emerges as a highly promising and reliable device for advanced electronic applications, combining superior performance with lower power consumption. As discussed

in **Chapter 2**, the boron-passivated GS-AGNRFET demonstrates significantly improved device performance when the edges of P - AGNR are passivated with boron. However, the study of the remaining Icosagens group elements, namely Al, Ga and In, in the context of GS-AGNRFET edge passivation remains unexplored in the literature. To address this research gap, the performance investigation of all Icosagens group elements using the Extended Hückel model are investigated in **Chapter 5**. The passivation of Icosagens elements at the edge of bulk configured P AGNR significantly enhances electronic and transport properties. This includes a decrease in bandgap and improved DOS analysis. Additionally, TS analysis demonstrated that Al, Ga, and In passivated GNRFETs have higher electron tunneling probability, further enhancing device performance. Also, the effect of Icosagens is analyzed in terms of bandgap and DOS on the AGNR (N = 7). The results states that the passivation with the heavier Icosagens elements like Al, Ga, and In makes AGNR (N = 7) metallic in nature which constraints its use in semiconducting applications. Further, the effect of Icosagens group element passivation in the channel material of the GS - AGNRFET with AGNR (N = 4) shows significantly increase in Ion (from 1.06 µA to 18.4 µA in Al AGNRFET), reduced I_{off} (from 1.49×10^{-10} A to 5.43×10^{-16} A in In AGNRFET), and better value of SR (from 0.71×10^{4} to 0.35×10^{10}) for passivated AGNRFETs as compared with P AGNRFET. Owing to fast switching, low I_{off}, and improved parameters like g_m, DE, PLDOS, TP, and TS, Al AGNRFET and Ga AGNRFET are suitable candidates for high speed logic, low power memory devices, quantum computing in space exploration, and neuromorphic computing applications. Additionally, on comparing all proposed devices from **Chapter 2 to 5**, the **Al AGNRFET** shows improved results in terms of I_{on}, Ioff in Al AGNRFET And SR. Following a comprehensive analysis of all proposed device configurations, it is necessary to address the

gas sensing application that is the final objective of the thesis using the Al AGNRFET device. Therefore, to investigate the gas sensor application suitability, the **Chapter 6** is extended to develop a toxic gas sensor. This chapter investigates the performance of the proposed Al-KQX] POb %o±%º‰oÅö±qozs%‰o±%‰sÅ±ö≠%ö≠%‰vs%‰s≈sq~wöÅº‰t%XY %‰Ar %XR 4%‰Å%‰vw±%‰qvoü≈s≠2%‰vs% two-step simulation methodology is employed, the LCAO-GGA for bulk configured analysis and the EH model with NEGF-SCF formalism for device-level simulation is used. The bulk configured analysis confirmed that the P-AGNR shows chemisorption with positive adsorption sÅs≠uws±%‰t%74 A%‰d %ö≠%XY %‰Ar %94=%‰d %ö≠%XR 2%‰wv%‰v”±wqozz”%‰Å≠sozw±wq%‰sqö–s≠”%‰v s±% öt%‰4 %%‰6 %±%‰Ar %‰47%%‰6 %‰2%‰s±üsctively. This confirms that P-AGNR is not suitable for practical gas sensing. In contrast, the Al-AGNR shows stable physisorption with negative or±ö≠ü≈wöÅ%‰Ås≠uws±%‰t%64=8%‰d %ö≠%XY %‰Ar %6478%‰d %ö≠%XR 2%‰wv%‰v”±wqozz”%‰ soÅwÅut. z% recovery times of 5.4 × 76 %‰Ar %‰47%%‰6 %‰2%‰s±üsq~ws≈z’4%‰vs%‰sÅ±wwv”%‰oz.s±%‰t%‰9>+ % tö≠%XY %‰Ar %77>+ %‰ö≠%XR %–vwqv%‰≠s%‰94>%‰Ar %‰4>0 times higher than the P-AGNR, respectively. Further, tvs%XR %‰r±ö≠ü≈wöÅ%‰qo.±s±%‰%‰st~%‰vwv~%‰Å%‰vs%‰$_d$-V_{gs} curve with V_{th} r sq≠so±wÅu%‰ö~ %‰4—%‰1 %‰ö%‰4 =%‰1 4%‰vs%XY %‰r±ö≠ü≈wöÅ%‰qo.±s±%‰%‰uv~%‰vwv~%‰wv%‰$_{th}$ increasing ≈ö%‰4‰6%‰1 4%‰vs±s%‰üüö±ws%‰v≠s±vözr %‰öz~ous%‰vwv~±%‰t%‰6476%‰1 %‰Ar %‰1647=%‰1 %‰qöÅtw≠ %‰vs%‰.oz- direction sensing response of the proposed device. The I_{on}-based sensitivity is 85.14% for NO_2 and 7.03% for NH_3, while the SR-based sensitivity is 99.86% for NO_2 and 99.47% for NH_3. The value of K_{SC} using I_{on}-based sensitivity reaches 12.12 with NO_2 as the target gas, which confirms that the device responds 12.12 times more strongly to NO_2 than to NH_3 in terms of on current. The opposite response of the Al-AGNRFET to NO_2 and NH_3 across all sensing parameters along with the high I_{on}-based K_{SC} of 12.12 confirms that the proposed device can not only detect both gases but also distinguish between them with high selectivity. From the

above analysis, the authors conclude that the proposed Al-AGNRFET is a highly sensitive, ±szsq~ws2%Ar%szwpzs%AoÅö±qozs%sÅ±ö≠%ö≠%ws%s~sq~wÄ%t%XY %Ar%XR %ö"wq%o±s±%~%ö~ % temperature. Overall, this chapter establishes the Al-AGNRFET as a promising candidate for next-generation low-power nanoscale toxic gas sensing applications like environmental air quality monitoring, industrial safety systems, medical breath diagnostics, and automotive emission control.

7.2 SOCIAL IMPACT

The social and strategic impact of the Proposed device are as follows:

- **Health and Environment:** The proposed Al AGNRFET device as a toxic gas sensor in **Chapter 6** has a direct impact in health and environment areas. The proposed device works at room temperature, shows selectivity between two gases (NO_2 and NH_3), which makes this device can be used for medical breath diagnostics, wearable health monitors, industrial leak detection and automotive emission control systems.
- **Defence:** The proposed devices in this thesis work shows fast switching, reduced off current and low- static power than the conventional GNRFET devices. These electronic characteristics making them suitable for use in high-speed logic and low power memory application in defence electronics and space exploration systems.
- **Energy efficient Nanoelectronics:** The proposed device configurations operate at a low supply voltage (V_{ds} = 0.5 V) and shows improvement in I_{on}, I_{off} and switching ratio. These improvements are suitable for energy efficient applications in biomedical devices, signal amplifiers and sensors.

7.3 FUTURE SCOPE

The present thesis provides a strong atomistic modelling of GS AGNRFET for low power and toxic gas sensing applications. However, there are some objectives that can be explored in future work.

1. The proposed GS-AGNRFET can be extended to circuit-level implementations, such as inverters, logic gates, and low-power arithmetic blocks, to validate device-level performance at the system level and assess its suitability for next-generation nanoelectronics circuits.
2. To develop Nano sensors for monitoring plant health with proposed device.
3. Dual-gate (DG) and Lightly doped Drain and Source (LDDS) engineering can be implemented on proposed device to improve the SCEs and ambipolar conduction.
4. Due to its favorable low-temperature performance, the proposed device can be explored for cryogenic electronics, including quantum computing interfaces, space electronics, and biomedical instrumentation operating under ultra-low-power conditions.
5. The proposed device can be extended toward biosensing applications, such as glucose monitoring, disease biomarker detection, and wearable health monitoring systems due to its high surface sensitivity and low operating power.
6. The modeling framework can be extended to hybrid AGNR-based heterostructures with other 2D materials (such as Hexagonal Boron Nitride or Transition Metal Dichalcogenides) to further tune electronic properties and explore novel device functionalities beyond conventional transistor applications.